2nd International Symposium on Radio Systems and Space Plasma

U.R.S.I.

Sofia, Bulgaria
25-27 August, 2010

Proceedings

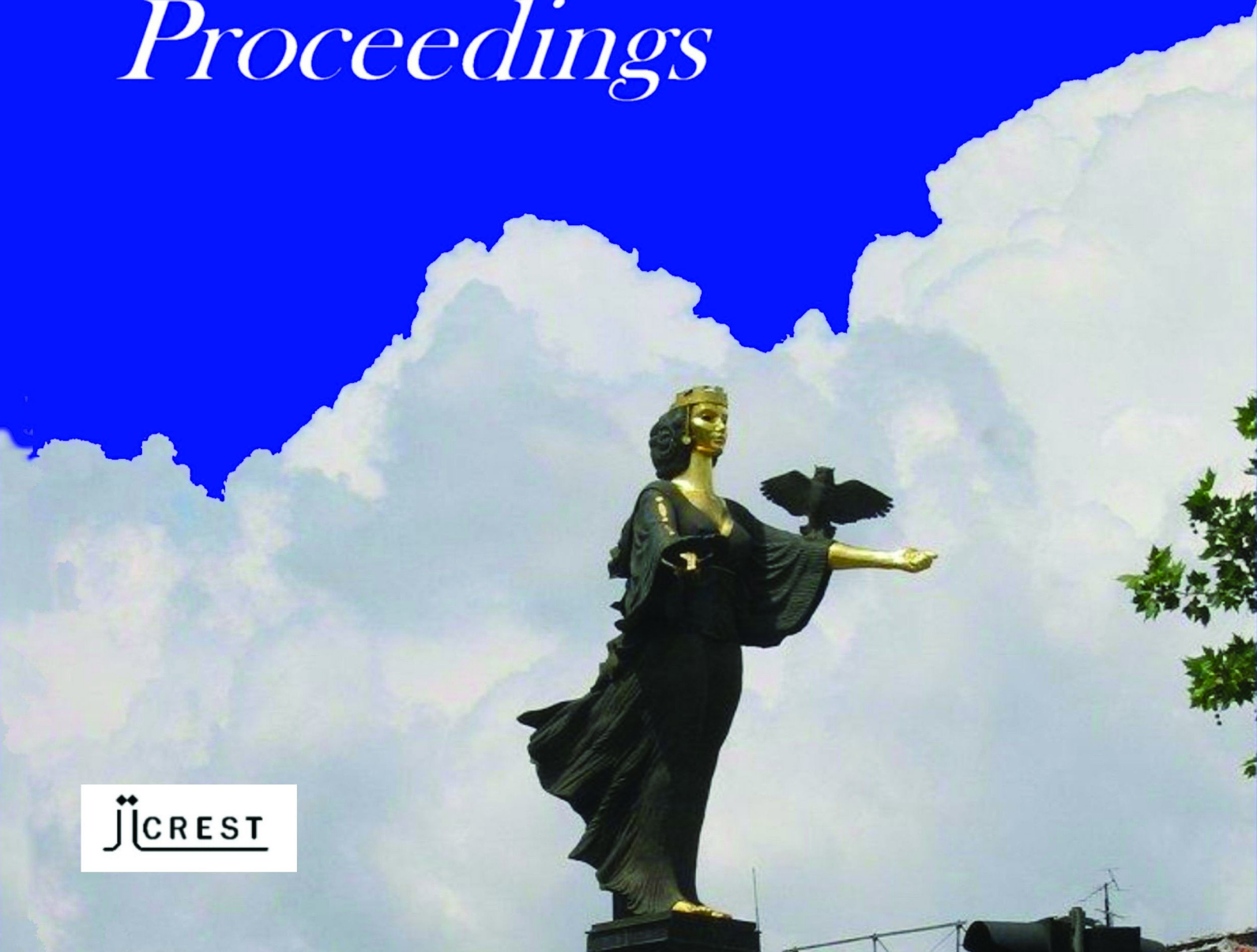

JICREST

ISRSSP 2010

PROCEEDINGS

of the

2nd International Symposium on Radio Systems and Space Plasma

Sofia, Bulgaria

August 25 – 27, 2010

Organized by

IICREST - Interdisciplinary Institute for Collaboration and Research on Enterprise Systems and Technology

in collaboration with

INSTICC - Institute for Systems and Technologies of Information, Control and Communication
BAS - Bulgarian Academy of Sciences
TU-Sofia - Technical University of Sofia

***

Technical Co-sponsorship by

Ruse University "Angel Kanchev"
Sofia Municipality
ARMSTECHNO Ltd.

***

Supported by

URSI - International Union of Radio Science

Copyright © 2010 SciTePress – Science and Technology Publications
All rights reserved

Proceedings of the 2nd International Symposium on Radio Systems and Space Plasma

Edited by Blagovest Shishkov

Cover Design: Canka Petrova Shishkova

Printed in Portugal
ISBN: 978-989-8425-27-0
Deposito Legal: 314702/10

http://www.isrssp.org

Brief Contents

Symposium Committees

STEERING COMMITTEE
Blagovest SHISHKOV, Bulgarian Academy of Sciences, Bulgaria
Canka PETROVA, Uniccord Research Center, Bulgaria

PROGRAM CHAIR
Blagovest SHISHKOV, Bulgarian Academy of Sciences, Bulgaria

PROGRAM COMMITTEE
Jorgen Bach ANDERSEN, Aalborg University, Denmark
Rumen ARNAUDOV, Technical University of Sofia, Bulgaria
A.K.M. BAKI, Independent University of Bangladesh, Bangladesh
Maurice BELLANGER, CNAM, France
Jun CHENG, Doshisha University, Japan
Peter DAVIS, ATR, Kyoto, Japan
Pierre KAUFMANN, Mackenzie Presbyterian University, Brazil
Hirotsugu KOJIMA, Kyoto University, Japan
François LEFEUVRE, LPCE/CNRS, France
Frank LITTLE, Texas A & M University, USA
Vladimir LYUBCHENKO, Russian Academy of Sciences, Russia
Hiroshi MATSUMOTO, Kyoto University, Japan
Yoshiharu OMURA, Kyoto University, Japan
Michel PARROT, LPCE/CNRS, France
Bodo REINISCH, University of Massachusetts - Lowell, USA
Michael RUDERMAN, University of Sheffield, UK
Tapan SARKAR, Syracuse University, USA
Naoki SHINOHARA, Kyoto University, Japan
Alexander SHMELEV, Radiotechnical Institute, Moscow, Russia
Tadashi TAKANO, Nihon University, Japan
Hideyuki USUI, Kobe University, Japan
Madalina VLAD, Association EURATOM/MEdC, Romania
Andrzej WERNIK, Polish Academy of Sciences, Poland
Ivan ZHELYAZKOV, Sofia University, Bulgaria

FOREWORD

This volume contains the proceedings of the Second International Symposium on Radio Systems and Space Plama (ISRSSP 2010).

This symposium is organized by the Interdisciplinary Institute for Collaboration and Research on Enterprise Systems and Technology (IICREST), in collaboration with the Institute for Systems and Technologies of Information, Control and Communication (INSTICC), the Bulgarian Academy of Sciences, Technical University of Sofia and technically co-sponsored by Ruse University “Angel Kanchev”.

ISRSSP 2010 is performed under the auspices of the International Union of Radio Science (URSI). Covering the topics of URSI commissions C, G, H (toward space plasma) and Space Solar Power System (SSPS), ISRSSP 2010 brings together influences from all of the above commissions. More exactly, the scientific program of the symposium is concerned with the international development and application of the broad range of aspects:

(i) Radio-Communication (RC) Systems and Signal Processing
(ii) Transionospheric Propagation. Investigation of Space Environments via Satellite Observations
(iii) Generation and Propagation of Waves in Plasmas. Interaction between Waves and Wave Particles
(iv) Solar Power Satellite (SPS) Systems and related Radio Technologies. Further Directions in SPS Systems

It is not only that ISRSSP 2010 adopts the URSI research agenda but it has as well spread its influence to a broader audience including all those researchers and practitioners who are interested in the topics of the symposium. Their participation is additionally strengthening the URSI-related research and the RC research developments. All this inspires the organizers to go forward with this event, contributing to the dissemination of radio science -related knowledge.

Considering two types of papers, namely Invited Papers and Regular Papers, and following the ISRSSP 2010 Call for Papers and received submissions, ISRSSP 2010 has selected papers for oral presentation during the symposium and for publication in these proceedings. These are papers authored by distinguished scientists from all over the World, reflecting their actual findings in the areas of ISRSSP. The selected papers are a good illustration of different relevant topics that are currently under research, presenting original contribution in the following broadly defined topics: Intelligent Methods of RC Systems and Signal Processing;Transionospheric Propagation and Satellite Observations; Methods for Analyzing Non-linear Interactions of Space Plasma; Radio Science Aspects of SPS Systems.

The ISRSSP'10 program includes not only the presentation of the papers that represent the main content of the current proceedings but also discussions that concern the further ISRSSP-URSI agenda. These high points in the symposium program definitely contribute to reinforce the overall quality of ISRSSP 2010.

The program for this symposium required the dedicated effort of many people. We must thank the authors, whose research and development efforts are recorded here. We thank also the members of the program committee for their support and enthusiasm. A special thanks to the President of URSI - Francois Lefeuvre whose collaboration was fundamental for the success of this symposium. Last but not least, we would like with great pleasure to thank also the IICREST team and especially Canka Petrova Shishkova for the brilliant collaboration.

We wish you all an inspiring symposium and an unforgettable stay in the beautiful city of Sofia.

Blagovest Shishkov
Bulgarian Academy of Sciences
President of Bulgarian URSI Committee
Chair of ISRSSP 2010

MESSAGES

Blagovest SHISHKOV
President of the Bulgarian URSI Committee
Chair ISRSSP’10

Dear Colleagues,

I turn to you in my capacity of President of the Bulgarian URSI Committee and as well Chair of the Second International Symposium on Radio Systems and Space Plasma (ISRSSP' 2010), extending to all a warm welcome and wishes for an inspiring symposium.

Covering the topics of URSI commissions C, G, H (toward space plasma) and Space Solar Power System (SSPS), ISRSSP 2010 brings together influences from all of the above commissions, recognizing URSI as the scientific body coordinating this research field on an international basis.

Considering radio and its application as core technological developments during the 20th century, we have witnessed the wide penetration of this technology, expanding the horizon of human activity into modern life style. The main application of this technology today concerns telecommunications, in general, and mobile communications, in particular. However, radio can also be used for other purposes in the light of human welfare. Hence, for adequately maintaining human welfare and avoiding perishing disasters, radio technology and its applications may be of essential use. Thus, this technology needs to be seriously discussed, steered and controlled and I am pleased to announce this as a key priority for the Bulgarian URSI Committee. With regard to this, I would like to stress especially on the importance of ISRSSP'10, organized by the Interdisciplinary Institute for Collaboration and Research on Enterprise Systems and Technology (IICREST) in close collaboration with the Bulgarian URSI Committee, under the auspices of URSI. The ISRSSP'10 event plays a role not only in the direction of reinforcing URSI research activities within and across different URSI commissions but also in the direction of disseminating research results as an inspiration for new applications.

With talks of distinguished scientists from many countries who present original research findings, ISRSSP'10 makes a useful contribution, in my opinion, at least in the following scientific directions, in line with this year symposium's topics: Intelligent Methods of RC Systems and Signal Processing; Transionospheric Propagation and Satellite Observations; Methods for Analyzing Non-linear Interactions of Space Plasma and Radio Science Aspects of SPS Systems.

I turn to all authors, sincerely appreciating their preparing papers of high quality. I would like to express gratitude to URSI for the support, to IICREST for the brilliant organization, and also to the publisher, SciTePress.

Let's come together for an inspiring ISRSSP'10 event!

François LEFEUVRE
President of URSI - International Union of Radio Science

Congratulations to the Steering Committee, and in particular to Professor D.Sc. Blagovest Shishkov, for the organisation of the ISRSSP'10 meeting. By covering specific aspects of the URSI commissions C, G, and H, with a few extensions to commission F thematic, the proposed programme perfectly fits with two major URSI priorities: the development of transversal activities between different domains of radio science, and the contribution to answering societal demands. On the other hand, as suggested by Professor D.Sc. Blagovest Shishkov in his meeting announcement, the ISSRSSP'10 meeting shows the importance of initiatives taken by URSI national committees for the future of URSI.

One of the originalities of URSI is the existence of ten scientific commissions covering in a complementary way all domains of radio science. It happens that a radio scientist is so specialized that he participates to activities of only one commission. However, most radio scientists come to URSI meetings to extend their competency domains, to look for new ideas and new techniques, and to set up or reinforce new partnerships. To this regards, the URSI Long Range Planning Committee has recently asked each commission Chair to look for points in the mission statements of other commissions which may be of interest for them. First results of this exercise have been discussed at the April 2010 "coordinating committee meeting" (i.e. the preparatory meeting for the 2011 GASS in Istanbul). A provisional conclusion is that numerous bridges exist between the commissions but that efforts have still to be made to draw all benefit from inter-commission activities. Meetings like ISSRSSP'10 provide an excellent opportunity for promoting transversal activities.

Answering to societal demands is a very difficult task for all Scientific Unions. The society is waiting for definitive answers. The scientists can only bring elements of answers. Following controversies appeared within the Union during the elaboration phase of the URSI White Paper on "Solar Power Satellites" (SPS), then on the start of the White Paper on "Communications, mobile and Health", the URSI Board recommends to radio scientists to be very careful to communicate on their domains of expertise only, i.e. on purely technical aspects. As observed with the final issue of the WP on SPS, this does not prevent from

misinterpretations, but it is the only way to reach a consensus in a scientific community. It is the same approach which is recommended for an URSI contribution to international programmes like the Integrated Research on Disaster Risk (IRDR) launched in 2008 by the International Council for Science (ICSU). Several papers which will be presented during the ISSRSSP'10 meeting clearly demonstrate the involvement of Radio Science in risk management. Reviews of those types of involvement are needed. At the 2008 URSI GA (Chicago) the URSI Inter-commission Working Group on "Natural and Human-Induced Hazards and Disasters" has been created for that reason. Thank you in advance to those of you who will accept to join this WG.

As a conclusion, let me take the advantage of the presence of Presidents and members of several URSI National Committees to tell a few words on the role of National Committees in the development of radio science in their country and abroad. As demonstrated by the ISSRSSP'10 meeting, the National Committees are in a good position to promote inter-commission activities and to explore specific domains like science and society. Besides, being directly in contact with national organizations, they provide natural interfaces between URSI and international organizations. A particularly good example concerns the telecommunications. Most National Committees have members involved in frequency Agencies and so in ITU (International Telecommunication Union) activities. They are the ones who may reinforce relationships between URSI and ITU. In the same way, scientific cooperation often starts between neighbouring countries. As a consequence they are mainly National Committee members who may help neighbouring committees when needed.8 I hope that, in between two scientific sessions, we have the opportunity to discuss all those points of first importance for the future of URSI. Obviously, Commission representatives who are present are welcome to those discussions.

I wish everybody a very exciting and very rich meeting.

François Lefeuvre

INVITED SPEAKERS

INVITED SPEAKERS

Dr. **Mauro Soares de ASSIS,** Professor
AFFILIATION:
Fluminense Federal University,
Niterói, BRAZIL

He was graduated at Pontifical Catholic University of Rio de Janeiro with a BScEE in 1964 and a MScEE in 1966. In 2000 he received the title of Notorious Knowledge (equivalent to Doctor degree) from the Military Institute of Engineering, Rio de Janeiro, Brazil. He is currently full time Professor at Fluminense Federal University, Niterói, Brazil. He is co-founder of the Center of Studies in Telecommunications of Catholic University (CETUC), being its Director from 1969 to 1979. From 1979 to 1981 he was with Promon Engenharia as Consulting Engineer, from 1981 to 1990 with EMBRATEL (Brazilian Enterprise of Telecommunications), and from 1990 to 2000 with the Federal Government (Ministry of Communications and ANATEL – National Agency of Telecommunications). His research areas are radio wave propagation and communication systems. The main topics of interest are: diffraction, radio meteorology, rain attenuation, ionospheric propagation and fixed and mobile communication systems. In November 2009 he was nominated President of the Brazilian Committee of URSI.

DSc **Christo KABAKCHIEV**, Professor
AFFILIATION:
Department of Software Technologies, Sofia University,
Sofia, BULGARIA
SCIENTIFIC INTERESTS:

• CFAR Techniques for Signal Detection in Pulse Jamming
• Multy Sensor Detection and Estimation - Performance Calculations with Simulation Approach
• Track Detection with Hough Transform
• Radar and Communication Signal Processing in Network
• Cluter and Jamming Cancelation with Space Time Adaptive Procesing
• Systolic and Multiprocessor Architecture for Signal Processing

Dr. **Mohamed LATRACH,** Professor
AFFILIATION:
Ecole Supérieure d'Electronique de l'Ouest (ESEO),
Angers, FRANCE

Mohamed LATRACH, Professor of Microwave Engineering with the Ecole Suprieure d'Electronique de l'Ouest (ESEO), Angers, France, where his research involves RF and Microwave. Field of interest is the design of hybrid, monolithic active and passive microwave circuits, metamaterials, Left Handed Materials, antennas and their applications in wireless communications, and wireless power transmission

Competences de Mohamed LATRACH: Microwave, Antennas, Wireless Power Transmission, Left handed materials, RFID, Rectennas

DSc **Andon D. LAZAROV,** Professor
AFFILIATION:
Bourgas Free University, Bourgas, BULGARIA
His field of interest includes SAR-ISAR-InSAR modeling and signal processing techniques: spatial correlation image reconstruction methods, recurrent Kalman procedures and iterative LMSE methods. He has authored above 100 research and conference papers. He is a member of the IEEE, the AES Society and CS of USA, and a member of Trans Black Sea Region Union of Applied Electromagnetism of Greece. He is a guest-editor of special issue on ISAR signal processing of IET Journal, Canada, and a member in editorial board of Applied Electromagnetism Journal -Greece.
Andon Dimitrov Lazarov was born in Bourgas, Bulgaria. He received the M.S. degree (1972) from Leningrad Electrotechnical Institute (Electrotechnical State University - Saint Petersburg), Russia, in electronical engineering, PhD. degree (1978) from Minsk Air-Defense Military University, Belaruss and D.Sc. degree (1998) from Shoumen Military University for Artillery and Air Defense. Since 1984 he is associate professor and since 2000 he is full professor at the Air Defense Department of the Military University for Artillery and Air-Defense of Shumen, Bulgaria. Since 2002 he is a full professor at Burgas Free University, Burgas. At the beginning of his scientific career his research interests are in the field of the analysis and realization of the maximum power transmitting characteristics of the active and passive multiport circuits.

DSc **Eugene NICKOLOV,** Professor
AFFILIATION:
Bulgarian Academy of Sciences, National Laboratory of Computer Virology, Sofia, BULGARIA
MAJOR FIELDS OF SCIENTIFIC RESEARCH: • Informatics. • Operating Systems - algorithms, effectiveness, protections. • Theoretical Basics - abstracts models, theory of programs. • Computer Technologies - simulation and modeling. • Communication Technologies - simulation and modeling. • Data - cryptographic, theory of information and coding. • Cyber security – data, computers, communications, systems. • Stegano Objects – analyze, syntheses, protection.
MEMBERSHIP IN SCIENTIFIC AND/OR PROFESSIONAL INSTITUTIONS, BODIES, AND ORGANIZATIONS: • Union of Scientists in Bulgaria, 1995 - continued; • Union of Automatics and Informatics (BG), 1995 - continued; • Union of Electronics, Electro-technique and Communications (BG), 1995 - continued; • Association for Computer Machinery, Bulgarian Chapter, 1992 - continued; • IEEE's Computer Society, Bulgarian Chapter, 1995 - continued.
HONOURS/TITLES/QUALIFICATIONS (ORGANIZATION, TITLE, YEAR OF AWARD):
PhD on Computer Engineering, CIITT, 1986,
DSc on Mathematics, NLCV, 2002,
Prof. on Informatics, NLCV, 2004.
PREVIOUS EXPERIENCE:
Bulgarian Academy of Sciences, Vice President, 2008 –
National Laboratory of Computer Virology – BAS, (CEO), Professor, DSc, 1991

Dr. **Yoshiharu OMURA,** Professor
AFFILIATION:
Computer Space Science, Radio Science Center for Space and Atmosphere, Kyoto University, Kyoto, JAPAN
AREAS OF INTEREST: • Space Plasma Physics • Computer Simulations of Plasmas • Solar Terrestirial Physics • Supercomputing Microwave Power Transmission
ACADEMIC SOCIETY:
• Institute of Electronics, Information and Communication Engineers
• Society of Geomagnetism and Earth, Planetary and Space Sciences
• American Geophysical Union

Dr. **Jacques PALICOT,** Professor
AFFILIATION:
SUPELEC/IETR, Cesson-sévigné, FRANCE
Jacques PALICOT received, in 1983, his PhD degree in Signal Processing from the University of Rennes. Since 1988, he has been involved in studies about equalization techniques applied to digital transmissions and new analog TV systems. Since 1991 he has been involved mainly in studies concerning the digital communications area and automatic measurements techniques. He has taken an active part in various international bodies EBU, CCIR, and within RACE, ACTS and IST European projects. He has published various scientific articles notably on equalization techniques, echo cancellation, hierarchical modulations and Software Radio techniques. He is currently involved in adaptive Signal Processing and in new techniques as Software Radio and Cognitive radio. From November 2001 to September 2003 he had a temporary position with INRIA/IRISA in Rennes. Since October 2003 he is with Supelec in Rennes where he leads the SCEE department.

Dr. **Erdal PANAYIRCI,** Professor
AFFILIATION:
Department of Electronics Engineering, Kadir Has University Istanbul, TURKEY.
Erdal Panayirci received the Diploma Engineering degree in Electrical Engineering from Istanbul Technical University, Istanbul, Turkey in 1964 and the Ph.D. degree in Electrical Engineering and System Science from Michigan State University, East Lansing Michigan, USA, in 1970. He spent 2008-2009 academic year in Princeton University as a Visiting Research Fellow. Currently he is the Department Head of the Electronic Engineering Department at Kadir Has University, Istanbul, Turkey. His research interests include communication theory, synchronization and equalization, multicarrier systems, coded modulation and interference cancellation with array processing and space-time coded and MIMO systems. He published extensively in the leading scientific journals and the international conferences. He has co-authored the book Principles of Integrated Maritime Surveillance Systems (Boston, Kluwer Academic Publishers, 2000). He is the director of the Network of Excellence in Wireless Communications (NEWCOM), representing Kadir Has University, established recently by the European Commission on the Sixth Frame Program which focuses on activities in the field of research, technological development and demonstration.
Prof. Panay?rc? was an Editor for IEEE Transactions on Communications in the areas of Synchronizations and Equalizations in 1995-1999. He was the Technical Program Co-Chair of the IEEE International Conference on Communications (ICC2006) held in Istanbul, Turkey in June 5-11, 2006 and Technical Program Chair of the upcoming IEEE PIMRC to be held in Istanbul Turkey in 2010.. He is a Fulbright-Hays Fellow, NATO Scientist Fellow and IEEE Fellow. He is Member of Sigma Xi.

Dr. **Michel PARROT,** Professor
AFFILIATION:
LPC2E/CNRS, Orle'ans, FRANCE
Employement : 1975 1991 : Ingenieur de Recherche au LPCE, 1991-2002: Charge de Recherche au LPCE, 2002- Directeur de Recherche au LPCE
Direction of thesis: 7 Area of activity: His work is essentially related to the analysis of natural and artificial signals observed in a frequency range from a few Hz up to 1 MHz by magnetospheric satellites. Concerning the emissions coming from the surface of the planets, he studied the effects of the waves emitted by the anthropogenic activities in the terrestrial ionosphere and the dust electrification in the Martian atmosphere. He participated in the definition and the data processing of many experiments onboard satellites (GEOS 1 and 2, ARCAD-3, INTERBOL, CLUSTER, and MARS96). He is currently the principal investigator of the DEMETER micro-satellite which is dedicated to the study of ionospheric perturbations in relation with the seismic activity (launched in 2004). He is author of 190 papers published in journal with referees.

DSc **Dimitar RADEV,** Professor

AFFILIATION:
Department of Communication Systems and Technologies, University of Russe, Russe, BULGARIA

Dimitar Radev, is a Professor at Department of Communication Technique and Technologies at the University of Rousse, Bulgaria. He is the Author of numerous publications. His mainly research interests are connected with teletraffic theory, simulation and modelling of communication networks, rare event simulation, evaluation of quality of service parameters, performance analysis of queuing systems and neural network modelling.

Dr. **Ilia ROUSSEV,** Professor

AFFILIATION:
Institute for Astronomy, University of Hawaii, Honolulu, USA
Ilia Roussev, Associate Astronomer/Professor, Institute for Astronomy
Ph.D. Solar Physics, Queen's University at Belfast, Belfast, Northern Ireland
M.S. Physics and Astronomy, Sofia University St. Kliment Ohridski, Sofia, Bulgaria

Specializations and Research Interests:
•Advance knowledge about the Sun, heliosphere and local cosmos
•Explore the nature of solar and astrophysical plasmas by developing high-performance computational models based on first principles and coupled with observations
•Pursue analytical and computational studies of the solar atmosphere, concentrating on processes that couple the photosphere with the overlying corona and solar wind

Dr. **Naoki SHINOHARA,** Professor

AFFILIATION:
Research Institute for Sustainable Humanosphere, Kyoto University, Kyoto, JAPAN

Naoki Shinohara received the B.E. degree in electronic engineering, the M.E. and Ph.D (Eng.) degrees in electrical engineering from Kyoto University, Japan, in 1991, 1993 and 1998, respectively. He was a research associate in the Radio Atmospheric Science Center, Kyoto University from 1998. He was a research associate of the Radio Science Center for Space and Atmosphere, Kyoto University by recognizing the Radio Atmospheric Science Center from 2000, and there he was an associate professor since 2001. From 2004, he has been an associate professor in Research Institute for Sustainable Humanosphere, Kyoto University by recognizing the Radio Science Center for Space and Atmosphere. He has been engaged in research on Solar Power Station/Satellite and Microwave Power Transmission system. He is a member of the IEEE, URSI Commission C (Signals and Systems), the IEICE and IEEJ.

DSc **Blagovest SHISHKOV,** Professor

AFFILIATION:
Institute of Mathematics and Informatics, Bulgarian Academy of Sciences, Sofia, BULGARIA

Blagovest Shishkov received the Ph.D. degree in Physics from the Institute of Electronics, Bulgarian Academy of Sciences and his D.Sc. degree from the Technical University of Sofia. Presently, he is at the Department Probability & Statistics in the Institute of Mathematics and Informatics (Bulgarian Academy of Sciences). He has published more than a hundred research papers and three books in Signals Transmission (Signals, Filtering and Detection) and especially asymptotic methods in parameter estimation,signal detection and identification, pattern recognition and data quantization. His latest investigations and results are connected by signal processing of cyclostationary signals and detecting and studying of nonlinear wave interactions by using higher-order statistics. Both areas are successfully incorporated into adaptive antenna beamforming and analysis of time series associated with space data. The last investigation was devoted to mathematical modeling and optimization of the side lobes of large antenna arrays toward SPS/MPT applications. He was Visiting Professor in Japan (seven times), France (three times), Spain etc. Official Member of the URSI Commission C, member of the IEEE, EURASIP, and IEICE (Japan).

DSc **Alexander SHMELEV**, Professor

AFFILIATION:
Radiotechnical Institute by Academician A.L.Mints, Moscow, RUSSIA

Prof. A.Shmelev is author of the monograph “Principles of the Markovian theory of random fields non-linear processing” - Moscow Inst. of Phys.&Technol. Press, 1998.

His research interests include: 1. Markovian theory of optimal random signals reception and processing in presence of noise and interference, including space-time non-linear detection of signals and estimation of their parameters in large-aperture and multipositional receiving or sensor systems. 2. Theory of wave scattering on randomly rough surfaces

Over 10 years A. Shmelev is the chairman of Commission C of the Russion National Committee URSI.

Alexander Shmelev was born in Moscow, Russia, in 1944. He was educated at Moscow Institute of Physics and Technology (MIPT), Faculty of Radioengineering and Cybernetics (1962-68) and at Post-graduate Studentship of MIPT, Faculty of General and Applied Physics (1968-71). He received degrees from MIPT: Candidate of Physical and Mathematical Sciences in 1971 and Doctor of Technical Sciences in 1986. Candidate dissertation topic – “Toward the theory of wave scattering by randomly rough surfaces on the basis of Kirchhoff’s method”. Doctoral dissertation topic – “Markovian theory of random fields non-linear processing”. From 1971 up to now he is working at the Radiotechnical Institute by Academician A.L.Mints (1971-75 – Junior Scientist, 1975-87 – Senior Scientist, 1987-present – Head of Science Department). He has the second job at MIPT (1985-93 – Assistant Professor and 1993-present – Professor of Radiophysics Chair).

DSc **Angela SLAVOVA,** Professor

AFFILIATION:
Institute of Mathematics and Informatics, Bulgarian Academy of Sciences, Sofia, BULGARIA

Professor Slavova has more than 60 publications in prestigious journals in Applied Mathematics, IEEE Journals, etc. She is an author and co-author of 2 monographs. Prof. Slavova is a member of AMS, SIAM, Board of Bulgarian Section of SIAM, Board of Bulgarian Section of WSEAS, EMS, IEEE Technical Committee on CNNAD.

She was visiting professor at the University of Ioannina, Greeece, University of Catania, Italy, University of Torino, Italy, Astronomical Observatory, Torino, Italy, College of Judea and Samaria, Ariel, Israel, University of Ferrara, Italy, University of Bologna, University of Florence, Italy, Ben-Gurion University, Israel, etc.

Prof. Slavova graduated at Technical University, Russe, Computer Engineering, M. Sc. in 1986. In the period 1992-1993 she got Fulbright Scholarship at Florida Institute of Technology, Florida, USA. She got her Ph.D. in Mathematics in 1994. In 2005 she became Doctor of Science and in 2007 Full Professor at the Institute of Mathematics and Informatics, Bulgarian Academy of Sciences. Since 2004 Prof. Slavova is a Head of the Department of Mathematical Physics, Institute of Mathematics, Bulgarian Academy of Sciences. She participated in more than 30 conferences, workshops and seminars as an invited speaker. She got in the period January-July 1998 - CNR Fellowship, University of Florence, Italy.

Dr. **Tadashi TAKANO,** Professor

AFFILIATION:
Nihon University College of Science and Technology, Department of Electronics and Computer Science, Narashino-dai, Funabashi, JAPAN

Professor Emeritus ISAS/ JAXA. He is the manager of the APAA Project. His current research interests include antenna engineering, and radio- and optical-wave applications.

Tadashi Takano Is a member of IEEE (Fellow), URSI, IEICE (Fellow), Japan Society of Information and Communication Research, Japan Society of Aeronautical and Space Sciences, Japanese Rocket Society, American Geophysical Union, Seismological Society of Japan.

Tadashi Takano was born in Tsukuba, Japan.

He received the B.S., M.S. and Ph.D. degrees in electric and electronics engineering from the University of Tokyo.

Dr. **Makoto TAROMARU,** Professor

AFFILIATION:

ATR Wave Engineering Laboratories, Kyoto, JAPAN

Makoto Taromaru was born in Fukuoka, Japan in 1962. He received BE and ME degrees in electronics engineering from Tokyo Institute of Technology, Tokyo, Japan, in 1985 and 1987, respectively, and PhD degree from Kyushu Institute of Technology, Fukuoka, Japan, in 1997. In 1987, he joined Kyushu Matsushita Electric Corporation where he worked on the development of radio signal processing for Personal Handy-phone System (PHS) and other digital cordless telephone systems. Between 2001 and 2004, he was with the Faculty of Engineering, Kyushu Sangyo University, Fukuoka, Japan, where he was an associate professor of the department of Electronics. Since April 2004, he has been with ATR Wave Engineering Laboratories, Kyoto, Japan, and he is currently the head of the Department of Wireless Communication Systems. His research interests include radio communicatio systems, especially on diversity and adaptive antenna systems. Taromaru is a member of IEEE and IEICE

Dr. **Hideyuki USUI,** Professor

AFFILIATION:

Graduate school of system informatics, Kobe University, JST/CREST, Kobe, JAPAN.

Hideyuki Usui received the B.S. degree from Department of electrical engineering, Kyoto University, Japan in 1986, and the M.S. and Ph.D degrees from Department of Electronics, Kyoto University, Japan in 1989 and 1994, respectively. He started working as a Research Assistance at Radio Science Center for Space and Atmosphere in Kyoto University, Japan at 1992. He stayed as a visiting scientist at the Plasma Theory and Simulation Group in the University of California Berkeley in 1997. In 1999 he was promoted to an associate professor and continued to work at Research Institute for Sustainable Humanosphere in Kyoto University. He moved to Kobe University in 2009 and he has been currently working as a professor at the graduate school of system infomatics in Kobe University.

Dr. **Madalina VLAD,** Professor

AFFILIATION:

National Institute of Laser, Plasma and Radiation Physics,Bucharest, ROMANIA

•2004-2009 member of Scientific Commetee of the European Fusion Theory Conference

•2006-2009: Director of the Project “Turbulence and quasi-coherent structures in fluids and space plasmas”.

•2007-2008:position for foreigner scientists as Director of Research at CNRS, Universite de Provence, France

•Since 1994, for various periods that add to more than 5 years, the „Departement de Recherche sur la Fusion Controlee”, Commissariat a l’Energie Atomique

•1998-2000, co-director of the NATO Linkage Grant CRG.LG 971484, “Statistical Physics for anomalous transport in plasmas”, collaboration between groups from DRFC-Cadarache (France), Universite Libre de Bruxelles (Belgium) and our institute.

•2000-2002, co-director of the NATO Linkage Grant PTS CLG 977 397, “Mathematical Physics for anomalous transport in plasmas and fluids”, collaboration between groups from DRFC-Cadarache (France), Universite Libre de Bruxelles (Belgium), Craiova University and our institute.

•In 2003 (January-June) - invited professor at the National Institute for Fusion Science, Toki, Japan

•In the period October 2004 to March 2005 - invited professor at Kyushu University, Japan.

•Since 2000, I am referee at several scientific journals (Physical Review Letters, Physical Review E, Physics of Plasmas, Plasma Physics and Controlled Fusion, Nuclear Fusion).

Dr. **Shigeto WATANABE,** Professor
AFFILIATION:
Department of Cosmoscience Hokkaido University, Sapporo, JAPAN
SPECIALIZATIONS AND RESEARCH INTERESTS:
• Computer Science
• Space Science
• Earth/Space Science
• Planetary Atmosphere and Magnetosphere

Dr. hab. **Andrzej WERNIK,** Professor
AFFILIATION:
Space Research Center, Polish Academy of Sciences, Warsaw, POLAND
FIELDS OF INTEREST:
• Ionospheric plasma physics
• Wave propagation in random media
• Nonlinear dynamics

Dr. **Yukihiro KAMIYA,** Associate Professor
AFFILIATION:
Tokyo University of Agriculture and Technology, Tokyo, JAPAN
• Faculty of Engineering Department of Electrical and Electronic Engineering
• Institute of Symbiotic Science and Technology Division of Advanced Electrical and Electronics Engineering
• Graduate School of Engineering Department of Electrical and Electronic Engineering
• Faculty of Engineering Department of Electrical and Electronic Engineering
EDUCATION: 2000 Completed Nagoya University; 1994 Completed Nagoya University; 1992 Graduated Faculty of Computer Science and Systems Engineering, Kyushu Institute of Technology; 1990 Graduated Toyota National College of Technology
FIELD OF SPECIALIZATION: Communication/Network Engineering
RESEARCH KEYWORDS: Mobile communication systems, Adaptive signal processing, Digital signal processing, Adaptive array antenna

Dr. **Hirotsugu KOJIMA,** Associate Professor
AFFILIATION:
Laboratory of space system and astronautics,
Research Institute for Sustainable Humanosphere, Kyoto University, Kyoto, JAPAN
RESEARCH SUBJECTS:
• Plasma wave investigation in space plasmas
• Sensor network system in space
Ph.D. of Kyoto University(Engineering), Department of Electrical Engineering, November, 1998
April, 1999-present Associate Professor, Kyoto University

Dr. **Yoshiyuki FUJINO,** Senior Researcher
AFFILIATION:
New Generation Wireless Communications Research Center, National institute of Information and Commuinications Technology (NICT), Tokyo, JAPAN.
Yoshiyuki Fujino received the M.S. and Ph.D. degrees in electrical engineering from Tohoku University, Sendai, Japan, in 1989 and 1999, respectively. After joining the Communications Research Laboratory (CRL), [currently NICT] in 1989,he engaged in research on numerical analysis of antenna characteristics and wireless power transmission technologies. He also has been researching for helicopter satellite communication system,large deployable antenna evaluation in orbit and satellite terrestrial integrated communication system. He is currently a Senior Researcher in the Space Communications Group of the NICT.

Mr. **Yoshiharu FUSE,** Senior Researcher

AFFILIATION:
Institue for Unmanne Space Experiment Free Flyer, Tokyo, JAPAN
EDUCATION:
1981 Graduated Dept. of Radio Communication Engineering, Faculty of Electro Communications, The University of Electro-Communications, Tokyo Japan
CAREER:
1981/04- MHI NAGOYA Aerospace Systems works, Space System Division
2007-2009 MHI SSPS Project Manager
2009/04- USEF(Institute for Unmanned Space Experiments Free Flyer), Senior Researcher
FIELD OF INTEREST:
Space Solar Power System
System Application of Wireless Power Transmission
Electric Systems for Space Vehicles, Large Strictures, and Space Crafts

Dr. **Michel HAMELIN**

AFFILIATION:
Université Versailles St Quentin CNRS/INSU LATMOS-IPSL, UPMC, Paris, FRANCE
Michel Hamelin, Dr. d'Etat, University of Orleans,1978, has been working in several laboratories of CNRS from 1969. He worked in the field of waves in space plasmas in LPCE, Orleans, being Co-I in several rocket and satellite experiments and PI of the DION experiment on the PHOBOS soviet mission. In CETP and now in LATMOS laboratories he has been working in the field of terrestrial and planetary atmospheric electricity with the PEASMA balloon experiment and in particular with the PWA-HASI experiment in the atmosphere of Titan. He was the leader of an ISSI team about Titan atmospheric electricity, from which salient results are presented.

Dr. **Frank LITTLE**

AFFILIATION:
Space Engineering Research Center, Texas A&M University, USA
Dr. Frank little is Associate Director of the Center for Space Power at Texas A&M University.
He was a member of the Texas A&M team that participated in the Japanese led ISY-METS space microwave power transmission experiment.
Dr. little is a TEES Distinguished Scientist at the Space Engineering Research Center at Texas A&M University. He received his PhD in Chemistry from the University of California, Davis in 1976. Following graduation, he served on the faculty of the Department of Chemistry at UC, Davis as a lecturer. From 1978 to 1982, he was on the staff of the Crocker Nuclear Laboratory at UC, Davis as a Research Associate. In 1982, he joined the Gas Research Institute in Chicago, Illinois, as Project Manager, Thermodynamics.
In 1986, he became Assistant Director of the Space Research Center at Texas A&M University. He helped to establish and then joined the Center for Space Power at Texas A&M in 1989, becoming Associate Director in 1993. The Center for Space Power was renamed the Space Engineering Research Center in 2009. He has been involved with wireless power transmission research for almost 20 years. He participated a collaborative project (it included William C. Brown) to design, fabricate and fly a rectenna panel on the Japanese led ISY-METS sounding rocket experiment in 1993.
He was active in the NASA "Fresh Look" and subsequent studies and has participated in research on microwave rectennas, retrodirective transmission systems and satellite design. Most recently, he participated in a project to demonstrate wireless power transmission that was filmed and shown on the Discovery Channel.

Dr. **Tomohiko MITANI**

AFFILIATION:
Laboratory of Applied Radio Engineering for Humanosphere, Research Institute for Sustainable Humanosphere (RISH), Kyoto University, Kyoto, JAPAN
CURRENT POSITION: Assistant Professor
EDUCATION
Ph.D. (Electrical Engineering, Engineering), 2006, Kyoto University. Title: Study on Noise Features of Magnetron and Low Noise Wireless Power Transmission;
Master Deg. (Communications and Computer Engineering, Informatics), 2001, Kyoto University;
Bachelor Deg. (Electrical and Electronic Engineering, Engineering), 1999, Kyoto University.
WORKING CARRIER
2003-2004: Instructor, Radio Science Center for Space and Atmosphere, Kyoto University.
20004-2007: Instructor, RISH, Kyoto University
2007-present: Assistant Professor, RISH, Kyoto University
RESEARCH INTERESTS: Applied microwave engineering; Microwave power transmission; Microwave heating technology; Vacuum electronics (especially magnetron).
ACADEMIC/RESEARCH AWARDS: URSI (International Union of Radio Science) Young Scientists, 2008
Memberships: IEEE(MTT, ED), IEICE

Dr. **Shoichi NARAHASHI**

AFFILIATION:
NTT DOCOMO Research Laboratories, Kanagawa, JAPAN
Executive Research Engineer, Shoichi Narahashi received his M.E. in Electronics from Kumamoto University in 1988 and his Ph.D. in Media and Network Technologies from Hokkaido University in 2008, respectively. He joined Nippon Telegraph and Telephone (NTT) Corporation in 1988 and transferred to NTT DOCOMO in 1992.
Now he is with the NTT DOCOMO Research Laboratories. He is leading research activities in the area of RF circuit technologies for future mobile communication systems such as multi-band RF devices with RF-MEMS, highly-efficient power amplifiers, non-linear distortion compensation schemes and cryogenic receiver front-end. He is a member of the IEEE, the Institute of Electronics, Information and Communication Engineers (IEICE), and the Society of Instrument and Control Engineers (SICE).

Dr. **Hiroshi OKAZAKI**

AFFILIATION:
NTT DOCOMO, INC. Kanagawa, JAPAN

Dr. **Hiroyuki TSUJI**

AFFILIATION:
Space Communications Group, National Institute of Information and Communications Technology, Tokyo, JAPAN
Hiroyuki Tsuji received B.E., M.E., and D.E. degrees in Electrical Engineering from Keio University, Tokyo, Japan, in 1987, 1989, and 1992, respectively. In 1992, he joined the Communications Research Laboratory (CRL, now part of the National Institute of Information and Communications Technology, or NICT). From 1999 to 2000, he was a visiting research fellow of the University of Minnesota. Since 2002, he has been working at Yokohama National University, Yokohama, Japan as a visiting professor, which is an additional post. His research interests are array antennas for wireless communications and signal processing for communications and other systems. Dr. Tsuji received the Young Engineer Award from IEICE (The Institute of Electronics, Information and Communication Engineers) of Japan in 1995. He is a member of IEICE of Japan.

CONTENTS

ORAL PRESENTATIONS

Commission "C"
Radiocommunication Systems and Signal Processing

Commission "G"

Transionospheric Propagation

Commission “H”
Waves In Plasmas (including space and laboratory plasmas)

Commission "SPS"
Solar Power Satellite (SPS) Systems

ORAL PRESENTATIONS

Commission “C”

Radiocommunication Systems and Signal Processing

Beam direction variation and compensation plan for large-scale deployable antenna mounted on geostational satellite for satellite communication.

Yoshiyuki Fujino [(1)], ***Mitsuteru Orikasa*** [(2)], ***Masaski Sato*** [(3)], ***Amane Miura*** [(4)], ***Naokazu Hamamoto*** [(5)], ***Ryutaro Suzuki*** [(6)]

[(1)] New Generation Wireless Communications Research Center, National institute of Information and Commuinications Technology, 4-2-1, Nukui-kita machi, Koganei, Tokyo, 184-8795 JAPAN,fujino@nict.go.jp
[(2)] t.orikasa@nict.go.jp, [(3)]sato@nict.go.jp, [(4)]amane@nict.go.jp,[(5)]nao@nict.go.jp, [(6)]ryutaro@nict.go.jp

Keywords: Satellite/Terrestrial Integrated mobile Communication System, large-scale deployable antenna

Abstract: Recently, it is turned out satellite mounted large-scale deployable reflector antenna(LDR) has variation of beam direction due to thermal environment on the orbit. So, this paper describes measurement experiment of beam direction variations up to 0.15 degree and its compensation method. Such result is very useful not only communication satellite with LDR but also satellite solar power system which needs large aerospace structure in the orbit.

1. Introduction

To achieve a secured and safe society, the securing communication method at the emergency disaster using the mobile satellite communication system with handheld terminal is desired. In such system, a communication satellite with a large-scale deployable reflector antenna (LDR) of 30m class in the geostationary orbit (GSO) is needed. Recently, it is turned out LDR has variation of beam direction due to thermal environment on the orbit. So, this paper describes measurement experiment of beam direction variations and its compensation plan.

2. STICS System

The utility of satellite-based mobile phone systems in disaster management is well known. Since the free-space path loss in such systems can be high, large antennas mounted on satellite terminals are needed. In recent years, mobile communication systems with integrated satellite/terrestrial functions have been developed to provide wide-ranging services; these systems employ a large deployable antenna in a satellite terminal along with a small terrestrial terminal [1,2,3].

Our system is called the satellite/terrestrial integrated mobile communication system (STICS). This system can be used to achieve “dual” communication and can be connected to both terrestrial and

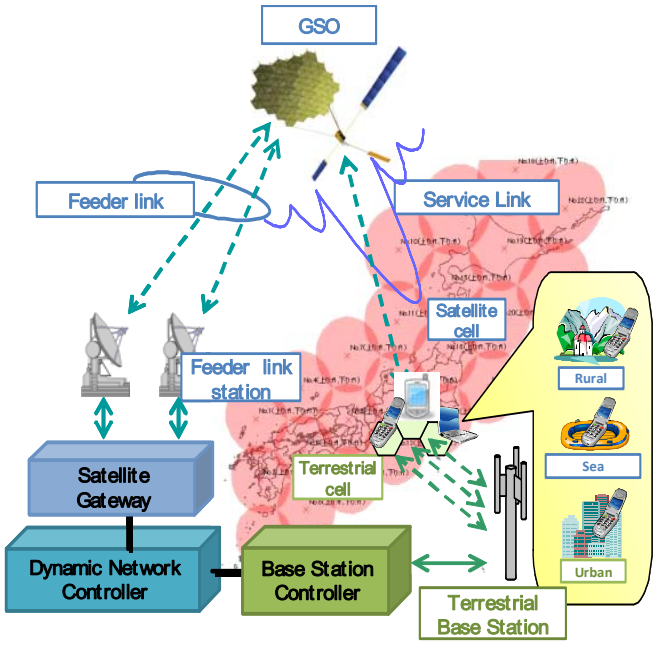

Figure 1 Conceptual figure of STICS

satellite systems; a common terminal is used for both communication. To realize this system, a deployable antenna having a diameter of 30 m will be installed in the satellite and approximately 100 multibeams will be used to cover Japan and exclusive economic zones (EEZs).

For each terminal, two types of cells can be considered. One is terrestrial cell connected to terrestrial base stations and the other is satellite cell connected to satellite gateway via geostationally satellite (GSO) (Figure1). User terminal can be select each of these cell. So, the feederlink station and the terrestrial base station are both equipped with a controller each. they can be simultaneously managed using the common controller via a core network. The main features of this system are as follows:

(1) The frequency can be effectively used by sharing the satellite system and the terrestrial system.
(2) The use of a satellite system makes the communication infrastructure safe and secure even when the terrestrial system infrastructure fails during disasters.
(3) A dual mode terminal having the same size and weight as a terrestrial cellular phone can be realized by installing a large-scale antenna (30 m class) in the satellite.
(4) The interference avoidance method is optimized as a result of the simultaneous management of the control information of the frequency assignment, transmitting power, and beam forming, from terrestrial and satellite systems.

In this system, frequency is assumed between 1980–2010 MHz (uplink) and 2170–2200 MHz (downlink), which is in accordance with the allocation by Mobile Satellite System(MSS) in International Mobile Telecommunications-2000 (IMT-2000)

To achieve such system, high EIRP and G/T communication satellite is needed by using multibeam antenna with the reflector in 30m class. Specifications of the satellite number of beams, antenna gain and G/T are 100 beams, more than 47dBi and more than 21dB/K, respectively[4]. Figure 2 shows the conceptual figure of the STICS Satellite.

This antenna consists of the phased array feeds and the reflector that has the function of the beam steering by offsetting the array feeds from the focal point. Merit of phased array feed reflector antenna is follows; (1) Flexibility of beam will be high and keep redundancy for failure of feeding element and feeding network component. (2) Feeding power problem can be moderated by spatial power composition using large number of amplifier element in the transmitter. (3)Power distribution between beams can be changed according to the traffic requirement. But, highly accurate of excitation in primary feeding array is necessary for keeping minimum area gain and beam isolation level.

So, super multibeam technology which enables more than 100 spot beams and low sidelobe technology which increase frequency re-allocation efficiency is required for developing.

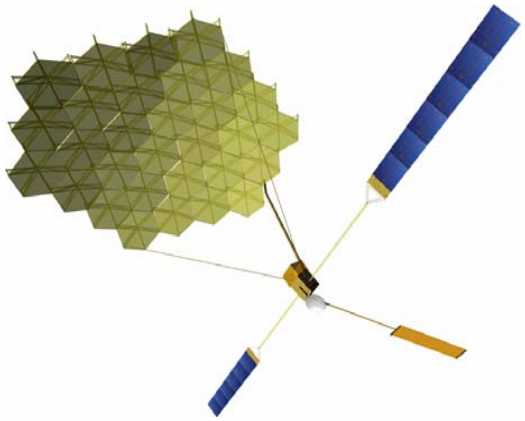

Figure 2 STICS satellite with LDR
(© JAXA)

3. LDR evaluation experiment in NICT

On concerning R&D of LDR related technologies, NICT continues the experiment of Engineering Test Satellite- 8 (ETS-8) since Dec., 2006. This satellite is equipped with the large deployable reflector antenna (LDR) for mobile communications with the size of 17m x 18 m, which is one of the largest size for communications satellite. NICT developed one of the beam forming network (BFN) for feeding network. Figure 3 shows five service beams around Japanese mainland by BFN in ETS-8.

To evaluate antenna pattern mounted in the satellite[5], signal received in multipoint on the Japanese main land. And satellite altitude is moved plue minus 2.5 degrees in Azimuth angle. Concerning sidelobe, inter beam isolation between beam #1 (Kyuchuu-beam) and beam #3 (Kanto-beam) is about 15dB in such experiment.

Signal receiving level of Kyushuu-beam is measured when eclipse in autumn at Kashima, Yokosuka, Akanshi, Kita-kyushuu. Result is shown in figure 4. Time variation of receiving level is observed at the ecripse and it is returned to former level when ecripse is finished. The output power of SSPA is not changed, it is understood that the temperature of the antenna has decreased by about 180K as a result of analyzing the telemetry of the satellite during the eclipse, and originates in the temperature change of the antenna part.

It is thought that beam shifted to east. And beam shift angle is about 0.1 to 0.15 degree from the figure 4.

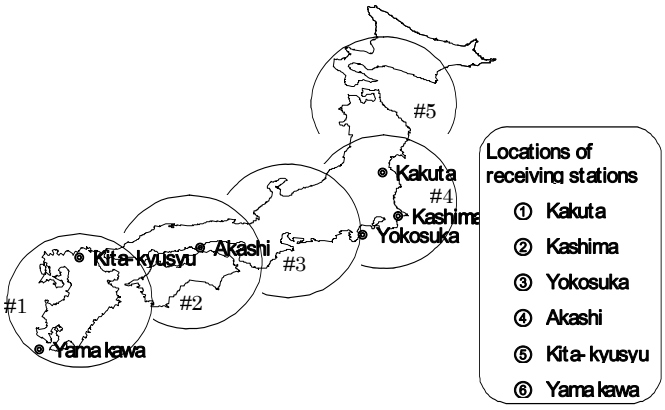

Figure 3 Beam allocation of ETS-8

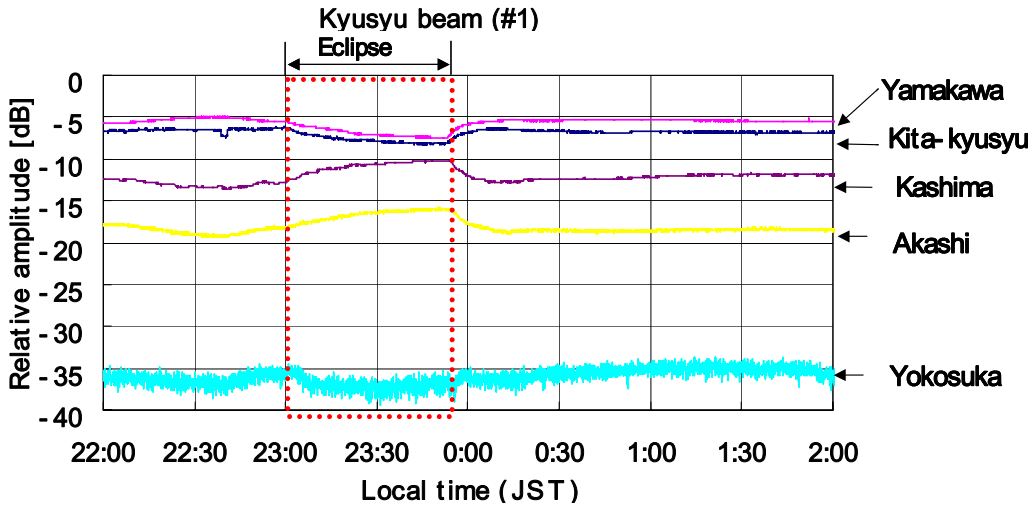

Figure 4 Receiving level variations at the time of eclipse

4. Compensation plan for STICS

For this experimental result, same beam shift can be worried in the STICS satellite, which reflector is larger than ETS-8. So, in the research and development of STICS, low sidelobe technology is one of the research items. And in this research items, the correction technique of the beam direction change that originates in the reflector equipped with the satellite and the change of the structure is examined, in addition, a basic examination on the sidelobe suppression begins. For this reason, simulation software for large-size deployment antenna direction variation is now creating.

This software is the additional function of a "transmitting excitation distribution simulator" to perform the analysis, a design, and evaluation of the 100 beam class multibeam for STICS satellite.

By using this simulator, to determine the beam direction of the antenna in orbit, the Rotating Element Vector method (REV method) is applied, and compute its relative phase and amplitude and it is due to receive the signal from an orbit in two or more ground stations.

Moreover, it is possible to presume compensation of beam direction variation (primary modification of reflector surface) on an orbit and to calculate the excitation phase with compensate of direction variation which becomes fundamental result for sidelobe suppression.

5. Summary

Outline of Satellite/Terrestrial Integrated Mobile Communication System for measures to deal with natural calamities is explained. For this R&D, thermal distortion of LDR in satellite will be serious problem by showing data of ETS-8. To compensate such beam variation of LDR, we proposed excitation distribution compensation of primary feeding array by using result of REV method with multiple ground station. Such result is very useful not only communication satellite with LDR but also satellite solar power system which needs large aerospace structure in the orbit.

References

[1] Thuraya Satellite Telecom (http://www. thuraya.com/)
[2] SkyTerra Communications (www.skyterra.com)
[3] T.Minowa, M.Tanaka, N.Hamamoto, Y.Fujino, N.Nishinaga, R.Miura and K.Suzuki, “Satellite/Terrestrial Integrated Mobile Communication System for Nation's Security and Safety”, Trans IEICE on Communication (Japanese edition), VolJ91-B, No.12, pp.1629–1640.
[4] M.Umehira, Y.Fujino, R.Suzuki,” Satellite/Terrestrial Integrated Mobile Communication System: STICS”, 2009 IEICE Soc. Conv., BT-1-1, Sep., 2009.
[5] M.Satoh, Y.Fujino, T.Orikasa, ”Characterization of Large-Scale Deployable Antenna Pattern Equipped with Engineering Test Satellite VIII on Orbit”, Trans IEICE on Communication (Japanese edition), VolJ91-B, No.12, pp.1641–1643.

MVDR Beamformer with a CFAR Processor for Jamming Suppression in GPS Receivers

Vera Behar [(1)]***, Christo Kabakchiev*** [(2)]***,Hermann Rohling*** [(3)]

[(1)] Institute for Parallel Processing, BAS, Acad. G. Bonchev Str., Sofia, Bulgaria
behar@bas.bg;
[(2)]Department of Software Technologies, Sofia University, J. Boucher Blvd., Sofia, Bulgaria
ckabakchiev@fmi.uni-sofia.bg;
[(3)] Technical University Hamburg-Harburg, Hamburg, Germany
rohling@tu-harburg.de

Keywords: Adaptive array processing; CFAR detection, satellite navigation systems.

Abstract: In this paper, the performance of a new three-stage algorithm for detection of weak GPS signals in heavy interference environment (GPS MDVR CFAR) is described and evaluated. Two different beamforming schemes, conventional and MVDR are applied to the input of a GPS receiver for jamming suppression before detection of the C/A code. The effect of beamforming on the detection performance is evaluated in terms of two quality factors: the signal-to-interference-plus-noise ratio (SINR) improvement factor estimated at the beamformer output and the detection probability evaluated at the CFAR detector output. The simulation results demonstrate the more effective anti-jamming protection of the new detection algorithm.

1. Introduction

The Global Positioning System (GPS), each of satellites transmits digitally coded data, and GPS receivers demodulate these signals from four or more satellites simultaneously in order to generate three time-difference-of–arrival estimates, allowing the user to measure the range to three satellites, and, as a result, to determine his position [1]. Since a direct sequence spread spectrum (DSSS) signal is used in transmission, relatively low powers can be transmitted by the satellites for accurate position estimation. In fact, these signals have the signal-to-noise ratio (SNR) in the range of -15 to -30 dB. In civil applications, therefore, the key to achieve the precise position estimation performance is the effective processing of very weak DSSS signals from satellites that contain coarse acquisition (C/A) digitally coded data. In each channel of a GPS receiver, detection of the C/A code that identifies the corresponding satellite is carried out by a cross-correlation algorithm. The objective of this algorithm is to search the presence of the GPS signal over a frequency range that covers every possible expected Doppler frequency. If 1 *ms* of data is processed coherently, the intensity maximum in n^{th} time discrete and i^{th} frequency bin gives the beginning point of C/A code and the carrier frequency if the signal maximum is above the predetermined threshold of detection. As in radar applications, various adaptive thresholding schemes that maintain a constant rate of false alarm (CFAR) can be used for detection of the C/A code [2]. Once the beginning point of the C/A code period and the carrier frequency of the input signal are measured, this information is passed on to the tracking algorithm in order extract the navigation data.

Though that the signals transmitted by satellites have antijamming protection the weak signal strength of the received signal makes it impossible to detect the C/A code signal in conditions of broadband interference If a strong broadband jamming source is nearby, the receiver noise may rise to the level where the SNR at the correlator output is below the detection threshold.

One of approaches to mitigate GPS interference before signal processing in a GPS receiver is to use different beamforming techniques for broadband nulling having in mind that the satellite signals and interfering

signals usually originate from different spatial locations [3]. The conventional (delay-and-sum) beamformer is the simplest of them but it is not effective in the presence of directional jamming signals. The others beamformers such as a Minimum Variance Distortionless Response (MVDR) can suppress interference from off-axis directions [4]. This beamformer requires only the information for the direction-of-arrival of GPS signals.

In this paper we present and evaluate the performance of a new algorithm for detection of weak GPS signals in heavy interference environment so call (GPS MDVR CFAR detector). The effectiveness of the new algorithm is expressed in terms of two quality factors evaluated at the beamformer and CFAR detector outputs. The goal of the study is to analyze the capability of the GPS MDVR CFAR detection algorithm to effectively operate in jamming environment. The impact of three important factors is also evaluated. These factors are: beamforming algorithm; interference-to-signal ratio; steering vector mismatch.

2. Signal Model

The input signal of a GPS receiver is composed of the satellite signal, thermal noise and interference. In conditions of jamming, the complex valued samples of the received signal at time instant *k* are:

$$x(k) = a_c s(k) + \sum_{l=1}^{L} b_l j_l(k) + n(k) \tag{1}$$

where *x(k)* is the data vector, *s(k)* is the desired satellite signal sample, $j_l(k)$ is the *l*th broadband jamming sample, a_c and b_l are antenna array response vectors of the satellite signal and the *l*th broadband interference, respectively, *n(k)* is the noise sample and *L* is the number of jamming sources. The satellite signal is given by:

$$s(k) = \sqrt{P_s}\, c(k) \cos(2\pi f_0 t + \varphi) d(k) \tag{2}$$

where P_s is the received signal power, *c(k)* is the C/A coded signal of length (20 x 1023), separate for each satellite, *d(k)* is the data bit which remains constant over the length of one cycle of the C/A code, and f_0 is the carrier frequency. The jamming signal *j(k)* is modeled as bandlimited additive white Gaussian noise (AWGN).

3. C/A Code Detection

The structure of a new GPS MDVR CFAR detection algorithm is shown in Fig.1. In our case, the signal processing includes three stages: beamforming, cross-correlation and CFAR detection

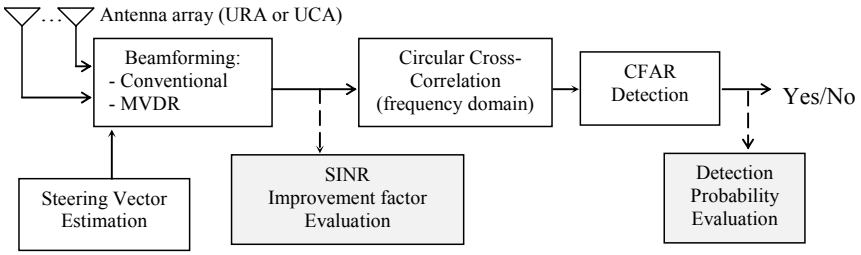

Fig.1: The flow-chart of the signal processing and the evaluation process

***Beamforming stage*:** The output signal of an antenna array with *M* elements is formed as:

$$y(k) = W^H x(k), \text{ where } k=1\ldots N \tag{3}$$

In a conventional beamformer, the complex vector of weights *W* is equal to the array response vector a_c defined by the array configuration [3,4]:

$$W_{conv} = a_c \tag{4}$$

In a MVDR-beamformer, the complex vector of weights *W* is found by maintaining the distortionless response toward the signal and minimizing the power at the filter output:

$$W_{MVDR} = \frac{K_{j+n}^{-1} a_c}{a_c^H K_{j+n}^{-1} a_c} \tag{6}$$

where K is the interference-plus noise correlation matrix.

***Cross-correlation stage*:** The standard circular cross-correlation algorithm consists of the following steps [1]:

- Perform the FFT of the input data *x(k)* converting them into frequency domain as *X(k)*.
- Take the complex conjugate *X(k)* obtaining the outputs *X*(k)*.
- Generate 21 local codes $l_{si}(k)$ as $l_i(k)=c(k)exp(2\pi jf_i)$, , where $f_i=f_c+i$ ·kHz, f_c- is the intermediate frequency and i=-10,-9,….9, 10. The local code is the product of the C/A code and a complex IF signal. The frequencies f_i of the local codes are separated by 1 kHz.
- Perform the FFT on $l_{si}(k)$ to transform them to the frequency domain as $L_i(k)$.
- Multiply *X*(k)* and $L_i(k)$ point by point obtaining the result $R_i(k)$.
- Take the IFFT of $R_i(k)$ to transform the result into time domain as $r_i(k)$ and find the value $|r_i(k)|^2$.

CFAR detection: To detect the C/A code in the incoming data, the following test statistics is formed:

$$q_{m,n} = \max\left|r_i(k)\right|^2 \quad for\ i = m, k = n \tag{7}$$

The intensity in n^{th} time discrete and m^{th} frequency bin gives the beginning point of C/A code and the carrier frequency if the test statistics (7) exceeds a threshold of detection $H_{m,n}$. The decision rule for detection is:

$$\Phi_{m,n} = \begin{cases} 1, & if\ q_{m,n} \geq H_{m,n} \\ 0, & otherwise \end{cases} \text{,where } H_{m,n} = T_\alpha \cdot w_{m,n}, \text{ and } w_{m,n} = \sum_{\substack{l=m-L/2 \\ l\#m}}^{m+L/2} \left|r_i(k)\right|^2 \tag{8}$$

The variable w in (8) is the estimate of the total noise power integrated over a reference window of length L. The scale factor Tα in (8) is determined to maintain the required level of false alarms:

$$P_{FA} = (1 + T_\alpha^L)^{-1} \tag{9}$$

3. Simulation Results

The effectiveness of the GPS MVDR CFAR detection algorithm is evaluated in terms of the signal-to-noise-plus-interference (SINR) improvement factor estimated at the beamformer output and the detection probability of the C/A code estimated at the cross-correlator output. In this study, 1000 computer simulations are performed to evaluate these quality factors. The simulation scenario is given in Table 1.

Variant	Jamming	GPS signal
Array: UCA, 7 elements IF carrier: 1.2513 MHz Sampling: 5.0053 MHz	Four jammers: Elevation: θ=40° Azimuth: φ_1=-70°; φ_2=60°; φ_3=60°; φ_4=70° ISR: 10dB … 100dB	Elevation: θ=40°; Azimuth: φ=0° Doppler shift-5 kHz; SNR -20dB; Duration- 1ms; C/A code- satellite 19

Table 1: Simulation scenario

For both beamformers, the two quality factors are evaluated as a function of the input Interference–to-Signal Ratio (ISR) in the range from 10dB to 100 db (Fig.2 and Fig.3). In Fig.3, the probability of detection is plotted for two values of the false alarm probability (P_{fa}) maintained by a CFAR algorithm. The results from Fig.2 confirm that unlike the conventional beamformer the MVDR-beamformer more successfully mitigates interference. However, the high probability of detection is maintained by the GPS MVDR CFAR detection algorithm only in the case when the jamming intensity is not high (ISR< 30dB). Otherwise, in order to increase the C/A code detectability, the detection performance must be realized over several neighbor periods of the C/A code detection, using coherent or non-coherent integration of the incoming signal.

Because the precise angular location of the GPS satellite is not always known, it is very important to analyze the sensitivity of the GPS MVDR CFAR detection algorithm to angular errors in satellite location (in both azimuth and elevation). The influence of angular (azimuth and elevation) errors in satellite location on the two quality factors of the GPS MVDR CFAR detection algorithm is shown in Fig.4 and Fig 5. One can see that for the MVDR-beamforming, the losses in SINR due to steering vector mismatch are tolerable when angular errors are less than 15°. However, for both beamformers the detection probability quickly degrades with

increase of angular errors in satellite location (ISR=25dB). One can see that the detection losses are insignificant if angular errors are less than 15° and 10° for $P_{fa}= 10^{-7}$ and $P_{fa}= 10^{-9}$, respectively.

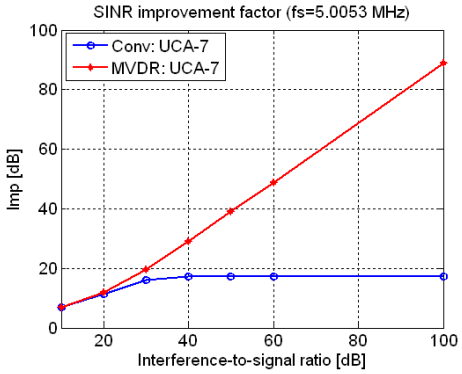

Fig. 2: SINR improvement factor

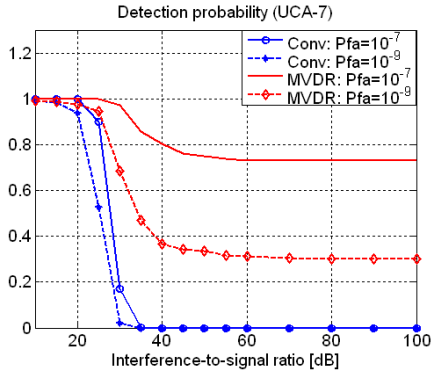

Fig 3: Probability of detection

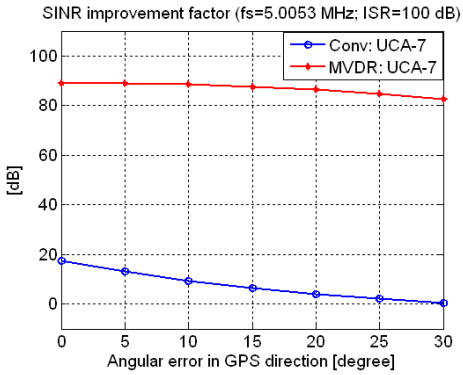

Fig.4: Probability of detection of the C/A code

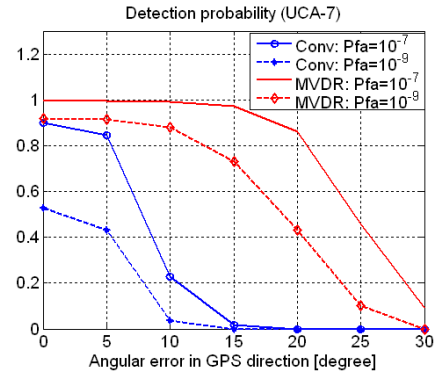

Fig.5: Detection losses due to steering vector mismatch

4. Conclusions

It is shown that the proposed three-stage algorithm for detection has good anti-jamming capability and improves the detectability of the C/A code in a GPS receiver.

Acknowledgment

This work is partially supported by the Bulgarian Science Fund (the projects, DO-02-344/2008, and MU-FS-05/2007, DTK02/28 – 17.12.2009).

References

[1.] James Bao-Yen Tsui, *Fundamentals of Global Positioning System Receivers: A Software Approach*, Wiley Interscience, John Wiley&Sons, 2005

[2.] Finn H M., R. S. Johnson, "Adaptive detection mode with threshold control as a function of spatially sampled clutter estimation", RCA Review, vol. 29, 3, pp. 414-464, 1968.

[3.] H. Van Trees Optimum Array Processing. Part IV of Detection, Estimation, and Modulation Theory. New York, NY: JohnWiley and Sons, Inc., 2002.

[4.] L. Tummonery, I. Proudler, A. Farina, J. McWhirter, "QRD-based MVDR algorithm for adaptive multi-pulse antenna array signal processing", in Proc. Radar, Sonar, Navig., vol.141, No 2, 1994, 93-102

A Spatial Resource Management Scheme Suitable for Wireless Ad Hoc Networks

Yukihiro KAMIYA

Tokyo University of Agriculture and Technology, Tokyo 184-8585, Japan
kamiya@ieee.org

Keywords: Wireless ad hoc network, adaptive array antenna, interference cancellation

Abstract: This paper introduces a new scheme for the spatial resource management in wireless ad hoc networks (WAHNs). WAHN is a network configured by nodes, without any centralized network control facilities. It has been considered that adaptive array antenna (AAA) is an effective means for improving the capacity of WAHN. This is because of its interference cancellation capability in the space domain. However, AAA is not perfect even though conventional studies concerning AAA for WAHN assume that it is a perfect tool for the interference cancellation. In this paper, a new scheme to utilize AAA more effectively, avoiding problems caused by the imperfect beamforming will be proposed. The concept of the proposed idea is comprehensively explained.

1. Introduction

It is said that wireless ad hoc network (WAHN) enables us to configure flexible and scalable networks. This is due to its feature that it does not require any centralized control facilities such as a server. Instead of such facilities, nodes form a network autonomously. One of the major obstacles to the realization of WAHN is inter-link interference (ILI). Since there is no coordination between and among links by the network control facility in WAHN, a communication link can often cause interference with other links. It is easily expected that ILI degrades the capacity of WAHN because few links would be able to be established at the same time.

Aiming at solving the problem of ILI, applications of directional antennas to WAHN have been proposed[1.][2.]. If each of the nodes is equipped with such an antenna, each node can transmit signals choosing the direction so as to avoid interfering with other links. As a more sophisticated antenna, the adaptive array antenna (AAA)[3.] has been also considered for the capacity enhancement of WAHN[4.].

AAA forms its directionality adapting to the environment. It is capable of maximizing the gain in the direction of arrival (DOA) of a desired signal while minimizing the gain in those of interferences. We might expect that AAA enables WAHN to increase the capacity since ILI can be cancelled entirely. However, in reality, it is not the case. The interference cancellation by AAA is not always perfect. This is due to the following two causes. Firstly, interferences incoming from a DOA which is too close to that of the desired signal cannot be cancelled entirely. In addition, secondly, if the number of ILIs exceeds the degree of freedom (DOF), the cancellation of ILI is also difficult. Since there is no coordination between the links in WAHN, AAA often faces at such situations. Therefore, these are the main causes of the performance degradation. Computer simulations also show the fact that the usage of AAA without addressing these two issues results in the inferior performance compared with WAHN without AAA.

2. Directional Antennas and Media Access Control on WAHN

2.1. Media Access Control for WAHN

The timing for the channel access of each node in WHAN has to be controlled in order to avoid collisions. This control scheme is referred to as media access control (MAC). However, the problem is the fact that there is no centralized control facility in WAHN. As one of the MAC schemes, carrier sensing (CS) is well-known. Since this MAC scheme is simple, it has been applied for wireless local area networks (WLANs). CS is summarized as follows:

1) Suppose that node A got a demand for data transmission to another node B. Then, node A listens to the channel prior to the transmission, measuring the power of the signals existing in the channel. If the measured power is higher than a threshold value, it is recognized that other nodes are communicating.

2) If no signal power is detected, node A believes that the channel is idle. Then, the node starts to transmit the signal.

3) If it detects the signal power, the signal transmission is postponed. Node A sets a waiting period. After the expiration of the period, the node goes back to 1) above, and retries the channel measurement.

Although we might easily expect that CS is also applicable to WAHN, this application is not very effective due to the following reason. In WAHN with CS, no node can start to communicate with another node while other pairs of nodes are communicating. Therefore, it is expected that very few nodes can start their communications while most of them are always waiting, as the number of nodes increases.
The simplest method to cope with this problem is to assign a separated channel to each link, such as the time, the frequency, or the spreading code in case of the spread spectrum. In addition to such channels, the space can be a channel if we assume that each node is equipped with a directional antenna. Since directional antennas can radiate the signal in a certain direction only, a pair of nodes might be able to communicate without interfering with other nodes.

2.2. Adaptive Array Antenna

Adaptive array antenna (AAA) is a directional antenna, whose directionality is formed electrically, *i.e.*, it is not formed by mechanical ways such as using reflectors.
Fig. 1 (a) shows a configuration of AAA. It consists of several antennas so-called element antennas. Signals received by the element antennas are added after multiplying it by weights. The weights are adaptively controlled by a digital processor. As a result, as shown in (b), peaks and nulls are formed on the directionality. It is possible to cancel interferences in the space domain by forming a null in the direction of arrival (DOA) of the interferences. It is emphasized that the peak and the null are generated adaptively in accordance with the environment where AAA is located. We would expect that the interference cancellation capability of AAA can contribute to increase the number of co-existent links at the same time.
However, the interference cancellation by AAA is not always perfect. There are mainly two causes as follows:

1) Limitation of the degree of freedom (DOF): The number of interferences that can be cancelled by AAA is limited by DOF, given as (N-1) where N denotes the number of element antennas. If a node is surrounded by many nodes that are transmitting signals, the node will suffer from so many interferences, exceeding DOF. Finally, the AAA on the node cannot cancel the interferences completely.

2) Limitation of the angular resolution (AR): When the DOA of the desired signal and that of the interference are very close, the gain of AAA in the direction of the desired signal is suppressed. This is because the AAA tries to form a null in the direction of the interference even though it is incoming from very close direction of

the desired signal. The degradation of the gain in the direction of the desired signal is mitigated as the number of element antennas increases.

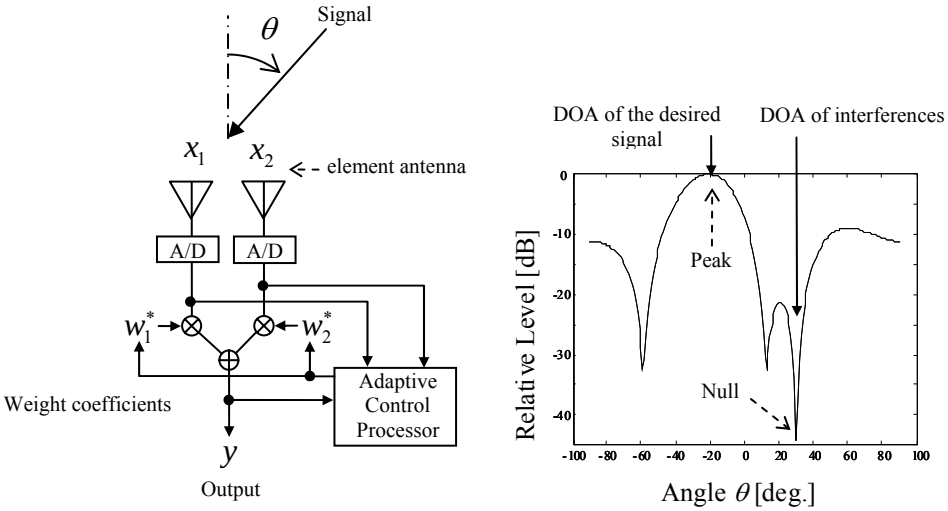

(a) Configuration of AAA.

(b) An example of the directionality generated by AAA.

Fig. 1 Configuration of AAA.

Based on the two points above, it is supposed that AAA achieves interference cancellation almost perfectly when the number of element antennas is large. However, it is expected that each node in WAHN is equipped with few element antennas due to the size limitation as a mobile terminal. Therefore, we need solutions for the limited DOF and AR in order to use AAA effectively.

3. FIA

Forward interference avoidance (FIA)[5.] has been proposed as a solution. This scheme provides a mechanism to check the peak and the null of AAA if they are properly generated, prior to the signal transmission. The advantages of FIA are summarized as follows:

1) Imperfect interference cancellation caused by the limited DOF and AR is avoided.

2) There is no need of any reference signals.

Procedures for FIA are explained in a step-by-step manner as the following. Suppose that there are *L* nodes, and each node is equipped with *N*-element array antenna.

Step 1. Each node sends a short burst in order to inform other nodes of its existence. This short bust is transmitted along CS as explained in 2.1. Each of the other nodes receiving the short burst calculates the correlation matrix $(N \times N)$. The matrix is decomposed by the eigenvalue decomposition (EVD) to obtain the maximum eivenvalue and the corresponding eigenvector $(N \times 1)$. Suppose that node #*n* sends the short burst and node #*m* receives it. Then, let $\lambda_{m \leftarrow n}$ and $\mathbf{v}_{m \leftarrow n}$ denote the maximum eigenvalue and corresponding eigenvector, respectively.

Step 2. After completing Step 1, each of the nodes holds the eigenvalues and the eigenvectors for all of the other nodes. By using them, each node can calculate the weights of AAA generating a peak in the direction of a certain node while nulls are generated in that of certain nodes. Assuming that node #2 wants to generate

a peak to node #1 while forming nulls to nodes #3 and #4, such weights at node #2 is obtained as follows:

$$\mathbf{w}_2 = \left\{\lambda_{2\leftarrow 3}\mathbf{v}_{2\leftarrow 3}\left(\mathbf{v}_{2\leftarrow 3}\right)^* + \lambda_{2\leftarrow 4}\mathbf{v}_{2\leftarrow 4}\left(\mathbf{v}_{2\leftarrow 4}\right)^*\right\}^{-1}\mathbf{v}_{2\leftarrow 1}. \quad (1)$$

It should be emphasized that there is no need of any reference signals.

Step 3. As explained in the previous section, the derived $\mathbf{w}_2$ of size $(N\times 1)$ might generate inappropriate peak and nulls. If so, it causes ILI. Therefore, $\mathbf{w}_2$ is verified by the following method prior to the transmission.

$$\left|\left(\mathbf{w}_2\right)^*\mathbf{v}_{2\leftarrow 1}\right|^2 \geq \Psi_{\text{peak}} \quad (2)$$

$$\lambda_{2\leftarrow 3}\left|\left(\mathbf{w}_2\right)^*\mathbf{v}_{2\leftarrow 3}\right|^2 \leq \Psi_{\text{null}} \quad (3)$$

$$\lambda_{2\leftarrow 4}\left|\left(\mathbf{w}_2\right)^*\mathbf{v}_{2\leftarrow 4}\right|^2 \leq \Psi_{\text{null}} \quad (4)$$

Here, Ψ_{peak} and Ψ_{null} are the threshold values. Equation (2) checks if the gain of AAA with $\mathbf{w}_2$ in the direction of node #1 is higher than Ψ_{peak}. It means that (2) verifies the peak generation by $\mathbf{w}_2$. In contrast, (3) checks if the gain of AAA with $\mathbf{w}_2$ in the direction of node #3 is lower than Ψ_{peak}, in order to verify the null generation. Likewise, (4) checks if the gain of AAA in the direction of node #4 is also sufficiently low by the null generation. The signal transmission is allowed if (2), (3) and (4) are satisfied simultaneously.

4. Conclusions

Through such a mechanism, each node takes advantage of the interference cancellation by AAA while avoiding ILI caused by the imperfect directionality control. Computer simulations show the performance improvement in terms of the number of co-existent links without interference. Such results will be introduced in the presentation.

References

[1.] R. R. Choudhury, X. Yang, R. Ramanathan, and N. H.Vaidya, " On Designing MAC Protocols for Wireless Networks Using Directional Antennas,"IEEE Trans. on Mobile Computing, Vol. 5, No. 5, May 2006.

[2.] T. Ueda, S. Tanaka, D. Saha, S. Roy and S. Bandyopadhyay,"Location-Aware Power-Efficient Directional MAC Protocol in Ad Hoc Networks Using Directional Antenna," IEICE Trans. on commun., Vol. E88-B, No. 3, pp.1169-1181, March 2005.

[3.] J. E. Hudson, "Adaptive Array Principles," Peter Peregrinus Ltd, December 1981.

[4.] T. Furuhi and T. Ohira, "Efficacy Consideration on Directional Antennas in Wireless Ad-hoc Networks," IEICE Trans. on commun., Vol.J85-B, No.12, pp.2223-2233, December 2002.

[5.] T. Sakaguchi, Y. Kamiya, T. Fujii and Y. Suzuki, "Forward Interference Avoidance in Ad Hoc Communications using Adaptive Array Antennas, " IEICE Trans. on Communications, Vol.E91-B, No.9, pp.2940-2947 , September 2008.

SAS and ISAR Signal Modeling and Image Reconstruction

Andon Dimitrov Lazarov

Bourgas Free University, No 62 San Stefano, Bourgas, Bulgaria
lazarov@bfu.bg

Keywords: Synthetic Aperture Radar (SAR). Inverse Synthetic Aperture Radar (ISAR). SAR/ISAR Signal Modeling. SAR/ISAR Image Reconstruction.

Abstract: Synthetic aperture radar (SAR) and Inverse Synthetic Aperture Radar (ISAR) are powerful tools for microwave imaging of the objects placed on the Earth surface and flying in the air or in the space. In this contribution a new concept of SAR and ISAR signal modeling is suggested. Analytical geometrical and kinematical equations for different SAR and ISAR scenarios are derived. Mathematical expressions for SAR signals reflected from the objects with complicated shape are devised. Image reconstruction procedures and their motion compensation interpretation are given. Verification of proposed signal models and image reconstruction procedures is performed by numerical experiments.

1. Introduction

SAR is a technique uses the motion of the aircraft on which the radar is mounted to synthesize a large effective aperture in order to achieve high cross-range resolution and wide frequency bandwidth to realize high range resolution, thus to gain SAR images of high quality [1, 2]. ISAR imaging is a well know processing algorithm for the mapping of moving object. The radar is stationary while the target exhibits relative motion with respect to the radar position. Motions of the target induce an azimuth resolution, while wideband emitted signals provide for a high range resolution [3, 4]. In case both target and radar are moving, the process can be defined as a generalized SAR/ISAR imaging process. It is of particular interest for maritime patrol aircraft missions as it permits long-distance all-weather imaging and recognition of ship targets [5]. The range Doppler technique is a method providing two-dimensional ISAR target images [6]. The position of point scatterers along the radar line of sight (LOS) axis (range axis) is given by time analysis while their position on the cross-range axis is provided by Doppler frequency analysis. The aim of this work is to suggest analytical geometrical description of three dimensional (3-D) ISAR/SAR scenarios, signal models and image reconstruction algorithm. The rest of the paper is organized as follows. In Section 2 the 3-D ISAR geometry and kinematical equation are presented. In Section 3 the 3-D ISAR/SAR geometry of ISAR and kinematical equation are presented. In Section 4 the ISAR/SAR signal model is described. In Section 5 results of numerical experiment are discussed. In Section 5 conclusions are made.

2. Geometry of ISAR Scenario

The object is detected in 3-D regular grid, defined in Cartesian system $O'XYZ$ [7]. The 3-D regular grid is moving in Cartesian coordinate system $Oxyz$ on a rectilinear trajectory with a vector velocity $\mathbf{V}$ (Fig. 1). The mass-center of the object, the geometric center of the 3-D grid and the origin of the coordinate system $O'XYZ$ coincide. The reference points of the object space are placed at each node of the 3-D grid. The range vector $\mathbf{R}_{ijk}(p)$ from ISAR, placed in the origin of the 3-D observation coordinate system $Oxyz$, to the ijk th point of the object space, is determined by the vector equation

$$\mathbf{R}_{ijk}(p) = \mathbf{R}_{00}(0) + \mathbf{V}.\left(\frac{N}{2} - p\right)T_p + \mathbf{A}\mathbf{R}_{ijk} \tag{1}$$

where $p = \overline{0, N-1}$ is the current number of the emitted pulse; N is the number of emitted pulses; T_p is the time repetition period of pulses, $\mathbf{R}_{00}(0)$ is the line-of-sight vector to the geometrical center of the object space at the moment $p = N/2$, $\mathbf{R}_{ijk}$ is the range distance vector to the ijk th reference point.

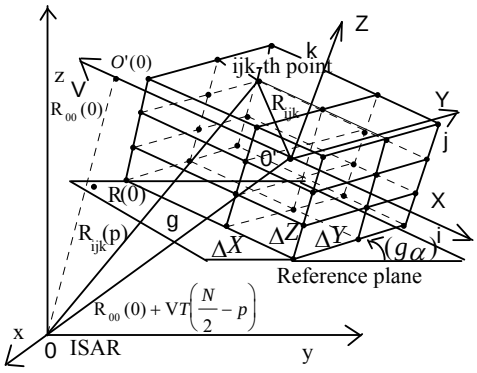

Fig. 1. ISAR geometry.

The transformation matrix $\mathbf{A}$ in equation (1) is defined in [8].

3. Geometry of ISAR/SAR Scenario

The stationary and moving objects are detected in two 3-D regular grids of reference points [7]. The grids are depicted in coordinate systems $O'XYZ$ and $O'^m X^m Y^m Z^m$, respectively. At the initial moment the 3-D grids coincide (Fig. 1), then they are moving relatively in Cartesian coordinate system of observation $Oxyz$ embedded with mass center of the SAR carrier, the stationary target at a constant vector velocity $\mathbf{V}$ and moving target at a vector velocity $\mathbf{V}^m = \mathbf{V} + \mathbf{v}^m$, respectively. The range distance vector to ijk th point of the stationary scene, $\mathbf{R}_{ijk}(p)$ is defined by (1) and range distance vector $\mathbf{R}^m_{ijk}(p)$ to ijk th point of the moving target is defined by the vector equation

$$\mathbf{R}^m_{ijk}(p) = \mathbf{R}_{00}(0) + \mathbf{V}^m.\left(\frac{N}{2} - p\right)T_p + \mathbf{A}^m\mathbf{R}^m_{ijk}, \tag{2}$$

The transformation matrix $\mathbf{A}^m$ in the kinematic equation (2) is defined in [8].

4. ISAR/SAR Signal Model

The ISAR/SAR transmits a series of N linear frequency modulated (LFM) pulses to the target. The deterministic component of the ISAR/SAR signal, reflected by ijk th point scatterer is modeled as [8]

$$\dot{S}(p,n) = \sum_{i,j,k} a_{ijk}\,\mathbf{rect}\frac{t - t_{ijk}}{T}\,\mathbf{exp}\left\{-j\left[\omega\left(t - t_{ijk}\right) + b\left(t - t_{ijk}\right)^2\right]\right\} \tag{3}$$

where
$$\mathbf{rect}\frac{t - t_{ijk}}{T}\begin{cases}1, 0 < \dfrac{t - t_{ijk}(p)}{T} \le 1,\\ 0, \text{ otherwise}\end{cases} \tag{4}$$

where a_{ijk} is the point scatterer intensity, $\omega = 2\pi\frac{c}{\lambda}$ is the signal angular frequency, $b = (2\pi\Delta F / T)$ is the LFM rate, T is the LFM pulse time duration, ΔF is the LFM bandwidth, $t = t_{ijk\min}(p) + (n-1)\Delta T$ is the fast time, $n = \overline{1, L_{\min}(p) + L(p) + K}$ is the sample number of the LFM pulse; $M = T / \Delta T$ is the number of samples of the LFM pulse, ΔT is the time duration of a LFM sample, $t_{ijk} = 2R_{ijk}(p)/c$ is the time delay and $R_{ijk}(p)$ is the module of the range vector to *ijk*-th point scatterer, $L_{\min}(p) = \text{int}\lfloor 2R_{ijk}(p)/\Delta T \rfloor$ is the range cell number where the signal, reflected by nearest pint scatterer is detected; $t_{ijk\min}(p) = 2R_{ijk\min}(p)/c$ is the minimal time delay of the ISAR/SAR signal reflected from the nearest point scatterer of the target, $L(p) = L_{\max}(p) - L_{\min}(p)$ is relative time dimension of the target, $L_{\max}(p) = \text{int}\lfloor t_{ijk\max}(p)/\Delta T \rfloor$, $t_{ijk\max}(p) = 2R_{ijk\max}(p)/c$ is the maximum time delay of the SAR signal reflected from the farthest point scatterer of the target.

The ISAR/SAR signal return is an additive sum of a deterministic component $\dot{S}(p,n)$ and zero mean delta correlated complex Gaussian noise $\dot{n}(p,n)$ induced by ionosphere plasma in case of space ISAR/SAR systems and can be expressed by

$$\dot{\xi}(p,n) = \dot{S}(p,n) + \dot{n}(p,n). \tag{5}$$

Demodulation

Demodulation of the signal return is performed by multiplication with complex conjugated amplitude of the emitted signal, i.e.

$$\hat{S}(p,n) = \sum_{k=1}^{K}\sum_{j=1}^{J}\sum_{i=1}^{I} a_{ijk}\,\textbf{rect}\frac{t-t_{ij}}{T_0}\exp\left\{j\left[\omega\left(t-t_{ijk}\right)+b.\left(t-t_{ijk}\right)^2\right]\right\}\times\exp\left[-j(\omega t + bt^2\right]. \tag{6}$$

Image reconstruction algorithm

The image reconstruction procedure does reveal the discrete complex reflectivity density function. It can be implemented by the following operations: **Phase correction** of the complex matrix $\dot{\xi}(n,p)$ by multiplication with complex conjugated exponential term $\exp\left[-j\Phi(p)\right]$, i.e. $\tilde{\xi}(p,n) = \dot{\xi}(p,n).\exp\left[-j\Phi(p)\right]$, where $\exp\left[-j\Phi(p)\right]$ stands for moving compensation autofocusing function, $\Phi(p) = a_0 + a_1 p + a_2 p^2 + ... + a_n p^n$ is the polynomial expansion of the phase correction function, defined by entropy minimization cost function [9]. **Range compression** of phase corrected signal $\xi(p,n)$ by FFT procedure, i.e.

$$\tilde{\xi}(p,q) = \sum_{n=1}^{M+L}\tilde{\xi}(p,n)\textbf{exp}\left(-j\frac{2\pi nq}{M+L}\right). \tag{7}$$

Azimuth compression of ISAR/SAR range compressed signal $\tilde{\xi}(p,n)$ by FFT procedure, i.e.

$$\tilde{\xi}(\bar{p},q) = \sum_{p=1}^{N}\tilde{\xi}(p,q)\textbf{exp}\left(-j\frac{2\pi p\bar{p}}{N}\right), \text{ where } \bar{p} = \overline{1,N},\ q = \overline{1,(M+L)}. \tag{8}$$

5. Numerical Experiment

Consider target depicted in a 3-D regular grid. The ISAR transmits LFM pulses with parameters: wavelength $\lambda = 3.10^{-2}$ m., time duration of the transmitted LFM pulse $T = 10^{-6}$ s., time repetition period $T_p = 3{,}9.10^{-3}$, number of samples of LFM transmitted signal is $M = 128$, number of transmitted pulses is $N = 256$.

The real and imaginary parts of the ISAR signal are shown in Fig. 2. 2-D ISAR image is presented in Fig. 3, *a*. Final focused ISAR image obtained by iterative entropy minimization procedure is illustrated in Fig. 3, *b*.

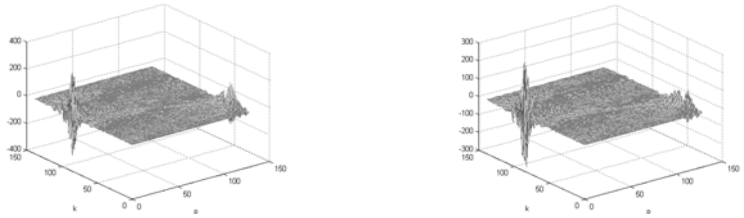

(*a*) (*b*)

Fig. 2. Real and imaginary components of the ISAR signal model after demodulation.

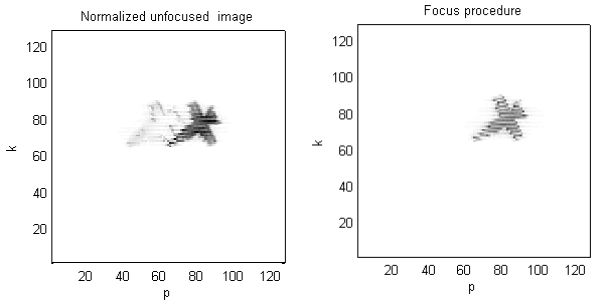

Fig. 3. 2-D ISAR unfocused image (a) and final focused ISAR image (b).

6. Conclusions

In this contribution an analytical geometrical concept of ISAR/SAR scenarios and signal modeling has been suggested. Analytical geometrical equations for ISAR/SAR scenarios have been described. Mathematical model of ISAR/SAR signals reflected from the objects with complicated shape has been devised. All stages of the image reconstruction procedure have been presented. Verification of proposed ISAR/SAR geometry, signal models and image reconstruction procedure has been performed by simulation results of numerical experiments.

References

[1.] Lacomme, P., J-P. Hardange, J-C. Marchias, E. Normant, Air spaceborne radar Systems, New York: William Andrew Publishing, 2001.
[2.] Martorella M. and F. Berizzi. Time windowing for highly focused ISAR image reconstruction, *IEEE*, *Trans. on AES*, vol.41, No. 3, pp. 992-1006, 2005.
[3.] M. Martorella, Novel approach for ISAR image cross-range scaling, *IEEE, Trans. on AES*, vol. 44, No. 1, , pp. 281-294, 2008
[4.] A.Maki, K. Fukui, Y. Kawawada and M. Kiya, Automatic ship identification in ISAR imagery: An on-line system using CMSM, in *IEEE Radar Conference*, Piscataway, NJ, pp206-211, 2002.
[5.] G. Hajduch, J.M Le Caillec and R. Garello, Airborne high resolution ISAR imaging of Ship targets at sea, *IEEE*, *Tran. on AES*, 40, No 1, pp. 378-384, 2004.
[6.] Boultadakis, G., K. Skrapas and P. Frangos, "Time – frequency analysis of radar signals," in RTO / SET 080 Int. Sym. on 'Target Identification and Recognition Using RF Systems, Oslo, Norway, 2004.
[7.] Iv. Garvanov and Ch. Kabakchiev, "One and two dimensions CFAR processors in the presence of strong pulse jamming," *Cybernetics and Information technologies*, №1, pp. 58-72. 2002.
[8.] A.D. Lazarov, Minchev Ch. SAR Imaging of a Moving Target, in Proc. RAST 2007, Istanbul, June, 2007.
[9.] A.D. Lazarov, Minchev Ch**.** ISAR Signal Modeling and Image Reconstruction with Entropy Minimization Autofocussing. In Procciding 25th DASC, Portland, OR,15-19 Oct. 2006**.**

Nonlinear Distortion Compensation Techniques for Future Mobile Communication Base Stations

***Shoichi Narahashi**, Yasunori Suzuki, Junya Ohkawara*

Research Laboratories, NTT DOCOMO, INC., 3-6 Hikari-no-oka, Yokosuka, Kanagawa 239-8536 JAPAN
narahashi@nttdocomo.co.jp; suzukiyasu@nttdocomo.co.jp; ookawaraj@nttdocomo.co.jp

Keywords: power amplifier, nonlinear distortion, linearizer, intermodulation distortion, feed-forward, predistortion

Abstract: A microwave power amplifier (PA) used in the base station of mobile communication systems requires high power efficiency to achieve low power consumption as well as to offer easy installation and maintenance of the base station. The PA can offer high power efficiency if it is operated around its saturation region; however, when doing so the PA generates a high level of nonlinear distortion components. Because these components cause adjacent channel interference and violate spectrum emission specifications of mobile communication systems, it is indispensable for the PA to employ a nonlinear distortion compensation technique that can compensate for the nonlinear distortion components while maintaining an appropriate output backoff level. This paper presents two nonlinear distortion compensation techniques. The first is a new feed-forward amplifier configuration that employs a harmonic reaction amplifier as the main amplifier for high-efficiency operation. The second is a digital predistortion linearizer that can compensate for the frequency-dependent intermodulation distortion components.

1. Introduction

Mobile communication systems have evolved approximately every ten years to provide state-of-the-art communication services. Long term evolution (LTE) was released as the next mobile communication system by the third generation partnership program (3GPP). Even though mobile communication systems evolve continuously, they will always require that the microwave power amplifier (PA) used in the base stations offers low nonlinear distortion because nonlinear distortion components generated by the PA cause adjacent channel interference and violate spectrum emmision specifications of mobile communication systems.

There are two main derivations in generating nonlinear distortion components. One is to derive the nonlinear distortion components from the saturated region of the PA. The other is to derive the nonlinear distortion components, called intermodulation distortion (IMD) components, from the imperfect linear characteristics of the PA. The IMD components have frequency-dependent characteristics caused by, for example, the memory effect [1]. Since only the IMD components can be compensated by nonlinear distortion compensation techniques, the PA must have the minimum output backoff to maintain the required linearity, although the PA is sometimes designed to be operated around its saturation region to achieve high power efficiency. The main idea behind configuring the PA with high power efficiency and high linearity is to employ an appropriate nonlinear distortion compensation technique as well as to have the minimum output backoff.

The feed-forward (FF) configuration [2]-[4] and digital predistortion linearizer (DPDL) [5]-[6] are well-known techniques that effectively compensate for the IMD components of the PA. A self-adjusting FF [4] configuration has been used for the base station PA of second generation (2G) and some of third generation (3G) mobile communication systems. The FF configuration is capable of compensating for any IMD components in principle; however, the FF configuration does not always achieve excellent power efficiency since it requires a linear amplifier as the error amplifier to amplify the input signal without generating any nonlinear distortion components. One of the technical issues facing for the FFPA is to improve its efficiency. The DPDL, on the other hand, has been used as a typical linearizer for 3G mobile base stations from the standpoint of its affinity with the modulation and demodulation units (digital signal processing) in the base

station equipment. For this reason, it is easy for the DPDL to adjust its performance in principle; however, it is necessary to improve the compensation capability of the DPDL because frequency-dependent IMD components are generated if the PA is operated in the vicinity of the saturation point for high-efficiency operation, which is difficult to compensate with a conventional DPDL.

This paper presents a new FFPA configuration and DPDL for high-efficiency operation: FFPA with a harmonic reaction amplifier (HRA) [7] as the main amplifier [8] and DPDL with a frequency characteristics compensator for the IMD components [9]. The proposed FFPA offers the efficiency of 19.3% for a 2-GHz band, 20-W class FFPA. The proposed DPDL achieves the efficiency of 28% for a 2-GHz band, 1-W class PA.

2. Proposed FFPA

2.1. Configuration

Fig. 1 shows the proposed FFPA configuration. The FFPA has two vector regulators (VRs) that adjust the amplitude and phase values of the input signal to the FFPA. It is of great importance to improve the maximum efficiency of the main amplifier to achieve higher efficiency of the FFPA since the efficiency of the FFPA is defined as the ratio of the output power of the FFPA to the power consumed by the main and error amplifiers [3]. The FFPA attains the efficiency of 20% if the main amplifier offers the efficiency of 68% with the output backoff of 3 dB [8]. The main amplifier employs the HRA since the HRA can offer a maximum power added efficiency higher than 68%. The error amplifier employs a class-A amplifier. The FFPA also uses a GaAs MMIC as a preamplifier. Configuration details are described in [8].

2.2. Experimental Results

Fig. 2 shows the adjacent channel leakage power ratio (ACLR) performance of the FFPA and main amplifier. The ACLR with 5-MHz and 10-MHz offsets are employed based on the 3GPP specification [10]. The FFPA attains the ACLR of -45 dBc with a 5-MHz offset at the output power of 39 dBm, which means that the FFPA improves the IMD by 15.5 dB at the output power of 39 dBm. The FFPA also achieves the ACLR of -50 dBc with a 10-MHz offset and improves the IMD by 7.0 dB at the output power of 40.8 dBm. The output backoff point of the main amplifier is 4.0 dB from the saturation output power at the ACLR of -45 dBc with a 5-MHz offset. Fig. 3 shows the efficiency performance of the FFPA and main amplifier. The efficiencies of the FFPA and main amplifier are 19.3% and 37.4% at the output power of 39 dBm, respectively. It is shown that the efficiency of the conventional FFPA ranges from 10% to 15% for typical multi-carrier signals [11]. The fabricated FFPA attains a higher efficiency than that for all conventional FFPA. Fig. 4 presents the spectrum of the main amplifier and proposed FFPA. The proposed FFPA can compensate for the frequency-dependent distortion shown in the spectrum of the main amplifier.

3. Proposed DPDL

3.1. Configuration

Fig. 5 shows the configuration of the proposed DPDL depicting up to a 5th-order path. The input signal, $x(t)$, is divided into a linear delayed path and distortion generation paths. The 3rd- and 5th-order distortion generators generate 3rd-order distortion components and 5th-order distortion components, respectively. The vector regulator adjusts the amplitude and the phase of the output signal of the distortion generator. When the IMD components are frequency dependent, the amplitude and phase set by the vector regulators are not optimum over the entire IMD bandwidth. Thus frequency characteristic compensators $H_3(\omega)$ and $H_5(\omega)$ give the frequency characteristics to the output signal of the distortion generator to cancel the frequency dependence. The signal from the linear path and the signal from the distortion generation paths are combined to yield $y(t)$. The combiner is followed by a digital-to-analog converter (DAC), a frequency upconverter, and a PA unit. The controller adjusts the vector regulators, the frequency characteristics compensators, and the monitor. The monitor

measures the power of the IMD components at the output of the PA with center frequency f_w and bandwidth Δf as instructed by the controller. Operation details are described in [9].

3.2. Experimental Results

Fig. 6 shows an example of a power spectrum at the output of the PA without and with the DPDL at the output backoff of 7.6 dB from the saturation output power. For comparison, a power spectrum without $H_3(\omega)$ is also shown in Fig. 6. This experiment employs a QPSK signal of 3.84 M symbols per second and root roll-off factor of 0.22 as the input signal. The DPDL without $H_3(\omega)$ yields different improvement levels for the lower and upper IMD components. From Fig. 6, the DPDL can compensate for the frequency-dependent IMD. Fig. 7 shows the ACLR at ±5-MHz offset frequency versus the output backoff from the output saturation power (P_{sat}). From Fig. 7, the DPDL with $H_3(\omega)$ achieves the same amount of IMD suppression at 5 MHz and −5 MHz offset frequencies in the measured power range. Fig. 8 shows the power added efficiency (PAE) versus ACLR. The DPDL improves the PAE from approximately 8% to 28% at the ACLR of -45 dBc as compared to the case without using DPDL.

4. Conclusions

This paper presented a new FFPA configuration and DPDL for high-efficiency operation. The FFPA configuration employing the HRA as the main amplifier offered the efficiency of 19.3% at the ACLR of -45 dBc with a 5-MHz offset and the output power of 39 dBm using a W-CDMA test signal. The experiment confirmed that the proposed FFPA attained, to the best of our knowledge, the highest efficiency of nearly 20% for 2-GHz band, 20-W class mobile communication base stations. The DPDL improved not only the frequency-dependent IMD components for QPSK singnals but also the power added efficiency of the power amplifier.

There still remain technical issues that must be investigated such as nonlinear distortion compensation using a multi-carrier modulated signal or a modulated signal with a wide bandwidth.

References

[1] H. Ku, M.D. McKinley, and J.S. Kenny, “Quantifying memory effect in RF power amplifiers,” *IEEE Trans. on MTT*, vol. 50, no. 12, pp. 2843-2849, December 2002.

[2] H. Seidel, “A microwave feed-forward experiment,” *Bell System Tech. Jour.*, vol. 50, no. 9, pp. 2789-2916, 1971.

[3] N. Pothecary, *Feedforward Linear Power Amplifier*, Boston, London: Artech House 1999.

[4] S. Narahashi, and T. Nojima, “Extremely low-distortion multi-carrier amplifier - Self-adjusting feed-forward (SAFF) amplifier -,” in *Proc. IEEE ICC’91*, 1991, pp. 46.5.1-46.5.6.

[5] N. Hongo, T. Miyatani, and Y. Akaiwa, “A predistorter for a power amplifier affected by the even-order distortion,” *IEEE Proc. Vehicular Tech. Conf.*, Vol. 1, pp. 266-270, October 2003.

[6] W.-J. Kim, K.-J. Cho, S. P. Stapleton, J.-H. Kim, “Piecewise pre-equalized linearization of the wireless transmitter with a Doherty amplifier,” *IEEE Trans. on MTT*, vol. 54, no. 9, pp. 3469-3478, September 2006.

[7] S. Nishiki, and T. Nojima, “Harmonic reaction amplifier - A novel high efficiency and high-power microwave amplifier,” in *Proc. IEEE MTT-S Int. Microw. Symp. Digest*, paper DD-5, pp. 963 - 966, 1987.

[8] Y. Suzuki, S. Narahashi, and T. Nojima, “Highly-efficient feed-forward amplifier employing a harmonic reaction amplifier,” *IEEE Radio and Wireless Symposium 2009*, pp. 550 - 553, January 2009.

[9] S. Mizuta, Y. Suzuki, S. Narahashi, and Y. Yamao, “A new adjustment method for the frequency-dependent IMD compensator of the digital predistortion linearizer,” *IEEE Radio and Wireless Symposium 2006*, pp. 255 - 258, January 2006.

[10] *UTRA (BS) FDD; Radio transmission and reception*, Third generation partnership project TS25.104, 1999.

[11] F.H. Raab et al., “Power amplifiers and transmitters for RF and microwaves,” *IEEE Trans. on MTT*, vol. 50, no. 3, pp. 814-826, March 2002.

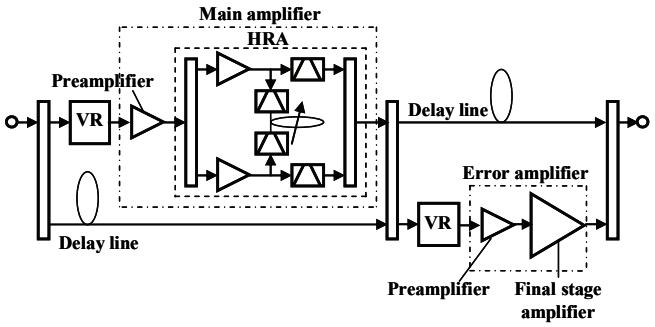

Fig. 1. Proposed FFPA configuration

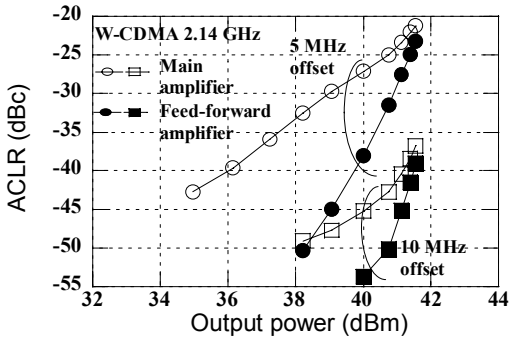

Fig. 2. ACLR performance

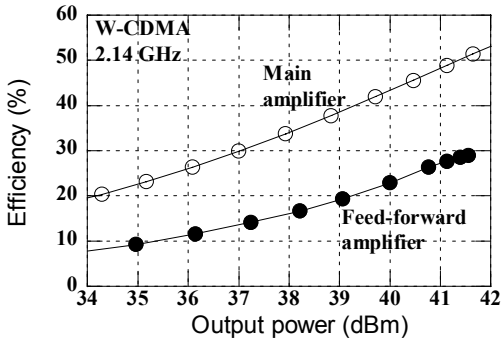

Fig. 3. Efficiency of fabricated FFPA and main amplifier

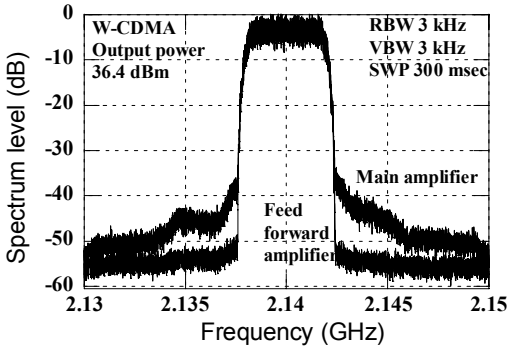

Fig. 4. Spectrum level

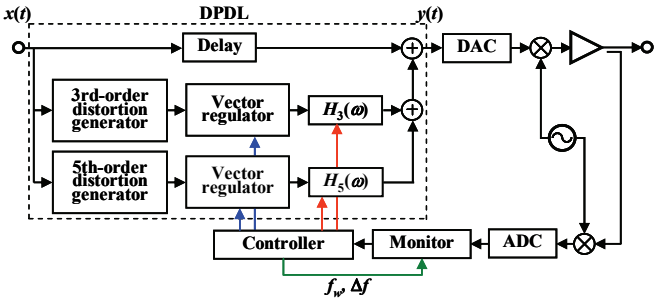

Fig. 5. Proposed DPDL configuration

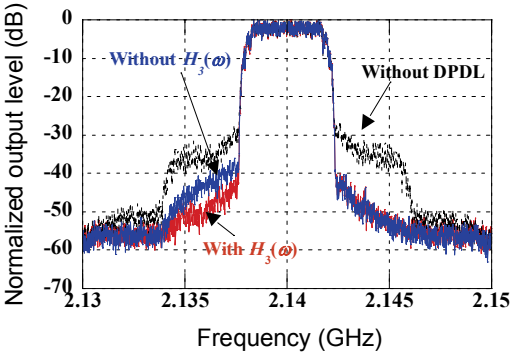

Fig. 6. Spectrum at output backoff of 7.6 dB

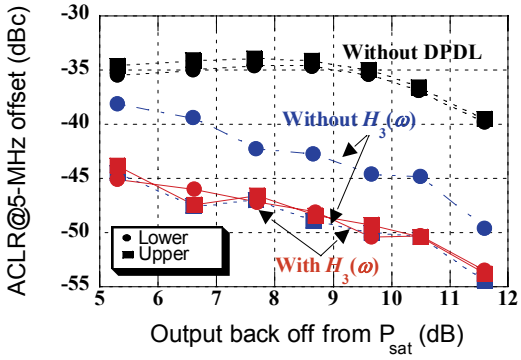

Fig. 7. ACLR versus output backoff from P_{sat}

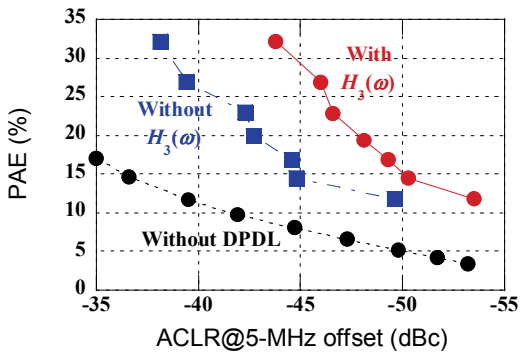

Fig. 8. Power added efficiency versus ACLR

Emission Security and Operating Environment Investigation

Eugene Nickolov

Bulgarian Academy of Sciences, National Laboratory of Computer Virology,
"Acad. Georgi Bonchev" Str., Block 8, 1113 Sofia, Bulgaria
eugene.nickolov@nlcv.bas.bg

Keywords: Emission Security, Malicious Attacks, Malicious Software, Computing Systems, Video Controllers, Protection Systems, Tempest Viruses, EmSec Viruses.

Abstract: In this paper the issues, related to the emissions from visualizing terminal devices are considered. Main accent on display devices of different types computing systems is set. Special attention to the possibility for creating and real implementing of malicious attacks by using electromagnetic emissions under computing systems, based on Windows OS, Linux OS and Mac OS, is paid. The possibilities for modifying video drivers, which manage video controllers in different computing systems, are considered. Possibilities for creating of software protections, which protects the video controllers against unwanted regime of increased emissions, are presented. In conclusion, the benefits and disadvantages of malicious attacks, based on emissions, are evaluated. The benefits and disadvantages of existing systems for protection against similar type of attacks, is also inspected. All analyses and investigations are carried out in case of clearly defined limit between specialized military applications, concerning the national security, and wide distributed commercial systems used in business activities.

1. Pre-restrictions

This report will not be considered military hardware and specialized software applications, usually affecting the national security of a country. Also will not be considered specialized applications, discussing anti-terroristic acts, accomplished at the territory of sovereign countries by their governments, and Internet activities, having a similar nature.

This report will examine commercial systems widely used in so-called bussiness activities. In the consideration the principle of prudent enough information will follow to not be allowed dissemination of sensitive information concerning the conduct of malicious attacks with electromagnetic emissions. For the same reasons technical features as frequency band and energy characteristics of electromagnetic emissions will not be commented.

2. Visualization devices of the type monitor of computing system

In this type of device hardware and software combinations, realizing the function *displaying* of information in computing systems based on the three most popular operating systems (Windows-based, LINUX-based and MAC-based Operating Systems) may be included.

The common characteristic of these devices is the use of electromagnetic energy in low energy potential for the goals of visualization by direct control of a device called a *video controller*.

The operating system manages processes in the video controller using a mediator called *video drivers*. It is this software module is the entry point for accomplishing malicious attacks with electromagnetic emissions (Fig.1).

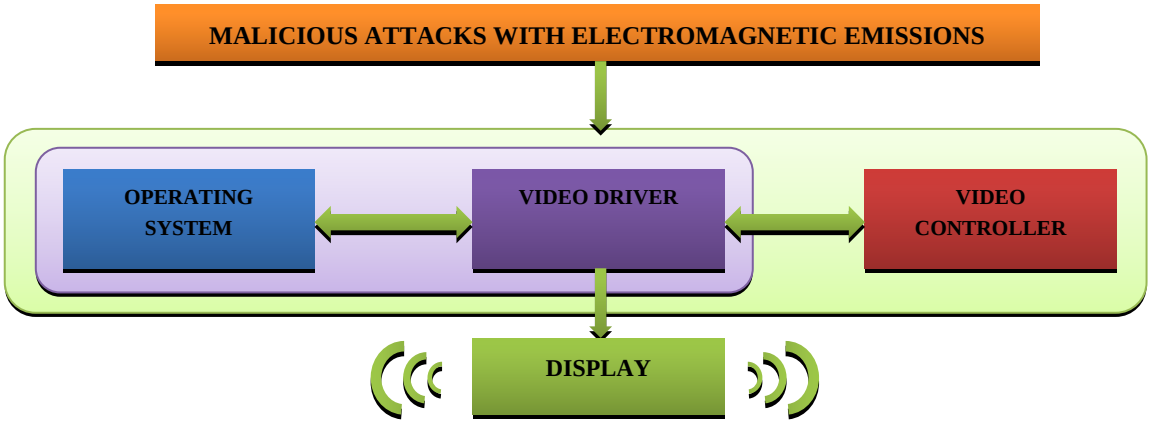

Fig. 1 Accomplishing malicious attacks with electromagnetic emissions

By modifying / replacing part of the code of the video driver can be achieved increased energy potential of electromagnetic energy. In consiquence, a visualization device of type display becomes much more emissive and it is possible remote scanning and buffering of information in real time.

Putting relevant scanners in one operation prior synchronized with malicious attacks enable a competitive company to realize smooth penetration to vital for the competitor information.

3. Malicious attacks with electromagnetic emissions

The main mechanism by which this type of malicious attacks are made is using false messages to update the video drivers, generated by different types of malicious sources as infected Web sites, infected e-mails, infected systems for instant messaging (Fig. 2).

Fig.2 Main mechanism for accomplishing of malicious attacks with electromagnetic emissions

Another less common, but very widespread mechanism is the use of a combination of Trojan horse, downloader and backdoor (Fig. 3). This mechanism allows to perform inidentified complete or partial replacement of the video driver of the attacked system and at the next system restart will be able its "implantation" at the core of the operating system.

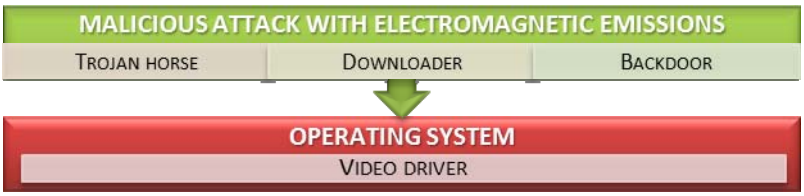

Fig. 3 Mechanism for accomplishing of malicious attacks with electromagnetic emissions by using a combination of Trojan horse, Downloader and Backdoor

The real mechanism, by which increased energy potential of the electromagnetic energy is achieved, is related to the unregulated increase the consumption of the video controller. As a result, besides the increased

heat emission, a significant electromagnetic emissions is caused, which has an impulsive character, functionally connected with the type and nature of the visual information.

4. Modifying video drivers, managing video controllers

The operation of modifying the video drivers supposes to find the initial input—output point in the operating memory, to define the functional modules making up the body of the video driver, to set the control module, to determine the interface modules towards the operating system and the video controller. The attack starts with a replacement or supplement to the first 256 bytes of the control module, and then recalculates the connection of the circuits with the peripheral modules and then replaces also their first 256 bytes (Fig. 4).

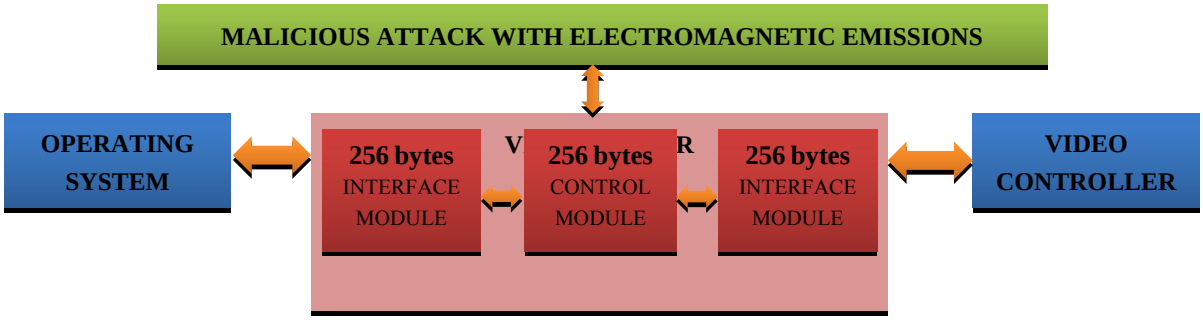

Fig. 4 Operation of modifying of video driver

The next step is verification for working capacity of the replaced (full or partial) video controller with video driver. Until that moment the real and replaced video drivers co-exist in operating memory. After successful verification, the replaced driver takes control of the basic graphic chip located on the video controller and its interface buffers to the graphic video memory.

5. Software methods for protection against unwanted modes of the video controllers

Known in public source software methods for protection against malicious attacks with electromagnetic emissions are based primarily on the use of dynamic checksums of sufficient length and with limited time of existence by accident election from the relatively large range methods for calculation. This ensures reasonable high security against replacement of the program code in the body of the video driver.

Another alternative method of software protection is associated with the use of pre-prepared ROM chips, which allow only reading of the video driver and absolutely impossible hypothesis to upgrade or update. This "dooms" the video system of the limited functionality and limited use over the time.

6. Advantages and disadvantages of the malicious attacks, based on electromagnetic emissions

The main advantage of this type of malicious attacks using electromagnetic emissions is in the apparent distance from the main file objects, the basic operations on files in an operating system, since loading the video driver and therefore its interface with the core of the operating system is carried out once when booting the system. Existing protection systems are designed with considerably less emphasis on the protection of operations related to drivers [1], [2].

Using electromagnetic emissions in the government and military applications has created a misleading perception that such attacks are rare, expensive and not renting for use in commercial systems [3], [4].

The main disadvantage of this type of attack is related to the need for positioning the device on a suitable distance that performs scanning, reading and buffered features. This naturally limits the possible applications and requires additional activities related to the arrange of scanners in a suitable environment and appropriate time [5].

Another serious disadvantage is the relatively high costs of implementing this type of attacks related to the design, manufacture, arrangement and elimination of scanning devices that could leave obvious physical traces of the enemy territory.

7. Advantages and disadvantages of the protection systems against attacks with electromagnetic emissions

The existing systems for the protection of a similar type attacks appear obsolete or significantly modified government or military systems that have been proven. This gives a serious advantage in their use when it is financially grounded.

The design of new protection systems against such attacks, specialized for use in commercial systems is significantly facilitated by the development of modern itegrated circuit technique, which allows the "embedding" checksums in the internal components of the integrated circuit.

The main disadvantage of existing protection systems against this type of attacks is their high cost and lack of flexibility to exchange or change the relationship between the video controller and video driver by the manufacturer. unfortunately This is often required condition in modern manufacturers of video controllers because using the later versions of the firmware, installed in a video controller and later versions of video drivers "press out" a lot better hardware capabilities of a video.

8. Assessments and recommendations

Applying of malicious attacks using electromagnetic emissions is real and significant problem for the commercial systems used in business activities.

Existing combinations of hardware and software created by different manufacturers, have serious laps in the shielding of electromagnetic emissions.

Outgoing electromagnetic emissions, generated by changing the video drivers which controls the video controllers is significantly more serious threat.

Existing features in the core of operating systems with graphical interface such as Windows-based, LINUX-based and MAC-based Operating Systems allow the building of serious enough protections against malicious attacks with electromagnetic emissions.

Existing practices for update and upgrade of video drivers through the use of unprotected network resources are the most serious problem concerning malicious attacks with electromagnetic emissions.

The use of digital signatures components, included in the video drivers and their corresponding verification by the core of the operating system, is a reliable mechanism to prevent from malicious attacks with electromagnetic emissions.

Applying of special trusted integrated circuits in the functional model of video drivers increasee to a maximum reasonable information security in the work of the video systems.

Sample References

[1.] American Society for Industrial Security, http://www.asisonline.org
[2.] American Statistical Association, Privacy, Confidentiality, and Data Security, http://www.amstat.org/comm/cmtepc/
[3.] M Anderson, W Seltzer, Official Statistics and Statistical Confidentiality: Recent Writings and Essential Documents, http://www.uwm.edu/%7 Emargo/govstat/integrity.htm
[4.] C Kopp, "*Electromagnetic Bomb–Weapon of Electronic Mass Destruction"*, http://www.abovetopsecret.com/pages/ebomb.html
[5.]MG Kuhn, "*Electromagnetic Eavesdropping Risks of Flat-Panel Displays*", in PET 2004, http://www.cl.cam.ac.uk/~mgk25/pet2004-fpd.pdf

A Reconfigurable Multi-band Power Amplifier for Mobile Terminals

***Hiroshi Okazaki**, Atsushi Fukuda, Takayuki Furuta, Kunihiro Kawai, Shoichi Narahashi*

Research Laboratories, NTT DOCOMO, INC., 3-6 Hikarino-oka, Yokosuka, Kanagawa 239-8536 JAPAN
okazakih@nttdocomo.co.jp; fukudaat@nttdocomo.co.jp; furutat@nttdocomo.co.jp;
kawaikun@nttdocomo.co.jp; narahashi@nttdocomo.co.jp

Keywords: High efficiency, Multiband, Power amplifier, Reconfigurable circuits, Switch

Abstract: This paper presents a highly-efficient multi-band power amplifier (PA) for future mobile terminals. The PA employs reconfigurable matching networks (MNs) that consist of transmission lines, semiconductor switches, and lumped capacitors. The MN achieves the desired matching condition in the target frequency band by controlling the on/off status of switches. The fabricated PA prototype has three stages and the reconfigurable MNs are employed in the second and final stages. The reconfigurable PA has 8 states to cover 9 frequency bands from 0.7 to 2.5 GHz. Experimental results show that the PA achieves a linear gain of over 30 dB, a saturated output power of greater than 34 dBm, and a maximum power added efficiency of over 40% at the supply voltage of 3.5 V when operating in each band.

1. Introduction

New broadband wireless systems will be utilized to achieve high-speed and high-capacity data transmission to cope with the diversification in user needs. Harmony among different coexisting wireless systems will be considered as a form of future mobile communications. Because the main specification for wireless systems is the frequency band, mobile terminals will be expected to function in all required frequency bands to support various wireless environments.

The RF front-end is a key component in future multi-band/multi-mode mobile terminals. In conventional cellular phones, multiple RF frond-ends are installed for multi-band use [1]. However, simply adding a large number of RF front-ends is not acceptable from the viewpoint of size. There have been studies on various ways of achieving multi-band or broadband circuits that comprise a multi-band front-end [2-5].

Reconfigurable or tunable RF front-ends [6] are a way to provide multi-band function in cognitive radio systems or future mobile terminals, which must consider the capability to support a large number of wireless systems that use different frequency bands. Fig. 1 shows a reconfigurable RF front-end that uses a single-path configuration and the use of single-band devices with distributed reconfigurable matching networks (MNs) [7-8].

A power amplifier (PA) and filter are key devices in the RF front-end. Multi-band PAs have been investigated for use in mobile terminals [6-10]. This paper presents a 3-stage high power and highly-efficient 9-band reconfigurable PA operating from 0.7 to 2.5 GHz [10]. The PA is designed to achieve a gain of over 30 dB for each frequency band. GaAs Field Effect Transistor (FET) switches are used in order to facilitate a high level of integration with amplification devices and other elements. The PA achieves an output power exceeding 34 dBm with the maximum power-added efficiency (PAE) of over 40% with a Continuous Wave (CW) test signal in the 9 targeted bands.

2. Reconfigurable Power Amplifier

The reconfigurable MNs, called band switchable MNs, proposed in [7-10] represent practical configurations of a reconfigurable PA. They employ simple single-pole-single-throw (SPST) switches to change the frequency response and provide an amplification device with the optimum impedance in each band. Fig. 2 shows the basic configuration of the proposed output band switchable MN. The characteristic impedance of the transmission line (TL) is set to Z_0. A block for matching is connected to the TL via a switch whenever a band is added. The length of the TL, d_n, in Fig. 2, and the n-th block are designed for the n-th band, which is set according to single stub impedance tuning. An on-state switch is not necessarily required in the first MN for the first band. Namely, N band operation is accomplished by (N-1) switches. Considering practical implementation, several switches including the (n-1)-th switch can be turned on when the MN is operated in the n-th frequency band. Since no switches are inserted directly into the input and output signal paths, the configuration is expected to have less of an effect on the output power (Pout) and PAE. The input MN can be designed in the same way as the output MN.

3. Design and Experimental Results of 9-Band PA

A 9-band PA employing the band switchable MNs was designed considering the influence of non-ideal characteristics of commercially available GaAs FET switches [10]. Nine-bands, 0.7, 0.8, 0.9, 1.4, 1.7, 1.8, 1.9, 2.3, and 2.5 GHz, are selected as applied or applicable bands for a cellular system. The PA is designed to have 3 stages to provide the total power gain of over 30 dB. Each stage is designed individually to match to 50 Ω of Z_0. A middle-power Heterojunction Bipolar Transistor (HBT) for the first stage and two high-power HBTs for the second and final stages are used as amplification devices. The final stage is designed to achieve power matching. The band switchable MN consists of a TL, switches, and lumped capacitors, which are blocks shown in Fig. 2. The MNs are adopted in not only the final stage but also the second stage to achieve proper matching conditions in the second stage. Fig. 3 shows a photograph of the fabricated PA [10]. A 0.2-mm-thick Au-clad substrate with a dielectric constant of 3.5 is used for the MNs.

Fig. 4 shows the measured frequency responses of the PA at several switch statuses to represent specific operation modes: (a) 0.7-GHz, (b) 0.8-GHz, (c) 0.9-GHz, (d) 1.4-GHz, (e) 1.7-GHz, (f) 1.8/1.9-GHz, (g) 2.3-GHz, and (h) 2.5-GHz modes. In Fig. 4, the 9-band PA achieves a gain of over 30 dB in each mode. The collector supply voltage and base supply voltage are set to 3.5 V and 1.28 V, respectively, for the first stage, and 3.5 V and 1.26 V, respectively, for the second and final stages. The results show that the 9-band PA successfully changes its frequency response through the activation of GaAs FET switches.

Fig. 5 shows the frequency responses for the saturated output power, Psat, and the maximum PAE with the CW test for the low band modes of 0.7/0.8/0.9 GHz (Fig. 5(a)), middle band modes of 1.4/1.7/1.8/1.9 GHz (Fig. 5(b)), and high band modes of 2.3/2.5 GHz (Fig. 5(c)). The HBTs are biased under the same conditions described above. The saturation power levels exceed 34 dBm in all bands. The maximum PAE values for the 0.7, 0.8, and 0.9-GHz modes are approximately 43%, 43%, and 41%, respectively, as shown in Fig. 5(a), those for the 1.4, 1.7, 1.8, and 1.9-GHz modes are approximately 47%, 43%, 40%, and 42%, respectively, as shown in Fig. 5(b), and those for the 2.3 and 2.5-GHz modes are approximately 42% and 39%, respectively, as shown in Fig. 5(c).

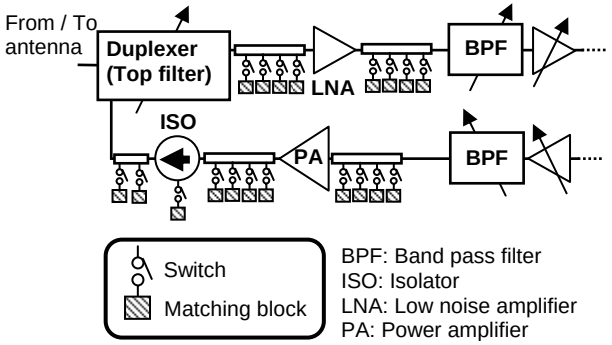

Fig. 1. Multi-band RF front-end configuration.

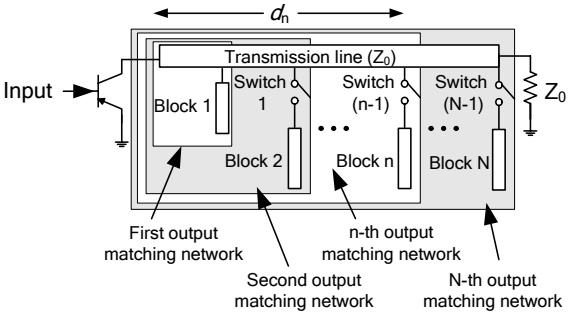

Fig. 2. Band switchable matching network for output.

Fig. 6 shows the gain and the PAE at various Pout at the representative frequencies of 0.83 GHz, 1.75 GHz, and 2.5 GHz. Gain expansion in a high output power range is observed in each frequency because of class-B operation for the PA. Similar results are confirmed at the other frequencies.

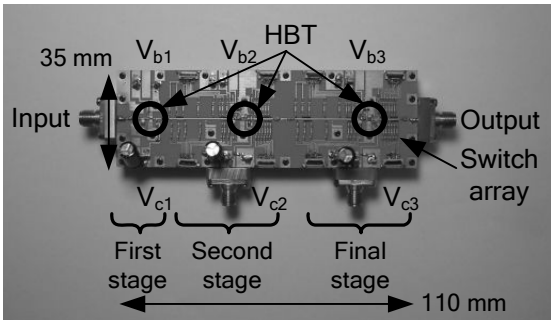

Fig. 3. Photograph of 9-band 3-stage reconfigurable PA.

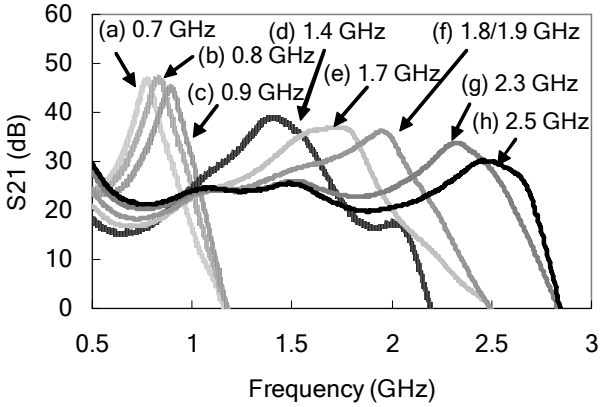

Fig. 4. Measured frequency responses.

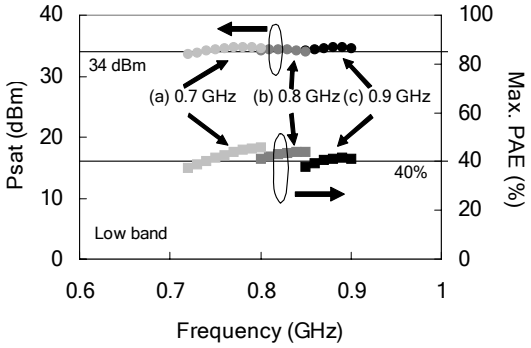

(a) Low band (0.7/0.8/0.9-GHz mode)

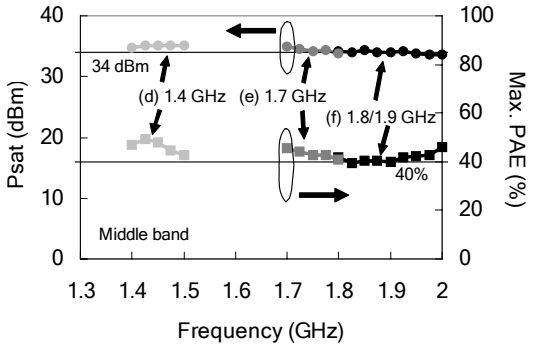

(b) Middle band (1.4/1.7/1.8/1.9-GHz mode)

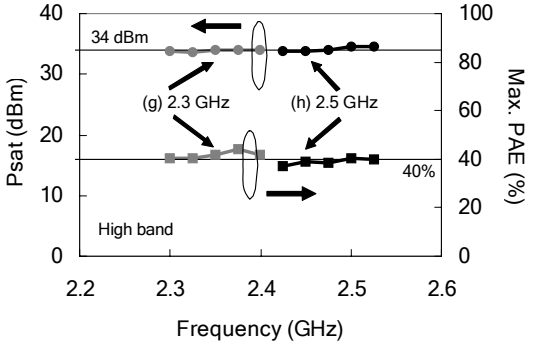

(c) High band (2.3/2.5-GHz mode)

Fig. 5. Measured frequency response for Psat and PAE with CW test signal of fabricated 9-band amplifier.

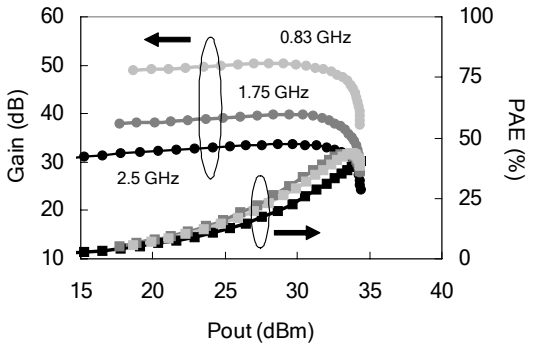

Fig. 6. Measured gain and PAE versus input power for 0.83 GHz, 1.75 GHz, and 2.5 GHz.

4. Conclusions

This paper presented a 3-stage 9-band reconfigurable PA. The band switchable MNs change the frequency response through activation of the GaAs SPST switches in the second and final stages. The 9-band PA, designed for the representative bands of 0.7, 0.8, 0.9, 1.4, 1.7, 1.8, 1.9, 2.3, and 2.5 GHz, was tested using CW signals. These results confirm that the proposed topology is feasible for nearly band-free operation from 0.7 to 2.5 GHz. Future issues to be addressed include reducing the entire circuit size so that the PA can be applied to practical applications.

References

[1.] M. Koiwa, F. Inoue, and T. Okada, "Multiband mobile terminals," *NTT DoCoMo Technical Journal*, vol. 8, no. 2, pp. 31–38, Sep. 2006.

[2.] G. Boeck, D. Pienkowski, R. Circa, M. Otte, B. Heyne, P. Rykaczewski, R. Wittmann, and R. Kakerow, "RF front-end technology reconfigurable mobile systems," in *Proc. SBMO/IEEE MTT-S Int. Microwave and Optoelectronics Conf.*, pp. 863–868, Sep. 2003.

[3.] C. Garuda and M. Ismail, "A multi-band CMOS RF front-end for 4G WiMAX and WLAN applications," in *Proc. 2006 IEEE Int. Symp. Circuits and Systems*, pp. 3049–3052, May 2006.

[4.] R. Malmqvist, A. Gustafsson, T. Nilsson, C. Samuelsson, B. Carlegrim, I. Ferrer, T. Vaha-Heikkila, A. Ouacha and R. Erickson, "RF-MEMS and GaAs based reconfigurable RF front-end components for wide-band multi-functional phased arrays," in Proc. *36th European Microwave Conf.*, pp. 1798–1801, Sep. 2006.

[5.] "Challenges and Technologies for 3G/4G Multi-Mode Front End Designs," *2010 IEEE Int. Microwave Symp. Workshops*, WSK, 2010.

[6.] "Tunable RF-components and modules for wireless communication systems," *2009 IEEE Int. Microwave Symp. Workshops*, WMA, 2009.

[7.] H. Okazaki, A. Fukuda, K. Kawai, T. Furuta, and S. Narahashi, "MEMS-based reconfigurable RF front-end architecture for future band-free mobile terminals," in Proc. *37th European Microwave Conf.*, pp. 1058–1061, Oct. 2007.

[8.] H. Okazaki, K. Kawai, A. Fukuda, T. Furuta, and S. Narahashi, "Reconfigurable amplifier towards enhanced selectivity of future multi-band mobile terminals," in *IEEE Int. Microwave Workshop Series on RF Front-ends for Software Defined and Cognitive Radio Solutions*, pp. 13–16, Feb. 2010.

[9.] A. Fukuda, H. Okazaki, T. Hirota, and Y. Yamao, "Novel 900 MHz/1.9 GHz dual-mode power amplifier employing MEMS switches for optimum matching," *IEEE Microwave and Wireless Components Lett.*, vol. 14, pp. 121–123, Mar. 2004.

[10.] A. Fukuda, K. Kawai, T. Furura, H. Okazaki, S. Oka, S. Narahashi, and A. Murase, "A high power and highly efficient multi-band power amplifier for mobile terminals," *2010 IEEE Radio and Microwave Symp.*, pp. 45-48, Jan. 2010.

Cognitive Radio and green communications: power consumption consideration

Jacques Palicot [(1)]***, Xun Zhang*** [(1)]***,Pierre Leray*** [(1)]***, Christophe Moy*** [(1)]
[(1)] SUPELEC/IETR, Cesson-sévigné, France
{jacques.palicot, xun.zhang, pierre.leray, christophe.moy,}@supelec.fr

Keywords: Cognitive Radio, Green communications, sensors, power consumption.

Abstract: Green Cognitive Radio (GCR) is a Cognitive Radio, which is aware of sustainable development and takes it as an additional constraint in the decision making function of the cognitive cycle. In this paper, we remind the Cognitive Radio concept, and then explain how the sensors distributed within the three layers of our model help to reach GCR. The use of these sensors, so as to make the correct decision and to comply with the sustainable development constraints, is explained through two examples related to power consumption

1. Introduction

Since Resolution 42/187 of the United Nations General Assembly in December 1987 , Sustainable Development (SD) has become an issue and an aspiration of our civilization. The most often-quoted definition of SD has been formulated by the Brundtland Commission [1] as the development that "meets the needs of the present without compromising the ability of future generations to meet their own needs". The first paper related to cognitive radio, as a way of decreasing electromagnetic pollution (mainly from the human exposure point of view) has been presented several years ago in [2]. But, at that time, this type of preoccupation was not in the trend. Now, mainly due to global warming, it is in the limelight. Currently, 3 % of the world-wide energy is consumed by the ICT infrastructure which causes about 2 % of the world-wide CO2 emissions (which is comparable to the world-wide CO2 emissions by airplanes or one quarter of the world-wide CO2 emissions by cars). In parallel another challenge of future wireless radio systems is to globally reduce the electromagnetic radiation levels in order to have a better coexistence of wireless system (less interference) as well as a reduced human exposure to radiations. This last point was the main objective of [2]. These values of carbon footprint are very impressive. They have been confirmed by a lot of studies and reported in many conferences and workshops as the recent "Next Generation Wireless Green Networks Workshop", held in SUPELEC in November 2009. Starting from the work presented in [3], we claim that Cognitive Radio, thanks to its sensors, is an enabling technology for Green Communications. IT is exactly what we named Green Cognitive Radio. In this paper we focus on power consumption issue and highlight that with adequate sensors as:

- Spectrum Hole detection sensor and Peak to Average Power Ratio (PAPR) sensor we can manage the High Power Amplifier (HPA) efficiency. In transmitters equipments (whatever the type of standard to be amplified) the major consumption is due to the HPA. It could reach during transmission up to 70 % of the total consumption. So, saving a few percent regarding HPA efficiency is of great interest in the context of GC. This example is extracted from [4].
- Thermal sensor and area occupancy ratio sensor. This example describes how to migrate a function from a hot location (high consumption) to a cooler location (lower consumption) by means of both thermal sensor and area occupancy sensor. This example is extracted from [5].

2. Cognitive Radio

2.1. The Cognitive Cycle

Cognitive Radio (CR) relies on Mitola's work in [6] and [7]. Mitola argues that radio will become more and more autonomous, and thanks to the support of flexible technology (namely software defined radio SDR [8]) will acquire some self-autonomy to dynamically modify its functionality. As explained in Fig.1, this relies on a cognitive cycle (part a) from [6]). Part b is a simplified view of the cycle, which can be summarized in three main steps [9]:

- Observe: gathers all the sensing means of a CR,
- Decide: represents all that implies some intelligence including learning, planning, decision making,
- Adapt: reconfigures the radio, designed with SDR principles in order to be as flexible as possible.

Cognitive Radio presents itself as a set of concepts and technologies that enable radio equipments to have the autonomy and the cognitive abilities to become aware of their environment as well as of their own operational abilities [6]. Thus it is a device that has the ability to collect information through its sensors and that can use the past observations on its surrounding environment, in order to improve its behavior consequently. Therefore the CR equipment adapts its behavior to the local context. We can conclude this very short description of CR by saying [3]: "CR is a decentralized view associated with a local optimization of needs and resources versus a centralized and static view based on the worst case scenario's needs".

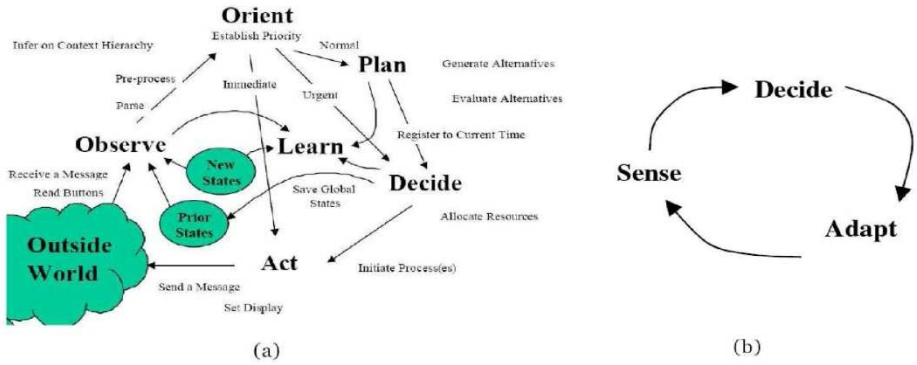

Figure 1: The cognitive cycle (a) and its simplified view (b)

2.2. Multilayer sensors

In order to make appropriate decisions, cognitive radio equipments rely on the information gathered from a set of sensors. Consequently, designing simple, accurate and reliable sensors enable the CR equipment to adapt the best possible way to its surrounding environment. In [9], the concept of "Sensorial Radio Bubble" (SRB) for cognitive radio equipments has been introduced, in order to model and process the environment seen from the sensors of the equipment. Thus it can be seen as the smallest cluster associated to the CR equipment. Through this cluster, the SRB has to manage (discriminate, fusion, filter, etc.) the information collected at its different sensors, in order to send reliable and useful information to the decision making engine inside the equipment. All the information that can help the radio to better adapt its functionality for a given service in a given environment is worth being taken into account. Then as we make no restriction on the sensors nature, it is possible to draw the general approach exposed in Table 1, already presented in [9]. Sensors were classified in function of the OSI layers they correspond to, with a rough division in three layers. In the lowest layer of our model, we find especially all the sensing information related to the physical layer: propagation, power consumption, coding scheme, information related to the hardware executionplatform, etc. At the intermediate level is all the information that participates to vertical handovers, or can help to make a standard choice, as a standard detection sensor for instance. The network load of the standards supported by the equipment may be of

interest also. It also includes the policies concerning the vicinity, the town or the country. The highest layer is especially related to the applications and all that concerns the human interaction with the communicating device. It is related to all that concerns the user, his/her habits, preferences, policies, profile. The equipment can be aware of its environment with the help of sensors such as microphone, video-camera, bio-sensors, channel estimation, battery level, etc.

Layer	Sensors
Upper Layer Application and IHM	User profile: Price, Operator, Personal choices, etc. Sound, Video, Speed, position, Velocity, Security, Indoor/outdoor, etc.
Intermediate Layer Transport, Network	vertical Handover inter/intra networks, Standards Recognition, Load on a link, etc.
Lower Layer Physical, link, medium, running hardware	Access mode, Power, Modulation, Cannel coding, Carrier /Symbol frequencies, horizontal Handover, Channel estimation, Direction of Arrival, Consumption, etc.

Tableau 1: The sensors according to the simplified three layer model [9]

3. Power consumption examples

3.1. PAPR sensor for High Power Amplifier efficiency

This section is based on the work published in [4] Future wireless reconfigurable multistandards equipments will amplify a lot of different standards, each one having each its PAPR. In order to amplify these signals with the same HPA, without modifying any hardware, the current solution is to take an Input Back Off (IBO) greater than the greatest PAPR of the standards. This is also the situation in the context of Dynamic Spectrum Access. Therefore the efficiency of the HPA is very low (see Fig. 2). Another solution we proposed in [4] is to use an algorithm to mitigate the PAPR in order to amplify every signals with a high efficiency at a low IBO. That means whatever the PAPR of the signal is, it should be lower than the predefined IBO after mitigation. In the CR context, we proposed in [10] to use the Spectrum Hole sensor to detect the hole and to use part of it to convey the correcting signal to mitigate the PAPR. The other part of the hole is used for useful data. The PAPR sensor is used, in this example, to select the best algorithm to mitigate the signal PAPR under the IBO threshold.

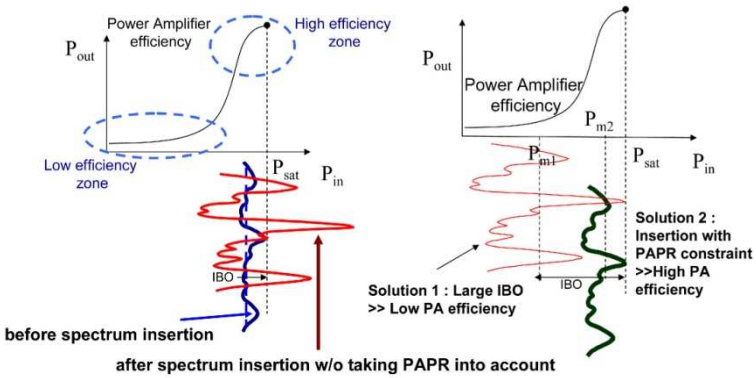

Figure 2 : Amplification of different signals with different PAPR and its effect on HPA efficiency

3.2. Function migration, in reconfigurable hardware, for temperature and power consumption management

This section is based on the work submitted in [5]. We measured and shown there is a strong connection between temperature of the FPGA block and the consumption of this block as it is presented Fig.3. Using this information given by the thermal sensor and using Partial Reconfiguration technology as described in [11], it is therefore possible to offer a strategy of migrating functions, as in [12], from hot blocks to cooler blocks as presented Fig.4.The area occupancy sensor informs if this cooler block is free to perform function migration.

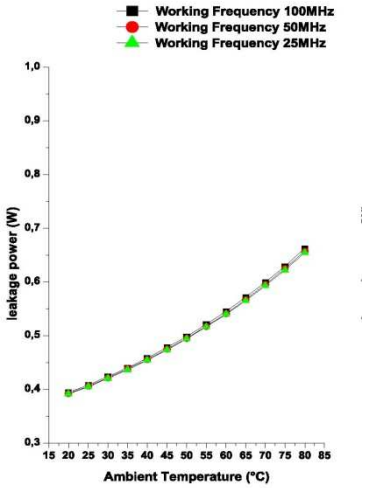

Figure 3 : relationship between temperature and consumption, leakage power example

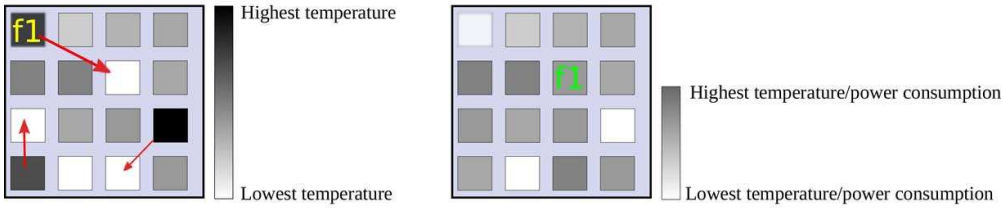

Figure 4: Moving hotspot function to a cooler zone

4. Conclusion

This paper deals with Green communications from the equipment power consumption point of view. We shown through two examples, that using cognitive cycle with proper sensors, we can decide actions which decrease the power consumption. This strategy is what we called Green Cognitive Radio. Further work will demonstrate this strategy through real demonstrations.

Acknowledgment

This work has been supported by Motorola Foundation.

References

[1] United Nations. 1987."Report of the World Commission on Environment and Development." General Assembly Resolution 42/187,11 December 1987. Retrieved: 2007-04-12.
[2] J. Palicot, C. Roland, "On The Use Of Cognitive Radio For Decreasing The Electromagnetic Radiations," URSI 05, XXVIII General Assembly , New Delhi, India, October 23-29, 2005.
[3] J. Palicot, "Cognitive Radio: An Enabling Technology for the Green Radio Communications Concept," IWCMC'09,Germany June 09.
[4] Jacques Palicot, Yves Louët, Mohamad Mroué, "Peak to Average Power Ratio sensor for Green Cognitive Radio", PIMRC 2010, Istanbul, Turkey.
[5] Xun Zhang, Pierre.leray, Christophe Moy, Jacques.Palicot, "Thermal and circuit occupation ratio sensors for Cognitive Radio systems: an opportunity for energy efficiency", IEEE Communications Magazine, unpublished.
[6] J.Mitola, Cognitive Radio An Integrated Agent Architecture for Software Defined Radio}, PhD thesis, Royal Institute of Technology (KTH), May 2000.
[7] J. Mitola III and GQ Maguire Jr. Cognitive radio: making software radios more personal. IEEE personal communications,6(4):13–18,1999.
[8] J.Mitola, "The software Radio Architecture," IEEE Communications Magazine, May 95, pp. 26-38.
[9] J. Palicot, C. Moy, R. Hachemani. Multilayer sensors for the sensorial radio bubble. Physical Communication, (2):151– 165, May 2009
[10] Palicot J, Louet Y, Hussain S, Zabre S, Frequency Domain Interpretation of Power Ratio Metric for Cognitive Radio Systems, Proceedings of IET Communications Journal, N° 2, pp 783-793, june 2008.
[11] Julien Delorme, Amor Nafkha, Pierre Leray, Christophe Moy. "New opbhwicap interface for realtime partial reconfiguration of fpga". *International Conference on Reconfigurable Computing and FPGAs, 2009.*
[12] Adwait gupte and Phillip Jones, "Hotspot mitigation using dynamic partial reconfiguration for improved performance", *International Conference on Reconfigurable Computing and FPGAs*, 2009.

Advanced Signal Processing Algorithms for Wireless Communications

Erdal Panayırcı

Department of Electronics Engineering, Kadir Has University
Istanbul, Turkey
e-mail:eepanay@khas.edu.tr

Keywords: SAGE algorithm, Gibbs sampling, CDMA system.

Abstract: In this paper advance signal processing techniques are presented and their application to the wireless communication systems as well as main knowledge gaps are discussed. Finally an application of some of these techniques to joint parameter estimation and data detection to the asynchronous code division multiple access (CDMA) systems is presented.

1. Introduction

Traditional wireless technologies are confronted with new challenges in meeting the ubiquity and mobility requirements of cellular systems. Hostile channel characteristics and limited bandwidths in wireless applications provide key barriers that future generation systems must cope with. Advanced signal processing methods, such as

- the expectation-maximization(EM) algorithm [1];
- the space alternating generalized expectation, maximization(SAGE) algorithm [2];
- the Baum-Welch algorithm [3]; the Kalman filters and their extensions;
- the Hidden Markov modeling [4];
- Markov Chain Monte Carlo (MCMC) techniques [5];

in collaboration with inexpensive and rapid computing power provide a promising avenue for overcoming the limitations of current technologies. Applications of advanced signal processing algorithms mentioned above include, but are not limited to, joint/blind/sequence detection, decoding, synchronization, equalization as well as channel estimation techniques employed in advanced wireless communication systems such as OFDM/OFDMA, Space-Time-Frequency Coding, MIMO, CDMA and with Multi User Detection, Time-and Frequency-Selective MIMO Channels [6–9]. Especially, the development of suitable algorithms for wireless multiple-access systems in non-stationary and interference-rich environments presents major challenges to us. While considerable previous work has addressed many aspects of this problem separately, e.g., single user-channel equalization, interference suppression for multiple access channels and tracking of time varying channels, the problem of jointly combating these impairments in wireless channels has only recently become significant. On the other hand, the optimal solutions often present a prohibitively high computational complexity, impeding thus their implementation. The statistical tools offered by the advanced signal processing techniques above have provided a promising new route for the design of low complexity signal processing algorithms with performance approaching the theoretical optimum for fast and reliable communication in the highly severe and dynamic wireless environment. Although over the past decade such methods have been successfully applied in a variety of communication contexts, many technical challenges remain in emerging applications, whose solutions will provide the bridge between the theoretical potential of such techniques and their practical utility. The main knowledge gaps identified for next generation wireless communication systems are as follows:

- Theoretical performance and convergence analysis of these Algorithms
- Some new efficient algorithms need to be worked out and developed for some of the problems mentioned above
- Computational complexity problems of these algorithms when applied to on-line implementations

- Implementation of these algorithms based on batch processing and sequential (adaptive) processing depending on how the data are processed and the inference is made has not been completely solved for some of the techniques mentioned above.
- Some class of algorithms requires efficient generation of random samples from an arbitrary target probability distribution, known up to a normalizing constant.
- So far two basic types of algorithms, Metropolis algorithm and Gibbs sampler have been widely used in diverse fields. But it is known that they are substantially complex and difficult to apply for on-line applications like wireless communications.

In the following we present an important example from wireless communications where advance signal processing techniques mentioned above are applied.

2. The EM and SAGE algorithms

A. The EM Algorithm

Consider estimating parameter vector s from data y (*Incomplete data*)

$$y = F(s, z) + n ,$$

where s is the parameter to be estimated and z random parameters (nuisance parameters). Then the ML estimate of s is

$$\hat{s}_{ML} = \arg\max_s p(y \mid s) = \arg\max_s E_z\{p(y \mid s, z)\}$$

Thus, obtaining ML estimates may require an expectation step (E-Step) which is often analytically intractable and a maximization step (M-Step) which is computationally intensive. The EM Algorithm is an iterative algorithm. If we define the *complete data* x as $x \rightarrow y(x)$, many-to-one mapping, having conditional density $f(x|s)$, the EM iteration at the i-th step can be described as

•E-Step: $Q(s|\hat{s}^{(i)}) = E\left\{\log f(x|s)\middle| y, \hat{s}^{(i)}\right\}$

•M-Step: $\hat{s}^{(i+1)} = \arg\max_s Q(s|\hat{s}^{(i)})$.

It is shown that, at each iteration the likelihood-function is monotonically non-decreasing and if the likelihood-function is bounded, then under some conditions, the algorithm converges to the ML estimate

B. The SAGE Algorithm

The SAGE algorithm is an extension of EM algorithm. It provides much faster convergence than EM. Algorithm updates only a subset of elements of the parameters in each iteration.
In the following we present two important examples from wireless communications where advance signal processing techniques mentioned above are employed.

3. A Monte-Carlo Implementation of the SAGE Algorithm for Joint Soft Multiuser and Channel Parameter Estimation

In this section, a computationally efficient, joint transmission delay and channel parameter estimation algorithm is proposed for uplink asynchronous direct-sequence code-division multiple access (DS-CDMA) systems [10]. Asynchronous CDMA received signal model for K users $r = S(\tau)\mathrm{A}d + w$.

Here, $S(\tau)$ contains the signature sequences of all the users $[S(\tau) = S_1(\tau_1), S_2(\tau_2), \cdots, S_K(\tau_K)]$, where τ_k's, $k = 1, 2, \cdots, K$ are the unknown transmission delays, $\mathrm{A} = \mathrm{diag}\{\mathrm{A}_1, \cdots, \mathrm{A}_K\}$ denotes the block diagonal channel matrix. $\mathrm{A}_k = \mathrm{diag}(ak, \cdots, ak)$ being the channel matrix for user k, and ak is the k-th user's channel coefficient $\sim N(0, \sigma_k^2).\tau_k$. τ_k is the k-th user's transmission delay is assumed to be uniformly distributed. Given the observation vector r, the ultimate goal of the receiver is to estimate the channel coefficients $a = [a_1, a_2, \cdots, a_K]^T$ and the propagation delays, $\boldsymbol{\tau} = [\tau_1, \tau_2, \cdots, \tau_K]^T$ jointly by the SAGE algorithm, when the transmitted data vector $\mathrm{d} = [\mathrm{d}_1, \mathrm{d}_2, \cdots, \mathrm{d}_K]^T$ is unknown. Let us choose the parameter vector as $\Theta = \{\mathrm{a}, \tau\}$. At iteration ($i$) of the SAGE algorithm, only the parameters of user k, $\Theta_k = (\mathrm{a}_k, \tau_k)$ are updated, while the parameters of the other users $\bar{\Theta}_k = \Theta \setminus \Theta_k$ are kept fixed. Then

• **E-Step** computes the objective function

$$Q(\Theta_k \mid \Theta^{(i)}) = E_{\mathbf{d}}\left\{\log p\left(\mathbf{r} \mid \mathbf{d}, a_k, \tau_k, \overline{\mathbf{a}}_k^{(i)}, \overline{\boldsymbol{\tau}}_k^{(i)}\right) \mid \mathbf{r}, \mathbf{a}^{(i)}, \boldsymbol{\tau}^{(i)}\right\}.$$

• **M-Step** maximizes the objective function Q with respect to _k to obtain the update

$$\widehat{\Theta}_k^{(i+1)} = \max_{\Theta_k} Q(\Theta_k \mid \widehat{\Theta}^{(i)}), \qquad \widehat{\overline{\Theta}}_k^{(i+1)} = \widehat{\overline{\Theta}}_k^{(i)}.$$

After some algebra, the E-step of the SAGE algorithm:

$$Q_k\left(\Theta_k \middle| \Theta^{(i)}\right) = \frac{2}{N_0}\sum_{l=0}^{L-1} a_k^*(l)\Psi(l,\tau_k) - \frac{L}{N_0}|a_k|^2 - \frac{1}{\sigma_k^2}|a_k|^2$$

where,

$$\Psi(\ell,\tau_k) \triangleq \Re\left\{\boldsymbol{S}_k^\dagger(\ell,\tau_k)\left(\rho_k^{(i)}(\ell)\mathbf{r} - \mathcal{I}_k\right)\right\}$$

and the interference term

$$\mathcal{I}_k \triangleq \sum_{j\neq k} a_j^{(i)}\Big(\boldsymbol{S}_j(\ell+1,\tau_j^{(i)})\rho_{k,j}^{(i)}(\ell,\ell+1) + \boldsymbol{S}_j(\ell,\tau_j^{(i)})\rho_{k,j}^{(i)}(\ell,\ell) + \boldsymbol{S}_j(\ell-1,\tau_j^{(i)})\rho_{k,j}^{(i)}(\ell,\ell-1)\Big).$$

Here,

$\rho_k^{(i)}(\ell)$, $\rho_{k,j}^{(i)}(\ell,\ell+u)$

are the expectations over data d = [d1, d2, · · · , dK]T .

Finally the M-step is realized by taking derivative with respect to τ and a, setting the results equal to zero, and solving: it follows that

$$\tau_k^{(i+1)} = \arg\max_{\tau_k}\left|\sum_{\ell=0}^{L-1}\Psi(\ell,\tau)\right|; \qquad a_k^{(i+1)} = \frac{1}{L + N_0/\sigma_k^2}\sum_{\ell=0}^{L-1}\boldsymbol{S}_k^\dagger(\ell,\tau_k^{(i+1)})\left(d_k^{(n_t)}[\ell]\mathbf{r} - \mathcal{I}_k\right).$$

The main computational problem here is the direct computation of the expectations below. It can be easily seen that this requires an exponential complexity.

$$\rho_k^{(i)}(\ell) = E\left\{d_k(\ell)|\mathbf{r},\boldsymbol{\tau}^{(i)},\mathbf{a}^{(i)}\right\} = \sum_{m\in\mathcal{S}} mP(d_k(\ell)=m|\mathbf{r},\boldsymbol{\tau}^{(i)},\mathbf{a}^{(i)}),$$

$$\rho_{k,j}^{(i)}(\ell,\ell{+}u) = E\left\{d_k(\ell)d_j(\ell+u)|\mathbf{r},\boldsymbol{\tau}^{(i)},\mathbf{a}^{(i)}\right\} = \sum_{m\in\mathcal{S}}\sum_{n\in\mathcal{S}} mnP(d_k(\ell)=m, d_j(\ell{+}u)=n|\mathbf{r},\boldsymbol{\tau}^{(i)},\mathbf{a}^{(i)}),$$

for $j \neq k$, and $\mathcal{S} \triangleq \{-1,+1\}$ and $u \in \{-1,0,+1\}$.

This very high complexity can be avoided by adopting the Markov chain Monte Carlo (MCMC) statistical method which provides computationally efficient way to calculate the expectations. The basic idea is first to generate a number of random samples $\overline{\mathbf{D}}^{(t)}, t = 1,2,\cdots,N_T$ from the joint conditional posterior distribution, $P(\mathrm{D}|\mathrm{r}, \tau^{(i)}, \mathrm{a}^{(i)})$. Then, approximate the expectations above based on the samples of $\overline{\mathbf{D}}^{(t)}$, by

$$\rho_k^{(i)}(\ell) \approx (1/N_s)\sum_{t=1}^{N_s}\xi^{(i)}(\overline{\mathbf{D}}^{(t)}), \quad \rho_{k,j}^{(i)}(\ell,\ell+u) \approx \frac{1}{N_s}\sum_{t=1}^{N_s}\xi^{(i)}\left(\overline{\mathbf{D}}^{(t)}\right).$$

4. Computer Simulation

An asynchronous DS-CDMA system is considered with parameters: No. of Users: $K = 8$; Processing gain $N_c = 8$ (i.e., system load $\eta \triangleq K/N_c = 1$) is considered; Blocks of size $L = 80$ symbols are transmitted; $L_p = 4$, pilot symbols are embedded in each block to determine the initial estimates $\mathrm{a}^{[0]}$ and $\tau^{[0]}$. We refer to this method as MMSE-separate detection and estimation (MMSE-SDE). For comparison purpose, the SAGE-JDE scheme for known transmission delays. We refer to these scheme as "SAGE-JDE, τ known". The average bit-error-rate ($\overline{\mathrm{BER}}$) of the proposed receiver is plotted versus the average *effective* SNR $\frac{L-L_p}{L}\overline{\gamma}_k$, $\overline{\gamma}_k \triangleq \sigma_k^2/N_0$, $k = 1,\ldots,K$.The number of stages in the receiver is limited to 5. Note that all users are updated once within one stage.

.

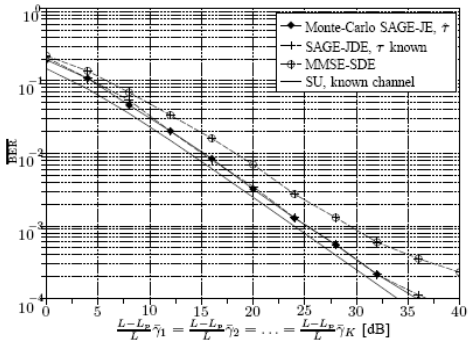

Fig. 1. Performance in quasi-static Rayleigh fading: $K = 8$, $N_c = 8$, $L_p = 4$, $L = 80$, 5 stages

From Fig. 1 we conclude the followings:

(i) The initial MMSE-SDE scheme exhibits floor out for average effective SNR values larger than 30 dB, indicating that the MMSE-SDE is not robust to high correlations between the users' signature sequences.

(ii) The proposed Monte-Carlo SAGE-JE scheme for unknown delay, "Monte-Carlo SAGE-JE, ^_" and "SAGE-JDE, _ known" perform roughly the same over the entire range of SNR.

(iii) Both schemes have a multiuser efficiency of roughly 1 dB over the entire range of SNR values.

5. Conclusions

Based on the developments on advanced signal processing techniques summarized in the above paragraphs and a specific example given on a wireless commination system we conclude the followings,

• Applications of advanced signal processing techniques, in collaboration with inexpensive and rapid computing power, seem to very promising way to overcome the limitations of current technologies.

• The statistical tools offered by the advanced signal processing techniques have enabled us to design several low complexity signal processing algorithms with performance approaching the theoretical optimum for fast and reliable communication in the highly severe and dynamic wireless environment.

• However, more research are needed to come up with some novel solutions to narrow the knowledge gaps, mentioned in Section 1.

References

[1] A. P. Dempster, N. M. Laird and D. B. Rubin, ""Maximum likelihood from incomplete data via the EM algorithm"," *Ann.Roy. Stat. Soc.*, pp. 1–38, Dec. 1977.

[2] J. A. Fessler and A. O. Hero, "Space-alternating generalized expectation-maximization algorithm," *IEEE Trans. Signal Process.*, vol. 42, no. 10, pp. 2664–2677, 1994.

[3] L. E. Baum, T. Petrie, G. Soules, and N. Weiss, "A maximization technique occurring in the statistical analysis of probabilistic functions of Markov chains," *Ann. Math. Statist.*, vol. 41, no. 1, pp. 164–171, Dec. 1970.

[4] L. R. Rabiner, "A tutorial on Hidden Markov Models and selected applications in speech recognition," *Proc. IEEE*, vol. 77, no. 2, pp. 257–286, Feb. 1986.

[5] B. F. Boroujeny and H. Zhu and Z. Shi, "A tutorial on Hidden Markov Models and selected applications in speech recognition," *IEEE Trans. Signal Process.*, vol. 54, no. 6, pp. 1896–1909, 2006.

[6] F. Simoens, D. Duyck, H. A. irpan, E. Panayirci, and M. Moeneclaey, "Monte-Carlo Solutions for Blind Phase Noise Estimation," *EURASIP Journal on Wireless Communications and Networking Communications*, vol. Article ID 570625, March 2009.

[7] E. Panayirci, H. A. Cirpan, "EM-Based MAP Channel Estimation and Data Detection for Downlink MC-CDMA Systems," *IEEE Wireless Communications and Networking Conference 2007*, Honk Kong, 15-17 March 2007.

[8] E. Panayirci, H. Senol and H.V. Poor, "Joint channel estimation, equalization and data detection for OFDM systems in the presence of very high mobility," *IEEE Trans. Signal Process.*, To appear in August 2010.

[9] H. Dogan, E. Panayirci, H.V. Poor, "Low Complexity joint data detection and channel equalization for highly mobile OFDM systems," *IET Communications*, vol. 4, no. 8, pp. 1000–1011, 2010.

[10] A. Kocian, E. Panayirci and H.V. Poor, "A Monte-Carlo implementation of the SAGE algorithm for joint-multiuser decoding, Channel parameter estimation and code acquisition," *IEEE Trans. Signal Process.*, To appear in 2010.

Queuing Modeling of Handovers in 4G Wireless Mobile Networks

Dimitar Radev [(1)]***, Dragan Stankovski*** [(1)]***, Svetla Radeva*** [(2)]

[(1)] Department of Communication Systems and Technologies, University of Russe, 8 Studentska Str., Russe, Bulgaria
dradev@abv.bg; draganstankovski@gmail.com
[(2)] Department of Wireless communications and Broadcasting, College of Telecommunications and Post, Sofia, Bulgaria
svetla_ktp@abv.bg

Keywords: Wireless Mobile Networks, Queuing Systems, Traffic Models, Handover.

Abstract: The queuing modelling of handover in 4G mobile networks is under consideration. Handover is the process of changing the channel (frequency, time slot, spreading code, or combination of them) associated with the current connection while a call is in progress. Call Admission Control and quality of service requirements are considered for determining of traffic classes in multimedia wireless networks. The existing models of the handover simplify the traffic processes and concern the multidimensional heterogeneous traffic only via queues in handover. In this paper is worked out a model, where as queues are presented channels in non-preemptive priority handover schemes. This queuing model is suitable for searching of effective solutions for handover parameters and quality of service parameters for multimedia traffic in modern wireless mobile networks. The model allows implementation of different methods for traffic parameters determination – Markov chains, diffusion equations etc.

1. Introduction

The mobility is one of the most important feature of a wireless cellular communication system. Usually, continuous service is achieved by supporting handover from one cell to another. Handover is the process of changing the channel (frequency, time slot, spreading code, or combination of them) associated with the current connection while a call is in progress [1]. It is often initiated either by crossing a cell boundary or by a deterioration in quality of the signal in the current channel. Handover is divided into two broad categories — hard and soft handovers [3, 4]. In hard handovers, current resources are released before new resources are used; in soft handovers, both existing and new resources are used during the handover process. In this paper the main attention is paid on the soft handover which is used mainly in 4G wireless mobile networks. Poorly designed handover schemes tend to generate very heavy signaling traffic and, thereby, a dramatic decrease in Quality of Service (QoS) [7]. The reason why handovers are critical in cellular communication systems is that neighboring cells are always using a disjoint subset of frequency bands, so negotiations must take place between the mobile station, the current serving base station, and the next potential base station. Other related issues, such as decision making and priority strategies during overloading, might influence the overall performance characteristics [5].

In 4G communication systems, especially when the cell size becomes relatively small, the handover procedure has a significant impact on system performance. Blocking probability of originating calls and the forced termination probability of ongoing calls are the primary criteria for indicating performance.

The existing models of the handover simplify the traffic processes and concern the multidimensional heterogeneous traffic only via queues in handover. In this way are searched simplified solutions, which can't lead to optimal or sooner to effective solution. The possible solutions are searched via reduction of steady states in two- and three-dimensional Markov chains [9] or via searching of simplified probability balance equations of

Markov chain states [8]. In this paper we suggest a model, where as queues are presented channels in non-preemptive priority handover schemes.

2. Call Admission Control and Traffic Classes in Multimedia Wireless Networks

Call Admission Control is a key element for ensuring of the quality of service of 4G mobile wireless networks. A suitable Call Admission Control for the cellular multimedia wireless networks is expected to make efficient use of the wireless resource while supporting different services with different QoS metrics.

The capacity allocation to each class of service is an important issue of a multiservice system. The author [9] suggests two access policies: complete sharing and complete partitioning. In complete sharing policy all users have equal access to the bandwidth which is available all the time, which results of maximum usage of available bandwidth. In this case there is no differentiation between users with different priorities. In complete partitioning policy the available bandwidth is divided into separate sup-pools according to the type of the user, which allows providing control on blocking probabilities.

An efficient call admission control has to provide balance between maximization the resource initialization and minimization the handover call dropping rate. When we have maximal resource initialization, the maximum number of calls enters into network, which may lead to unacceptable high handover call dropping rate. That is the reason for searching a dynamic call admission control which estimates future resource demands, provide high resource initialization and receive the minimum amount of necessary resources for acceptable call dropping rate. This corresponds to the QoS requirements [1], where quality of service refers to the collective effect of service performances that determine the degree of satisfaction the end user of the services. According to these requirements, the traffic classes are: conversational, streaming, interactive and background. As the conversional class traffic mainly include voice traffic and here is concerned as real-time traffic. This traffic class is basic for the quality of service of the handover. The video traffic as usual is accepted as a non-real time traffic and together with the data traffic are going into streaming class. More details about it are given in [9].

3. Modeling of Handover

Nevertheless that there exists some differences in 4G traffic, which are results of the full IP transfer, the handover model keep his multimedia character. The model has two thresholds N-C_{RT} and N-C_H. A handover request is served when is found an available channel and otherwise the request is queued. Each cell contains two queues for real-time requests with length M_{RT} and non-real-time requests with length M_{NRT}. In the suggested model it is supposed that the cannels in mobile station, which are N are concerned as three queues, as is seen from fig.1. Their maximal length is determined from the reserved in the cell channels for new calls and channels for handover calls:

- C_H is a number of channels, which can be used for handover;
- C_{RT} is a number of channels, which can be used for real-time traffic;
- N is a number of available channels per cell;
- M_{RT} and M_{NRT} are respectively real-time and non-real-time queues capacity.

The two parallel queues in handover suppose that the traffic is divided into real-time traffic and non-real-time traffic out of this cell. When appears new calls, the probabilities for serving the channels p_{C1} and p_{C2} determine the choice of acceptable number of channels for real-time traffic (maximum N-C_H) and non real-time traffic (maximum C_H-C_{RT}). The priority of real-time traffic in handover of this multiple scheme $\mu_C.(1\text{-}p_{C1})$ is realized via including feedbacks: $\mu_C.p_{C4}$ at the input of non-real-time traffic with queue length M_{NRT}; $\mu_C.p_{C3}$ and $\mu_C.p_{C5}$ for new coming calls.

In this way the free channels at serving of the handover μ_H, can be used for non-real-time traffic, which wait for serving of handover. On the input of the queue for non-real-time traffic with length M_{NRT} are coming requests with transfer rate $\mu_C.(1\text{-}p_{C2}\text{-}p_{C4})$. In the same way are received the probabilities for channel serving p_{C3}, p_{C4}, p_{C5}, and are received the transfer rates on the input of channels for new coming calls: $(\lambda_{RT} - \mu_C.p_{C3})$ and $(\lambda_{NRT} - \mu_C.p_{C5})$.

The input parameters of the model are traffic transfer rates λ_{RT}, λ_{NRT}, number of the channels into the cell N The model gives possibility via initialization of values for service probabilities in handover and in channels - p_{C1}, p_{C2}, p_{C3}, p_{C4} and p_{C5} to determine the threshold values for system parameters for channel's sharing in mobile station C_H, C_{RT}. As a final result the model allows to calculate the queue lengths M_{RT}, M_{NRT} and service rate μ_H in handover in dependence of the input multiple traffic parameters.

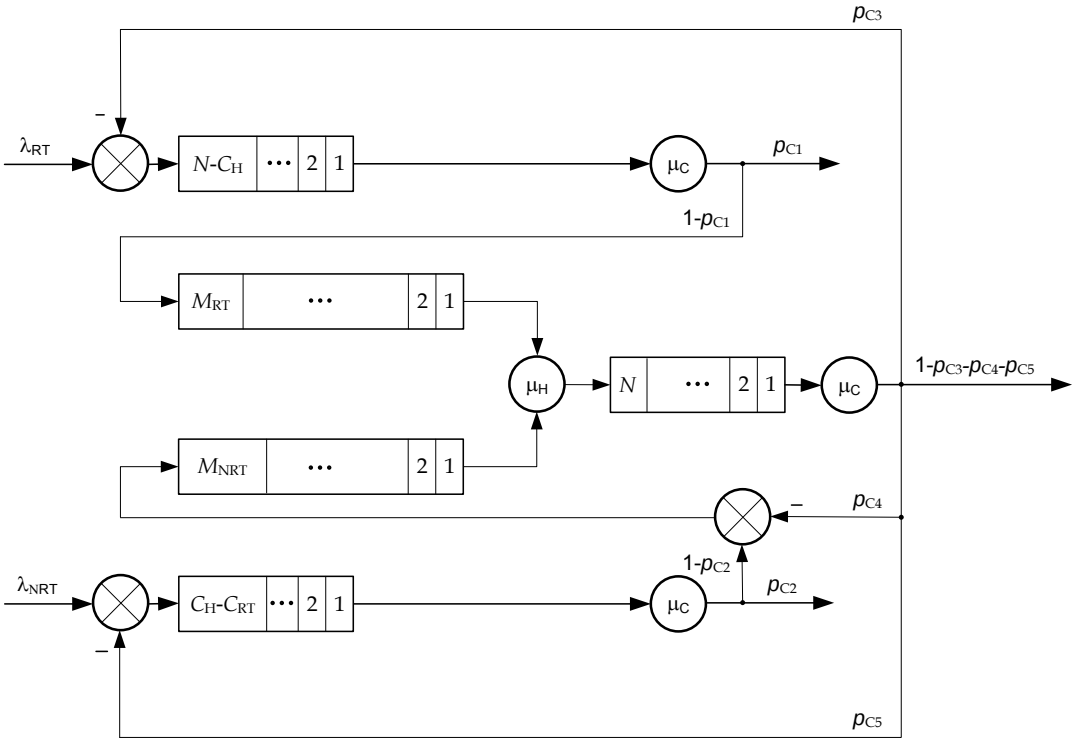

Fig.1. Nonpreemptive priority handover scheme

The common service of queues in handover for this model made it closer to the real schemes for call admission control in modern wireless mobile networks, which are characterized with soft control, state dependent processor sharing according to the vertical mobility.

4. System Analysis

For an illustration of the simplicity of suggested analytical model is assumed that the service times of the channel and the handover are exponential distributed with mean values, respectively $E[T_C] = 1/\mu_C$ and $E[T_H]=1/\mu_H$. It was taken as well the assumption, that the new calls traffic in handover has Poisson distribution.

After implementation of the Little-Love low for new calls, the transfer rate in real time λ_{RT} and non-real-time λ_{NRT} is received as:

$$\lambda_{RT} - \mu_C p_{C3} = (N - C_H).\mu_C p_{C1}, \quad (1)$$

$$\lambda_{NRT} - \mu_C p_{C5} = (C_H - C_{RT}).\mu_C p_{C2}. \quad (2)$$

The queues length in handover can be presented via transfer rate of input traffic, with taking in mind the real-time traffic priority, as follows:

$$\mu_C(1 - p_{C1}) = M_{RT}.\mu_H \quad (3)$$

$$\mu_C(1 - p_{C2} - p_{C4}) = M_{NRT}.\mu_H \quad (4)$$

The local exponential service time for handover service in queuing model easy can be calculated via sojourn time of the M/GI/2-PS traffic system, e.g. as system of two queues with generalized processor sharing of service time.

The number of channels for handover is generalized via probabilities for serving the channels in the cell:

$$\mu_{\mathrm{H}} = N.\mu_{\mathrm{H}}(1 - p_{\mathrm{C3}} - p_{\mathrm{C4}} - p_{\mathrm{C5}}) \quad (5)$$

The solving equations (1)-(5) give a possibility to find the optimal lengths of queues M_{RT}, M_{NRT}, and service rate μ_{H} in handover in such a way to minimize the blocking probability in these queues, e.g. to guarantee the quality of service in wireless mobile network. Most often in this case is used three dimensional Markov chains, for which are constructed state transition diagram and are determined the balance equations.

5. Conclusions and Future Work

In this work is suggested a model, which contains two queues for traffic calls in real-time and non-real-time in handover of a multimedia wireless mobile network. Additional, as a multitude of queues are presented as well the radio channels of mobile station. Thresholds are developed for services of new coming calls in real-time and non-real-time. Nonpreemptive priority for serving real-time calls in handover is implemented.

This queuing model is suitable for searching of effective solutions for handover parameters and quality of service parameters for multimedia traffic in modern wireless mobile networks. The model allows implementation of different methods for traffic parameters determination – Markov chains, diffusion equations etc.

A solution, which gives possibility for calculation of optimal queuing length and service rate in handover is working out. It gives possibility to minimize the blocking probability of these queues and to guarantee quality of service in wireless mobile network.

At the moment we are working on development of suitable methods for effective calculation of the basic traffic parameters in these mobile networks.

Acknowledgment

This work is a part of the scientific project DSAB 02/5 of the Bulgarian National Science Fund. The authors are thankful for the financial support.

References

[1.] 3GPP. Technical Specification Group Radio Access Network. *High Speed Downlink Packet Access; Overall UTRAN Description.* (*3GPP TR 25.855 version 5.0.0*).

[2.] D. Radev, I. Lockshina, V. Denchev, „Queuing Networks in Equilibrium and Markov Chains: Numerical Solution Methods", *World Review of Entrepreneurship, Management and Sustainable Development* (*WREMSD*), vol.3, No.3/4, Inderscience Publishers, pp. 302-316, 2007.

[3.] D. Wong, T.J. Lim, „Soft Handoffs in CDMA Mobile Systems", *IEEE Personal Communications*, pp.6-17, 1997.

[4.] G. Tamea , T. Inzerilli , P. Rea , R. Cusani, „Vertical handover among broadcast networks, Proceedings of the 6th Ïnternational Conference on Symposium on Wireless Communication Systems", pp.418-422, Siena, Italy, 2009,

[5.] H.J. Wang, R.H. Katz, J Giese, „Policy-Enabled Handoffs Across Heterogeneous Wireless Networks" *Proceedings of the Second IEEE Workshop on Mobile Computer Systems and Applications*, p. 51, 1999.

[6.] J. McNair, Zhu Fang, „Vertical handoffs in fourth-generation multinetwork environments", *IEEE Wireless Communications Magazine*. Vol. 11, 3, pp. 8-15, June 2004.

[7.] P.J. Gutierrez, „Packet Scheduling and Quality of Service in HSDPA", Department of Communication Tecnology, Institute of Electronic Systems, Aalborg University, Ph. D. Thesis, October 2003.

[8.] Q-A. Zeng, D.P. Agrawal „Handoff in wireless mobile networks", *Handbook of wireless networks and mobile computing*, John Wiley & Sons, New York, NY, 2002.

[9.] R. Naja, S. Tohmé „Adaptive QoS and Handover Issues in Wireless Multimedia Networks Using a Dynamic Adaptive architecture: DYNAA", *Proceedings of the IFIP TC6/WG6.8 Working Conference on Personal Wireless Communications*, pp.133 – 140, 2002.

Markovian Approach to Optimal Information-Measuring Facilities Integration Problems

Alexander B. Shmelev

Radiotechnical Institute by Academician A.L.Mints, 10, bld.1, 8 Marta st., Moscow, 127083, Russia
abshmelev@yahoo.com

Keywords: Markovian theory, a priori description, probability density function (PDF), Stratonovich equation, Gaussian approximation, nonlinear estimation, joint processing, a posteriori correlation matrix, phase-modulated signal, phase lock loop (PLL), signal/noise ratio.

Abstract: Application of the Markovian nonlinear processing theory to optimal information-measuring facilities integration problems is considered. The integration purpose consists in estimation error reduction at the expense of joint processing of signals observed by several receivers in Gaussian noise background. Generalized Stratonovich equations for a posteriori probability density function (PDF) of information parameters under estimation are deduced. They cover the most general situations when these parameters are generated under the influence of both Gaussian and non-Gaussian external force on nonlinear system. In addition, signals and noises may be both random processes and random fields. Gaussian approximation equations for Bayesian estimates and a posteriori correlation matrix are obtained and discussed. The joint demodulation problem of phase-modulated radio signals with various carrier frequencies is considered. These signals are observed by several receivers in presence of additive white Gaussian noise. Structure scheme of joint processing which includes interconnecting phase lock loops (PLL) is synthesized and filtering error reduction due to receivers integration is calculated in terms of general signal/noise ratio enhancement.

1. Introduction

The output data veracity is overriding characteristic of every information-measuring system. Perspective technique of its enhancement consists in integration of separate measuring facilities into information-measuring complex with unified signal and data processing system, which optimally integrates all useful information. Integrated facilities can apply various operating frequencies, frequency ranges and even different physical principles of operation. For example, location complex can include some ground- and space-based radars operating in various frequency ranges, as well as sonars and lidars if necessary. Telecommunication complex can consist of several radio channels having various carrier frequencies and modulation types. It can include also cable and fiber optics links.

Increase in measuring instruments, especially with different operation principles, leads to enhancement of complex operating performance. In particular, simple duplication of facilities, measuring the same parameters, enhances measurement reliability. Integration of radio and non-radio facilities enhances its radio interference immunity. Measuring of the same parameters by various instruments leads to information redundancy which yields measurement error reduction via appropriate data processing.

The purpose of this paper consists in application of the Markovian approach [1,2] to the problem of information-measuring facilities optimal integration. As an illustration, the joint demodulation problem of phase modulated radio signals having various carrier frequencies in presence of additive Gaussian noises is considered.

2. The Problem Statement in Markovian Approach

Let M receivers be intended for measurement of some parameters depending, in general, on time t. Let signal and noise mixture observed by m-th receiver be in the form

$$y_m(t) = S_m(t,\xi) + n_m(t), \qquad m=1,\ldots,M, \tag{1}$$

where signals $S_m(t,\xi)$ have deterministic form and depend on the range of information parameters $\xi(t)=(\xi_1(t),\xi_2(t),...,\xi_L(t))$, which we need to estimate taking into account a priori data; $n_m(t)$ – Gaussian noises having correlation matrix $\overline{n_m(t)n_n(t')}=N_{mn}(t)\delta(t-t')$ and zero mean values. Every signal S_m can include the whole range of parameters under estimation or some part of them. Moreover, some signals may be independent on ξ_i at all. Nevertheless, such receivers may occur useful because they introduce additional information about noises in integrated complex. To distinguish between L-dimensional parameter ranges (like $\boldsymbol{\xi}$) and M-dimensional vectors (like $\vec{y},\vec{S},\vec{n}$) we denote ranges by bold letters and apply indexes *i, j, l, p, r* for their components. For vectors we use upper arrows and indexes *k, m, n*.

Let us dwell on a priory description of the parameter range $\boldsymbol{\xi}$ in Markovian approach to problem under consideration. We assume that parameters ξ_i form L-dimensional Markovian process which is the result of external random forces $\chi_i(t)$ influence upon dynamic system describing by stochastic differential equations

$$d\xi_i/dt + f_i(t,\xi)=\chi_i(t), \qquad \xi_i(t_0)=\xi_{0i}, \tag{2}$$

where random forces can be both Gaussian and non-Gaussian, but they must be delta-correlated in time so that L-dimensional random process $\boldsymbol{\xi}$ became Markovian one; f_i may depend on all parameters $\boldsymbol{\xi}$ or on any their part.

Evolution of transition probability density function $V(t,\boldsymbol{\xi})=P(t,\boldsymbol{\xi}/t_0,\boldsymbol{\xi}_0)$ both for Gaussian and non-Gaussian external forces follows partial derivatives equation [3]

$$\frac{\partial V(t,\xi)}{\partial t}=\sum_{i=1}^{L}\frac{\partial(f_i V)}{\partial\xi_i}+\sum_{q=1}^{\infty}\frac{(-1)^q}{q!}\sum_{l_1,\ldots,l_q=1}^{L}\kappa_q^{l_1\ldots l_q}(t)\frac{\partial^q V}{\partial\xi_{l_1}\partial\xi_{l_2}\cdots\partial\xi_{l_q}}, \qquad V(t_0,\xi)=\delta(\xi-\xi_0), \tag{3}$$

where $\kappa_q^{l_1\ldots l_q}(t)$ is multiplier before delta-functions in q-order cumulant of random forces $\chi_{l_1},\chi_{l_2},\ldots,\chi_{l_q}$.

When these forces are Gaussian with zero mean values, (3) leads to Einstein-Fokker-Plank equation. Only second order cumulants $\overline{\chi_i(t)\chi_j(t')}=\kappa_2^{ij}(t)\delta(t-t')=\kappa_{ij}\delta(t-t')$ are nonzero in this case. Another important example of (3) gives Kolmogorov-Feller equation, which corresponds to the case, when external forces are described by Poisson delta-impulses [3]. Optimal integration problem under consideration consists in synthesis and analysis of algorithms realizing optimal joint estimation of useful parameters taking into account observation data (1) and parameters' a priori description (2) or (3).

At first sight a priori Markovian model described looks rather artificial. But really it covers a lot of practical situations. So, its simplest particular case $d\xi_i/dt=0$ corresponds to constant information parameters under estimation. Another case, when functions f_i are linear and random forces χ_i are Gaussian, leads to well known Gauss-Markov models of real random processes widely applied in radio engineering. If, in addition, functions S_m in (1) are linear, we obtain the typical linear Kalman-Bucy filtering problem. Anyway, Markovian approach enables revealing key elements of joint processing system and appreciating main potential characteristics. As for effectiveness in reality, it can be examined by computer simulation and full-scale investigation.

3. General Equations of Joint Processing

Joint estimation algorithms and their potential possibilities are described by equations for a posteriori characteristics. They can be calculated via a posteriori probability density function (PDF) $W(t,\xi)=P\left(t,\xi/\overrightarrow{y_0^t}\right)$, which is the probability that parameters have values $\boldsymbol{\xi}$ at time point t under the condition that during time interval $(0,t)$ realizations (1) of signal and noise mixtures were observed at all receivers. Vector of such realizations is designated as $\overrightarrow{y_0^t}$. Equation describing evolution of $W(t,\boldsymbol{\xi})$ was firstly obtained by Stratonovich and it bears his name. Derivation of this equation in respect to problem under consideration can be performed in accordance with the procedure described in [2]. This leads to the generalized Stratonovich equation

$$\frac{\partial W(t,\xi)}{\partial t}=\mathbf{L}W(t,\xi)+W(t,\xi)\left[F(t,\xi)-\left\langle F(t,\xi)\right\rangle\right], \tag{4}$$

$$F(t,\xi)=\sum_{k,m=1}^{M} Q_{km}(t)S_k(t,\xi)\left[y_m(t)-1/2\cdot S_m(t,\xi)\right], \tag{5}$$

where **L** is a priori linear operator analogous to that of the right hand side of (3). Matrix Q_{km} is inverse correlation matrix of observation noises, it obeys set of equations $\sum_{k=1}^{M} N_{mk}Q_{kn}=\delta_{mn}$. Averaging over a posteriori PDF is indicated by corner brackets. If observation noises n_m are stationary and mutually independent, then $Q_{km}=1/N_m\cdot\delta_{km}$ and double sum in (5) reduces to single one. When, in addition, *k*-th receiver realizes spatio-temporal reception, its input mixture (1) has to be considered as the random field $y_k(t,\mathbf{r})=S_k(t,\mathbf{r},\xi)+n_k(t,\mathbf{r})$. Stratonovich equation (4) keeps its form even so, but the *k*-th term in the single sum (5) includes now integration over the aperture D_k of *k*-th receiver and thus takes the form $1/N_k\cdot\int_{D_k} S_k(t,\mathbf{r},\xi)\left[y(t,\mathbf{r})-1/2\cdot S_k(t,\mathbf{r},\xi)\right]d\mathbf{r}$.

In general, (4) is a non-linear integro-differential equation with partial derivatives. Its immediate solution or simulation is very difficult if possible. Nevertheless, it provides the basis for synthesis and analysis of realizable quasi-optimal processing algorithms in some approximations. The most fruitful among them is the Gaussian approximation, which is valid when a posteriori PDF can be approximated by the Gaussian law. Mostly this is the case when signal/noise ratio in the system is rather high and, respectively, estimation error is rather low. It is important to note that estimation error is referred to the whole integrated complex but not to its separate facilities.

Derivation of the Gaussian approximation equations doesn't differ, in essence, from that described in [2]. For the case of a priori description by (3) they have following form

$$\frac{d\hat{\xi}_l(t)}{dt}=-f_l\left(t,\hat{\xi}\right)+\frac{\partial F\left(t,\hat{\xi}\right)}{\partial\xi_i}K_{il}-\frac{1}{2}\frac{\partial^2 f_l\left(t,\hat{\xi}\right)}{\partial\xi_i\partial\xi_j}K_{ij}+\kappa_1^l(t), \tag{6}$$

$$\frac{dK_{ij}(t)}{dt}=-\frac{\partial f_i\left(t,\hat{\xi}\right)}{\partial\xi_l}K_{lj}-\frac{\partial f_j\left(t,\hat{\xi}\right)}{\partial\xi_l}K_{li}+\frac{\partial^2 F\left(t,\hat{\xi}\right)}{\partial\xi_l\partial\xi_p}K_{li}K_{pj}+\kappa_2^{ij}(t)-\frac{1}{2}\left[\frac{\partial^3 f_i\left(t,\hat{\xi}\right)}{\partial\xi_l\partial\xi_p\partial\xi_r}K_{lj}K_{pr}+\frac{\partial^3 f_j\left(t,\hat{\xi}\right)}{\partial\xi_l\partial\xi_p\partial\xi_r}K_{li}K_{pr}\right]. \tag{7}$$

Here $\hat{\xi}_l(t)\equiv\langle\xi_l(t)\rangle$, $\hat{\xi}=\left(\hat{\xi}_1,\ldots,\hat{\xi}_L\right)$ are the required mean a posteriori (Bayesian) estimates of information parameters, $K_{ij}=\left\langle\left(\xi_i-\hat{\xi}_i\right)\left(\xi_j-\hat{\xi}_j\right)\right\rangle$ is their a posteriori correlation matrix, which yields estimation error variances when *i*=*j*. For brevity we mean summation from 1 to *L* of terms having twice repeated indexes (Einsteins rule). A priori known quantities $\hat{\xi}_l(0)=\xi_{0l}$ and $K_{ij}(0)=K_{ij}^0$ are used as initial values.

In contrast to (4) equations (6)-(7) don't include partial derivatives with respect to unknown functions. All partial derivatives belong to coefficients only. Therefore these equations allow investigation and modeling by analog and digital technique.

4. Joint Demodulation of Several Phase Modulated Signals in Noise Background

As an illustrative example let us consider the problem of useful message ξ(*t*) optimal estimation in the complex of *M* receivers operating at various frequencies and observing mixtures of phase modulated signals and mutually independent white Gaussian noises. Let input mixture (1) be in the form

$$y_m(t)=A_m\cos\left[\omega_m t+b_m\xi(t)\right]+n_m(t),\qquad m=1,\ldots,M, \tag{8}$$

where A_m, ω_m, b_m are the known amplitude, carrier frequency and modulation factor of useful signal at *m*-th receiver, $\overline{n_m(t)n_k(t')}=N_m\delta_{km}\delta(t-t')$.

As a model of useful message we choose Gauss-Markov process describing by stochastic differential equation $d\xi/dt+\gamma\xi=\chi(t)$, where Gaussian external force has correlation function $\overline{\chi(t)\chi(t')}=\kappa\delta(t-t')$. Frequency spectrum of such message has the form of γ-wide resonance curve. Equations (6) and (7) after some ordinary simplifications take the form

$$\frac{d\hat{\xi}(t)}{dt} = -\gamma\hat{\xi}(t) - K(t)\sum_{m=1}^{M}\frac{A_m b_m}{N_m} y_m(t)\sin\left[\omega_m t + b_m\hat{\xi}(t)\right], \qquad \frac{dK(t)}{dt} = -2\gamma K(t) - \mu K^2(t) + \kappa, \tag{9}$$

where $\mu = \sum_{m=1}^{M} A_m^2 b_m^2 / 2N_m = \sum_{m=1}^{M}\mu_m$ is the effective signal/noise ratio which equals the sum of signal/noise ratios μ_m at all receivers. Advantage of joint processing in comparison with independent one consists in enhancement of the effective signal/noise ratio. It amounts *M*-times when all μ_m are the same. Ratio of message's ξ a posteriori variance $\sigma_{ps}^2 \equiv K$ to a priori one $\sigma_\xi^2 = \kappa/2\gamma$ for steady-state filtering (dK/dt=0) is equal to

$$\sigma_{ps}^2 / \sigma_\xi^2 = 2\Big/\left(1+\sqrt{1+2\alpha}\right), \tag{10}$$

where parameter $\alpha = \mu\sigma_\xi^2/\gamma$ is proportional to the effective signal/noise ratio during correlation time γ^{-1}.

Quasi-optimal joint processing algorithm (9) can be represented by the structure scheme shown in figure.

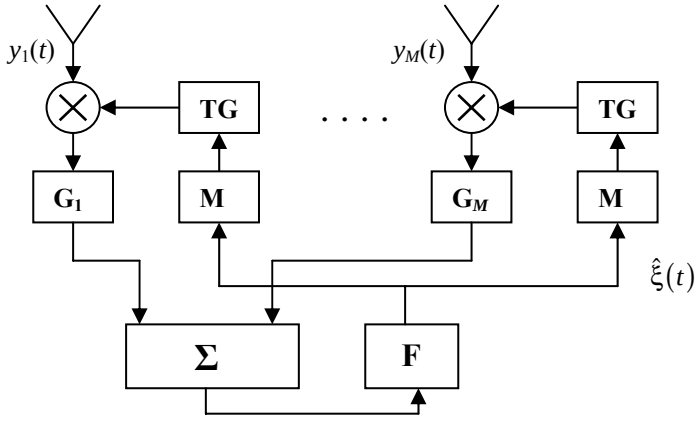

⊗ - multiplier,
G_m – amplifier,
Σ – summator,
F – low-pass filter,
M – phase modulator,
TG – tunable generator

Each *m*-th receiver includes phase-lock loop (PLL) tuned to carrier frequency ω_m. Input signals $y_m(t)$ are multiplied by output signals of tunable generators TG $u_m(t) = \sin\left[\omega_m t + b_m\hat{\xi}(t)\right]$. After $G_m = KA_m b_m / N_m$-fold amplification signals are summed and filtered by low-pass filter F having transfer function $1/(d/dt + \gamma)$. The filter output signal yields required estimate of useful information process $\hat{\xi}(t)$, which is used then for phase modulators M control. Thus feedback circuits in PLLs became closed. Of course, integration scheme synthesized can be realized in digital form.

5. Conclusions

It is demonstrated once more that the Markovian approach represents a powerful tool for variety of signal processing problems. Possibility of its application to information-measuring facilities integration problem considered seems to be promising for future investigations.

References

[1] R.L. Stratonovich, "Detection and estimation of signals in noise when one or both are non-Gaussian," *Proc.IEEE*, vol.58, No.5, pp. 670-679, 1970.

[2] A.B. Shmelev, *Principles of the Markovian theory of random fields non-linear processing*, Moscow, Moscow Institute of Physics and Technology Press, 1998 (in Russian).

[3] V.I. Klyatskin, *Stochastic equations through the eye of the physicist (basic concepts, exact results and asymptotic approximations)*, Amsterdam, Elsevier, 2005.

Cellular Neural/Nonlinear/Nanoscale Network (CNN) Computing

Angela Slavova
Institute of Mathematics and Informatics, Bulgarian Academy of Sciences, Sofia, Bulgaria
slavova@math.bas.bg

Keywords: Cellular Neural Networks, Cellular Nano Networks, Image Processing, Image Recognition, Image Coding

Abstract: In this paper we present various cellular architectures. Equations describing cellular nonlinear networks are introduced and some approximation properties are provided. Applications of these architectures in nanotechnology is given well.

1. Cellular Neural Network model

We are witnessing a technical development in our fields where the sensing, computing, activating circuits and systems are becoming inherently connected; physically and theoretically, as well. Moreover, as a result of this, our notion about sensory computing, even about computing, is in a continuous transformation. Hence, we have to make a closer look about the fundamentals of computing.
How, now, can we characterize a brain-like system?
We might summarize the key properties as follows:
- Continuous time continuous (analog) valued signal arrays (flows)
- Several 2Dimensional strata of analog "processors" (neurons)
- Typically, mainly local, or sparse global (bus-like) interconnections
- Sensing and processing are integrated
- Vertical interconnections between a few strata of neuron "processors"
- Variable delays
- Spatial-temporal active waves
- Events are patterns in space and/or time

These features are already strongly modifying our view and practice in building complex electronic systems, including sensing, computing, activating and communicating devices and systems. This way of thinking, however, is supposing a completely different architecture, physical and algorithmic alike, and supposes tens of thousands or millions of parallel physical processing devices.
In developing a universal and canonical computing architecture, after having been decided the forms of data, we are tending to use the simplest possible building blocks, with the simplest possible interconnections, elementary instructions and programming constructs. Then we introduce algorithmic stored programmability to make it universal and practical. A most successful example is the digital computer, with a core universal machine on integers (Turing machine). What if we would make a brain-like computer with the properties shown above? The data are topographic (image) flows. In the simplest case, a pixel array with each pixel having a light intensity of gray values between black (say, +1) and white (say, -1) values. Color pictures are composed of several pictures with different color content. A special case is a binary mask. Now, let us construct a programmable topographic cellular sensory dynamics, as implementing the protagonist elementary instruction. The recipe is as follows.
- Take the simplest dynamical system, a cell (with input u, state x and output y)
- Take the simplest spatial grid for placing the cells with the simplest neighborhood relation (2D sheets)
- Introduce the simplest spatial interactions between dynamic cells, being programmable (called cloning template or gene, or simply template)
- Add cellular sensors.

CNN is simply an analogue dynamic processor array, made of cells, which contain linear capacitors, linear resistors, linear and nonlinear controlled sources. Let us consider a two-dimensional grid with 3 X 3 neighborhood system as it is shown on Fig.1.

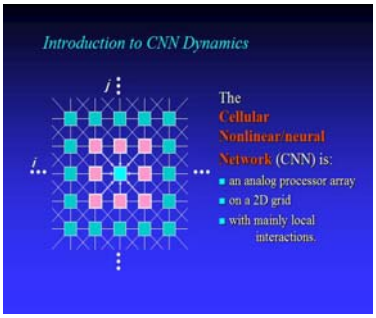

Fig. 1. Basic CNN architecture

The squares are the circuit units - cells, and the links between the cells indicate that there are interactions between linked cells.

Cellular Neural Networks (CNNs) are complex nonlinear dynamical systems, and therefore one can expect interesting phenomena like bifurcations and chaos to occur in such nets. It was shown that as the cell self-feedback coefficients are changed to a critical value, a CNN with opposite-sign template may change from stable to unstable [3]. Namely speaking, this phenomenon arises as the loss of stability and the birth of a limit cycles [3]. Moreover, the appearance of a strange attractor in a periodically driven two-cell CNN have been reported. In a three-cell autonomous CNN this attractor has properties similar to the double scroll attractor [5].

CNN is simply an analogue dynamic processor array, made of cells, which contain linear capacitors, linear resistors, linear and nonlinear controlled sources. It is known that some autonomous CNNs represent an excellent approximation to nonlinear partial differential equations (PDEs). In this paper we will present the receptor-based model by a reaction-diffusion CNNs. The intrinsic space distributed topology makes the CNN able to produce real-time solutions of nonlinear PDEs.

We will give the general definition of a CNN which follows the original one [3]:

Definition 1. The CNN is a

a). 2-, 3-, or n - dimensional array of

b). mainly identical dynamical systems, called cells, which satisfies two properties:

c). most interactions are local within a finite radius r , and

d). all state variables are continuous valued signals.

Definition 2. An M X M cellular neural network is defined mathematically by four specifications:

1). CNN cell dynamics;

2). CNN synaptic law which represents the interactions (spatial coupling) within the neighbor cells;

3). Boundary conditions;

4). Initial conditions.

Now in terms of definition 2 we can present the dynamical systems describing CNNs. For a general CNN whose cells are made of time-invariant circuit elements, each cell C(ij) is characterized by its CNN cell dynamics :

$$\dot{x}_{ij} = -g(x_{ij}, u_{ij}, I_{ij}^{s}), \tag{1}$$

where $x_{ij} \in R^{m}$, u_{ij} is usually a scalar. In most cases, the interactions (spatial coupling) with the neighbor cell C(i+k,j+l) are specified by a CNN synaptic law:

$$I_{ij}^{s} = A_{ij,kl} x_{i+k,j+l} + \tilde{A}_{ij,kl} * f_{kl}(x_{ij}, x_{i+k,j+l}) + \tilde{B}_{ij,kl} * u_{i+k,j+l} \tag{2}$$

The first term of (2) is simply a linear feedback of the states of the neighborhood nodes. The second term provides an arbitrary nonlinear coupling, and the third term accounts for the contributions from the external inputs of each neighbor cell that is located in the neighborhood.

Complete stability, i.e. convergence of each trajectory towards some stationary state, is a fundamental dynamical property in order to design CNN's for accomplishing important tasks including image processing problems, the implementation of content addressable memories and the solution of combinatorial optimization problems [5]. The most basic result on complete stability is certainly the one requiring that the CNN interconnection matrix be symmetric [3]. Also some special classes of nonsymmetric CNN's such as cooperative (excitory) CNN's, were shown to be completely stable [6]. In the general case, however, competitive (inhibitory) CNN's may exhibit stable nonlinear oscillations [5].
It is known [3,5,6] that some autonomous CNNs represent an excellent approximation to nonlinear partial differential equations (PDEs). In this paper we will present the receptor-based model by a reaction-diffusion CNNs. The intrinsic space distributed topology makes the CNN able to produce real-time solutions of nonlinear PDEs. Consider the following well-known PDE, generally referred to us in the literature as a reaction-diffusion equation [6]:

$\frac{\partial u}{\partial t} = f(u) + D\nabla^2 u$, where $u \in R^n$, $f \in R^n$, D is a matrix with the diffusion coefficients, and $\nabla^2 u$ is the Laplacian operator in R^2. There are several ways to approximate the Laplacian operator in discrete space by a CNN synaptic law with an appropriate A -template [5,6].

2. Various cellular architectures

Cellular automata, introduced also by J. von Neumann, are fully parallel array processors with all discrete space, time and state values. Their beautiful properties are recently rediscovered, showing the deeper qualitative properties. Clearly, if we allow the states and time being continuous values like in CNN, a broader class of dynamics will be generated. Even more, the fundamental condition to generate complex features at the edge of chaos had been established: the need of local activity [3]. If we take one step further, and use the CNN-UM architecture, a new world of algorithms is opening. Interestingly, these cellular wave computers are, in a way, around us in many forms, we will explore a few subsequently. Seemingly, if we increase the complexity of any system, after a while, cellular architectures are becoming prevalent.

3. Towards topographic, including visual, microprocessors

CMOS technology became the mainstream silicon technology for making digital microprocessors. Indeed, there are various ways to implement CNN Universal Machine chips. These are the o Mixed mode, analog and logic technology o Emulated digital technology with different granularity o FPGA based implementations One major opportunity is to integrate the topographic sensors. In particular, visual and tactile sensors are the most natural choices, however, auditory sensor array might equally be important.

Fig. 2. Development of CNN technology

The emerging tactile sensor arrays are made via MEMS technology [1,2,4], their bio-inspired processing allows the direct use of CNN algorithms for various sensing tasks when each tactile element (called taxel) senses all 3

component of the pressure vector. Clearly, the most advanced area is related to vision and the programmable visual microprocessors are integrating the camera and the computing parts of vision; indeed, they are inseparable in more complex tasks. Unlike in "smart sensors", here, we are talking about stored programmable algorithms and related software to program our visual microprocessors. The developments on the field are illustrated on Figure 2.

4. CNN principles in optics and nanotechnology

The principle that physics is doing the computation leads us to uncover other physical and/or biological effects to implement our topographic sensory computer architecture. A quite natural choice is to turn to optics, keeping in mind that a spatial correlation can be made "instantly", with the speed of light. Taking a so called 4f focal plane system using two lenses and a programmable light valve, containing a plain with programmable light transmissivity in each pixel, a spatial correlation can be achieved. From this simple effect, a stored Programmable Opto-electronic Analogic CNN Computer (POAC) has been successfully constructed recently [4]. The simplified scheme is shown in Figure 3, using two different lasers (red and green) and a bacterio-rhodopsine film as the programmable light valve or Local Analog Memory array. The size of the templates might be as big as 31x31, presently using an acusto-optical deflector (later replaced by a semiconductor laser array). Needless to say, this cellular architecture will be a must in many nano-systems, already emerging. What kind of nano and molecular devices will be useful and practical in these new sensory computers? What would be the easy-to-implement multi-input functional units, the non-transistor-based elementary devices? Or, what are the "nano-friendly" devices and interconnections that are optimally suited to our cellular wave computing paradigm? What are the convenient computing architectures? What if the input flow, is really a continuous flow in time that contains no snapshots (like in the retina)? Instead of forcing the design of devices that we have been accustomed to, e.g. gates or amplifiers, we have to accept some functions that a given nanodevice could offer, defined by its layout. If it is locally active we can make an array of them, and locally interact the devices including also some very sparse global or semi-global lines, may be achieved via radiation or optical interconnection. The Laptop-size implementation is shown in Figure 3.

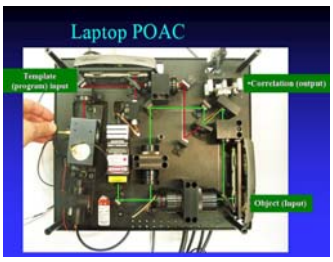

Fig. 3. Laptop size implementation

Acknowledgments.

This paper is supported by the project DID 02/15.

References:

[1] T.Roska and Á.Rodriguez-Vázquez, “Towards Visual Microprocessors”, Proc. IEEE, July 2002
[2] T.Roska, “Computational and Computer Complexity of Analogic Cellular Wave Computers”, Journal of Circuits, Systems and Computers, vol. 12, pp. 539-562, 2003
[3] L. O. Chua, CNN: A Paradigm for Complexity, World Scientific, Singapore, 1998
[4] D. Bálya, I. Petrás, T. Roska, R. Carmona, and Á.Rodríguez-Vázquez, “Implementing the multilayer retinal model on the complex-cell CNN-UM chip prototype”, International Journal of Bifurcation and Chaos vol 14, pp. 427-451, 2004
[5] L.O.Chua and T.Roska, Cellular Neural Networks and Visual Computing, Cambridge University Press, Camridge, UK, 2002
[6] A.Slavova, Cellular Neural Networks:Dynamics and Modelling, Kluwer Academic Publisher, 2003.

Radio Resource Control Technologies among Autonomously Operating Radio Systems for ISM Band

Makoto Taromaru[*]*, Kazuto Yano, Yasuo Suzuki, Satoshi Tsukamoto, and Masazumi Ueba*

ATR Wave Engineering Laboratories, 2-2-2 Hikaridai, Seika-cho, Kyoto, 619-0288 Japan
http://www.atr.jp

Keywords: Spectral efficiency, dynamic spectrum access, dynamic spectrum control, control channel, ISM band.

Abstract: As 900MHz, 2.4GHz, and other ISM bands are getting used more and more densely to realize ubiquitous network society by SRDs: short range radio devices of wireless LAN, Bluetooth devices and so on, it is expected that ISM bands will become crowded and that available spectrum resources will be scarce. To cope with such radio resource problems, Ministry of Internal Affairs and Communications of Japan annually plans R&D projects. This paper introduces the activities of one of the projects, named Research and development on radio resource control technologies among multiple radio systems on same frequency band," applicable to SRD systems and shows its scope, goal, approach, and recent study results.

1. Introduction

Frequency spectrum resources below 6GHz are getting used more and more densely toward "ubiquitous network society." For personal or indoor systems, unlicensed bands are desirable, and these systems are operated mainly in ISM bands, 2.4 GHz for example. Since the demand for these systems is increasing, it is expected that available spectrum or radio channels in ISM bands become short, and that the throughput will be decreased. In an ISM band generally, various SRDs (short range radio devices and systems) and RF (radio frequency) equipment are independently and asynchronously operating, such as wireless LANs (local area network), cordless telephones, microwave ovens, and etc., with their own PHY (physical) and MAC (medium access control) layer protocols. Because those ISM systems and equipment select radio frequency channels to use after carrier sense without any intersystem coordination, the band spectrum is occupied randomly; the vacant spectrum space is becoming fragmented and scattered. Consequently, a new radio device cannot commence communications in case that any of the space is too narrow. Fig. 1 illustrates an example that a new system cannot transmit a signal of bandwidth W even if the total bandwidth of the vacant spectra, drawn as the horizontally hatched rectangles, is more than W. For such radio environments, OFDMA with frequency scheduling [1] and single-carrier based dynamic spectrum control (SC-DSC) [2], [3] seem applicable since they can divide a modulation spectrum into several groups of subcarriers, or spectrum pieces, which are called "subspectra" hereafter, so they can split the subspectra to place into the vacant spaces. These techniques, however, are hardly applied to systems in ISM bands because of interference to/from the other systems using the adjacent spectra. This is because each subspectrum forms $\sin\omega/\omega$ due to IFFT processing accompanied with

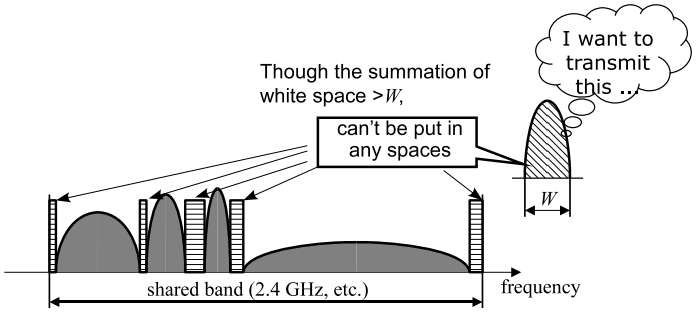

Fig. 1. Spectrum use and fragmented spaces in ISM band.

[*] Currently with Department of Electronics Engineering and Computer Science, Faculty of Engineering, Fukuoka University, Fukuoka, 814-0180 Japan.

a cyclic prefix (CP), where ω is the angular frequency relative to its center normalized by the sampling rate.

In this paper, a novel radio system for SRDs is proposed. It adopts a single carrier transmission system with low ACPR (or ACLP, adjacent channel leakage power ratio) [4]–[8]. It divides the spectrum of single carrier modulation into a few subspectra with band-limiting filters, with cosine roll-off characteristics for example, and frequency-converts the subspectra to allocate them into the vacant spectra of the band. In Section 2, the band-limited dynamic spectrum control scheme named "band-limited divided-spectrum single carrier transmission" is explained. Next, in Section 3, some measurement results of spectral-temporal radio resource usage among conventional systems in 2.4 GHz band are shown, and issues on MAC protocols and fairness among SRDs and the other radio systems/devices are also discussed. Finally, concluding remarks are given in section 4.

2. Proposed Single Carrier Transmission Scheme

2.1. Dynamic Spectrum-Controlled Transmission System

The proposed transmission system uses a filter bank of bandlimiting filters: $H_1(\omega)$, $H_2(\omega)$, . . . , $H_N(\omega)$, to divide a normal single carrier modulated spectrum of $H(\omega)$ into N pieces of subspectra, and each subspectrum is frequency-converted by ω_n, (n=1, 2, . . ., N) so that it can be allocated in the vacant spectra. $H(\omega)$ can typically be selected as root Nyquist characteristics. The block diagram of the proposed transmission system is shown in Fig. 2 in case N=4. The receiver has the matched filter bank for the divided spectra, and the outputs are frequency-converted by $-\omega_n$ respectively; then they are combined into the original single carrier signal of $H(\omega)$ if the radio channel is flat. From this point of view, the transfer functions should be designed so as not to generate intersymbol interferences, but this is not strictly required since radio channel is generally frequency selective. Therefore, the receiver must have an equalizer function, which can be implemented as a frequency domain equalizer by weighting the output signals of the matched filter bank. Since each subspectrum is bandlimited by the filter $H_n(\omega)$, ACPR can be well reduced [8].

2.2. Implementation of Spectrum-Shaping and Channel Filters

The typical way to implement the filters of $H_n(\omega)$ is frequency domain processing using DFT/IDFT or FFT/IFFT. Not to use the CP, each of the DFT or FFT block has to overlap each other at the both sides. Another straightforward way is time domain processing with FIR filters. When the system bandwidth is 80MHz, and the minimum width of the subspectra is 1MHz, their tap interval or sampling duration is 10 ns or less, and the impulse response length has to be at least 3–5 μs; then each filter should have as much as 300–500 taps. However, it should be noted that the filtering

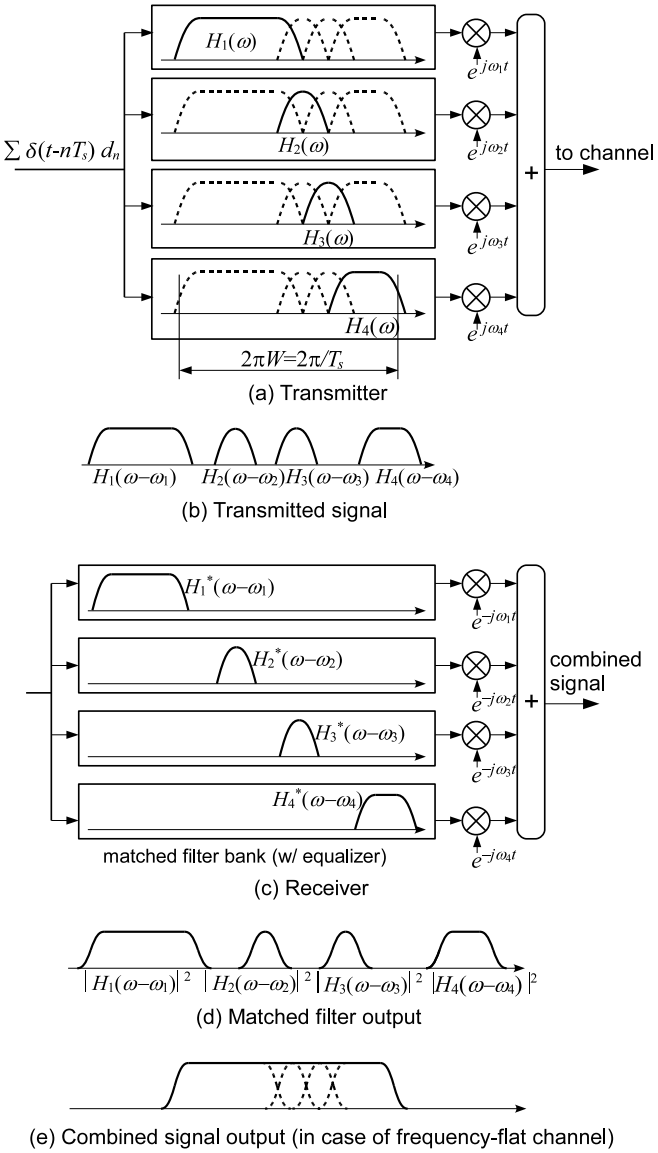

Fig. 2. Spectrum use and fragmented spaces in ISM band.

complexity can be reduced by polyphase decomposition and DFT in the same manner shown in [6], [7].

2.3. PAPR Reduction [8]

This system can be designed so that the PAPR of the modulated signal is low. First, the number of subspectra *N* should be necessity minimum; second, the order of subspectra should not be changed; and bandwidth of the subspectra should be distributed as biased and centralized to one or two of them as possible. This is because each subspectrum has low PAPR properties of a band-limited single carrier signal, and PAPR is dominated by the widest subspectrum, which has the highest power than the others, if the bandwidth distribution is biased.

3. Radio Resource Usage and MAC Protocols

3.1. Grasp of Current Radio Resource Usage for Advanced MAC

It is important, as the first step to study MAC for the SRD systems, to grasp the use of spectrum in current ISM bands in order to design the desirable and suitable MAC protocol for the proposed radio system. We measured the spectral and temporal use of radio resources in 2.4 GHz band in real environment of our office. Fig. 3 shows the measurement environment. There are three access points (APs) of IEEE 802.11b wireless LAN (WLAN), laptop PCs as the terminals communicating with the APs respectively, a pair of laptop PC also linked by the WLAN, and another pair of Bluetooth terminals equipped on other PCs. At the beginning, we made four 802.11b WLAN links at ch. 1, 5, 9, and 13, and executed long file transfer using FTP; then, we started another FTP transfer on the pair of Bluetooth terminals. The use of radio resource in 2.4GHz band were observed by a real-time spectrum analyzer located in the room as illustrated in Fig. 3.

An example of measurement result is shown in Fig. 4. It can be seen that Bluetooth's transmission makes residual, vacant, and fragmented radio resources uselessly (the darkest region) and reduces transmission rate of WLAN. In some conditions, Bluetooth takes position of WLAN's channel. It makes more residual

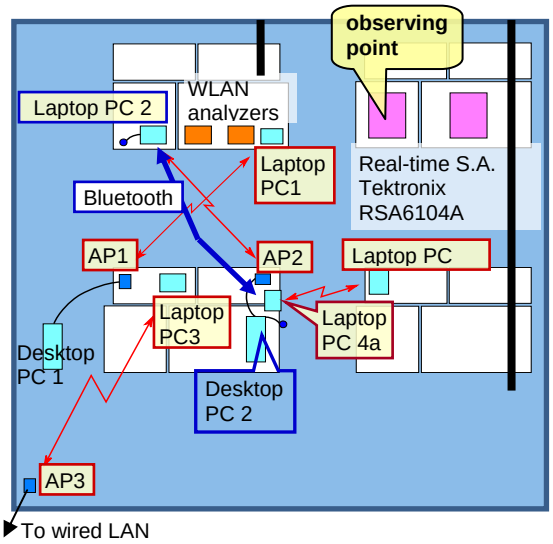

Fig. 3. Measurement field and layout of radio equipment.

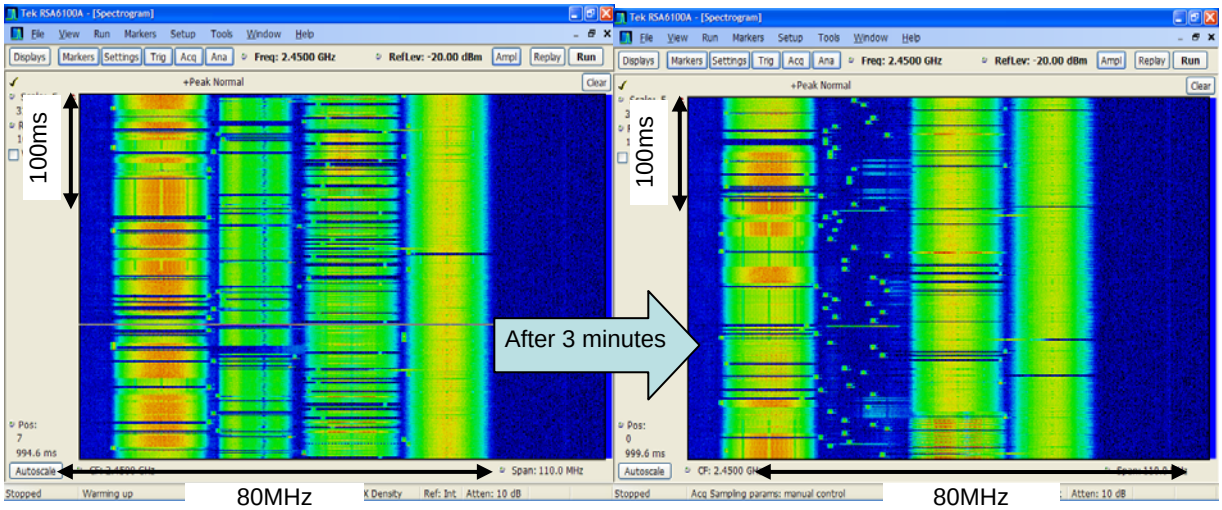

Fig. 4. Use of radio resource in 2.4GHz band and its transition after Bluetooth's commencing communication.

and useless radio resources and decreases spectral efficiency. Therefore, it is assured that the PHY technology of dynamic spectrum control is desirable and necessary for the new systems in ISM bands as is described in Sec. 1 and 2.

3.2. MAC Protocol and Fairness

Even if our developing system uses those residual vacant radio resources effectively, it is important to consider the followings: how long the system can continue to use and occupy the resources; whether it should use the resources immediately after they get cleared or not; how long it has to wait before its transmission considering the intentionally designed inter frame spaces, SIFS, DIFS, etc., of standardized conventional CSMA/CA MAC protocol. It is certain that DIFS at least should be protected, but the maximum back-off time of contention window (CW) would not have to be protected. A possible way is to define random or fixed carrier sensing/contention window longer than DIFS and shorter than CWmax for co-existence with the conventional systems. The MAC protocol is now being studied, and we would have to discuss these issues and "Air Etiquette" in ISM or unlicensed bands for SRDs and WLAN for the future.

4. Conclusion

A system concept of a radio system operating in ISM and unlicensed frequency bands where various radio systems are autonomously operating is introduced, and Dynamic Spectrum Access/Control with spectrum sensing is adopted for efficient spectral use. Measurement results show residual vacant radio resources are generated in case multiple radio systems are operating. The system utilizes the vacant spectrum to increase spectrum use efficiency in ISM and unlicensed bands, but we would have to discuss and establish *Air Etiquette* toward the ubiquitous network world.

Acknowledgment

The authors would like to thank Dr. M. Ohira and Mr. T. Miyasaka of ATR Wave Engineering Laboratories for their helpful discussion and support. This work is supported by the Ministry of Internal Affairs and Communications under a grant "Research and development on radio resource control technologies among multiple radio systems on same frequency band."

References

[1] 3GPP TS 36.211 V.8.5.0, "Physical layer aspects for evolved universal terrestrial radio access (UTRA) release 7," Dec. 2008.

[2] T. Ohnishi, S. Ibi, and S. Sampei, "A partial spectrum retransmission scheme using a dynamic spectrum control for broadband single carrier transmission systems," *Proc. IEEE Int. Symp. Personal, Indoor and Mobile Radio Commun.* (*PIMRC'07*), *Athens*, Sep. 2007.

[3] 3GPP TSG RAN on LTE-Advanced, TR36.814, V.0.3.1, "Further advancements for E-UTRA physical layer aspects," Jan. 2009.

[4] S. D. Sandberg and M. A. Tzannes, "Overlapped discrete multitone modulator for high speed copper wire communications," *IEEE J. Select. Areas Commun.*, vol. 13, no. 9, pp. 1571–1585, Dec. 1995.

[5] K. Matheus and K. Kammeyer, "Optimal design of a multicarrier systems with soft impulse shaping including equalization in time or frequency direction," *Proc. IEEE Global Telecommun. Conf.* (*GLOBECOM'97*), vol. 1, pp. 310–314, Nov. 1997.

[6] H. Suzuki, Y. Nomura, S. Suyama, and K. Fukawa, "Gaussian multicarrier transmission system with turbo detection for power line communications," *Proc. Int. Symp. Power Line Commun., Zaragona Spain*, A6-4, Mar.–Apr. 2004.

[7] T. Ohori, J. Onodera, K. Goto, T. Terao, S. Suyama, and H. Suzuki, "Feasibility investigation of gaussian multicarrier transmitter via FPGA implementation," *IEICE Technical Report*, RCS2007-220, pp. 205–210, Mar. 2007.

[8] Y. Suzuki, M. Taromaru, K. Yano, and M. Ueba, "Proposal of band-limited divided-spectrum single carrier transmission for dynamic spectrum controlled access in ISM band," *Proc. IEEE Int. Symp. Personal, Indoor and Mobile Radio Commun*. (*PIMRC'09*), Tokyo, pp. 132–136, Sep. 2009.

Measurement Experimentation of Interference From Mobile Terminals and Base Stations in Satellite-Terrestrial Integrated Mobile Communication Systems

Hiroyuki Tsuji[(1)], Amane Miura[(1)] , Yoshiyuki Fujino[(1)] , Naokazu Hamamoto[(1)], and Ryutaro Suzuki[(1)]

[(1)] Space Communications Group, National Institute of Information and Communications Technology
3-4-1, Nukui-Kitamachi, Tokyo, Japan
tsuji@nict.go.jp; amane@nict.go.jp; fujino@nict.go.jp; nao@nict.go.jp; ryutaro@nict.go.jp

Keywords: STICS, satellite mobile communication system, interference, IMT2000

Abstract: The National Institute of Information and Communications Technology (NICT) has been studying a new satellite mobile communication system, named Satellite-Terrestrial Integrated Mobile Communication Systems (STICS), in which terrestrial mobile and satellite communication systems coexist and which is seamlessly integrated in the same frequency band. The interference from the terrestrial base stations or mobile terminals to the satellite system is one of the important parameters for realization of the STICS and must be evaluated. There are no studies that evaluate the amount of radiation of cellular base stations and mobile terminals toward the satellite to our knowledge. We conducted an experiment to measure the radiation power of the existing mobile base stations and mobile terminals toward satellites using an airship as part of the interference evaluation against this background. As one of the results of the experiment, we observed that the received power at the airship in the downlink channel is larger than in the uplink channel to 25-30 dB. This paper gives the overview of the experiment and some of the results.

1. Introduction

The National Institute of Information and Communications Technology (NICT) has been studying a new satellite mobile communication system, named Satellite-Terrestrial Integrated Mobile Communication Systems (STICS) [1]. We launched the basic studies for the realization of the system, which maximizes the total communication throughput by controlling the system resources such as the frequencies, output power and antenna beams of the satellite system while avoiding the interference between the terrestrial and the satellite terminals depending on their traffic distribution and changes. Therefore, the interference from the terrestrial base stations or mobile terminals to the satellite system is one of the important parameters for the STICS and must be evaluated [2]. There are no studies that evaluate the amount of radiation of cellular base stations and mobile terminals toward the satellite to our knowledge. We conducted an experiment to measure the radiation power of the existing mobile base stations and mobile terminals toward satellites using an airship as part of the interference evaluation against this background. This paper gives the overview of the experiment and some of the results.

2. Overview of STICS

The STICS is a mobile phone system in which terrestrial mobile and satellite communication systems coexist, and is seamlessly integrated in the same frequency band. Fig.1 explains the system overview of the STICS. The STICS ground mobile phones can directly communicate both terrestrial base stations and a satellite station depending on the situation. When the allocated frequency band is shared between the satellite and terrestrial systems, the high frequency-use efficiency is expected but a kind of interference rejection technique is required.

Considering the frequency usage in the STICS, the frequency sharing technique between terrestrial and satellite communication systems is one of the essential fundamental technologies for the system. Two frequency sharing methods can be considered if the 1980-2010 MHz frequency band of the uplink allocated for Mobile Satellite Service (MSS) is used: a frequency simultaneous usage method which shares the same frequency band for terrestrial and satellite communication systems, and a frequency separation usage method which divides the frequency band for each system. As for the frequency simultaneous usage methods, there are two possible frequency-division duplexing systems: the normal system, in which the terrestrial mobile terminals and the satellite mobile terminals share the same up- and down-links as shown in Fig.2, and the reverse system, in which the uplinks and downlinks are allocated for the reverse way from the normal system as shown in Fig.3. For example, Fig.3 shows the possible interference between the mobile and satellite stations when the uplink from the satellite mobile terminals to the satellite uses the same frequency band of the downlink from the ground base stations to the ground mobile terminals. The interference from the ground base stations to the satellite station is considered to be dominant in the STICS from Fig.3.

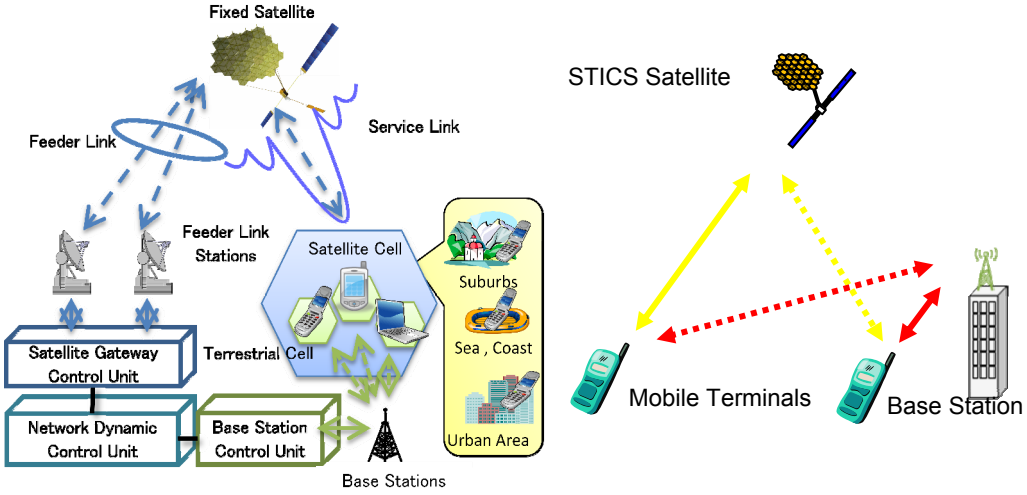

Fig.1. STICS Conception

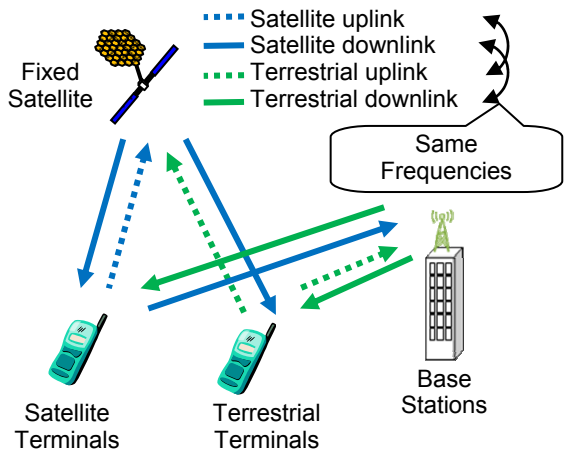

Fig.2. Interference paths in the frequency concurrent use and normal system

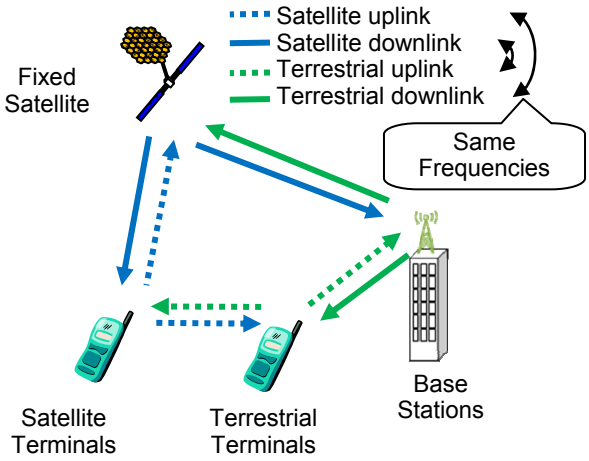

Fig.3. Interference paths in the frequency concurrent use and reverse system

3. Interference Evaluation Experiment

The interference from the terrestrial mobile terminals could be a dominant interference in the normal system because the number of terrestrial mobile terminals is large and the accumulated transmitted power may cause interference to satellite system. As for the reverse system, the downlink of base stations could be a dominant interference to the satellite. Although there are some studies about the characteristics of transmitted power of mobile terminals and its statistical data are released, there are no studies that evaluate the amount of radiation of cellular base stations and mobile terminals toward the satellite to our knowledge. We, therefore, conducted an experiment to measure the radiation power of the existing mobile base stations and mobile terminals toward satellites using an airship as part of the interference evaluation.

4. Platform and Measurement System

In the experiment, we used a manned airship 'Zeppelin NT', as shown in Fig.4: left, as a platform for the measurement equipment. The airship is classified as a semi-rigid airship and is constructed 75 m long with a volume of 8,225 m³. The Zeppelin NT airship was chosen as a platform of the experiment for the following reasons: precise on-the-spot hovering, flight at very low airspeeds, flight at low altitudes, made possible due to the very low noise levels, very low vibration levels in the cabin, and max payload 1.95 ton.

The experimental system was loaded in the airship's cabin (Fig.4: middle) and a receiving horn antenna was also mounted in the cabin sticking out of the floor hatch of the cabin as shown in Fig.4: right. The receiver can receive the radio signals in the 1.9-2.1 GHz bands by selecting the receiver's channel and measure the received power. The antenna system also equipped a GPS system and a gyro-sensor to obtain the position and attitude of the array antenna.

Fig.4. Zeppelin NT airship (left), measurement equipment (middle) and horn receiving antenna (right)

5. Platform and Measurement System

The experiment was conducted in 2009 within a 100 km area north and south of the Tokyo area which includes rural and urban areas around Tokyo in Japan. There are more than ten IMT2000 base stations in the urban area of 1 km^2 and one or two base stations in the rural area of 1 km^2. As shown in Fig.5, we measured the incoming power from three uplink channels and three downlink channels of the IMT2000 by moving north and south over 100 km while the airship's altitude was kept at about 600 m.

Figs.6 and 7 show the change of the received powers in an uplink and a downlink channels, respectively when the measurement was continuously done from the rural to urban area. The vertical axes in Figs.6 and 7 do not indicate the absolute received powers but they can be converted to the absolute received power by using the calibration results in an anechoic chamber. The current results show that the received power in the downlink channel (base station's transmitting power) is larger than in the uplink channel (mobile phone's transmitting power) to 25-30 dB and that the received power in the urban area is larger than in the rural area to about 15 dB. We also observed that several peaks during the urban area and the decrease of the received power as moving to the rural area. We thought that the peaks of the received power were due to passing through base stations.

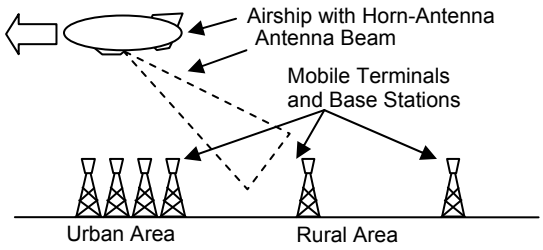

Fig.5. Measurement conception

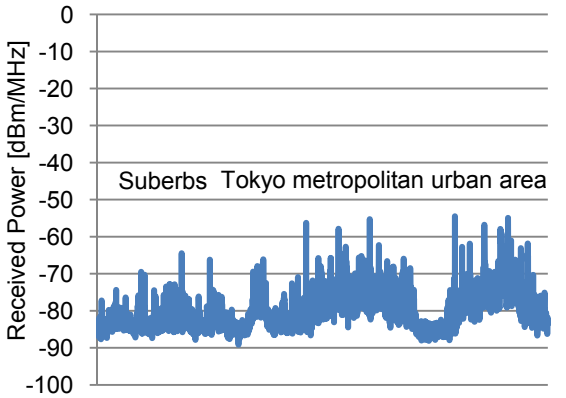

Fig.6. Received power changes for a uplink channel of IMT2000 terminal

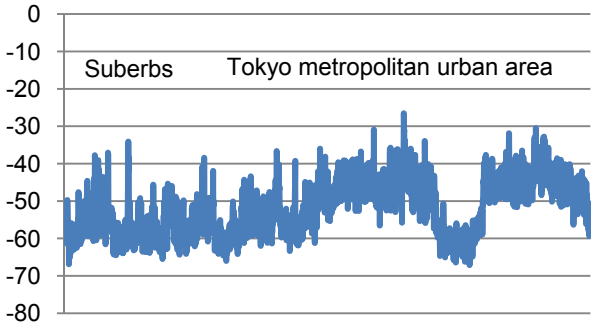

Fig.7. Received power changes for a downlink channel of IMT2000 base station

6. Conclusions

We reported on the overview of the experiment and some results of evaluating the interference from IMT2000 uplink and downlink channels using a horn antenna equipped with an airship. As one of the results of the experiment, we observed that the receiving powers varied depending on the areas and that the received power in the downlink channel is larger than in the uplink channel to 25-30 dB. The result shows that the introducing 'the normal frequency-division duplexing system in STICS may reduce the interference to the satellite. We will carry out further analysis for the obtained data.

Acknowledgment

This study is carried out under a government-commissioned research project of the Ministry of Internal Affairs and Communications.

References

[1.] Y. Fujino, T. Minowa, N. Hamamoto, H. Tsuji, and R. Suzuki, "R&D plan for Satellite/Terrestrial Integrated mobile Communication System", 2009 IEICE General Conference, No. B-3-23, March 2009.

[2.] H.Tsuji, Y. Fujino, N. Hamamoto, and R. Suzuki, "Interference Measurement Experiment of Mobile Base Station Downlinks Using an Aircraft in Satellite-Terrestrial Integrated Mobile Communication systems," The 2009 International Symposium on Antennas and Propagation (ISAP 2009), October 20-23, 2009, Bangkok, THAILAND

Algorithm for determination the moments of closing the glottis within phonation

Vassil Galabov [(1)]***, Damyan Damyanov*** [(2)]

[(1)] Technical University Sofia, Bld. 9, floor 4, room 9409, 1756 Darvenitsa, Kliment Ohridski Blv. 8, Sofia, BG
vtg@tu-sofia.bg

[(2)] Technical University Sofia, Bld. 9, floor 4, room 9409, 1756 Darvenitsa, Kliment Ohridski Blv. 8, Sofia, BG,
ellov@abv.bg, ellov_ie@yahoo.co.uk

Keywords: Speech signal processing, Glottis wave, Periodical continuations, Recursive algorithm.

Abstract: An algorithm for detection the moments of closing the glottis within phonation for speech signals is introduced. One problem in this field is that the voiced segments of the speech signal may consist of only a couple periods. Another problem is that the fluctuations of the frequency of the phonation and of the magnitude of the speech signal may be significant, without following a certain law of change. The proposed algorithm is tuneable and is easy for implementing in different systems for signal processing. It can be also used for seeking of periodic sequels in quasiperiodical signals in other domains of use, such as radiolocation, hydro location, seismology, electrocardiography, electroencephalography, economical analysis and others.

1. Introduction

The phonation is the process of auralisation of the exhaled air current in the glottis, which constitutes the middle part of the larynx. As a consequence of this process the current of the sound speed immediately after the voice stings it shows a periodical character, which determines the pitch of the speech signal. That way the phonation of the vowels and voiced consonants is accomplished. In the process of the unvoiced consonants the voice strings do not approach each other and their position is the same as by the physiological breathing.
In some cases regarding the speech signal processing the right moment of the closing of the glottis is needed. In the phase of closed glottis the acoustic signal is generated as a consequence of the resonance processes in the vocal tract, i.e. the process is in the state of free oscillations.

2. Methods to determine the moment of the closing of the glottis

In this paper some of the most spread methods for the glottis closing are analyzed, following these criterions:

- A1 Usability for natural speech signals, regardless the gender of the speaker
- A2 Low sensitivity to external noises in the signal
- A3 Relative independence to the current speech message,
- A4 Low sensitivity to fluctuations in the period of the pitch, caused by instantaneous psycho-physiological condition of the person.
- A5 Implementation of the method with adequate cost of computational recourses, which allows implementation in common low-budget devices and systems (Mobile cell phones and computers, biometrical devices)

2.1. Methods based on the linear prediction error

These methods are well known ever since the first attempts for developing of functional systems for coding and decoding of speech signals were made. These methods also do a good job for estimating the different parameters of these signals [2, 12], when the speech is without noise (low estimate according to criterion A2).

2.2. Parthasarathy's method

It is well known, that the first format is generated in the moment of the closing of the glottis [5, 15]. The proposed model [14] is based on this fact. This method cannot exactly estimate the moment of the closing of the glottis, because the appearance of the maximums of the format energy is influenced by the coarticulation effects, which makes the method dependent form the current speech message, (low estimate according to criterion A3).

2.3. Cheng's method

This method is based on the idea of finding of the periodical continuations of the speech signal, which correspond of the pitch period [3]. For this purpose, linear prediction of the signal is made, with a low-order model, and subsequently the crosscorelation between the predicted and the original signal is made. The method gives good results, but only when the pitch frequency is low enough, i.e. when a male person's speech (good estimate on A2 and bad estimate according to A1).

2.4. Common methods to determine the periodical continuations

An attempt for applying the common theory for determining the periodic continuations has been made in [1]. It is based on some properties if the forward and inverse Fourier transform, and it uses filter synthesis of the periodical continuations. The method gives some good results even if the pitch period is two short (good estimate on A1), as long as the non-stationary of the period is bounded within certain limits. For real speech signals this is not always true, especially if the human is in a phase of varying psycho-physiological condition (low estimate according to A4). Another disadvantage of the method is the big computational cost (low estimate according to A5).

2.5. Strube's method

This method [20] is based of the technique of [19], and the latter is modified in such way, that the determinant of the autocovariation matrix is reaches its maximum, if the beginning of the interval, over which is has been evaluated, coincides with the moment of the closing of the glottis. The method produces stable results (good estimates according to A1, A2 and A4, and satisfactory estimate on A3). As a whole the method requires a big computational cost, even if a effective decomposition of the autocovariation matrix is used, as in Choleski [21]. This is why the method is unusable for real-time applications (low estimate according to A5).

2.6. Ma's method

In the method, proposed by Ma [10] a so called C-criterion is used. It is the mean value of the eigenvalues of the full rank square matrix. The experimental results confirm the correlation of the maximums of the C-criterion and the moment of closing the glottis. The results are close to these, obtained by the Strube's method (good estimates according to A1, A2, A4) but the C-criterion is considerably more sensitive towards impulse noise (low estimate by A3). Ma's method requires considerably lower computational cost when compared to Strube's method. Despite this, is gets a low estimate according to A5.

3. Theoretical background of the proposed algorithm

The above described methods give a good notion about the basic principles, which constitute the most known practical and usable algorithms for solving the problem of closing the glottis for the analysis of the speech signal. They all solve the problem with a compromise among A1-A5. We propose an algorithm, which is based on the modification of the proposed in [6] method. In the latter, with means of heuristic approach a fusion of the advantages of the above mentioned methods is achieved, with an adequate computational cost. For the stable

functioning of the algorithm though, an optimization of its parameters according to the current work conditions is needed. The modification, which we propose allows this optimization to be realized by means of distribution in the algorithm itself.

The phonation process could be conditionally characterized with the following phases of the behavior of the glottis – opening, fully open, closing, and fully closed. Besides that in the moment of closing of the glottis the first formant is generated [5, 15], in this moment the amplitude of the acoustic wave reaches its maximum value [18], because the accumulated in the resonance system of the vocal tract energy is maximal, it enters a state of free auto oscillations. From this moment on the accumulated energy decreases due to emission through the lips and the losses in the walls of the tract. In the phase of opening in the resonance system external energy is bought, which violates the process of auto oscillations, and prevailing driven oscillations come as result. The direct study of the motion of the vocal strings with the methods of the laryngoscopy and laryngoednoscopy, combined with filming in utra-high resolution [4,13] and others, show that the process of opening of the glottis is a continuous asymptotical process, which allows the phases of opening and of fully opened glottis to be considered as one phase. Obviously, the nature of the phonation process shows that for the exact estimation of the moment of closing of the glottis, a corresponding part of the speech signal to this phenomenon has to be found, which has a local maximum energy. The performed analysis states that the following points, regarding the characteristics, which can be used for the exact estimation of the moment of the closing the glottis, are true:

- In a isolated vocal segment, which is part of the speech signal, there are always several periodical continuations, which mean correspond to the pitch period;
- The fluctuation of the period of these periodical continuations in one sentence rarely goes over 10% [9];
- Each periodical continuation is characterized by one local energy peak, which corresponds to the moment of closing of the glottis;

Actually, one can prove, that all of the above mentioned methods can be transformed in an equivalent (characterized by its input and output) system, which first determines a certain function, which have some correlation with the short-time energy of the speech signal. Next, the local maximums of this function have to be found, and these maximums are expected to coincide with the moments of closing the glottis. The differences between the methods constitute in:

- In the function, which can be a certain non-linear transformation, which lowers the sensitivity towards noise and distortion;
- In the form and size of the window function;
- In the strategy of filtering the candidates for maxima, when in one periodical continuation there are more than one maxima, which have similar value.

4. Realization of the proposed algorithm

For a function, which has to act as a criterion for the moments of the closing the glottis, in this paper short time energy of the speech signal is used. Depending on the individual characteristics of the speaker the length of the vocal segments in the speech signal, during which they have a quasi-stationary behavior, is about 10 to 30 ms [11, 16]. This allows us to chose a window in the interval from 0.1 to 1 ms. The smaller the window is, the more precise the local maximums of the short-time energy will coincide with the moment of the closing the glottis. On the other hand the bigger window will reduce the impact of external distortion, added to the speech signal. Another reason for the exact coincidence is the usage of central symmetrical window function with odd number of samples. Due to the its optimal characteristics of decease in the time and frequency domain, as well as due to the good spectral contrast, caused by the high PSLR, the preferred choice is the Hamming window. Some good results could be obtained with the common triangle function as well (Bartlett window).

So obtained, the curve of the short-time energy contains and other local maximums, except these, coinciding with the moments of the closing of the glottis. Two facts from the process of phonation allow these peaks to be filtered. The first is, that in the moment of the closing of the glottis the local energy of the signal is

maximal. This allows us to accept, that the global maximum in the frame of one segment coincide with the corresponding moment of the closing of the glottis, if any is available in the segment. The second fact is, that the length of the separate periods of the pitch in the frame of the segment changes insignificantly. We accept the hypothesis, that from all possibilities of dividing of the analyzed segment of separate periodical continuations, the borders of which coincide with the moment of the closing the glottis, the best coincidence with the real periods of the pitch will be in this option, which has the lowest coefficient of variation of the obtained periods of the pitch. That way we choose this option, which is characterized by with the lower variation of the separate periods in the borders of the segment. This choice can be interpreted this way too: if we assume, that the process of phonation generates equal periods of the pitch, and their variation is caused by noise, then the minimal coefficient of variation corresponds to the maximum SNR. On fig.1 the structure of the algorithm of this optimization procedure is shown, marked as CRIBRUM. The input parameters are the short-time energy of the speech signal and the borders dmin and dmax, in which one can expect the period of the pitch, evaluated in number of samples. Because the frequency of the pitch, which depends on the gender and physiological characteristics of the speaker, it can be evaluated even in the phase of the preliminary processing, and that way in the phase of the analysis the separate speech segments close borders can be used, i.e. smaller number of iterations. The procedure gives a vector Ymin, corresponding to vector U, in which only the values of these elements are saved, which coincide with the moment of the closing of the glottis, and the rest are taken to be zero. The optimization is implemented in block number 4, which goes through dmax-din+1 steps. Each step evaluates a new separation of the vector U in periodical continuations with period, not smaller than d and with the corresponding coefficient of variation q - block 4.5. Block 4.6 takes care of preserving the vector with the smaller coefficient of variation from all other iterations. If there are more than one vector with a smaller difference than epsilon coefficients of variation, for a optimal the first discovered is used. On fig 2. The srtucturegramm of the procedure for the periodical continuations in a given segment is given. The procedure is called Peniclus; it has as local paremeters the left and the right border of the segment block 4.2.2, and is uses the global variables d and U of CRIBRUM. The procedure Peniculus is typical recurcive procedure from the type “divide and rule” according to the classification of Sedgewick [17]. The procedure transforms the row of samples from the vector U into new row, in which only the local maxima, standing one to each other on a length not less than d, and all the others are taken to be zero. This can be achieved, when in each recursion the procedure finds the global maximum between the left and the right border, which are given, when the procedure is called – block 4.2.2. After that, its zeros the samples, standing on a length of d samples to the left and to the right from this maximum. For the parts of the segments, standing to the left and to the right of the zeroed samples next to the global maximum, the procedure is called again – blocks 4.2.4.1 and 4.2.5.1 with the corresponding new borders for processing. Of course, when a high computational effectivity is needed, the recursive procedure can be transformed into iterative, but then its elegancy and comprehensibility is lost.

The proposed algorithm is implemented by the authors in different applications for speech signal processing and it produces excellent results. On fig.3 a speech segment of the vocal ‘o’ from the mantra ‘AUM’, pronounced by a yogi during psycho-physiological research [8], with a sampling frequency 22050 Hz. On fig 3b a short-time energy of the speech signal is shown, evaluated with a Hamming window, from 11 sample, which corresponds to a window from 0.5 ms. On fig 3c the samples of the short-time energy of the signal, corresponding to the moments of the closing the glottis. They are obtained by the procedure CRIBRUM in borders of search dmin = 63, corresponding to lower limit of the pitch of 350 Hz, and dmax = 350, corresponding of lower limit of the pitch of 60 Hz. The mean period of the pitch is 178.2 samples or 127.3 Hz.

5. Conclusion

The proposed algorithm is a powerful tool for determine the periodical continuations in signals with a qausi-periodical character. It is applicable in many cases, where the classical spectral methods for analysis are not (say where just a couple a periods are available; there is a big fluctuation in the length of the periods, a very string noise.

References

[1.] Ananthapadmanabha, T.V., B. Yegnanarayana.” Epoch Extraction of Voiced Speech” *IEEE ASSP-23, No.6*, Dec. 1975, 562-570

[2.] Atal, B., S. Hanauer. “Speech Analysis and Synthesis by Linear Prediction of the Speech Wave”., *JASA, 50,* 1971, 637-655

[3.] Cheng, Y.M., D. O’Shaughnessy. “Automatic and Reliable Estimation of Glottal Closure Instant and Period”., *IEEE ASSP-37, No.12*, Dec. 1989, 1805-1814

[4.] Farnsworth, D.W. “High-speed motion pictures of the human vocal cords”., *Bell Laboratorium Record 18*, 1990, 204-208

[5.] Fry, D.B. “The Physics of Speech.” *University Press, Cambridge*, 1989

[6.] Galabov, V. “Probability Approach for Error Reduction by Recognition of the Bulgarian Speech.” *ICAI-96, Sofia* 1996, 351-354

[7.] Galabov, V. “Epoch Determination of Quasi-Periodic Signals.” *Proc. Automatica and Informatics 2000, Vol. 2, SAI, Sofia*, 2000, 38-41

[8.] Galabov, V. “Bedienerdiagnose - ein Beitrag zur Steigerung der Mensch-Maschine-Systemverfügbarkeit.” *Automatisierungs-technische Praxis. 42 (2000) Heft 6, Oldenbourg, München*, 2000

[9.] Hilger, S. “Entwicklung eines Systems zur interaktiven Analyse und Synthese von Sprache unter besondere Berücksichtigung der Glottissimulation.“ *Diss., Universität zu Köln*, 1988

[10.] Ma, Ch., Y. Kamp, L.F. Willems. “A Frobenius Norm Approach to Glottal Closure Detection from the Speech Signal.” *IEEE Trans. Speech and Audio Processing, Vol. 2, No.2,* April 1994, 258-265

[11.] Markel, J.D., A.H. Gray, Jr. “Linear Prediction of Speech”. *Springer-Verlag, Heidelberg*, 1976

[12.] Miyoshi, Y., K. Yamoto, R. Mizoguchi, M. Yanagida, O. Kakusho. “Analysis of Speech Signals of Short Pitch Period by a Sample-Selective Linear Prediction.” *IEEE ASSP-35, No.9*, Sept. 1987, 1233-1239

[13.] Moore, G.P., F.D. White, H. von Leden, Ultra High-Speed Photography in Laryngeal Physiology. Speech Hear. Disord. 27, 1962, 165

[14.] Parthasarathy, S., W. Tufts. “Exitation-Synchronous Modeling of Voiced Speech.”, *IEEE ASP-35 No.9*, Sept. 1987, 1241-1249

[15.] Pickett, J.M.” The sounds of speech communication.” *University Park Press, Baltimore*, 1989

[16.] Rabiner, L., R. Schafer. “Digital Processing of Speech Signals.”, *Prentice-Hall Inc., Englewood Cliffs, New Jersey*, 1992

[17.] Sedgewick, R. “Algorithmen”. *Addison-Wesley, Bonn*, 1998

[18.] Seto, W.W. “Theory and Problems of Acoustics.” *New York, McGraw-Hill Inc*., 1991

[19.] Sobakin, A.N. “Digital Computer Determination of the Formant Parameters of the Vocal Tract from a Speech Signals”. *Soviet Physics-Acoustics, Vol. 18, No.1*, July-Sept., 1972, 84-90

[20.] Strube, H.W. “Determination of the instant of glottal closure from the speech wave”. *JASA, Vol. 56, No.5*, November 1974, 1625-1629

[21.] Werner, H.” Praktische Mathematik.”, *Bd.1, Springer*, Berlin, 1995

CRIBRUM

(1.) *Input*: $d_{\min}, d_{\max}, \mathbf{U} = (u_i)_{N,1}$

(2.) $q_{\min} = \infty$

(3.) $d = d_{\min}$

(4.) $d \le d_{\min}$

(4.1.) $\mathbf{Y} := \mathbf{U}$

(4.2.) Peniculus$(l := 1, r := N)$

(4.3.) $\mathbf{K} := \{k_i : y_j > 0;\ j = \overline{1,N};\ i = \overline{1,M}\}$

(4.4.) $\mathbf{T} := \{t_i : t_i = k_{i+1} - k_i;\ i = \overline{1,M-1}\}$

(4.5.) $q := \dfrac{\sqrt{\mathrm{var}(\mathbf{T})}}{\mathrm{E}(\mathbf{T})}$

(4.6.) $q(1+\varepsilon) < q_{\min}$

true

(4.6.1.) $q_{\min} = q$

(4.6.2.) $\mathbf{Y}_{\min} := \mathbf{Y}$

(4.7.) $d = d + 1$

(5.) *Output*: $\mathbf{Y}_{\min}$

Fig.1.

PENICULUS

(4.2.1.) *Input*: l, r

(4.2.2.) $p := \min\{n : y_n = \max\{\mathbf{Y}\};\ l \le n \le r\}$

(4.2.3.) $y_n := 0, \quad \forall n \in [p-d, p+d] \setminus p$

(4.2.4.) $p - d - 1 > l$

true

(4.2.4.1.) Peniculus$(l := l, r := p - d - 1)$

(4.2.5.) $p + d + 1 < r$

true

(4.2.5.1.) Peniculus$(l := p + d + 1, r := r)$

(4.2.6.) *RETURN*

Fig.2.

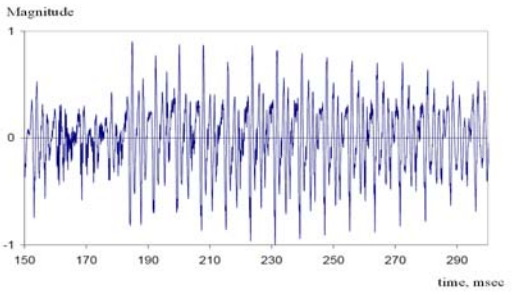

Fig.3.a

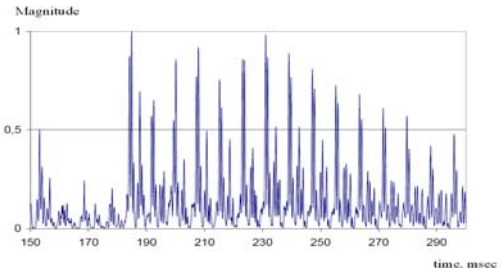

Fig.3.b

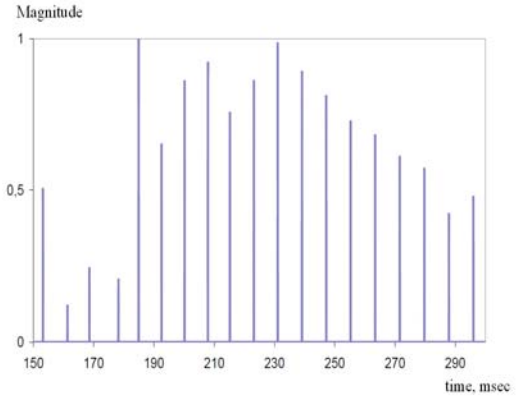

Fig.3.c

CDMA Wireless Communication System with Variable Information Rate Based on Families of Generalized Orthogonal Complementary Codes

Mihail Petkov Iliev [(1)]***, Borislav Yordanov Bedzhev*** [(2)]

[(1)] Faculty of Electrotechnics, Electronics and Automatic, University of Ruse "Angel Kanchev", Ruse, Bulgaria
miliev@uni-ruse.bg

[(2)] Faculty of Technical Sciences, University of Shumen "Bishop Konstantin Preslavsky", Shumen, Bulgaria
bedzhev@abv.bg

Keywords: CDMA wireless communication system, Families of orthogonal complementary codes.

Abstract: The wireless communication systems are in very rapid progress today. Despite of this the users and industry expect an even more significant enhancement of the quality of the services and the transmission rate, offered by these systems. A promising approach for meeting of the today requirements are the so – named families of orthogonal complementary codes (FOCCs), which are the mathematical model of radio signals possessing both autocorrelation functions (ACFs) with a small level of the side-lobes and small cross-correlation functions (CCFs) among all pairs of members of a family. With regard to the valuable correlation features of the FOCCS, in the paper we present a scheme of CDMA wireless communication system based on FOCCs. The main advantages of the proposed scheme are: the so-named self-interference (SI), caused by multipath spreading of electromagnetic waves, can be significantly reduced by a separate processing of the direct and reflected signals; the negative effect of simultaneous transmission of numerous users, named multi user interference (MAI), can be practically eliminated; the information transmission rate can be adjusted according to the concrete necessities of the users.

1. Introduction

The number and quality of services offered by wireless communication systems can be increased according to the expectations of the people only by extremely optimal using of the electromagnetic spectrum. Today this hard technical problem is solved by applying of so-named Code Division Multiple Access (CDMA) to the system resources. The most important positive features of CDMA systems are: resistance to negative effects of multipath wave spreading (often noted as self – interference (SI)), invulnerability to unauthorized access, low interference with other electromagnetic sources and etc. These valuable abilities are result of that the radio signals are transmitted in a frequency band much wider than the minimal band required for sending the information. The spreading of the frequency spectrum over a wider band is reached by phase and/or frequency manipulation of the radio signals.

The spread spectrum signals must meet many requirements. The most important of them are: complex pseudorandom structure, ideal autocorrelation function (ACF), similar to the delta impulse, close to zero cross-correlation function (CCF) for all of the signals used in the communication system. With regard to these requirements, recently Chinese, Japanese and Russian authors have proposed a new CDMA architecture for the next generation mobile communications, based on so named families of orthogonal complementary codes (FOCCs) [1], [2], [3]. The most distinguishable advantage of this architecture is possibility to operate without multiple access interference (MAI) and SI. As a result, the system capacity, secrecy, and electromagnetic compatibility can be improved significantly. With regard the to positive features of the FOCCs in the paper we

propose a method for exploiting of the FOCCs in the so-named beyond thirdh generation (3G) mobile communication systems. The method allows the information transmission rate to be adjusted according to the instant necessities of the users.

The paper is organized as follows. First, the basics of the mobile communication systems, using the positive features of the FOCCs, are recalled. After that, our method for adjusting of the information transmission rate is presented. Finally, the advantages of our method are summarized.

2. CDMA Wireless Communication System with Variable Information Rate Based on Families of Generalized Orthogonal Complementary Codes

Let $K \geq 2, M \geq 2, N \geq 1,$ be integers and let us consider a family $V(K, M, N)$, comprising K sets as every set consists of M sequences with (code) length N:

$$\{a_k(m,n)\}_{n=0}^{N-1} = \{a_k(m,0), a_k(m,1), ..., a_k(m,N-1)\}, m = 0,1,...,M-1 \quad (1)$$

Then $V(K, M, N)$ is called family of orthogonal complementary codes (FOCCs) if the following conditions are satisfied [1], [2], [3], [4], [5]. First, the aggregated ACFs of the sequences of every set are zero except for the zero time shifts. Second, the aggregated CCFs of the sequences of all pairs of sets are zero for every time shift. These conditions can be mathematically described as follow:

$$R_{A_k,A_s}(r) = \begin{cases} M.N, & k = s \cap r = 0; \\ 0, & k \neq s \cup r \neq 0, \end{cases} \quad (2)$$

where:

- r is the time shift, $r = -(N-1),(N-2),...,-1,0,1,...,N-1$;
- A_k, $k = 0,1,...,K-1$ is the matrix, denoting the k-th set of the family V(K, M, N), i.e.:

$$A_k = \begin{bmatrix} a_k(0,0) & a_k(0,1) & ... & a_k(0,N-1) \\ a_k(1,0) & a_k(1,1) & ... & a_k(1,N-1) \\ ... & ... & ... & ... \\ a_k(M-1,0) & a_k(M-1,1) & ... & a_k(M-1,N-1) \end{bmatrix} \quad (3)$$

- $R_{A_k,A_s}(r)$ is the aggregated CCF (ACF if $k = s$) of the rows of the k-th and s-th sets (matrices), $k, s = 0,1,...,K-1$.

The aggregated $R_{A_k,A_s}(r)$ CCF (ACF if $k = s$) is evaluated by the well known formula [1], [2], [3], [4], [5]:

$$R_{A_k,A_s}(r) = \begin{cases} \sum_{m=0}^{M-1} \sum_{n=0}^{N-1-|r|} a_k^*(m,n).a_s(m,n+|r|), & -(N-1) \leq r \leq 0, \\ \sum_{m=0}^{M-1} \sum_{n=0}^{N-1-r} a_k(m,n).a_s^*(m,n+r), & 0 \leq r \leq N-1. \end{cases} \quad (5)$$

Here the symbol "*" means "complex conjugation".

The structures of a transmitter and a receiver of a CDMA communication system, using the positive features of the FOOCs, are shown on Fig. 1. There the following abbreviations are made:

- "PMd" means "Phase Modulator";
- "PDM" – "Phase Demodulator";
- "SbFF" – "Subband Frequency Filter";
- "Σ" is "Adder".

Besides it should be stressed on the fact that according to [1], [2], [3] inputs of the matrices (3) are only -1 and $+1$. This means that in the system binary phase modulation of the carrier frequcies is exploited.

In the transmitter of the k[th] user every bit of the information input has duration T. It is added modulo 2 in M subchanels with the corresponding rows of the matrix A_k . Consequently, if the input data has information

transmission rate C, the derivative sequence of chips (which duration is T/N) has transmission rate NC. After modulo 2 adding, the frequency carriers f_m, $m = 1, 2, ..., M$ are binary phase manipulated, according to the sequences of minus and plus ones of the m^{th} row of the matrix A_k. As a result every input information bit is conveyed to the receivers by means of M subchannels. Besides in each subchannel every information bit is divided into N chips.

The other users of the system receive the signals, sent by the k^{th} user. In the receiver of the s^{th} user, a set of subband frequency filters separates the complex frequency signals in M subchanels. After that, in every subchanel signals are phase demodulated by a match filter and aggregated. If the message is directed to the s^{th} user, i. e. $k = s$, then the result of summation is a sequence of bits, which is very close to the transmitted sequence. Otherwise, if the data isn't for the s^{th} user, i. e. $k \neq s$, the sum is zero at all time shifts of data transmission.

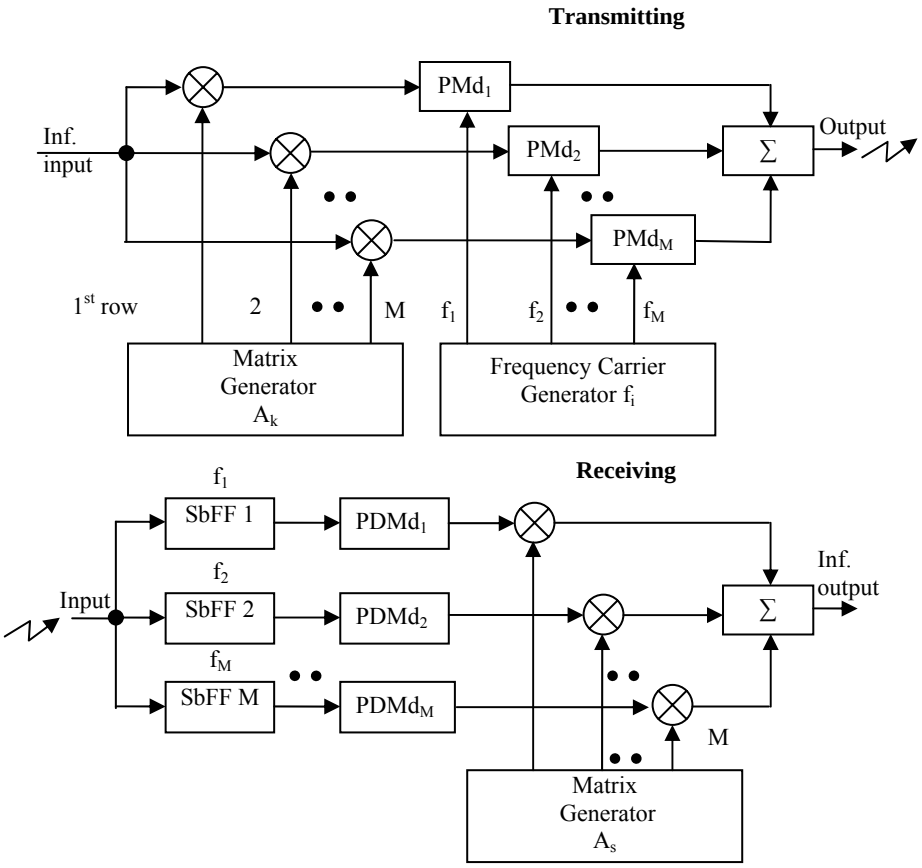

Fig. 1: A transmitter and a receiver of a CDMA communication system, based on the FOOCs

From all above stated, it is not hard to see that the perfrect correlation properties of the FOCCs (according to (2)), used in the mobile communication system, allow the users to communicate practically without of MAI and SI. It should be stressed that capabilities of the system, shown on Fig. 1, outperform significantly the capabilities of the 2G and beyond mobile communication systems [1], [2], [3], [4], [5].

Anyway, the presented scheme has an important disadvantage. Namely, its spectral (or spreading) efficiency (SE) is low. As it is known [3] SE is measured by the number of bits of information carried out by each chip and it shows how effectively the spectral band of the system is exploited. On the base of the above analisys it is easy to calculate that SE of the presented on Fig. 1 scheme is only 1/(MN). With regard to this situation, a method for improvement of the SE of the communication systems, based on FOCCS, has been suggested [2], [3]. This method is caled offset stacking (OS) and it can be brifly descriebed as follows [2], [3].

In the calssical CDMA communication systems at every time interval T a bit of information in each frequency subchannel is conveyed (spreaded) by N chips. In other words the "pure" information rate is:

$$C = T^{-1}\,[b/s]\,. \tag{6}$$

At the other hand, the perfect correlation properties of the FOCCs allow the transsmission of the next bit of information to begin "instanly" with a gap of T/N [s] after the transmission of the former bit of information. Here T/N [s] is the duration of a chip. Consequently, as a result of the applying of the OS method, the SE can be increased N times from 1/(MN) to 1/M.

The analisys of the OS method shows that in fact it can be viewed as N-level pulse amplitude modulation. As it is well known, the main disadvantages of the pulse amplitude modulation are: the low power effectiveness and hardness of providing of linear work regime of the transmitter. With regard to these disadvatges, our opinion is that applying of Q-level ($Q \geq 2$) phase modulation (Q-level fhase shif-keying (PSK)) is more appropriate. In this case the entries $a_k(m,n), k = 0,1,...,K-1, m = 0,1,...,M-1, n = 0,1,...,N-1$ of the matrices (3) should be complex numbers, belonging to the set of the Qth roots of the unity, i.e.:

$$a_k(m,n) \in \{\exp[(2\pi il)/Q; l = 0,1,...,Q-1\},\ i = \sqrt{-1}\,. \tag{7}$$

It should be stressed on the following facts:

First, general methods for synthesis of FOCCs, which satisfy the condition (7) are presented in [5]. These methods make posslible the constructing of CDMA mobile communication systems, exploiting FOCCs, generated by means of Q-level PSK.

Second, if Q is chosen to be:

$$Q = M.N\,, \tag{8}$$

then the SE of the CDMA mobile communication system will be 1.

Third, the information transmission rate can be adjusted according to the instant necessities of the users. Namely, it can be $C/V\,[b/s]$, where V is an arbitrary factor of Q.

3. Conclusions

In the paper a method for exploiting of the FOCCs in the so-named beyond thirdh generation (3G) mobile communication systems is presented. This method generalizes known up to day methods for enhancing of the spectral efficiency of the systems. Namely, it allows:

- very effective usage of the limited natural resource – the electromagnetic spectrum as a result of eliminating of MAI and SI;
- avoiding of the disadvantages of the so-named offset stacked method;
- adjusting the information transmission rate according to the instant necessities of the users.

References

[1.] H.-H. Chen, S. Yat-Sen S., J.-F. Yeh, N. Suehiro, "A multi-carrier CDMA architecture based on orthogonal complementary codes for new generations wideband wireless communications", *IEEE Communication Magazine*, 2001, vol. 39, № 10, pp. 126 – 135

[2.] V. V. Ignatov, S. A. Dobrovol'skiy, A. Yu. Guzhva, "Matrix signal systems used in CDMA systems", *Electrosviaz*, 2003, № 9, c. 41-42 (in Russian)

[3.] H.-H. Chen, *Next Generation CDMA Technologies*, John Wiley&Sons, Chichester, West Sussex, England, 2007

[4.] B. Y. Bedzhev, "Generalized orthogonal complementary codes for CDMA wireless communications", in Proc. *The 2004 European Conference on Wireless Technology*, pp. 329–332, Amsterdam, Kingdom of Netherlands, Oct. 2004.

[5.] B. Y. Bedzhev, M. P. Iliev "A General Method for Synthesis of Families of Orthogonal Complementary Codes," in press.

Analysis of forward error correction codes for improvement of the energy consumption in WSN

Georgi Hristov[(1)], Teodor Iliev[(1)], Dimitar Radev[(1)], Plamen Zahariev[(1)], Mihail Iliev[(1)]

[(1)]Department of Communication systems and technology, University of Ruse, Studentska Street 8, Ruse, 7017, Bulgaria, Phone: (+359) 82 888 663, Fax: (+359) 82 888 841, E mail: ghristov@uni-ruse.bg; tiliev@ecs.uni-ruse.bg; dradev@abv.bg; pzahariev@uni-ruse.bg; miliev@ecs.uni-ruse.bg;

Keywords: Wireless sensor networks, forward error correction codes, sensor nodes, sensor network lifetime.

Abstract: In this paper we study the effect of forward error correction codes on the energy consumption for communications in wireless sensor networks. These networks are extremely energy constraint, due to the limited battery capacity at each node, so the goal is to maximize the network lifetime. Channel coding can decrease the energy consumption, increase reliability and eliminate the need of costly retransmissions for sensor data.

1. Introduction

Sensor networks play a major role in many aspects of society including home automation, consumer electronics, military application, agriculture, environmental monitoring, health monitoring and geophysical measurement [1]. Usually sensor devices are small and inexpensive, so they can be produced and deployed in large numbers. Their resources of energy, memory, computational speed and bandwidth are severely constrained [2]. Therefore, it is important to design sensor networks aiming to maximize their life expectancy. Different aspects of sensor networks such as data aggregation or fusion, packet size optimization, target localization, design challenges, network protocols are discussed in the literature with respect to crucial energy limitations and network lifetime maximization [3]. Forward error correction (FEC) is a classic approach used to increase link reliability and lower the required transmitted power. However, lowered power at the transmitter comes at the cost of extra power consumption due to the decoder at the receiver. Stronger codes provide better performance with lower power requirements, but have more complex decoders with higher power consumption than simpler error control codes. If the extra power consumption at the decoder outweighs the transmitted power savings due to using FEC, then FEC would not be energy-efficient compared with an uncoded system.

2. Radio and Communication Models

For the purposes of our study we use a simple radio energy dissipation model presented in Fig. 1. According to this model in order to achieve an acceptable Signal-to-Noise Ratio (SNR), while transmitting a message with size $L=B$ bits, over a distance d, the energy utilized by the radio can be given by:

$$E_{TX}(B,d) = \begin{cases} BE_{elect} + BE_{fs}d^2 & if \quad d < d_0 \\ BE_{elect} + BE_{ms}d^4 & if \quad d \geq d_0 \end{cases}, \tag{1}$$

where E_{elect} is the energy dissipated per bit of the transmitter or receiver, E_{fs} and E_{ms} depend on the transmitter amplifier model used and d is the distance between the sender and the receiver. By equating the two expressions at $d=d_0$, we have $d_0 = \sqrt{E_{fs} / E_{ms}}$. The energy dissipated by the sink for the reception of the message is:

$$E_{RX}(B) = BE_{elect}, \tag{2}$$

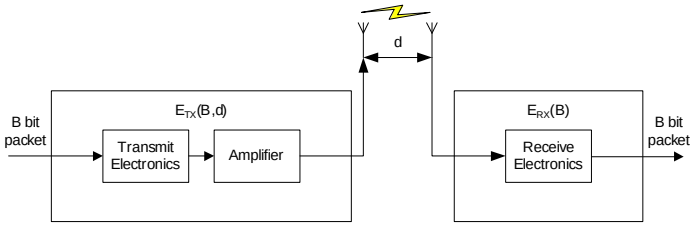

Fig.1. Radio Energy Dissipation Model.

3. Forward Error Correction Codes

Forward error correction codes (*FEC*) introduces redundancy into an information sequence u of length k by the addition of extra parity bits, based on various combinations of bits of u, to form a codeword x of length $n_C>k$. The redundancy provided by these extra n_C-k parity bits allows the decoder to possibly decode noisy received bits of x correctly which, if uncoded, would be demodulated incorrectly. This ability to correct errors in the received sequence means that use of ECC over a noisy channel can provide better bit error rate (*BER*) performance for the same signal-to-noise ratio (*SNR*) compared to an uncoded system, or can provide the same BER at a lower SNR than uncoded. This difference in required SNR to achieve a certain BER for a particular code and decoding algorithm compared to uncoded is known as the coding gain for that code and decoding algorithm. Typically there is a tradeoff between coding gain and decoder complexity. Very long codes provide higher gain but require larger decoders with high power consumption, and similarly for more complex decoding algorithms. Several different types of ECC exist, but we may loosely categorize them into two divisions [4]:

- Block codes, which are of a fixed length n_C, with n_C-k parity bits, and are decoded one block at a time;
- Convolutional codes, which, for a rate k/n_C code, input k bits and output n_C bits at each time interval, but are decoded in a continuous stream of length $L>>n_C$;

Block codes include repetition codes, Hamming codes, Reed-Solomon codes, and BCH codes. The terminology (n_C, k) or (n_C, k, d_{min}) indicates a code of length n_C with information sequence of length k, and minimum distance (the minimum number of different bits between any of the codewords) d_{min}. Short block codes like Hamming codes can be decoded by syndrome decoding or maximum likelihood (ML) decoding by either decoding to the nearest codeword or decoding on a trellis with the Viterbi algorithm or maximum a posteriori (MAP) decoding with the BCJR algorithm. Algebraic codes such as Reed-Solomon and BCH codes are decoded with a complex polynomial solver to determine the error locations. Convolutional codes are decoded on a trellis using either Viterbi decoding, MAP decoding, or sequential decoding [4].

Another categorization is based on the decoding algorithms:

- Noniterative decoding algorithms, such as syndrome decoding for block codes or maximum likelihood (ML) nearest-codeword decoding for short block codes, algebraic decoding for Reed-Solomon and BCH codes, and Viterbi decoding or sequential decoding for convolutional codes;
- Iterative decoding algorithms, such as turbo decoding with component MAP decoders for each component code, and the sum-product algorithm or its lower complexity approximation, min-sum decoding, for low-density parity-check codes (LDPC);

The noniterative decoding category may be further divided into hard- and soft-decision decoders; hard-decision decoders output a final decision on the most likely codeword, while soft-decision decoders provide soft information in the form of probabilities or log-likelihood ratios (LLRs) on the individual codeword bits. Viterbi decoding can be either hard-decision or soft-decision, with a 2 dB gain in performance for soft-decision decoding. Second category is all soft decision algorithms by nature, as iterative decoding requires soft information as a priori input for each iteration. Iterative decoding algorithms provide significant coding gain, at the cost of greater decoding complexity and power consumption [5]. Fig. 2 shows BER performance versus E_b/N_0 for several types of error-correcting codes, compared to uncoded BPSK (binary phase-shift keying) modulation. The E_b stands for energy per bit and the N_0 stands for the noise power spectral density ratio. For each simulation, a curve showing the bit-error rate (*BER*) versus E_b/N_0 was computed. Transmission is over an additive white Gaussian noise (*AWGN*) channel, with variance $N_0/2$ and zero mean, using BPSK modulation for all encoded bits.

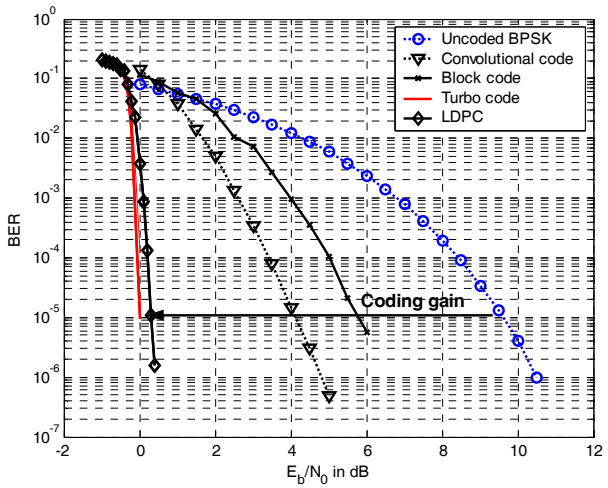

Fig.2. BER performance versus E_b/N_0 for several forward error correction codes

The block code is nonsystematic Golay code (23, 12) and the use of this simple block code provides an improvement of 2,6 dB in the required E_b/N_0 for achieving an error rate of 1 in 100 000 transmitted bits. The convolutional code is with code rate R=1/2, 64-state constraint length 7 and uses soft-decision Viterbi decoder. The soft-decision decoder performs about 2 dB better than the hard-decision decoder. Two iteratively decoded codes are displayed as well, and the power of iterative decoding is clearly shown. These three codes provide the best performance on the graph. The parallel concatenated convolutional code (PCCC) is a classic turbo code, and used in the 3GPP standard, although it is short; it has an interleaver and information sequence size of 40 bits. The code LDPC is with rate R=1/4, length 16200 and 100 decoding iterations.

4. Single-Hop versus Multi-Hop – Comparison of the Data Delivery Models

The single-hop model consists of a base station (BS) and a set of sensors nodes [1]. The BS is normally not powered by batteries and thus is not energy limited. The nodes, on the other hand, are strongly energy limited [2]. We assume that they communicate in one hop with the BS (Fig. 3). In what follows we will discuss separately the uplink and the downlink (as seen from the BS).

For the uplink, advanced coding is implemented to extend the range of the sensor nodes, so that they can reach the BS with a single hop and at a reasonable energy cost. The code used has to be asymmetric – the power consumption of the encoder must be much lower than that of the decoder. Using the single-hop data delivery model, the nodes have very low power consumption. The power consumption of the BS is high, but since it is energy independent, this has no effect on the overall performance of the system. This idea can be extended further with the reduction of the nodes receiver sensitivity, by compensating with increase of the BS's. This will result in significant decrease of the power for communication of the nodes in both transmit and receive modes. The single-hop model also allows the use of centralized MAC designs, which are not feasible for multi-hop data delivery. Another advantage is the possibility to power down the nodes before and after their scheduled time slots. To extend further our analysis, in what follows, we will compare the average power consumption of the nodes in both single-hop and multi-hop systems (Fig. 4). If we consider the uplink, with N hops between the BS and a node, N transmissions and (N − 1) receptions will be carried out. In the downlink, the power consumption in the single-hop model is definitely lower since no forwarding is needed. Hence we will focus on the comparison of the uplink. We assume the following - the required BER is the same for both models, collisions-free environment, only data packets are sent and no time is spent in overhearing/monitoring, and both BS and nodes have the same receiver sensitivity. For the results we use a convolutional code (soft decision, K=7, 1/2 rate). The experiments show, that the single-hop model outperforms the multi-hop model at distances up to 140 meters. For many applications of the sensor network, this range is good enough. The reason that the single-hop has lower total energy consumption at short ranges is that the implementation of advanced coding has reduced the power consumption sensitivity to the range.

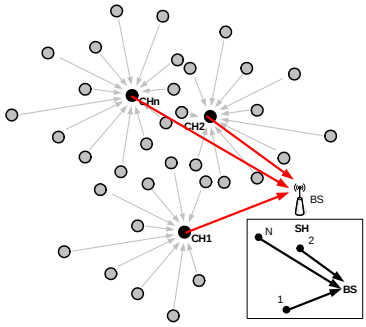

Fig.3. Single-hop data delivery model

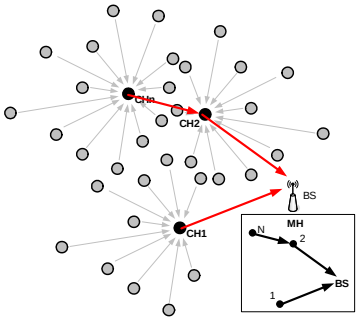

Fig.4. Multi-hop data delivery model

Another reason for this is the overhead in the multi-hop model. As the range goes beyond 140 meters, the exponential growth of power consumption in the single-hop surpasses the linear growth in the multi-hop case. Hence, the single-hop model should not be used if the distance is too long. As the level of the noise increases, this threshold will decrease. On the other hand, the use of a better code makes this threshold higher.

5. Conclusion

In this paper we have compared the energy consumption between the single-hop and the multi-hop data delivery models. This comparison is not quite precise, because in multi-hop sensor networks, there are many additional factors, which have to come into consideration. Some of these factors are the spatial diversity, the use of data aggregation and scalability. In single-hop networks partial scalability can also be achieved by having the BS polling different types of sensors at different frequencies. Based on the observations from this paper, the decision whether to use multi-hop or single hop is still open. The use of FEC can allow a system to operate at significantly lower SNR than an uncoded system, for the same BER. However, there are many factors need to be considered. First, a trade-off between the BER and the number of iterations used in the decoding algorithm need to be made, e.g., more iteration will get lower BER, but the decoding delay is also longer. Secondly, the effect of the frame size on the BER also needs to be considered. Although the forward error correction code with larger frame size has better performance, the output delay is also longer. Thirdly, the code rate is another factor that needs to be considered. The higher coding rate needs more bandwidth.

Acknowledgment

This work is a part of the projects: BG051PO001/07/3.3-02/8–"MEQSIS", funded by scheme "Support of the development of PhD students, postdoctoral, post-graduate and young scientists" from the program "Development of human resources" of the "European social fund"; and DMU-02/13-2009 "Design and performance study of an energy-aware multipath routing algorithm for wireless sensor networks" of Bulgarian Science Fund at Ministry of Education and Science.

References

[1.] G. Hristov, P. Zahariev, T. Iliev and M. Iliev, "An approach for energy optimization in wireless sensor networks", *33rd International Convention MiPRO*, Opatija, Croatia, pp. 203 – 206, 2010
[2.] P. Zahariev, G. Hristov and T. Iliev, "A method for reducing the energy dissipation in wireless sensor networks using edge node", *33rd International Convention MiPRO*, Opatija, Croatia, pp. 207 – 210, 2010
[3.] G. Hristov, P. Zahariev and T. Iliev, Study on the impact of node density and sink location in WSN, Technological Developments in Networking, Education and Automation, Springer, 2010, (in press)
[4.] E. Biglieri, *Coding for wireless channels*, Springer, 2005
[5.] T. Iliev, G. Hristov, Simulation estimation of the forward error correction of turbo codes. *Proceedings of the IEEE Conference TELSIKS'2007*, Nis, Serbia, pp. 521 – 524, 2007

2D-DoA Estimation with Pilot Signals and Select Technique

Jun Ozawa, Tomoyuki Kitada, Jun Cheng, and Yoichiro Watanabe

Dept. of of Intelligent Information Eng. & Sci., Doshisha University, Kyotanabe, Kyoto 610-0321 Japan.
Email: joza19@gmail.com, jcheng@ieee.org, and watanabe@muc.doshisha.ac.jp

Keywords: DoA estimation, beamforming, pilot

Abstract: A two-dimensional direction-of-arrival (2D-DoA) estimation using pilot signals and select technique with 7-element hexagonal array is proposed. An estimate candidate of 2D-DoA, associated with a pilot signal, is estimated with two set-of-subarrays, where the estimation is based on the computation of the phase shift between the two subarrays with subarray beamforming. The estimate DoA is selected from the estimated elevation and azimuth angles in the three estimate candidates obtained from the three combinations of two set-of-subarrays. Benefiting from the multiple subarrays and the pilot signals, the proposed algorithm suppresses the error dependence on relation of subarrays, and gives a larger estimation capacity than the number of subarray elements. Simulation verifies the efficiency of error suppression and estimation capacity.

1. Introduction

There are many algorithms to be developed for direction-of-arrival (DoA) estimation with array antenna. One of the common used algorithms is the estimation of signal parameters via rotational invariance technique (ESPRIT) [1], [2]. For ESPRIT algorithm, two subarrays are used to obtain two signal subspaces such that the eigenvectors of one signal subspace relative to the eigenvectors of the other are rotated in terms of the DoAs of the signals. The DoAs are then estimated by resolving equations related to the two subarrays.

Recently, subarray beamforming (SB) [3] technique with pilot signals is presented to estimate the DoAs. In SB, the target signal is an output of one subarray by rejecting interference signals through the beamforming on the subarray. The phase shift between the two subarrays, which is a function of the target DoA, is then estimated. Since all the signals and interferences other than the target one can be efficiently rejected before DoA estimation, the capacity of DoA estimation can be far larger than the number of antenna elements.

Both ESPRIT and SB, however, suffer from the estimate error arisen from dependence of a practical value of DoA and the used subarrays, due to the employed translational invariance subarrays. In our previous work [4], we employ multiple subarrays in a 7-element hexagonal array. We have applied 1D-ESPRIT algorithm to each of two subarrays and have grouped the estimate DoAs into candidate set. The DoA are successively selected among the candidate set with maximum value of 1D-MUSIC spectrum in which the previous estimated signal components are removed. It seems to be straightforward to extend the one-dimensional estimation to two-dimension (elevation /azimuth) parameter estimation, i.e., 2D-ESPRIT. Actually this extension is possible, since there are multiple subarrays in the 7-element hexagonal array. Unfortunately, when we do this extension, we find that a) the previous estimated signal components can't be completely removed from the 2D-MUSIC spectrum, an b) the high precision for both azimuth and elevation can't be obtained simultaneously if one simply selects the angle pair among the candidate set. Furthermore, it is well-known that 2D-ESPARIT requires to pair the individual parameters, which are estimated separately in each dimension. Incorrect pairings would lead to faulty estimations.

In this paper, we also focus on the geometry, i.e., multiple subarrays, of the 7-element hexagonal array. We propose a 2D-DoA estimation algorithm with the select technique and pilot signals to suppress the estimation error arisen from the translational invariance subarrays (referred to set-of-subarray). We estimate the phase shifts of each set-of-subarray with one of pilot signals. Then DoA candidates (three pairs of elevation and azimuth angles) are estimated with three combinations of two sets-of-subarrays, respectively. We join every elevation and every azimuth in the three pairs to form 3×3 pairs, and select the optimal angle pair, among the 3×3 pairs, with the criterion of the directional constraint maximum power.

The proposed 2D-DoA estimation algorithm employs the multiple subarrays, and thus suppresses the error dependence on related subarrays. Moreover, it is obvious that there exists only one DoA signal, associated with a pilot, in each output of subarray because of the subarray beamforimg. This avoids the pairing problem in 2D estimation [2] and successive selection among the candidates of multiple DoAs, as in [4]. The simulations show that the proposed method gives high accuracy of 2D-DoA estimation, and the estimation capacity can be larger than the number of subarray elements.

2. Hexagonal array and its signal model

In this section, we describe the signal model of hexagonal array. Let's consider an M (=7)-element hexagonal array, where a single central element is surrounded by a 6-element hexagon (see Fig. 1(a)). In the array, each grouping of three nearby elements has equal central element spacing, $d=\lambda/2$, where λ is the wavelength.

We assume that signals from different sources are uncorrelated or have negligible correlation with each other. In the case that there are L pilot sources and J unknown interference sources, denote by DoA (θ_i, φ_i) (i=1, 2, …, $L+J$) the signal from source i with the elevation angle θ_i and azimuth angle φ_i in radians. Let $\boldsymbol{a}(\theta_i, \varphi_i)$ be an M-dimensional array steering vector. Thus the received signal vector after down-converting to baseband with additive noise can be represented by

$$\boldsymbol{x}(t) = \sum_{i=1}^{L+J} s_i(t)\boldsymbol{a}(\theta_i, \varphi_i) + \boldsymbol{n}(t). \tag{1}$$

Here $s_i(t)$ (i = 1, 2, …, L) is a pilot signal component, $s_i(t)$ (i = L+1, L+2, …, L+J) is an unknown interference component, and $\boldsymbol{n}$(t) is an M-dimensional Gaussian noise vector.

The idea behind our proposed algorithm is to make the best use of the geometry of the hexagonal array. It is not difficult to see that there are three sets of subarrays, i.e., the sets (1), (2), and (3), in the hexagonal array (see Fig. 1). In each set, there are two 4-element subarrays having translational invariance. This observation motives us to improve the precision of the conventional 2-D DoA estimation.

3. 2D-DoA estimation with pilot signals and select technique

3.1 Phase shift of pilot signal in each set of two subarrays

In this section, we describe the phase shift of the l-th pilot in the k-th set of two subarrays. Consider the set (k) of the two subarrays A(k) and B(k) (see Fig. 1). The received signal vectors of the subarray A(k) and the subarray B(k) can be represented by $\boldsymbol{x}_{\mathrm{A}}^k = \mathbf{T}_{\mathrm{A}}^k \boldsymbol{x}(t)$ and $\boldsymbol{x}_{\mathrm{B}}^k = \mathbf{T}_{\mathrm{B}}^k \boldsymbol{x}(t)$, respectively, Here $\mathbf{T}_{\mathrm{A}}^k$ and $\mathbf{T}_{\mathrm{B}}^k$ are transportation matrices, which pick up the subarrays A(k) and B(k) from the hexagonal array, respectively. The matrix component at row i and column j is 1 if it corresponds to a selected array element, and 0 otherwise. Using (1), we obtain that

$$\boldsymbol{x}_{\mathrm{A}}^k(t) = \mathbf{T}_{\mathrm{A}}^k \sum_{i=1}^{L+J} s_i(t)\boldsymbol{a}(\theta_i, \varphi_i) + \boldsymbol{n}_A(t), \qquad \boldsymbol{x}_{\mathrm{B}}^k(t) = \mathbf{T}_{\mathrm{B}}^k \sum_{i=1}^{L+J} s_i(t)\boldsymbol{a}(\theta_i, \varphi_i) + \boldsymbol{n}_{\mathrm{B}}(t) = \mathbf{T}_{\mathrm{A}}^k \sum_{i=1}^{L+J} e^{j\Theta_k} s_i(t)\boldsymbol{a}(\theta_i, \varphi_i) + \boldsymbol{n}_{\mathrm{B}}(t) \tag{2}$$

where
$$e^{j\Theta_l^k} = \exp(j2\pi d \sin\theta_l(\varphi_l - \psi^k))/\lambda. \tag{3}$$

Here Θ_l^k is the phase-shift factor between the l-th components of signals $\boldsymbol{x}_{\mathrm{A}}^k$ and $\boldsymbol{x}_{\mathrm{B}}^k$, thanks to the translational invariance of the two subarrays.

We now estimate the phase shift of the l-th pilot signal. We find a weight vector $\boldsymbol{w}_l^k(t)$ by subarray beamforming in the subarray A(k), and then apply the weight vector to the subarray B(k). Then we estimate the phase shift by employing the Lagrange multiplier method to the output of the subarray B(k) and the reference signal. Specifically, first, let's focus on the beamforming of the subarray A(k). For the l-th pilot $s_l(t)$ we find a weight vector $\hat{\boldsymbol{w}}_l^k(t)$ at the subarray A(k) such that the error between the output signal of the subarray A(k) after the beamforming and the known reference signal r_l is minimized.

$$\hat{\boldsymbol{w}}_l^k(t) = \arg\min_{\boldsymbol{w}_l^k} E[|(\boldsymbol{w}_l^k)^{\mathrm{H}} \boldsymbol{x}_{\mathrm{A}}^k(t) - r_l(t)|^2]. \tag{4}$$

Weiner solution gives the optimal weight $\hat{\boldsymbol{w}}_l^k = (R_{\mathrm{A}}^k)^{-1}\boldsymbol{h}_l^{\mathrm{A}}$, where $R_{\mathrm{A}}^k = E[\boldsymbol{x}_{\mathrm{A}}^k(t)(\boldsymbol{x}_{\mathrm{A}}^k)^{\mathrm{H}}(t)]$ and $\boldsymbol{h}_l^{\mathrm{A}} = E[\boldsymbol{x}_{\mathrm{A}}^k(t) r_l^*(t)]$.

Second, we apply the weight $\hat{\boldsymbol{w}}_l^k(t)$, obtained at the beamforming of the subarray A(k), to the subarray B(k). Let $\hat{r}_l^k(t) = (\hat{\boldsymbol{w}}_l^k)^{\mathrm{H}} \boldsymbol{x}_{\mathrm{B}}^k(t)$ denote the output signal after beamforming of the subarray B(k). Since $\hat{r}_l^k(t)$ is an estimation of the phase shifted reference signal $e^{j\Theta_l^k} r_l^k(t)$ in MMSE, it can be written as $\hat{r}_l^k(t) = e^{j\Theta_l^k} r_l^k(t) + n_l(t)$ which represents the reference signal shifted plus an estimation error n_l(t). Let $\boldsymbol{r}_l^k$ and $\hat{\boldsymbol{r}}_l^k$ denote vectors with samples of the reference signal $r_l^k(t)$ and the estimated reference signal $\hat{r}_l^k(t)$ in a snapshot interval, respectively. By the Lagrange multiplier method, we obtain

$$\hat{\Theta}_l^k = \arg(\boldsymbol{r}_l^{\mathrm{H}} \hat{\boldsymbol{r}}_l^k) = 2\pi d \sin\hat{\theta}_l \cos(\varphi_l - \psi^k)/\lambda \tag{5}$$

which is the angle of the complex inner product of the reference signal vector and its phase shift. Note that in (5), the phase shift $\hat{\Theta}_l^k$ is composed of two variables $\hat{\theta}_l$ and $\hat{\varphi}_l$, which are the elevation angle and azimuth angle to be estimated.

3.2 Select technique for DoA estimation

In Section 3.1, we have shown that the phase shift of the l-th signal, which is composed of the elevation and azimuth to be estimated, with a set of two subarrays. Thus two sets, each of which has two subarrays, give two equations. The elevation and azimuth can be estimated by solving the two equations. However, as we stated in Section 1, due to the

estimate error dependency on the related subarrays and non-simultaneous estimate precision for elevation and azimuth, we require multiple combinations of two-set to improve the estimate performance. Fortunately, there exist three combinations of the two-set, each of which has two subarrays in the array.

In this section, for the *l*-th pilot, we obtain the DoA candidates (3 pairs) by each combination of set-of-subarray from their phase shifts (see previous section), and select the DoA among the rearrangement pairs of elevation and azimuth from the above candidates.

We have observed that $\hat{\Theta}_l^k$ is composed of two variables $\hat{\theta}_l$ and $\hat{\varphi}_l$. To estimate the DoA of the *l*-th signal, including the elevation angle θ_i and azimuth angle φ_i, we need to select the two equations of (5) (*e.g.*, *k* =1 & 2). This implies that we select the two sets-of-subarrays. Then we obtain the estimated DoAs $(\hat{\theta}_l^{(1)}, \hat{\varphi}_l^{(1)})$ from $\hat{\Theta}_l^k \ (k=1\&2)$.

$$\hat{\phi}_l^{(1)} = \arctan\left(\frac{v_l^2 \cos\psi^1 - v_l^1 \cos\psi^2}{v_l^1 \sin\psi^2 - v_l^2 \sin\psi^1}\right), \qquad \hat{\theta}_l^{(1)} = \arcsin\left(\frac{v_l^1}{\cos(\hat{\varphi}_l^{(1)} - \psi^1)}\right). \tag{6}$$

Here $v_l^k = \lambda\hat{\Theta}_l^k / 2\pi d$, and $\psi^1 = 0$, $\psi^2 = \pi/3$ are the translation directions of the subarrays (see Fig. 1), respectively. It is obvious that there exists only one DoA signal, associated with the pilot, in each output of subarray because of the subarray beamforimg. This avoids the pairing problem in 2D estimation [2] and successive selection among the candidates of multiple DoAs, as in [4].

We have stated that there are three combinations in the hexagonal array. Equations (6) are obtained from the combination 1 of set-of-subarray, i.e., the sets (1) & (2). Similarity, for the combination 2 (*k* = 2 & 3), and the combination 3 (*k* = 1 & 3), we can obtain the estimated DoAs $(\hat{\theta}_l^{(2)}, \hat{\varphi}_l^{(2)})$ and $(\hat{\theta}_l^{(3)}, \hat{\varphi}_l^{(3)})$, respectively.

We have stated that the estimate error of elevation (or azimuth) angle is depended on the relation of a practical value of DoA and the employed translational invariance subarray. This implies that the estimate errors of elevation (or azimuth) angle are different when we use different combination of two set-of-subarrays. Therefore, more precision 2-D estimation exists in the candidate set $\Omega_l = \{(\hat{\theta}_l^{(q_e)}, \hat{\varphi}_l^{(q_a)}) \ (q_e = 1,2,3; q_a = 1,2,3)\}$, which are the rearrangement of the estimated elevation angles and azimuth angles from the different combinations.

We now select the optimal DoA candidate from the candidate set (consisting of 3×3 pairs). For the *l*-th impinging wave of the pilot, we obtain its DoA estimate, $(\hat{\theta}_l^*, \hat{\varphi}_l^*)$, by performing the following maximization

$$(\hat{\zeta}_l, \hat{\eta}_l) = \underset{(\hat{\theta}_l^{(q_e)}, \hat{\varphi}_l^{(q_a)}) \in \Omega_l}{\operatorname{argmax}} S(\hat{\theta}_l^{(q_e)}, \hat{\varphi}_l^{(q_a)}) \tag{7}$$

where the selection function are

$$S(\hat{\theta}_l^{(q_e)}, \hat{\varphi}_l^{(q_a)}) = \frac{1}{\boldsymbol{a}^{\mathrm{H}}(\hat{\theta}_l^{(q_e)}, \hat{\varphi}_l^{(q_a)}) R_{xx}^{-1} \boldsymbol{a}(\hat{\theta}_l^{(q_e)}, \hat{\varphi}_l^{(q_a)})}. \tag{8}$$

It is well known that right term of (8) is the power spectrum of the array under the criterion of the directional constraint maximum power. The power spectrum exhibits peaks toward to the true signal DoA during other angle maximization. Note that no peak search is carried in our proposed method. The calculation is only carried out at 3×3 points of the function (8) for each pilot signal. This procedure is repeated for all the *L* DoAs.

4. Simulation

In this section, we employ our proposed method to the 2D-DoA estimation with 7-element hexagonal array. In simulation, there are *L* known pilot signals and *J* unknown interference signals in BPSK modulation. The number of sources is $N_s = L + J$. The estimation performance is evaluated by root mean square error (RMSE) obtained from N_t independent trials. The RMSE for DoA estimation is defined as $\mathrm{RMSE} = (1/L)\sum_{l=1}^{L}(\mathrm{RMSE}(\theta_l) + \mathrm{RMSE}(\varphi_l))$,

where $\mathrm{RMSE}(\theta_l) = \left[\frac{1}{N_t}\sum_{n=1}^{N_t}(\theta_l - \hat{\theta}_l(n))^2\right]^{\frac{1}{2}}$, $\mathrm{RMSE}(\varphi_l) = \left[\frac{1}{N_t}\sum_{n=1}^{N_t}(\varphi_l - \hat{\varphi}_l(n))^2\right]^{\frac{1}{2}}$.

For comparison, we also employ the conventional 2D subarray beamforming (SB) method with a single combination of set-of-subarray (i.e., without select technique).

Let's first consider the case of a single signal (*L*=1 and *J*=0) with the elevation angle at 45° and the azimuth angle varying from 0° to 360° with 1° increment. Signal-to-noise ratio (SNR) was taken to be 20 dB. The number of snapshots is N_L=100. Figures 2 and 3 show RMSEs of elevation and azimuth angles under N_t=10000 trials runs with the proposed method and the conventional SB method, respectively. For the conventional SB method with the single combination of set-of-subarrays, we see that the error curves of elevation (or azimuth) with different combinations are different. The estimate error of elevation (or azimuth) angle depends on the relation of a practical value of DoA and the employed translational invariance subarray. Furthermore, we find that it is difficult to get simultaneously a good estimation for both elevation and azimuth if a single combination is employed. For example, for an elevation of 45° with an azimuth over 30° to 60°, the error of elevation is the lowest with the combination of sets (1) & (2) (see Fig. 2), while the error of azimuth is not the lowest with the same combination (see Fig. 3).

For the proposed method, we observe that the RMSE curve is a selected result of the minimum errors among those of SB method with three combinations of set-of-subarray. For example, in Fig. 2 the curve of elevation error over the azimuths 30° to 60° in our proposed method is the corresponding part of SB method with the combination of sets (1) & (2), which is the lowest error among the three combinations. Meanwhile, in Fig. 3 the curve of azimuth error over the same range (i.e., the azimuths 30° to 60°) is also the lowest but corresponding to the combination of sets (2) & (3). Our proposed method can obtain simultaneously good estimation both in elevation and azimuth by using multiple combinations of set-of-subarray and selecting a best one among its DoA candidates.

Next, we show that the estimation capacity of our proposed method can be larger than the number of subarray elements. In the simulation, without lose of generality, the number of pilot signal is set to L=1. The number N_s of signal sources, including the pilot signal, varies from 1 to 10. The azimuth of the target signal with pilot and the azimuths of unknown signals from other sources were randomly distributed from 0° to 360° in each simulation run. The elevations of all the signals are fixed to 45°. The snapshot lengths were set to N_L=100 and 500, respectively. Figure 4 illustrates that the RMSEs of the estimated pilot DoA averaged over 100000 runs versus the number N_s of signal sources. We observe that our proposed method can estimate the DoA of pilot, even if the number N_s of signals is larger than the number 4 of subarray elements (see Fig. 4). In particular, using snapshot length such as 500, the proposed method with select technique leads to an RMSE of less than 3° in the presence of 10 signals.

5. Conclusion

We have proposed 2D-DoA estimation with select technique and pilot signals in 7-element hexagonal array. Pilot signal helps subarray reject all the interference signals. Thus we can obtain a phase shift between subarrays for one desired signal. The select technique, thanks to multiple subarrays, suppresses the estimate error of dependence on related subarrays. The simulations have shown that the proposed method gives high estimate accuracy, and the estimation capacity is larger than the number of subarray elements.

References

[1] R. Roy and T. Kailath, "ESPRIT – Estimation of signal parameters via rotational invariance techniques,'' *IEEE Trans. Acoust., Speech, Signal Process.*, vol. 37, no. 7, pp. 984-995, July 1989.

[2] T. Kuroda, N. Kikuma, and N. Inagaki, "DoA estimation and pairing method in 2D-ESPRIT using triangular antenna array,'' *IEICE Trans. Commun.*, Part 1, vol. 86, No. 6, pp. 59-68, Aug. 2003. (in Japanese)

[3] N. Wang, P. Agathoklis, and A. Antoniou, "A new DoA estimation technique based on subarray beamforming," *IEEE Trans. Signal Process.*, vol. 54, no. 9, pp. 3279-3290, Sep. 2006.

[4] E. Taillefer, J. Cheng, and Y. Watanabe, "Full azimuth direction-of-arrival estimation with successive-selection technique," *IEEE Trans. Signal Process.*, vol. 56, no. 12, pp. 5903-5913, Dec. 2008.

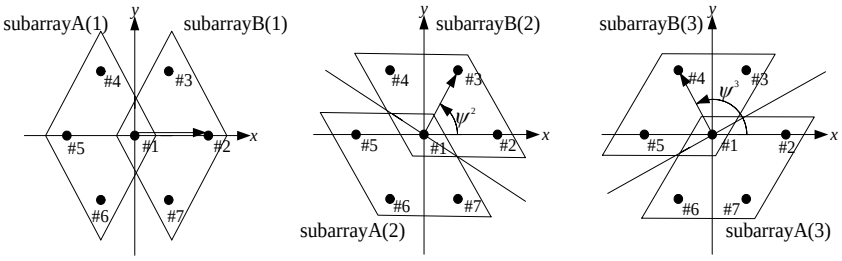

(a) set (1) ($\psi^1 = 0°$) (b) set (2) ($\psi^2 = 60°$) (c) set (3) ($\psi^3 = 120°$)

Fig. 1: Three sets of two-subarray with translational invariance in 7-element hexagonal array.

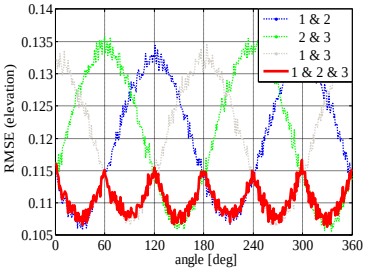

Fig. 2: RMSEs of elevation with proposed algorithm (with sets (1), (2) and (3)), and the conventional SB with a) sets (1)&(2), b) sets (2) &(3), and c) sets (1)&(3).

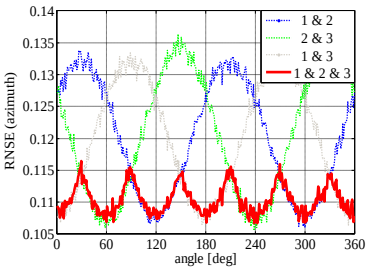

Fig. 3: RMSEs of azimuth with proposed algorithm (with sets (1), (2) and (3)), and the conventional SB with a) sets (1)&(2), b) sets (2) &(3), and c) sets (1)&(3).

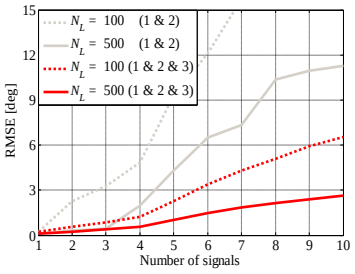

Fig. 4: RMSEs of DOA with proposed algorithm (with sets (1), (2) and (3)), and the conventional SB with sets (1)&(2).

Influence of Amplitude Fluctuations on Nonlinear Estimation of Wave Front

Viacheslav A. Potapov

Radiotechnical Institute by Academician A.L.Mints, 10, bld.1, ul. 8 Marta, 127083, Moscow, Russia,
Email: aletam@mail.ru

Keywords: nonlinear estimation; Markov process; random field.

Abstract: Inclusion of amplitude fluctuations estimation in the procedure of signal processing can improve estimation of phase of a signal, whose wave front was distorted during propagation through a random medium. On the basis of Markovian methods of the nonlinear filtration theory, conditions are formulated under which the joint processing of amplitude and phase may be appropriate.

1. Introduction

The problem of random field estimation is important in many modern applications in communication, optics, etc. Often amplitude of wave front is considered as uniform over the aperture or is estimated irrespective of a phase. However, amplitude and phase fluctuations may be correlated if signal was distorted during propagation through a random medium. In this case due to joint processing of amplitude and phase of the received signal it is possible to improve estimation of phase distortions. On the other hand, joint processing inevitably leads to the complicated receiver. In the present work, on the basis of Markovian methods of the nonlinear filtration theory we study conditions under which a joint processing of amplitude and phase may be desirable.

2. Algorithm of Nonlinear Estimation

Let us suppose that it is necessary to estimate phase distortions of wave front accepted on the plane antenna with aperture D in the presence of white noise

$$y(t,\mathbf{r}) = A_0 e^{\eta(t,\mathbf{r})} \cos(\omega t + \phi(t,\mathbf{r})) + n(t,\mathbf{r}),$$

where $n(t,\mathbf{r})$ – spatially distributed Gaussian white noise having constant power spectral density N

$$< n(t_1,\mathbf{r}_1) n(t_2,\mathbf{r}_2) > = N \delta(\mathbf{r}_1 - \mathbf{r}_2) \delta(t_1 - t_2).$$

Assuming that the distortions of wave front are caused by isotropic random medium, we use the stochastic differential equations to describe fluctuations of phase and log-amplitude

$$\frac{d\phi(t,\mathbf{r})}{dt} = -\gamma \phi(t,\mathbf{r}) + \chi_1(t,\mathbf{r}),$$

$$\frac{d\eta(t,\mathbf{r})}{dt} = -\gamma \eta(t,\mathbf{r}) + \chi_2(t,\mathbf{r}),$$

where $1/\gamma$ determines the time scale of instability of the medium and

$$\overline{\chi_1(t_1,\mathbf{r}_1)\chi_1(t_2,\mathbf{r}_2)} = 2\gamma \psi_1(\mathbf{r}_1 - \mathbf{r}_2) \delta(t_1 - t_2),$$

$$\overline{\chi_2(t_1,\mathbf{r}_1)\chi_2(t_2,\mathbf{r}_2)} = 2\gamma\psi_2(\mathbf{r}_1-\mathbf{r}_2)\delta(t_1-t_2),$$

$$\overline{\chi_1(t_1,\mathbf{r}_1)\chi_2(t_2,\mathbf{r}_2)} = \overline{\chi_2(t_1,\mathbf{r}_1)\chi_1(t_2,\mathbf{r}_2)} = 2\gamma\psi_3(\mathbf{r}_1-\mathbf{r}_2)\delta(t_1-t_2).$$

Let us also suppose that Rytov method is applicable to describe the wave front scattering in random medium. Then we can express two-dimensional Fourier transforms $\tilde{\psi}_i(q)$ through spatial spectral density of permittivity fluctuations $\Phi_\varepsilon(q,0)$ [1]

$$\tilde{\psi}_1(q) = \frac{\pi k^2 z}{4}\left(1+\frac{k}{zq^2}\sin\left(\frac{zq^2}{k}\right)\right)\Phi_\varepsilon(q,0),$$

$$\tilde{\psi}_2(q) = \frac{\pi k^2 z}{4}\left(1-\frac{k}{zq^2}\sin\left(\frac{zq^2}{k}\right)\right)\Phi_\varepsilon(q,0),$$

$$\tilde{\psi}_3(q) = \frac{\pi k^3}{2q^2}\left(\sin^2\left(\frac{zq^2}{2k}\right)\right)\Phi_\varepsilon(q,0),$$

where $k = 2\pi/\lambda$, λ is the wavelength, z is the wave front path length.

Using the Gaussian approximation of the generalized Stratonovich equation for posterior conditional density functional [2], we obtain the equations of a nonlinear stationary filtration for estimations of amplitude and phase fluctuations $\hat{\eta}(t,\mathbf{r})$, $\hat{\phi}(t,\mathbf{r})$ and second-order conditional cumulants K_{ij}

$$\frac{d\hat{\eta}(t,\mathbf{r})}{dt} = -\gamma\hat{\eta}(t,\mathbf{r}) +$$
$$+\frac{A_0}{N}\int_D d\boldsymbol{\rho}\, e^{\hat{\eta}(t,\boldsymbol{\rho})}\,(K_{\eta\eta}(\boldsymbol{\rho},\mathbf{r})\,y(t,\boldsymbol{\rho})\cos(\omega t+\hat{\phi}(t,\boldsymbol{\rho})) - K_{\phi\eta}(\boldsymbol{\rho},\mathbf{r})\,y(t,\boldsymbol{\rho})\sin(\omega t+\hat{\phi}(t,\boldsymbol{\rho})) - \frac{A_0}{2}K_{\eta\eta}(\boldsymbol{\rho},\mathbf{r})e^{\hat{\eta}(t,\boldsymbol{\rho})}),$$

$$\frac{d\hat{\phi}(t,\mathbf{r})}{dt} = -\gamma\hat{\phi}(t,\mathbf{r}) +$$
$$+\frac{A_0}{N}\int_D d\boldsymbol{\rho}\, e^{\hat{\eta}(t,\boldsymbol{\rho})}(K_{\phi\eta}(\boldsymbol{\rho},\mathbf{r})\,y(t,\boldsymbol{\rho})\cos(\omega t+\hat{\phi}(t,\boldsymbol{\rho})) - K_{\phi\phi}(\boldsymbol{\rho},\mathbf{r})\,y(t,\boldsymbol{\rho})\sin(\omega t+\hat{\phi}(t,\boldsymbol{\rho})) - \frac{A_0}{2}K_{\phi\eta}(\boldsymbol{\rho},\mathbf{r})\,e^{\hat{\eta}(t,\boldsymbol{\rho})}),$$

$$2\gamma\psi_1(\mathbf{r}_1-\mathbf{r}_2) - 2\gamma K_{\phi\phi}(\mathbf{r}_1,\mathbf{r}_2) = \mu\int_D d\boldsymbol{\rho}\, e^{2\hat{\eta}(t,\boldsymbol{\rho})}(K_{\phi\eta}(\mathbf{r}_1,\boldsymbol{\rho})K_{\phi\eta}(\boldsymbol{\rho},\mathbf{r}_2) + K_{\phi\phi}(\mathbf{r}_1,\boldsymbol{\rho})K_{\phi\phi}(\boldsymbol{\rho},\mathbf{r}_2)),$$

$$2\gamma\psi_2(\mathbf{r}_1-\mathbf{r}_2) - 2\gamma K_{\eta\eta}(\mathbf{r}_1,\mathbf{r}_2) = \mu\int_D d\boldsymbol{\rho}\, e^{2\hat{\eta}(t,\boldsymbol{\rho})}(K_{\phi\eta}(\mathbf{r}_1,\boldsymbol{\rho})K_{\phi\eta}(\boldsymbol{\rho},\mathbf{r}_2) + K_{\eta\eta}(\mathbf{r}_1,\boldsymbol{\rho})K_{\eta\eta}(\boldsymbol{\rho},\mathbf{r}_2)),$$

$$2\gamma\psi_3(\mathbf{r}_1-\mathbf{r}_2) - 2\gamma K_{\phi\eta}(\mathbf{r}_1,\mathbf{r}_2) = \mu\int_D d\boldsymbol{\rho}\, e^{2\hat{\eta}(t,\boldsymbol{\rho})}(K_{\phi\phi}(\mathbf{r}_1,\boldsymbol{\rho})K_{\phi\eta}(\boldsymbol{\rho},\mathbf{r}_2) + K_{\phi\eta}(\mathbf{r}_1,\boldsymbol{\rho})K_{\eta\eta}(\boldsymbol{\rho},\mathbf{r}_2)),$$

where $\mu = A_0^2/N$ is a signal-to-noise ratio. K_{ij} describe the posterior spatial correlation of the wave front fluctuations. Under assumption that D is large in comparison with correlation region of the wave front fluctuations, the equations for K_{ij} may be solved easily by means of Fourier transform. If we neglect the

fluctuations of amplitude ($K_{\eta\square} = K_{\eta\eta} = 0$), the equations of nonlinear filtration transform into the equations for nonlinear estimation of phase fluctuations only considered in detail in [2].

3. Influence of Amplitude Fluctuations on Estimation of Phase

If $\Phi_\varepsilon(q,0)$ has no singularity, we may define posterior diffraction parameter as $d_{as} = 4\pi z/kS_{as}$, where

$$S_{as} = \frac{2\pi\tilde{K}_{\phi\phi}(0)}{\int_0^\infty \tilde{K}_{\phi\phi}(q)qdq},$$

$\tilde{K}_{ij}$ are two-dimensional Fourier transforms of K_{ij}. Here S_{as} describes the area of a part of the plane antenna from which it is necessary to collect the signal to estimate the phase in each element of the antenna array. If the distance between elements of the antenna array exceeds the characteristic scale $\sqrt{S_{as}}$, we shall consider phase distortions of a signal as spatially not correlated even if the characteristic scale of their spatial correlations initially exceeds this value a priori. If the signal-to-noise ratio μ is small, then S_{as} differs from prior area of correlation region of phase distortions S a little. But for very special case of uniform spatial spectrum of fluctuations $\Phi_\varepsilon(q,0)$ ($\Phi_\varepsilon(q,0)$ is uniform when $q < q_m$ and is equal zero when $q > q_m$), S_{as} is equal S for any μ.

We should consider three cases depending on value of "prior" diffraction parameter $d = 4\pi z/kl^2$ (l is a characteristic scale of spatial correlation of permittivity fluctuations of random medium): geometric optical region ($0 < d << 1$), Fresnel diffraction zone ($d \sim 1$), Fraunhover diffraction zone ($d >> 1$). If $d \to \infty$ or $d \to 0$, cross correlation of amplitude and phase fluctuations is small a priori [1], in particular

$$\frac{\tilde{\psi}_3(q)}{\tilde{\psi}_1(q)} = \frac{2k}{zq^2}\sin^2\left(\frac{zq^2}{2k}\right) \xrightarrow[d\to\infty]{} 0.$$

A priori cross correlation has an appreciable value in Fresnel diffraction zone only. However, a posteriori the contribution of cross correlation of amplitude and phase may be changed.

If we estimate the wave front in Fraunhover diffraction zone, then

$$\tilde{K}_{\eta\eta}(q) \approx \tilde{K}_{\phi\phi}(q) \approx \frac{\gamma}{\mu}\left(\sqrt{\Phi_\varepsilon(q,0)\frac{\pi z k^2}{2\gamma}\mu + 1} - 1\right), \qquad \frac{\tilde{K}_{\phi\eta}(0)}{\tilde{K}_{\phi\phi}(0)} \geq \frac{\pi}{d_{as}}.$$

If the major contribution to the spectrum $\Phi_\varepsilon(q,0)$ brings low-frequency components, then S_{as} is less than S and the role of posterior cross correlation of amplitude and phase decreases. If random medium has some regular structure and high-frequency components in $\Phi_\varepsilon(q,0)$ are sufficient, then in Fraunhover diffraction zone the estimation of amplitude fluctuations may be important for the estimation of phase fluctuations.

In case of geometrical optic region the diffraction parameter d accepts values close to 0 and amplitude distortions of wave front are small a priori

$$\tilde{K}_{\phi\phi}(q) \approx \frac{\gamma}{\mu}\left(\sqrt{\Phi_\varepsilon(q,0)\frac{\pi z k^2}{\gamma}\mu + 1} - 1\right), \quad \frac{\tilde{K}_{\phi\eta}(0)}{\tilde{K}_{\phi\phi}(q)} \geq d_{as}, \quad \frac{\tilde{\psi}_3(q)}{\tilde{\psi}_1(q)} \sim d.$$

But in geometrical optic region the contribution of amplitude fluctuations may be sufficient a posteriori when the major contribution to spectral density of fluctuations of permittivity fluctuations $\Phi_\varepsilon(q,0)$ brings low-frequency components.

Now we may formulate a condition under which joint processing of amplitude and phase of wave front is appropriate: a posteriori diffraction parameter d_{as} should have value that corresponds to prior diffraction parameter for Fresnel diffraction zone.

$$d_1 > d_{as} > d_2,$$

where d_i are some threshold values ~ 1.

An example of $\Phi_\varepsilon(q,0) = \sigma_\varepsilon^2 \exp(-q^2 l^2/2)$ is illustrated in Fig.1. The solid line corresponds the prior normalized correlation $\psi_3(0)/\psi_1(0)$, the dashes line describes the posterior correlation as $K_{\phi_1}(0)/K_{\phi\phi}(0)$.

In the case of a turbulent medium, we can't define the diffraction parameter in general. To study nonlinear filtration equation we may use the numerical methods. In Fig.2 we show the normalized prior and posterior correlations depending on μ for the case of Karman spectrum $\Phi_\varepsilon(q,0) = a\,(q^2 + q_0^2)^{-11/6}$. Fig.2 demonstrates that the posterior correlation may be sufficient even if the prior correlation is small. For small μ the posterior and prior correlation are almost the same.

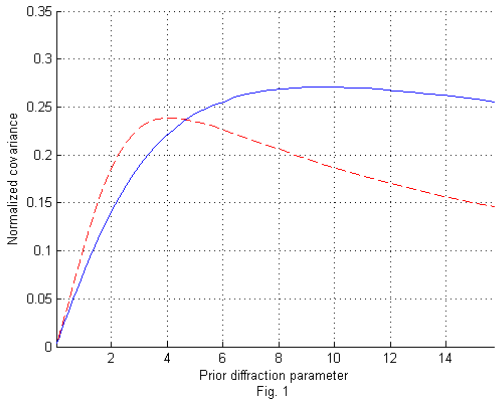

Fig. 1

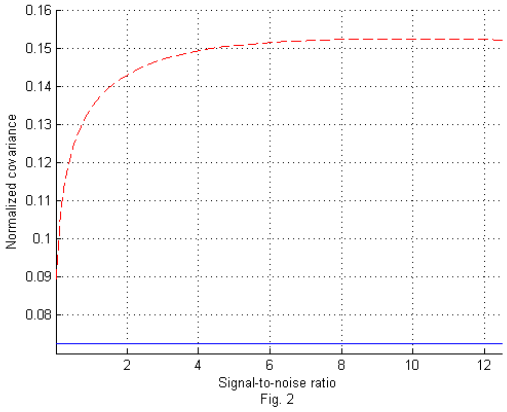

Fig. 2

I thank Dr. Shmelev for fruitful discussion.

References

[1.] A. Ishimaru, *Wave Propagation and Scattering in Random Media,* vol.2, Academic Press, 1978.

[2.] A.B. Shmelev, "Markovian approach and digital technique of random field's phase fluctuations estimation", in *Proc. International Symposium on Radio Systems and Space Plasma, Sofia, Bulgaria, September 2-5,* pp.67-70, 2007.

Single-RF diversity for OFDM system using ESPAR antenna with periodically changing directivity

Satoshi Tsukamoto, Tomoya Kozu, Minoru Okada

Graduate School of Information Science, Nara Institute of Science and Technology
8916-5 Takayama, Ikoma-shi, Nara, 630-0192 Japan.
satoshi-t@is.naist.jp

Keywords: OFDM, ESPAR antenna, diversity, frequency selective fading.

Abstract: This paper presents a single-RF diversity scheme for orthogonal frequency division multiplexing (OFDM) receiver using Electronically Steerable Passive Array Radiator (ESPAR) antenna with periodically changing directivity at the OFDM symbol rate. OFDM is widely used for mobile communication systems because of its broadband digital wireless transmission capability in a severe time dispersive multipath propagation channel. OFDM is, however, is not efficient for mitigating the performance degradation due to fading. Diversity is a well-known efficient technique for solving this problem. Although maximal ratio combining diversity is the most efficient technique for compensating for the degradation, it requires the same number of RF and baseband signal processing circuitry. ESPAR antenna based diversity requires only a Single-RF and baseband components, however, the convergence is not fast enough to track the fast variation of the channel state. Furthermore, it is not efficient in a frequency selective channel. In this paper, we propose a new OFDM diversity scheme using ESPAR antenna with periodically changing directivity. The proposed scheme is capable of obtaining the diversity gain in a frequency selective fading environment and it solves the slow convergence rate problem in the conventional ESPAR antenna based diversity scheme. Computer simulation result shows that the proposed scheme gives diversity gain in a frequency selective fading channel, and also works well on fast fading environment.

1. Introduction

Orthogonal frequency division multiplexing (OFDM) is a widely used transmission technique for establishing broadband wireless communication systems because of its broadband digital wireless transmission capability in a severe time-dispersive multipath propagation channel. OFDM is, however, not efficient for mitigating the bit error rate performance degradation due to fading.

Space diversity is an efficient technique to solve the performance degradation. Among them, maximal ratio combining diversity is known to be the optimum in terms of maximizing the signal-to-noise power ratio (SNR) after combining. However, it requires huge hardware complexity. The maximal ratio combining diversity receiver requires the same number of radio frequency (RF) circuits, analog digital converters and multiple discrete Fourier transform (DFT) blocks as of diversity branches.

Electronically Steerable Passive Array Radiator (ESPAR) antenna [1] based diversity is one of the solutions to reduce the size of circuit. However, the convergence is not fast enough to track the fast variation of the channel state. Furthermore, the conventional ESPAR antenna based diversity scheme is not efficient in a frequency selective channel.

In order to solve the problems, we propose a new diversity scheme based on ESPAR antenna, whose beam direction is changing at the same frequency as the OFDM symbol rate. This fast directivity variation causes an interference amongst adjacent subcarriers or ICI (inter-channel interference). The frequency domain equalizer followed by the DFT processor is not only capable of suppressing this ICI, but also gives implicit space diversity effect even in the frequency selective fading environment. On the last report [2], we have carried out

the computer simulation using the simplified ESPAR antenna and channel model. This report, we employ the practical simulation model for computer simulation analysis. The simulation result shows that the proposed scheme gives the diversity gain in a frequency selective fading channel.

2. ESPAR Antenna

ESPAR antenna is a kind of reactively controlled antenna which has single RF port. Fig. 1 shows typical configuration of ESPAR antenna. In this case, the antenna consists of seven quarter-wavelength monopole antennas. The center element, or radiator, is connected to the RF input of a receiver. The other six elements surrounded by the center element, namely, parasitic elements, are terminated with variable capacitance diodes (Varicap). Radiation patterns can be controlled by changing the capacitance of the Varicaps.

As an application of ESPAR antenna, the direction of arrival (DoA) estimators have been proposed in conjunction with the multiple signal classification (MUSIC) or the estimation of signal parameters via rotational invariance techniques (ESPRIT) algorithm. [3] and [4]. The diversity receiver based on ESPAR antenna is also proposed. However, the conventional ESPAR antenna based diversity receiver has problems in frequency selective fading and convergence rate.

3. Configuration of the proposed ESPAR antenna based diversity receiver

Fig. 2 shows the block diagram of the proposed diversity receiver. In this paper, we assume a two-element ESPAR antenna. The radiator element is connected to an input of the receiver while the Varicap which terminates the parasitic element, is controlled by the oscillator. The frequency of the oscillator is the same as the OFDM symbol rate. In case of widely used IEEE802.11a/g wireless LAN, the frequency is 325 kHz.

This receiver is composed of RF front-end, analog-to-digital converter (ADC) and baseband digital signal processing unit. The received signal from the radiator element of ESPAR antenna is applied to RF front-end followed by ADC to obtain the received signal in the equivalent low-pass expression. The output of ADC is first applied to FFT (fast Fourier transform) processor to decompose the received OFDM signal to sub-carrier components.

Since the FFT output suffers from ICI due to fast directivity variation of ESPAR antenna, suppression of ICI is required. ICI suppression is divided into two stages, that is, a channel response estimation stage and a frequency domain equalization stage.

The channel response is estimated using a pilot symbol which is transmitted prior to the data symbols. Let us suppose that a pilot symbol is transmitted before the data symbols are transmitted. The pilot symbol vector **p** is defined as $\mathbf{p} = [p_0, p_1, \cdots, p_{N-1}]^T$, where p_k is pilot symbol of k-th subcarrier; N is a number of subcarriers. The transmitted pilot symbol **v** is then propagated through the multipath fading channel.

The received signal after FFT is given by

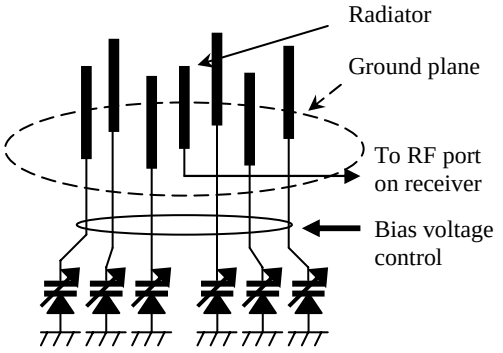

Fig.1. Conventional seven elements ESPAR antenna.

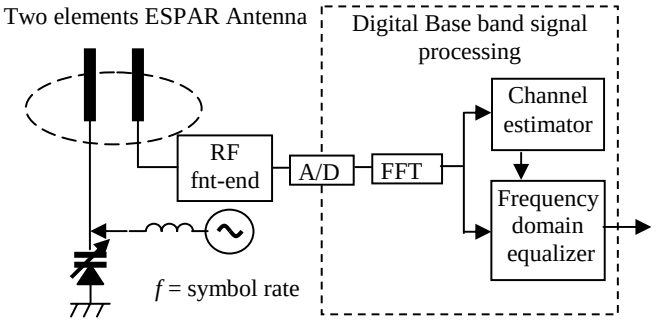

Fig.2. Proposed system block diagram.

$$\mathbf{u} = (\mathbf{G}_{-1}\mathbf{H}_{-1} + \mathbf{H}_0 + \mathbf{G}_1\mathbf{H}_1)\mathbf{p} + \mathbf{z}, \tag{1}$$

where $\mathbf{H}_i = \mathrm{diag}(\mathbf{h}_i)$ is a diagonal matrix, whose diagonal elements represents the frequency response corresponding to the *i*-th element, and $\mathbf{z}$ is the thermal noise component in frequency domain. $\mathbf{G}_i = \left[g_{kl}^{(i)}\right]$ are the negative (i=–1) and positive (i = 1) frequency shift matrices where

$$g_{kl}^{(i)} = \begin{cases} 1 & (k+i=l) \\ 0 & (\text{otherwise}) \end{cases} \tag{2}$$

We can rewrite Eq. (1) as

$$\mathbf{u} = \mathbf{G}_{-1}\mathbf{P}\mathbf{h}_{-1} + \mathbf{P}\mathbf{h}_0 + \mathbf{G}_1\mathbf{P}\mathbf{h}_1 + \mathbf{z}, \tag{3}$$

where $\mathbf{P} = \mathrm{diag}(\mathbf{p})$ is the diagonal matrix expression of the pilot symbol. The minimum mean square error (MMSE) estimate of $\mathbf{h}_i$ is then given by

$$\tilde{\mathbf{h}}_i = \left(\mathbf{R}^{-1}\mathbf{B}_i\right)^H \mathbf{u}\ , \tag{4}$$

where

$$\mathbf{R} = E\left[\mathbf{u}\mathbf{u}^H\right] = \mathbf{G}_{-1}\mathbf{P}\mathbf{R}_h\mathbf{P}\mathbf{G}_{-1} + \mathbf{P}\mathbf{R}_h\mathbf{P} + \mathbf{G}_1\mathbf{P}\mathbf{R}_h\mathbf{P}\mathbf{G}_1 + \sigma_z^2\mathbf{I} \tag{5}$$

is the covariance matrix for the frequency domain received signal and

$$\mathbf{B}_i = E\left[\mathbf{u}\mathbf{h}_i^H\right] = \mathbf{G}_i\mathbf{P}\mathbf{R}_h \tag{6}$$

is the cross correlation matrix between the received signal and the *i*-th channel response vectors, where $\mathbf{R}_h = E\left[\mathbf{h}_i\mathbf{h}_i^H\right]$ is the covariance matrix for channel response vector. $\mathbf{R}_h$ corresponds to the delay profile of the channel.

After channel estimation was carried out using Eq. (4), the frequency domain equalization is performed. The received data symbol in frequency domain is given by

$$\mathbf{u} = (\mathbf{G}_{-1}\mathbf{H}_{-1} + \mathbf{H}_0 + \mathbf{G}_1\mathbf{H}_1)\mathbf{d} + \mathbf{z} = \mathbf{H}\mathbf{d} + \mathbf{z}\ , \tag{7}$$

where $\mathbf{d} = \left[d_0, d_1, \cdots, d_{N-1}\right]^T$ is the data vector. Let us employ an MMSE equalizer. The data vector can be estimated by the following equation:

$$\tilde{\mathbf{d}} = (\mathbf{R}_d^{-1}\tilde{\mathbf{H}})^H \mathbf{u}\ , \tag{8}$$

where $\tilde{\mathbf{H}} = \mathbf{G}_{-1}\tilde{\mathbf{H}}_{-1} + \tilde{\mathbf{H}}_0 + \mathbf{G}_1\tilde{\mathbf{H}}_1$ is the estimated channel response matrix where $\tilde{\mathbf{H}}_i = \mathrm{diag}(\tilde{\mathbf{h}}_i)$ and $\mathbf{R}_d = \tilde{\mathbf{H}}\tilde{\mathbf{H}}^H + \sigma_z^2\mathbf{I}$ is the estimated covariance matrix.

The other type of frequency domain equalizer such as zero forcing and maximum likelihood sequence estimation equalizers can be used for the receiver. In the following we have analyzed the bit error rate performance using the MMSE equalizer depicted in Eq. (8).

3. Computer Simulation

The system configuration in order to run the simulation is shown in Table 1. In the simulation, we did not apply forward error correction coding. Fig. 3 shows the bit error rate (BER) performance of the proposed diversity scheme in a two-ray Rayleigh fading environment. The dashed and solid lines show BER of the proposed scheme with perfect and MMSE channel estimation, respectively. The bold line shows theoretical BER in a Rayleigh fading channel[5]. The proposed diversity receiver effectively gives the diversity gain in a frequency selective two-ray Rayleigh fading channel.

Table 1. Simulation settings.

Modulation type of subcarriers	QPSK
Number of subcarriers	48
Guard interval ratio	1/8 symbol
Path model	Two rays Rayleigh fading
Power of rays	Identical
Doppler	Static during symbol period
Noise type	AWGN
Synchronization of symbols	Perfect
Trial sequence	20000 times

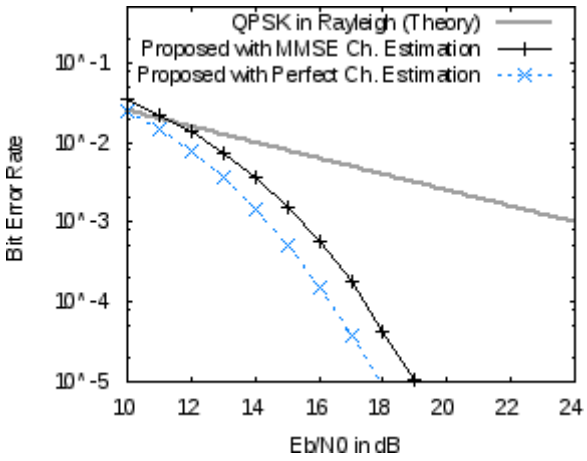

Fig. 3. Bit error rate in Reyleigh fading channel.

4. Conclusions

This paper presented a single-RF diversity scheme for OFDM receiver using ESPAR antenna whose direction changes in the symbol time period. Difference between Conventional ESPAR antenna diversity and proposed one was described. Then a principle of proposed diversity receiver was explained. Finally, computer simulation results were shown for performance verification of the proposed scheme. It is confirmed that the proposed scheme gives diversity gain in a frequency selective fading channel, and also works well on fast fading environment.

Acknowledgment

The authors would like to thank Dr.Masazumi Ueba of ATR Wave Engineering Laboratories for his encouragement in this work. This study was supported by Industrial Technology Research Grant Program in 2010 from New Energy and Industrial Technology Department Organization (NEDO) of Japan.

References

[1.] K.Gyoda and T.Ohira, “Design of electronically steerable passive array radiator (ESPAR) antennas,” *Proc. Antennas and Propagation Society International Symposium, Salt Lake City, UT, USA*, vol. 2, pp.922-925, July 2000.

[2.] S.Tsukamoto and M.Okada, “Single-RF maximal ratio combining diversity for OFDM system using an ESPAR antenna whose direction is oscillated in the symbol time,” *Proc. of Thailand-Japan Microwave forum 2009, Bangkok, Thai*, FR7-2, August 2009.

[3.] C. Plapous, Jun Cheng, E. Taillefer, A. Hirata and T. Ohira, “Reactance domain MUSIC algorithm for electronically steerable parasitic array radiator,” *IEEE Trans. Antennas and Propagation*, vol. 52, issue 12, pp. 3257-3264, Dec. 2004.

[4.] E. Taillefer, A. Hirata and T. Ohira, “Reactance-domain ESPRIT algorithm for a hexagonally shaped seven-element ESPAR antenna,” *IEEE Trans. Antennas and Propagation*, vol. 53, issue 11, pp.3486-3495, Nov. 2005.

[5.] J. G. Proakis, ”*Digital Communications - Fourth Edition*,” McGraw-Hill, Singapore, 2001.

Commission “G”

Transionospheric Propagation

Radio Wave Propagation in the Amazon Region – A Review

Mauro S. Assis

Fluminense Federal University, Rua Passo da Pátria 156, Niterói, Brazil
msassis@openlink.com.br

Keywords: Forest environment; radio wave attenuation; propagation mechanisms; lateral wave; search and rescue.

Abstract: This paper deals with radio wave propagation in a forest environment. Depending on the relative position of the radio stations, three propagation paths should be considered in the analysis of the problem: (a) Both equipments immersed in the jungle; (b) One radio equipment inside and the other on the ground outside the jungle; (c) A radio link between one equipment located in the forest and the other in a plane or helicopter. Comments on the application of these models to search and rescue, scientific and military missions in the jungle are also addressed.

1. Introduction

Radio wave attenuation due to vegetation is the major constraint to the path range of a communication system within a jungle. Based on measurements carried out in the Amazon region, different aspects of the problem are considered in this paper. It should be emphasized that the Amazon region is an environment particularly critical, once it is characterized by a hot and humid climate, covered by a dense rain forest and crossed by a large number of rivers. In spite of the difficulties associated to this scenario, it is of paramount importance the knowledge of mathematical models to be used in the assessment of the performance of radio sets operated in forests. In this context, the following items are discussed in this paper: (a) Both stations immersed in the jungle; (b) Both stations on the ground, where one is within and the other outside the jungle; c) A radio link between a ground station located within the forest and the other in an airplane or an helicopter (ground-to-air link). In case (a), for distances lesser than about 10 km, the lateral wave component of a plane conducting-slab [1] is the predominant propagation mechanism. In case (b) there is a discontinuity between the forest and the ground. Although the rigorous solution is quite complicated [2], it is shown that a simple mathematical approximation can be used in practical situations [3]. Finally, in case (c), a solution based on the geometrical optics seems to be sufficient to assess the maximum distance covered by the ground station [3].

The signal attenuation depends critically on the operating frequency and on the values of the electrical parameters of vegetation. The optimum frequency is chosen as the best compromise between low signal attenuation, an acceptable level of atmospheric noise and the physical dimension of a portable transceiver compatible with the mobility required for operation within the forest. According to these considerations, the HF band appears to be the best choice, the optimum frequency being around 10 MHz [4,5]. On the other hand, the electrical characteristics of vegetation were estimated through an experimental procedure which involves the comparison of direct measurement of field strength decay versus distance with numerical values derived from the theoretical model of the lateral wave. The best fit were achieved for $\varepsilon_f = 1.2$ and $\sigma_f = 0.2$ mS/m [6].

2. Lateral Wave

Radio wave propagation characteristics in a forest environment are usually predicted by the plane conducting slab model shown in Fig. 1[1]. At a first glance, the plane geometry seems to be a limitation to this model. However, as this paper deals with radio paths of a few kilometers, the effect of the earth curvature can be disregarded. Theoretically, there are three propagation mechanisms in the transmitting-receiving path depicted in Fig. 2: a) forest geometric-optical components (direct and reflected rays); (b) sky-wave component; (c) lateral wave component. For distances larger than 0.5 km the forest geometric-optical components are highly

attenuated. On the other hand, the sky-wave component can be neglected for distances lesser than about 10 km. Consequently, the lateral wave represents the predominant mechanism.

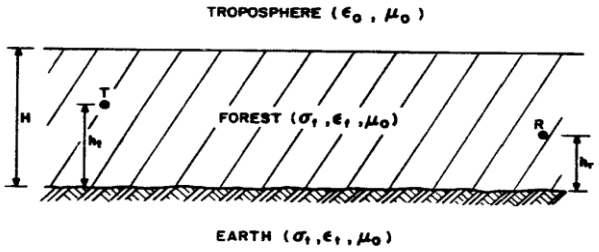

Fig. 1- Plane conducting slab model

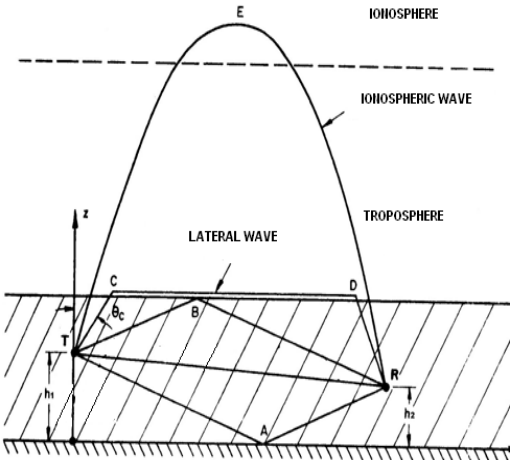

Fig. 2 – Propagation mechanisms

The lateral wave corresponds to the radiation emitted at the critical angle of total reflection given by,

$$\sin\theta_c = \frac{1}{n_f} \tag{1}$$

where $n_f = (\varepsilon_f - j60\ \sigma_f\ \lambda)^{1/2}$ is the index of refraction of the forest, λ is the wavelength and ε_f and σ_f are the relative permittivity and the conductivity of the forest, respectively. The lateral wave occurs when the energy propagates from a denser to a less dense medium. The ray associated to the lateral wave arises from the transmitter and travels along the boundary forest-air while lacking energy back into the forest in the direction of the angle θ_c. Part of this energy reaches the receiver point through the path DR shown in Fig. 1. It must be pointed out that theoretically the angle θ_c is defined for n_f real only. However, the above physical interpretation is still valid if Im $n_f << |n_f|$, where Im n_f means the imaginary part of n_f. In this case, the radio wave attenuation relative to free space is then given by [1],

$$A_f\,(dB) = -20\log\left|2F_A\,f(h_1)\,f(h_2)\right| \tag{2}$$

where $F_A = \frac{\lambda}{2\pi d}\frac{1}{n_f^2 - 1}$ – lateral wave function; $f(h_{1,2}) = \exp\left\{-\frac{2\pi}{\lambda}\,\mathrm{Im}\left[(n_f^2 - 1)^{1/2}(h_f - h_{1,2})\right]\right\}$;

d – distance between transmitter and receiver; h_f – forest height; and the other parameters are shown in Fig. 2.

3. One Terminal Inside and the Other outside the Jungle

The general solution to this problem is quite complicated [2], once there is a discontinuity between the forest and the ground. However, in a case of practical interest, one terminal is near the forest along a road or a river, while the other one is far from the transition forest-ground. In this situation, the attenuation introduced by the discontinuity can be approximated by,

$$20\log|F| = -20\log\left|\sqrt{2}\int_0^{\nu}\exp\left(-j\frac{\pi u^2}{2}\right)du\right| \tag{3}$$

The above integral is the well-known Fresnel integral which appears in the diffraction by a knife-edge, being $\nu = \sqrt{2}\,(h_f - h_2)/R$ the Fresnel parameter and *R* the first Fresnel radius at C (see Fig. 3). The total attenuation in the path AB is then [4],

$$A(dB) = -20\log\left|\frac{\lambda}{2\pi d}\frac{1}{n_f^2 - 1}\right| - 20\log\left|\exp\left\{-\frac{2\pi}{\lambda}\mathrm{Im}\left[(n_f^2 - 1)^{1/2}(h_f - h_1)\right]\right\}\right| - 20\log|F| \tag{4}$$

It is evident that each parcel of (4) corresponds to one of the sub-paths detached in Fig.3. The first parcel is the lateral wave along the forest top. The second represents the loss due to the penetration into the forest. Finally, the third one is the mathematical approximation to the effect of the discontinuity between the forest and the ground.

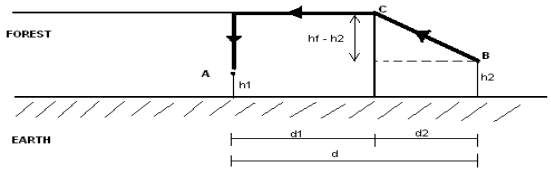

Fig. 3 – Simplified propagation model for the forest-earth discontinuity

4. Ground-to-Air Link

The problem here is to define the maximum distance covered by the radio equipment on the ground. The basic geometry for this case is illustrated in Fig.4. A rigorous analysis of this problem was developed by Brekhovskikh [7]. However, the observation of Fig. 4 allows to infer the following considerations:

a) ABC is the main propagation path;
b) Path AB encompasses the attenuation due to forest;
c) Free-space propagation in path BC;
d) Path AB << Path BC.

Based on the above points and neglecting the effect of earth reflection, a simplified solution based on the geometrical optics can be developed. The attenuation relative to free-space in the path ABC is then given by [3]

$$A(dB) = -20\log\left\{\exp\left[-\frac{2\pi\ell}{\lambda}\mathrm{Im}(n_f^2 - 1)^{1/2}\right]\right\} \tag{5}$$

where $\ell = \dfrac{h_f - h_1}{\cos\theta_C}$; $sen\,\theta_C = \dfrac{1}{\mathrm{Re}(n_f)}$ and $\mathrm{Re}(n_f)$ means the real part of n_f.

In using (5), for distances up to 10 km a fair agreement between theoretical calculations and experimental data was observed [3]. For distances larger than 10km there was evidence that the earth curvature must be taken into account.

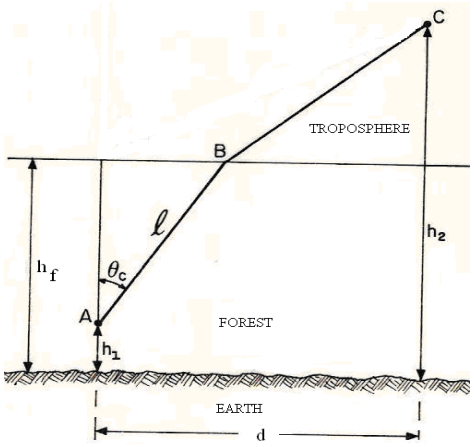

Fig. 4 – Ground-to-air propagation path

5. Final Remarks

Search and rescue is an important application of the mathematical models discussed in this paper [3]. The unknown radio equipment to be localized in the jungle must be capable to operate with a voice channel or emitting a help radio signal put in action by some automatic device. The position of this radio station can be settled by air with the aid of a searcher equipment mounted in a plane or helicopter, complemented by another equipment on the ground, inside the forest with a portable radio set or outside in a vehicle on a road or in a boat along a river. In this context, the option to be considered depends on the access available in the region where the mission is being carried out. Of course, the receiver of the searcher equipment must have a high sensitivity to detect very low radio signals.

For military and scientific missions the interest relays mainly on the case where the manpack radio sets used are immersed into the jungle. The coverage of the equipment should be adequate to guarantee the contact between all the persons engaged in the operation. Anyway, to be effective, radio links within the forest must be operated with a safety distance margin relative to the maximum range of the equipment.

References

[1] Tamir, T. "On radio-wave propagation in forest environment", *IEEE Trans. Antennas and Propagation*, Vol. AP-15, pp. 806-817, November 1967.
[2] Furutsu, K., "On the theory of radio wave propagation over inhomogeneous earth", *Journal of Research of the NBS*, vol. 67D, No 1, pp.39-62, January-February 1963.
[3] Assis, M. S., "Search and rescue in a forest environment", *IMOC 09*, pp. 249-252, Belém, Brazil, November 2009.
[4] Assis, M. S., "HF tactical communication in the Amazon region", *ICCS 90*, vol.2. pp. 1273-1277, Singapore, November 1990.
[5] Assis, M.S., M.H.C. Dias and J.C.A. Santos, "Ongoing research and development on antennas in Brazil", *EuCAP 2010*, Barcelona, Spain, April 2010.
[6] Assis, M.S. and R.C. Pinto Filho, "Measurements of the electrical characteristics of vegetation in a dense jungle", *EuCAP 2010*, Barcelona, Spain, April 2010.
[7] Brekhovskikh, L.M., *Waves in layered media*, Academic Press, New York, USA, 1960.

Low Latitude Earthquakes and Perturbation in the Atmosphere: a Study in Relation to Identifying Precursors and Epicenters Utilizing EM Techniques

Minakshi Devi and A.K. Barbara

Department of Physics, Gauhati University
Guwahati 781014, Assam, India
md555@sify.com

Keywords: TEC; Earthquake; VHF anomalous propagation; SODAR; Effective earth radius

Abstract: The paper addresses aspects involved in identifying precursors of an impending low latitude earthquake by using electromagnetic techniques. One of the methods discussed here is the use of VHF signals from GPS and geostationary satellites providing columnar or Total Electron Content (TEC) profiles. Here the focus is on application of TEC in extraction of features related to dynamical and physical processes induced in the atmosphere by an approaching earthquake and then in identification of epicentre position. For this purpose the phenomena of extension/suppression of radio horizon of the transmitter- receiver by earthquake modified tropospheric situation reflected in pre-earthquake TEC, are brought in to the discussion. The paper then presents methodology adopted for extraction of earthquake time low-latitude foF2 features from ground based and topside ionosonde. The role of 'Anomaly Effect' at low latitudes in identifying precursors of earthquake is highlighted. It also covers techniques for un-earthing pre-seismic characters in F-region electron density even when the density profile maintains a Quiet day (Q-day) pattern. The anomalous VHF propagation of audio and video signals received before an earthquake is introduced in relation to identification of an epicenter. Pre–earthquake seismic echo characters seen in Sodar echograms are also presented in the ambit of discussion.

1. Introduction

Electromagnetic methods be it for identifying pre -earthquake induced natural electromagnetic phenomena or for elucidating effects of an impending earthquake on near earth to deep in the ionosphereric environment are gaining importance of late [1-3]. In this paper earthquake induced effects at low latitude stations will be considered and the approaches for possible identification of epicenters only at such stations will be addressed to.

2. Techniques adopted: Analysis and results

2.1. Anomalous TEC features and forecasting of earthquake day

Our attempt here is to uncover association between earthquake and TEC obtained from GPS based observation taken at Gauhati University (GU, 26ºN, 92ºE) and also from Faraday Rotation (FR) data collected through satellite Radio Beacon (RB) signal. Because of the influence of solar-geomagnetic variabilities on the ionosphere, it is essential to obtain TEC variation with respect to Quiet day (TECq) as a reference, before

extracting earthquake induced effects on it .So maximum value of TEC mainly during noon hours ($TECq_{noon}$) is calculated at least five Q-days of a month and then standard deviation (Sd) of $TECq_{noon}$ along with its excursions are found out. Two basic earthquake situations dealt-with here are: i) Equatorial (magnetic inclination of the epicenter location is not more than ≈ ±5º) earthquakes**,** (M≥5) occurring within ±5° longitudinal zone from Guwahati, (ii) Low-latitude earthquakes, both strong (M≥5) and weak (4<M <5) with epicenters scattered about ±5° latitude and longitude (preferably) from observing station.

Fig.1a is a plot of day-to-day variations of the TEC_{noon} peaks, for the profiles of March 2006. With respect to conditions (i) and (ii), Fig.1a shows (A) enhancement trends on TEC from a few days before an earthquake exceeds the maximum excursion bar of TEC_q just a day or a few hours prior to the event and then (B) on attainment of such maximum, the peak TEC abruptly decreases. On days near to or at the trough of TEC decline, occurrence of a low latitude earthquake is noted .It is significant that isolated equatorial earthquakes have no influence in changing TEC features .Based on these observations a number of earthquake events are examined and a precursor magnitude is calculated as percentage deviation of TEC from its maximum Sd limits. This magnitude vary in a complex manner with longitudinal separation between epicentre and observing station and also with the epicentre direction as can be seen from Fig.1b where precursor magnitudes for a large number of low latitude earthquakes are plotted with longitudinal separations between epicenter and observing station .

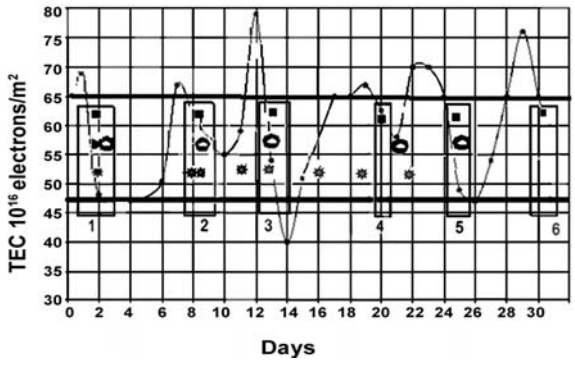

Fig.1a

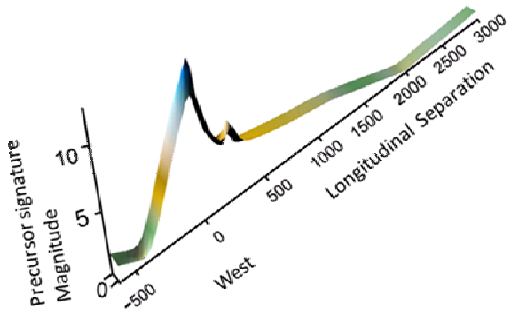

Fig.1b

Fig.1: (a) TEC $_{noon}$ (peak) and Sd limits (thick lines) for (a) March 2006. ■ identified day for possible earthquake . ⬭ low latitude earthquake occurrence days and ✸ lone equatorial earthquake day. Numbers 1, 2, 3 etc. marked below the rectangles highlight the association of a low latitude earthquake and our identified possible earthquake date.(b) Precursor magnitudes for a large number of low latitude earthquakes are plotted with longitudinal separations between epicentre and our observing station.

2.2 Fof2 and earthquake precursor and identification of location

In reference to the approaches adopted for identifying earthquake by taking foF2 as a tool, Fig.2a shows its diurnal variations over Ahmedabad (23.01º N, 72.36º E) before a number of low latitude earthquakes. The formation of high density zones with bite-out phenomenon before an earthquake can be taken as a prelude [2]. It has now become possible to extract earthquake induced information near epicenter even when foF2 variation is like that of a Q-day. Depueva et al. [3] have identified features using both spatial and temporal variations in the critical frequencies foF2 before the strong earthquake of August 15, 1963 with epicenter location at φ=-13.8° and λ=-69.3°. Fig.2b presents their method where they have shown that by evaluating percentage deviation of [fof2-median/fof2] mainly for stations inside (Lapaz) and outside (Natal) the disturbed area, one can identify earthquake epicentre even when foF2 has a Quiet day character.

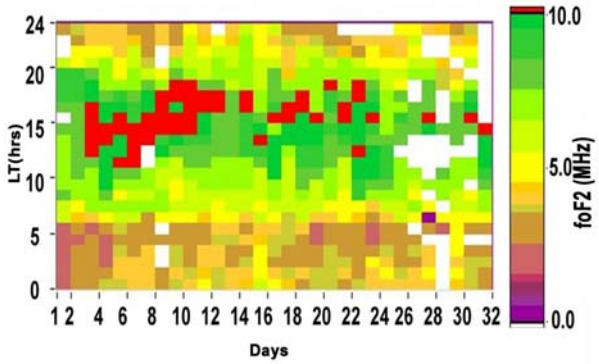

Fig.2a

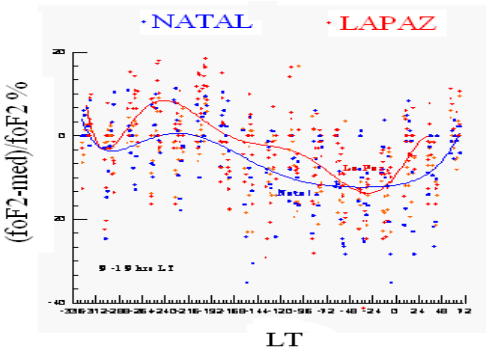

Fig.2b

Fig.2: (a) Diurnal foF2 variation over low latitude station in May 1994. Note the development of bite out prior to and during earthquake of 8th May 1997 at 08.20 hrs. with epicentre 24.89 N, 92.25 E , M=6.0 and for 22nd May 1997, at 04.20 IST with epicentre 23.08^0 N, 80.04^0 E and M scale 6.0 . May 12 is a false alarm. (b) Percentage variation of [fof2-median/fof2] for stations inside (Lapaz) and outside (Natal) disturbed area for strong earthquake of August 1963 [3] one can identify earthquake epicentre even foF2 bears Q-day pattern.

2.3 Anomalous structures in Sodar echograms at earthquake time

Sodars have been widely used in the study of atmospheric boundary layer with aims to elicit structure parameter of temperature and wind fluctuations in the lower atmosphere. Interestingly, Sodars do exhibit information for identifying an impending earthquake. We have seen from Sodar at GU occurring of sudden break-down of surface boundary layer accompanied by undulating structures in the echogram prior to strong earthquake [5]. These anomalous features are reflection of seismic induced atmospheric waves suggested by radio sonde data on Radio Refractive Index (RRI) gradient, temperature lapse rate and wind prolife up to the tropopause.

2.4 Identification of epicentre location through modification of Effective Erath Radius

For explaining the identification aspect we present here the strong China earthquake of May 12, 2008, with magnitude 7.9 and epicenter at 31º 24' N, 103º 58' E as observed from the GPS data received at GU . The number such satellites passes seen at different azimuth positions from May 7 to May 12 is presented in Fig.3. One can see explosive enhancements on passes from May 9 i.e. on three days prior to the earthquake, [D (-3)] along with shift in azimuth positions. It is to be noted, [4] that low azimuth satellites are seen even from 50˚ on May 9 and 10 and they disappear as the days eventually reach the earthquake day (D. May 12). Along with the absence of low azimuth satellites from May 11, a gradual decrease of number of satellite passes just before the earthquake day is also apparent from Fig.3. On converting azimuth positions to satellite latitude and longitude, it is noted that on D (-3), satellites that give abnormally high TEC are seen from 30˚ N, 94˚-100˚ E longitude, coinciding with epicenter position and a large number of passes giving anomalous TEC values are observed covering a zone from 25˚ N, 94˚-100˚ E. This situation though remained same on the D (-2), number of satellites passes has declined except from the location 30˚ N, 94˚-100˚ E. On D (-1), few satellites are seen from 30˚ N, 94˚-100˚ E and there is a dramatic wane in number of satellite passes.

2.5 Location of epicentre position through monitoring of VHF signals

TV and FM signals (lower VHF range) are monitored at Gauhati as part of a programme for understanding atmospheric modification related to anomalous propagation. Steerable antenna scans the horizon looking for

anomalous TV signal from east to west whereas a fixed polarized antaean monitors fringe area FM programme. The observation shows that 6-7 days prior to an earthquake, TV screen displayed clear pictures associated with programmes running in station near to the epicenters, [5].

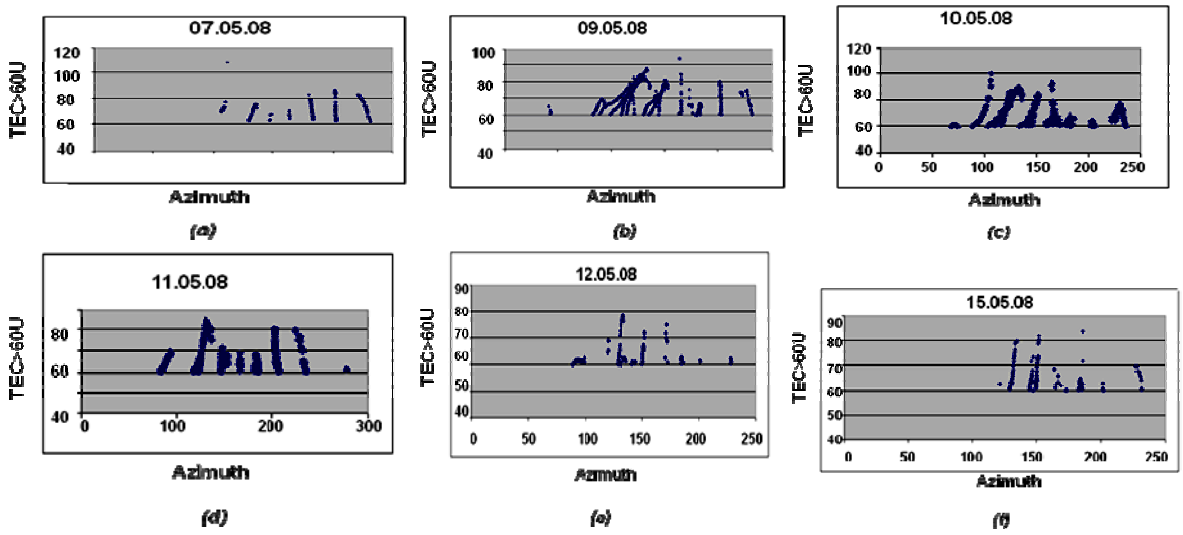

Fig.3 Presents enhancement in records of TEC > 60 U for different satellite passes (as given by azimuth position) for the days May 7 , 9 , 10 , 11,12 and 15 i.e. prior to ,during and after the occurrence of May 12, 2008 earthquake . Each dot of the figures corresponds to a satellite pass. Appearance of large number of satellites passes before the earthquake day is to be noted. TEC unit is given in U=10^{16} electrons /m^2.

3. Conclusion

Starting with anomalous TEC and foF2 characters the paper shows that through enhancement of field of view dictated by the satellite passes one can identify the epicentre position prior to strong earthquakes. Perturbations in Sodar echogram as well as beyond the horizon VHF audio –video reception characters can be used as effective tools for locating an epicentre.

References

[1.] J.Y. Liu, Y.I Chen, Y.J .Chou, and H.F. Tsai, "Variations of ionospheric total electron content during the Chi-Chi earthquake". *Geophysical Research Letters*, vol. 28, pp. 1383-1386, 2001.

[2.] M. Devi, A.K. Barbara, and A.H. Depueva, "Association of total electron content (TEC) and foF2 variations with earthquake events at the anomaly crest region,".*Annals of Geophysics,* vol.47. N.1, P.83-92, 2004.

[3.] A. Depueva, A. Mikhailov, M. Devi, and A.K. Barbara, "Spatial and time variations in critical frequencies of the ionospheric F region above the zone of equatorial earthquake preparation," *Geomagnetism and Aeronomy,* vol.47. N.1, P.129-133, 2007.

[4.] M. Devi, A.K. Barbara, A.H. Depueva, Yu. Ya . Ruzhin, and V. Depuev, "Anomalous total electron content (TEC) and atmospheric refractivity prior to very strong China earthquake of May 2008," *IJRS* (in press)

[5.] M. Devi, A.K. Barbara,Yu. Ya Ruzhin, and A.H. Depueva, "Beyond the horizon propagation of VHF signals" :atmospheric features and earthquake. Электронный журнал *"Исследовано в России"*, 129e, pp. 1331-1340, http://zhurnal.ape.relarn.ru/articles/2007/129e.pdf.2007.

Microwave emission due to material fracture and its application to earthquake monitoring

Tadashi Takano [(1)]

(1) Nihon University, Department of Electronics and Computer Science
7-24-1 Narashino-dai, Funabashi, 274-8501 Japan
takano@ecs.cst.nihon-u.ac.jp

Keywords: hypervelocity impact, rock crash, microwave emission, mechanism, field test, earthquake, volcanic activities.

Abstract: This paper describes a series of researches relevant to microwave emission phenomena due to material fracture. We found the phenomena using a hypervelocity impact or by a static pressure in laboratory. As earthquakes and volcanic activities are associated with rock fractures, we conceived the practical applications of the phenomena to monitor such natural events. In a field test, we successfully detected the microwave emissions in strong correlation with the collapses of a volcano crater. Then, the brightness temperature data obtained by a remote sensing satellite were analyzed. Actually, the emission was confirmed in great earthquakes and volcanic eruptions. As a result, the microwave emission phenomena can be applied to the detection and monitoring of earthquakes or volcanic activities.

1. Introduction

In hypervelocity impacts, there were few experimental results concerning radio frequency emission [1]. A flash of light was investigated [2]. In the cases of rock fractures, electromagnetic emission was also reported [3] [4] [5]. The monitoring of EQ and volcanic eruption is quite important for social security. Besides mechanical and chemical methods, there were proposed electrical methods: VAN method [6], anomalies in the ionosphere in ULF, ELF or VLF [7], the propagation effects on FM radio waves [8]. These methods are not based on laboratory experiment, especially, of the signal power.

In contrast to the former experiments in low-frequency band and light waves, microwave emissions at 22 GHz-band due to hypervelocity impacts were first discovered experimentally [9]. This microwave emission phenomena were intensively studied [10] [11] [12]. The microwave emission was also found in rock fracture by a static pressure [13]. In order to confirm the microwae emissin in natural events, we planned and carried out a field test in a volcano in virtue of the known location and time [14]. Analyzing the data of a remote sensing satellite, we succeeded to extract local and faint change of the brightness temperature which is caused by microwave emission [15] [16].

In this paper, I first introduce some important experimental facts in laboratory. As for the field test, the outline and some results will be presented. Finally, some results of the unique data analysis of the remote sinsing satellite will be described

2. Laboratory Experiment to Detect Microwaves due to Material Fracture

A nylon projectile of 7 mm diameter and 0.21 g weight was accelerated to a speed of 3.8 km/sec, and hit a target plate of a 2 mm thick aluminum plate. The plate was completely penetrated as shown in Fig. 1. The waveform of the detected microwave is a train of pulses as shown in Fig. 2, and contains the frequency component of 22 GHz in the envelope. The emitted energy is dependent on the target materials. In the case of aluminum, the energy was 3.7×10^{-14} J. The IF bandwidth of the receiver was ±500MHz.

The injected kinetic energy is sufficient for a molecule of the projectile to excite an electron into free space, or to dissociate the crystalline bond of aluminum. The dependency of the emitted energy on the target's thickness and projectile velocity was studied [10] [12].

Figure 3 shows the emitted waveforms in the rock fracture experiment at three frequency bands together with loading. The emission is again in a raondom train of sharp pulses. The experiment was performed for several kinds of rocks, and the emitted power is dependent not only on piezo-electricity [13].

3. Field Test to Observe Microwave Emission in Volcanic Activities

The field test was held at the volcano on Miyake Island located 150 km south of Tokyo. The scenery of the test site is shown in Fig.4. Microwave antennas were implemented to point at the rock cliff of the volcano crater. The observation frequency was 300 MHz, 2 GHz, and 18.7 GHz. The total measuring system in Fig. 5 is robust, and enables us to discriminate the local phenomena at the mountaintop relevant to a crater collapse from those at the mountain foot [14].

All data of microwave signals received at the mountaintop at 300 MHz are shown in Fig. 6 from January 9 to February 4, 2008. The signals appeared not continuously but occasionally in clusters. In particular, there were strong pulses on January 12, 18, and February 4. We can clearly discriminate the signal waveform due to a rock fracture from that due to a thunder. This discrimination was supported by the meteorological data and the detection comparison with that at the mountain foot. The fast sampled data revealed that each intermittent signal was composed of pulses of the width narrower than several micro sec.

The seismic waveform taken at the same time as the microwave detection has the features of landslide cases. The rock cliff of the crater significantly changed its shape between the photo shots on January 9 and March 11 in 2008. These facts support that the microwave was generated by cliff collapse.

4. Microwave Feature Extraction from the Data of a Remote Sensing Satellite

Microwave emission due to a rock fracture should be measured as the brightness temperature increase by the microwave radiometer AMSR-E on the remote-sensing satellite AQUA. We have developed a new interpolation algorithm which, regardless of the conical scan of AMSR-E, enables to obtain physical values at any location.

Brightness temperature changes also according to a physical temperature of the ground, climate conditions, soil moisture and vegetation. As the spatial correlation length of a rock fracture is shorter than that of other factors, the differential brightness temperature ΔT between a focused point (FP) and reference point (RP) can eliminates those contaminations.

We calculate ΔT at all FPs in combinations with the surrounding RPs during the whole observation period. At each FP, ΔT becomes largest in the whole period at a peculiar time. In the case of Reventador volcano in Ecuador which erupted on November 3, 2002, ΔT was calculated for 10000 FPs or 40 000 combinations. Right after the eruption, ΔT for the 605 combinations has become largest, as shown in Fig. 7 [15]. Here, ΔT is divided by the time averaged value to give a peak factor δ which represents unusual increase of ΔT. The points Ci correspond to the flow of the erupted smoke.

Next, we analyzed the data of Morocco earthquake which occurred on February 24, 2004. In order to eliminate the effects by the water and moisture contents, we adopted ΔT at 23.8 GHz in addition to 18.7GHz. The result is shown in Fig. 8. In the area A, the anomalous increase of FPs with large δ is significant in number and value. It is clear that the area A is correspondent to many faults and fissures shown in Fig. 9 [16].

5. Conclusions

A series of the research works clarified only a part of the problem, and showed the availability of the practical applications. We need further study, in particular, collaboration work with seismologists and volcanologists.

Acknowledgment

These works were executed or supported by many colleagues and students. In particular, the field test in Miyake-jima was supported by JAXA and the Meteorological Agency in Japan. I would like to express my sincere gratitude to all of them.

References

[1.] R. Bianchi, F. Capaccioni and P. Cerroni, “Radiofrequency emission observed during macroscopic hypervelocity impact experiments”, Nature, vol.308, no.26, pp.830-832 (1984).
[2.] G. Eichhorn, “Measurements of the light flash produced by high velocity particle impact”, Planet. Space. Sci., Vol.23, pp.1519-1525(1975).
[3.] G. O. Cress, B. T. Brady, and G. A. Rowell, "Sources of electromagnetic radiation from fracture of rock samples in the laboratory", Grophys. Res. Lett., 14, 331-334, 1987.
[4.] U.Nitsan, "Electromagnetic emission accompanying fracture of quartz-bearing rocks", Geophys. Res. Lett., 4, 333 – 336, 1977.
[5.] Yoshida, S. and T. Ogawa, "Electromagnetic emissions from dry and wet granite associated with acoustic emissions", J. Geophys. Res., 109, B09204, doi: 10.1029/2004JB003092, 2004.
[6.] P. Varotsos et al, "Latest aspects of earthquakes prediction in Greece based on seismic electric signals, Two", Tectonophysics, 224, 1-37, 1993.

[7.] A. C. Fraser-Smith, A. Bernardi, P. R. McGill, M. E. Ladd, R. A. Helliwell, and O. G. Villard, Jr., "Low-frequency magnetic field measurements near the epicenter of the MS 7.1 Loma Prieta earthquake", Geophys. Res. Lett., 17, 1465-1468, 1990.
[8.] T. Yoshida et al., "Observation of Co-seismic Electromagnetic Phenomena in VHF Associated with the Tottori-ken Seibu Earthquake in 2000 and the Geiyo Earthquake in 2001", Zishin-Journal of the Seismological Society of Japan, Vol.55, No.2, pp.107-118, 2002.
[9.] T. Takano, Y. Murotani, K. Maki, T. Toda, A. Fujiwara, S. Hasegawa, A. Yamori and H. Yano, "Microwave emission due to hypervelocity impacts and its correlation with mechanical destruction", J. Appl. Phys. 92, 5550 (2002).
[10.] K. Maki, E. Soma, T. Takano, A. Fujiwara, and A. Yamori,"Dependence of microwave emissions from hypervelocity impacts on the target material",Journal of Applied Physics, vol.97, pp.104911/1-6, 2005.
[11.] K.Maki, T.Takano, A.Fujiwara and A.Yamori, "Radio-Wave Emission due to Hypervelocity Impacts in Relation to Optical Observation and Projectile Speed", Advances in Space Research, 34, pp.1085-1089, 2004.
[12.] H.Ohnishi, S.Chiba, E.Soma, K.Ishii, K.Maki, T.Takano, S.Hasegawa, "Study on microwave emission mechanisms on the basis of hypervelocity impact experiments on various targat plates", Journal of Applied Physics, vol. 101, no.9, pp.124901-1-8, May 2007.
[13.] K.Maki, T. Takano, E. Soma, K. Ishii, S. Yoshida and M. Nakatani, "An experimental study of microwave emission from compression failure of rocks", J. of the Seismological Society of Japan, 58, 4, 375 – 384, 2006.
[14.] T. Takano, T. Maeda, Y. Miki, S. Akatsuka, S. Yoshida, K. Nagata, K. Hattori, M. Nishihashi, D. Kaita, and T. Hirano, "Field Test of the Signal Detection at Microwave Frequency Bands due to Volcanic Activity in Miyake-jima", IEEJ Trans. FM, Vol. 129, No. 12, pp.853-858, December 2009.
[15.] T. Maeda and T. Takano, "Discrimination of Local and Faint Changes from Satellite-borne Microwave Radiometer Data", IEEE Trans. on Geoscience and Remote Sensing, vol 46, issue 9, pp. 2684-2691, 2008.
[16.] T. Maeda and T. Takano, "Detection Algorithm of Earthquake-related Rock Failures from Satelliteborne Microwave Radiometer Data", IEEE Trans. on Geoscience and Remote Sensing, vol. 48, no. 4, pp. 1768-1776, April 2010.

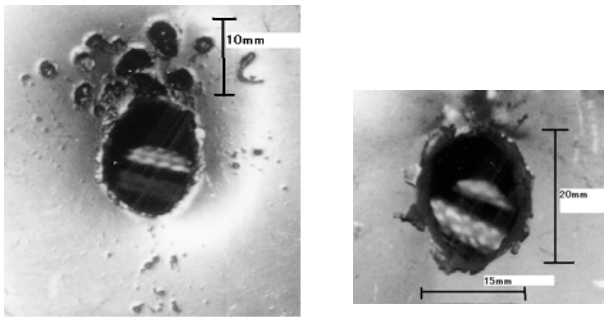

(a) Front (b) Back

Fig. 1. Destruction of an aluminum plate of 2 mm thickness by hypervelocity impact [5].

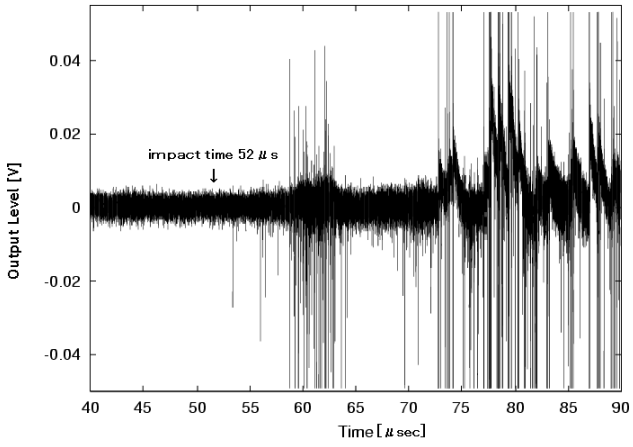

Fig.2. Emission at 22GHz in the case of a 2mm thick aluminum plate.

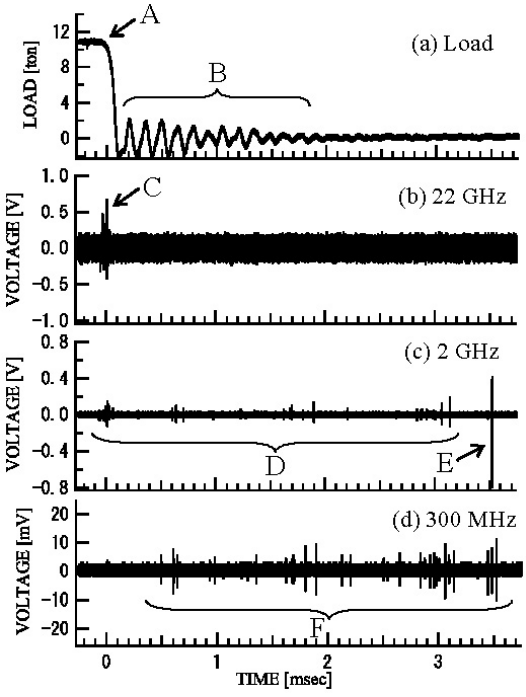

Fig. 3. Obtained data in rock fracture experiment in the case of quartzite. The moment of triggering is taken to be 0 sec.

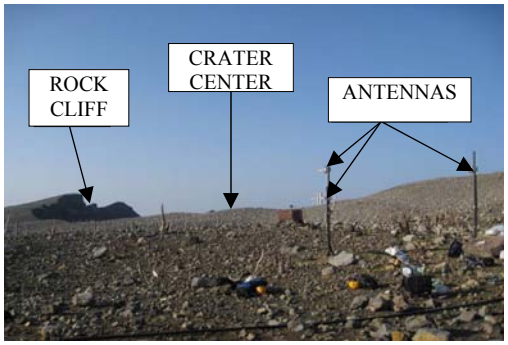

Fig. 4. View of the mountain top and the installed antennas in the field test.

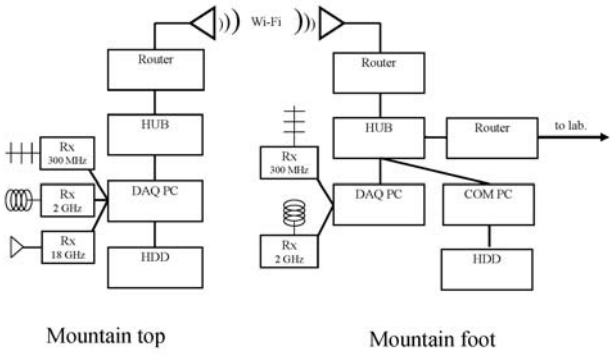

Fig. 5. Configuration of the total measuring system.

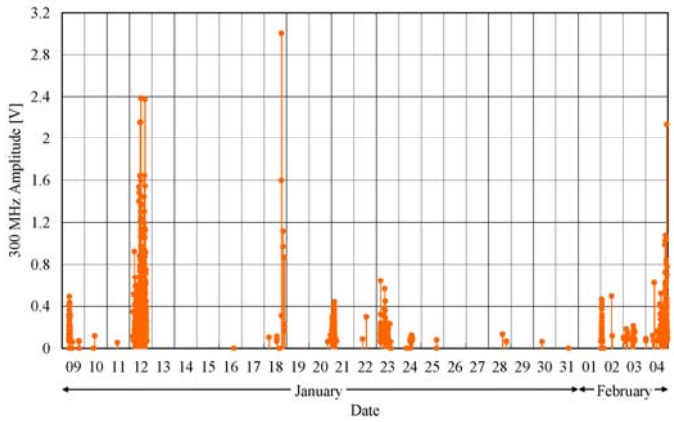

Fig. 6. Pulses of 300 MHz microwave signals received at the mountaintop during the observation period.

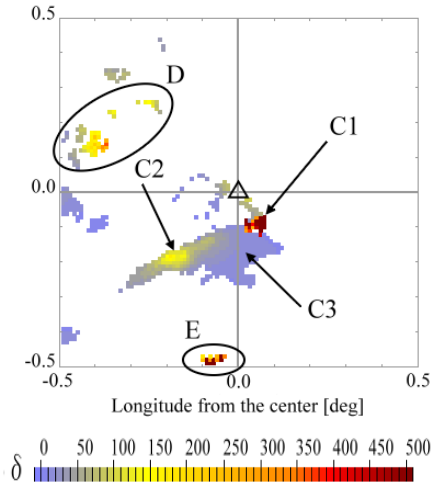

Fig. 7. Occurrences of the greatest δ with its value at 18.7 GHz around Reventador on the next day of the eruption.

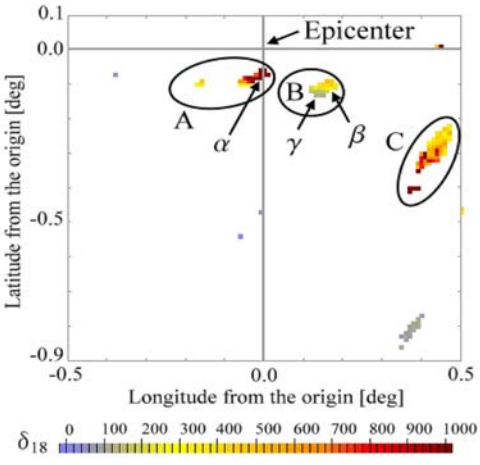

Fig. 8. Occurrences of the greatest δ with its value at 18.7 GHz in the case of Morocco earthquake two day before the main shock.

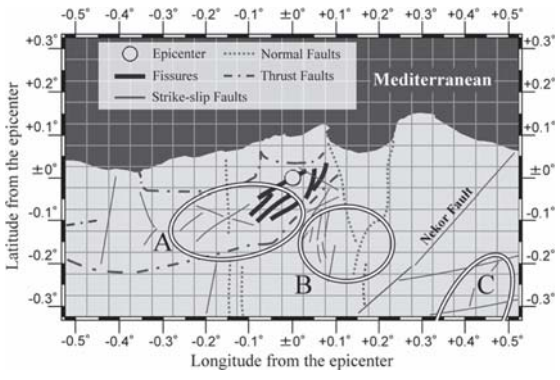

Fig. 9. The epicenter (35.142◦ N, 3.997◦ W) and its suburban terrestrial features.

Dynamical Coupling of the Low Latitude Ionosphere-Thermosphere

Shigeto Watanabe

Department of Earth and Planetary Sciences, Hokkaido University, Japan
shw@ep.sci.hokudai.ac.jp

Keywords: Ionosphere, Thermosphere, Super-rotation, Equatorial ionization anomaly

Abstract: The zonal neutral wind flows strongly at the Earth's magnetic dip equator instead of the geographic equator around 20 magnetic local time (MLT) in the thermosphere. On the other hand, the fast zonal plasma drift occurs in the low latitude F region of evening ionosphere, but the velocity decreases at the magnetic dip equator. Therefore, the fast plasma drift velocity structure forms an arch in the frame of latitude and altitude in the evening. The fast zonal neutral wind occurs inside of the arch. Since the fast zonal plasma drift is strongly associated with equatorial ionization anomaly (EIA), we suggest that the ionosphere-thermosphere coupling associated with F region dynamo is significantly important in the low latitude F region ionosphere/thermosphere. The fast neutral wind occurring at the magnetic dip equator in the evening of F region may result in atmospheric super-rotation in the low latitude thermosphere.

1. Introduction

Though the ionization rate is less than 1% in the region of low latitude thermosphere, the dynamics of neutral atmosphere is strongly controlled by the plasma. The coupling process between the neutral atmosphere and the plasma has been investigated by satellites such as DE-2, CHAMP, etc. The observations showed similar local time variation of plasma drift velocity to neutral wind [1], atmospheric super rotation in thermosphere [2], and equatorial temperature and wind anomaly (ETWA) [3]. From CHAMP satellite data, Liu et al. [4] presented that the equatorial zonal winds of day- and night-time upper atmosphere at ~400 km altitude are significantly influenced by the solar flux, and the winds show atmospheric super rotation in thermosphere depending on the season and solar flux. The coupling between neutral atmosphere and plasma is a key process to understand the dynamics and the structure of thermosphere and ionosphere, but we don't have enough information on the coupling process because the direct simultaneous observations of neutral atmosphere/plasma and the comparison with modeling are not yet performed in detail.

In this paper, the fast zonal neutral winds [5] obtained by CHAMP and DE-2 satellites are shown. Those winds are compared with plasma drifts and electron densities obtained by DE-2 satellite, associated with the equatorial ionization anomaly (EIA).

2. Data

Two sets of independent data are used in this study. One is the data from the CHAMP satellite and the other is the data from the DE-2 satellite. CHAMP is in a near-circular orbit with an inclination of 87.3◦. The average altitude in the year of 2002 is ~400 km. Its orbital plane moves through all local times every 3 months. It effectively probes the in-situ neutral wind with an accuracy of ~20 m/s. On the other hand, the inclination of DE-2 satellite is 90◦. It samples through all local times every 6 months. The DE-2 satellite in the thermosphere has measured zonal neutral wind, zonal plasma drift and electron density by WATS (Wind and Temperature Spectrometer), RPA (Retarding Potential Analyzer) and LANG (Langmuir probe), respectively. The data at altitudes between 200km and 600km are used. Since the data is limited for local time, altitude, latitude and

longitude, we did not investigate the seasonal dependence. The chosen data periods are Jan. 2002-Dec. 2002 and Aug. 1981-Feb. 1983 for CHAMP and DE-2, respectively. The year of 2002 is chosen for CHAMP, since the average solar radio flux value (F10.7=179) is comparable to that for DE-2 (F10.7=180). Data during very magnetically active periods (Kp ≥ 5) are excluded in the following analysis.

3. Results

Figure 1 illustrates the zonal neutral wind distribution in the frame of magnetic dip latitude and magnetic local time. Although some differences exist in the mean values of the neutral wind and also in the local time of the second maximum, both CHAMP and DE-2 observations reveal similar neutral wind patterns. The neutral wind flows eastward during night and westward during day in the low latitude region. Towards higher latitude, the morning wind reversal from eastward to westward occurs at earlier local times. The reversal time is ~2 magnetic local time (MLT) near ±30◦ latitude. This leads to a pronounced triangle shape in the 2-D distribution of the neutral wind shown in Figure 2. On the night side, the latitudinal variation of the wind exhibits a maximum at the magnetic dip equator. This fast neutral wind continues throughout the time of eastward wind. During 5–8 MLT, both observations show a minimum westward flow at the magnetic dip equator (see pink curves). After 9 MLT, however, the strongest westward flow is again found at the magnetic dip equator (blue curves). There is a good agreement in the features revealed by CHAMP and DE-2 observations. The averaged wind in the local time at the magnetic dip equator is eastward. It is same to the super-rotation of atmosphere in the thermosphere as shown in [4].

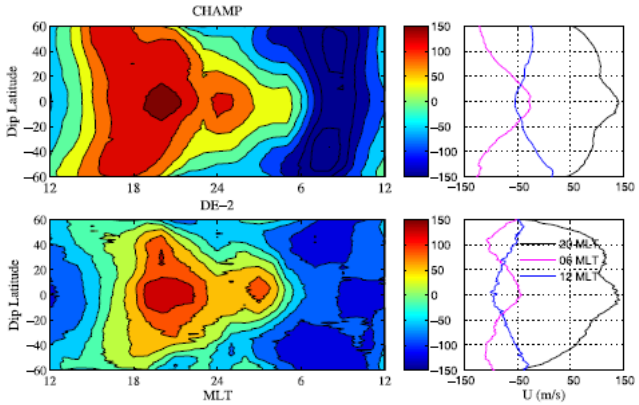

Figure 1. Distribution of the seasonally averaged zonal neutral wind velocity (in unit of m/s) in the frame of magnetic dip latitude and magnetic local time. Positive means eastward. The upper row is for CHAMP and the lower row for DE-2. Corresponding latitudinal profiles at 6 MLT, 12 MLT, and 20 MLT are shown in the right panels.

Figure 2 shows the zonal plasma drifts obtained by DE-2 satellite in the frame of geomagnetic local time and latitude, and in the frame of geographic longitude and latitude. Data in each bin are averaged in 1 hour and 1◦ geomagnetic longitude/latitude. The averaged data between 300 and 600 km altitudes are used. The zonal plasma drift velocity indicates symmetric pattern on either side of the magnetic dip equator. The zonal plasma drift flows strongly in the low latitude region. The zonal plasma drift around 16 MLT changes the direction from westward to eastward. We note that the zonal plasma drift shows similar variation to the zonal neutral wind as shown in Figure 1. Both zonal neutral wind and zonal plasma drift velocities increase in the period between 18 MLT and 20 MLT. The plasma drift velocity reaches ~100 m/s. However, the fast zonal neutral wind appears with eastward direction around 20 MLT, and the velocity reaches about 150 m/s. On the other hand, the zonal plasma drift forms a velocity anomaly from 18 MLT to 20 MLT, so that the velocity trough occurs at magnetic dip equator and the fast zonal plasma drift velocity is in ±10◦ magnetic latitudes. The zonal plasma drift velocity at magnetic dip equator is ~50 m/s smaller than that in ±10◦ magnetic latitudes. The zonal plasma drift velocity anomaly disappears around 22 MLT, and then the zonal plasma drift flows strongly at magnetic dip equator until the morning.

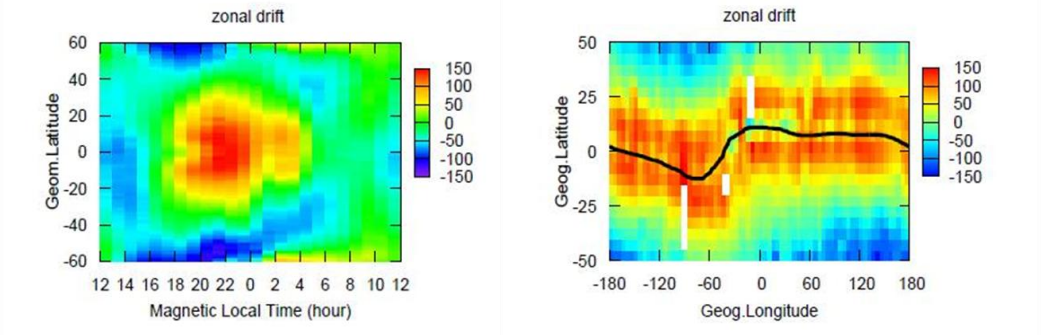

Figure 2. Distributions of zonal plasma wind velocity (Left) in the frame of geomagnetic local time and geomagnetic latitude and zonal plasma drift velocity (Right) in the frame of geographic longitude and latitude (in unit of m/s). The averaged zonal plasma drift data at altitudes between 300 and 600 km is used. Right panel shows the drift velocity during 18-24 MLT. Black solid line represents magnetic dip equator.

Figure 3 shows zonal neutral wind (left), zonal plasma drift (middle) and electron density (right) observed by DE-2 satellite in the frame of magnetic latitude and altitude in 19-21 magnetic local time (MLT). The data are averaged in the bin of 10 km in altitude and 1◦ in latitude. The zonal neutral wind flows strongly at magnetic dip equator, and the velocity increases with increasing altitude in the low and middle latitudes. There is no data over 600 km altitude, because of the sensitivity of WATS (Wind and Temperature Spectrometer) instrument in low neutral density region. Both zonal neutral wind velocity and zonal plasma drift velocity increase with increasing magnetic local time in the evening to midnight. The shape of fast zonal plasma drift velocity is seen as an arch. We say here this is zonal plasma drift velocity anomaly (PDA). Such kind of feature does not appear in the other local time. At altitudes between 300 km and 500 km of geomagnetic dip equator, the plasma drift velocity is small. The maximum plasma drift velocity of ~100 m/s occurs at ~600 km altitude of magnetic dip equator. The distribution of fast zonal plasma drift is similar to that of equatorial ionization anomaly (EIA), but the fast zonal plasma drift occurs at lower altitudes than that of EIA, i.e., there is inside of EIA. Note that the shear of zonal plasma drift velocity occurs below 600 km altitude at magnetic dip equator.

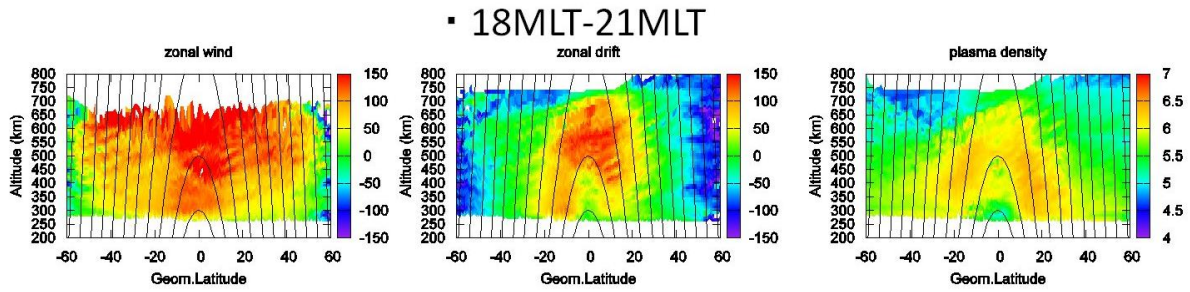

Figure 3. Zonal neutral wind, zonal plasma drift and plasma density distributions in the frame of magnetic latitude and altitude in 18-21 MLT. Velocity and density units are m/s and logscale of m^{-3}. Solid lines represent magnetic field lines.

4. Discussion

The CHAMP probes the in-situ neutral wind with a tri-axis accelerometer, while the DE-2 measured the wind with a wind and temperature spectrometer (WATS). The CHAMP and the DE-2 measurements confirm strongly the existence of the fast neutral wind and its stable location at the magnetic dip equator. This fast neutral wind along the Earth's magnetic dip equator instead of the geographic equator demonstrates strong magnetic control of the thermospheric dynamic. In the upper atmosphere of low latitudes, the atmospheric pressure gradient is the primary driver of the neutral wind, with the ion drag being an important impeding force. With the development of the equatorial ionization anomaly (EIA) in the equatorial ionosphere after ~9 magnetic local time (MLT), the

plasma density forms a trough at the magnetic dip equator [6]. This consequently leads to lower ion drag, which facilitates faster neutral wind to flow at the magnetic dip equator. During the period of 5–8 MLT, however, the EIA structure disappears and a peak of the plasma density forms at the magnetic dip equator instead of a trough [7]. This causes the ion drag to peak at the magnetic dip equator as well, hence to slow down the zonal neutral wind considerably. As a result, the magnetic dip equator becomes a channel of slow flow instead of fast flow as shown in Figure 3.

The zonal plasma drift forms a trough at magnetic dip equator and crests in ±10◦ magnetic latitudes, which was already reported by [8]. From Jicamarca radar data, Fejer et al. [9] showed that the zonal plasma drift increases with increasing altitude in the F region of magnetic dip equator. However, a 3-D structure of zonal plasma drift has not been understood in detail. Figure 4 shows at the first time that the fast zonal neutral wind occurs inside of the fast zonal plasma drift. The shape of fast zonal plasma drift in latitude and altitude frame is similar to equatorial ionization anomaly (EIA). The fast zonal plasma drift is strongly associated with the EIA developing after sunset to midnight. We suggest that F region dynamo also contributes the generation of fast zonal neutral wind at magnetic dip equator, and the ionosphere-thermosphere coupling associated with F region dynamo is significantly important in the low latitude F region ionosphere/thermosphere. The fast zonal neutral wind occurring at the magnetic dip equator in the evening of F region may result in a source of atmospheric super-rotation in the low latitude thermosphere.

In summary, both the CHAMP and DE-2 observations reveal a fast zonal neutral wind at the Earth's magnetic dip equator instead of the geographic equator, demonstrating the strong magnetic control of the neutral dynamics via ion drag. The fast zonal neutral wind occurs in zonal plasma drift velocity anomaly (PDA) in the evening and associated with equatorial ionization anomaly (EIA). This is one of the processes of ionosphere-thermosphere coupling in the low latitude.

Acknowledgment

The author thanks H. Liu, T. Kondo and H. Luhr for discussing data and its analyses. The CHAMP mission is supported by the German Aerospace Center (DRL) in operation and by the Federal Ministry of Education and Research (BMBF) in data processing. The author thanks the use of the DE data in NSSDC of NASA.

References

[1.] Rishbeth, H. (1972), Thermospheric winds and the F-region: A review, J. Atmos. Terr. Phys., 183 34, 1–47.
[2.] Coley, W. R., R. A. Heelis, and N. W. Spencer (1994), Comparison of low-latitude ion and neutral zonal drift using DE2 data, J. Geophys. Res., 99, 341–348.
[3.] Raghavarao, R., L. E. Wharton, N. W. Spencer, H. G. Mayr, and L. H. Brace (1991), An equatorial temperature and wind anomaly (ETWA), Geophys. Res. Lett., 18(9), 1193–1196.
[4.] Liu, H., H. Luhr, S. Watanabe, W. Kohler, V. Henize, and P. Visser (2006), Zonal winds in the equatorial upper thermosphere: decomposing the solar flux, geomagnetic activity, and seasonal dependencies, J. Geophys. Res., 111, A09S29, doi:10.1029/2005JA011415.
[5.] Liu, H., S. Watanabe, T. Kondo, Fast thermospheric wind jet at the Earth's dip equator, Geophys. Res. Lett., VOL. 36, L08103, doi:10.1029/2009GL037377, 2009
[6.] Balan, N., G. J. Bailey, and R. J. Moffett (1994), Modeling studies of ionospheric variations during an intense solar cycle, J. Geophys. Res., 99, 17,467–17,475.
[7.] Lin, C. H., J. Y. Liu, T. W. Fang, P. Y. Chang, H. F. Tsai, C. H. Chen, and C. C. Hsiao (2007), Motions of the equatorial ionization anomaly crests imaged by FORMOSAT-3/COSMIC, Geophys. Res. Lett., 34, L19101, doi:10.1029/2007GL030741.
[8.] Aggson, T. L., N. C. Maynard, F. A. Herrero, H. G. Mayr, L. H. Brace, and M. C. Liebrecht, Geomagnetic Equatorial Anomaly in Zonal Plasma Flow, J. Geophys. Res., 92, 311-315, 1987.
[9.] Fejer, B. G., E. Kudeki, and D. T. Farley, Equatorial F Region Zonal Plasma Drift, J. Geoghys. Res., 90, 12249-12255, 1985

Identification of low latitude earthquake epicentre: An attempt utilising GPS and ionosonde data

M. Devi [(1)]***, A.K. Barbara*** [(1)] ***and P. Kashyap*** [(1)]
A. Depueva [(2)]***, Ya Yu Ruzhin*** [(2)] ***and V. Depuev*** [(2)]

[(1)]Department of Physics, Gauhati University, Guwahati 781014
md555@sify.com; kashyapprakash8@gmail.com
[(2)]IZMIRAN, Troisk, Moscow Region, Russia

Key words: Earthquake epicentre; TEC; foF2; magnetic field H

Abstract: The interest here is to examine spatial quake-time low-latitude TEC variations when epicenter is not far from the observing station (±5° latitudinal separation) and to focus on dynamical situations in the ionosphere associated with the earthquake events. Prelude to earthquake-induced TEC features i.e. enhancements and depletion in density is obtained through analysis on noon and post noon diurnal variations. The paper also presents a few observations in an attempt to identify epicentre of low latitude earthquakes. Contribution of earthquake induced current system at the epicentre zone to the modification in Low latitude TEC is suggested. In spatial mode of analysis when ionosonde data of foF2 are available from a number of stations in and around equator, special iterative method is adopted for extraction of earthquake induced anomaly magnitudes for locating an epicentre.

1. Introduction

Ionospheric Appleton anomaly occupies a ≈20º zone around equatorial belt, which has been extensively studied to understand equatorial and low-latitude dynamics. With availability of large pool of electron density and Total Electron Content (TEC) data collected from ISR, GPS, and ionosonde observations, it has become possible to realize variation of this anomaly with solar and geomagnetic conditions, [1,2] and also the extension or other wise of the anomaly belt associated with such variabilities. Of late seismic activity effects on equatorial anomaly belt have received serious attention, [3-5] and to extract pre-seismic features there from. From a network of GPS stations in Taiwan, Liu et al. [4] have extracted TEC characters prior to three strong (M=6.2-7.3) low-latitude earthquakes and interpreted from results that anomaly crests moves towards the equator by pre-seismic effects.
In this paper GPS data on TEC taken at Guwahati (26° N, 92° E), a seismically active anomaly crest station in sub Himalayan region, are examined in relation to earthquake induced spatial redistribution of density at ionospheric heights and quake-time low-latitude TEC variations when epicenter is not far from the observing station (±5° latitudinal separation). The paper then aims to find out prelude to earthquake by induced signature on TEC distribution and hence to understand the system dynamics in association with ionospheric current system.

2. Observations

2.1. Anomalous TEC aspects and earthquake characters

As a step in finding out earthquake induced imprints on TEC, anomalous features associated with earthquake are extracted from TEC profiles on quiet days Q-days (TEC_q). Selecting at least five Q-days of a month the average

TEC at each hour is calculated. However as TEC is subject to statistical variations even on Q-days, standard deviation (Sd) of TEC_q and its maximum and minimum excursions are found out. Deviation in TEC from this excursion base during pre-earthquake and on earthquake days will be the first filter for extraction of earthquake-induced information. TEC peaks during noon (TEC_n) and post-noon (TEC_{pn}) periods (depending on season) will be considered and the Q-day excursion limit for each case is calculated separately.
Two basic earthquake situations will be dealt-with here in association with TEC, these are:

i) Equatorial (magnetic inclination of the epicenter location is not more than ≈ ±5º) earthquakes**,** strong (M≥5) earthquakes occurring within ±5° longitudinal zone from Guwahati;

ii) Low-latitude earthquakes, both strong (M≥5) and weak (4<M <5) with epicenters scattered about ±5° latitude and longitude (preferably) from Guwahati.

Fig.1 is a plot of day-to-day variations of the two significant peaks, i.e. noon and post-noon maxima, for the profiles of February.
With respect to the two conditions (i) and (ii), Fig.1a shows a few significant features on diurnal TEC profiles:
1. There are enhancement trends on (TEC_n)/ (TEC_{pn}) from a few days before an earthquake. The magnitude of enhancement then exceeds the maximum excursion bar of TEC_q just a day or a few hours prior to the event. Interestingly this increase follows depletion in TEC.
2. On attainment of such maximum, the peak TEC abruptly decreases.
3. On days near to or at the trough of TEC decline, the occurrence of a low-latitude earthquake is noted.
Another case is shown in Fig.1b for a low latitude earthquake of June 2007. The identified day from prelude to earthquake and the day of occurrence of earthquake are shown in the figure satisfying our analysis approach.

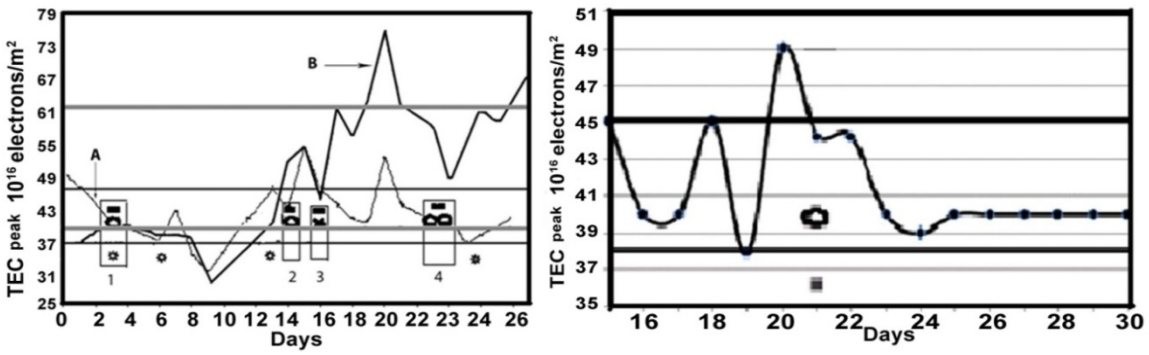

(a) (b)

Fig.1a TEC peak variations (A, noon TEC_n and B, post noon TEC_{pn}) for the month of February 2006 earthquakes are shown with predicted days from the TEC extracted features and earthquake events**.** Equatorial and low-latitude earthquakes, Sd-variation limits for Q-day TEC_n and TEC_{pn} peaks are also shown by light and dark lines.

- Identified days are marked as group [number 1, 2, 3, 4].
- Earthquake (M ≥ 5, i.e. strong, S) occurrence days in the equatorial region (2° N to 12° N).
- Earthquake (M ≥ 5, i.e. strong, S) occurrence days in the low-latitude region (26° N ± 5°N).
- Earthquake (M < 5, i.e. weak, W) occurrence days in the low-latitude region (26° N ± 5°N).

Fig.1b: TEC_{noon} (peak) and Sd limits (thick lines) for a single earthquake of June 2007

2.2 Influence of low-latitude and equatorial earthquake on TEC profiles

The case studies for February 2006 show that isolated equatorial earthquake has no significant role in shaping earthquake-time TEC characters. This feature can further be viewed from Fig.2a for February 2006 and Fig.2b for March 2006. These two months' are selected as there were number of low latitude and equatorial earthquakes occurring within the longitude zone of our study. Here "prediction strengths" are plotted with magnitude of equatorial as well as low-latitude earthquakes. One can see that prediction reliability increases mainly with magnitude of low-latitude earthquake, though influence from equatorial ones cannot be ruled out.
In the light of this approach, a number of earthquake cases in association with TEC are analysed to assess the reliability of prediction.

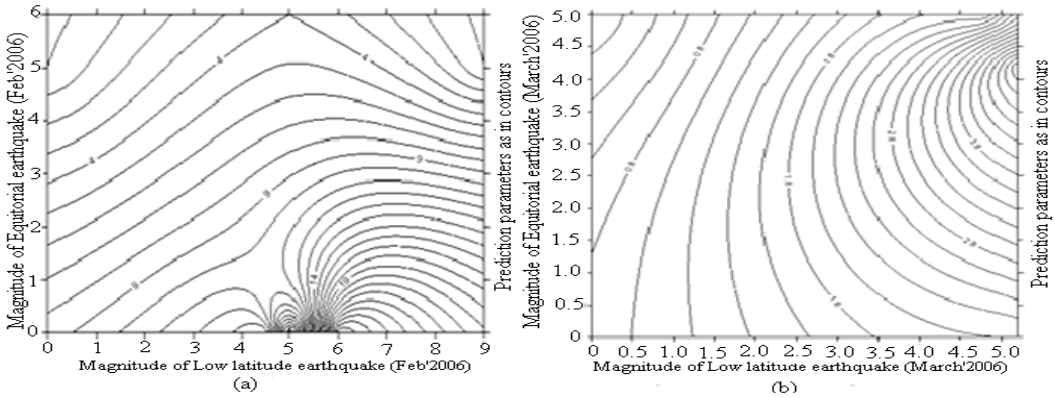

Fig.2a. Prediction magnitude (February 2006) in presence of low-latitude and equatorial earthquakes. Note the increase in prediction reliability mainly with magnitude of low-latitude earthquake. Prediction weight from a lone equatorial earthquake is weak. Fig.2b. Shows prediction magnitude for March 2006. Here too this factor is more significant with low latitude earthquake though presence of equatorial earthquake along with low-latitude ones can not be neglected.

2.3 foF2 parameter as a precursor of earthquake:

There are extensive studies on understanding on the perturbation of ionosphere prior to earthquake by using foF2, [4,5] as a tool. Devi et. al., [5] have shown that the anomaly effect can be taken as a tool for identifying an impending earthquake. Depueva et. al., [6] had analysed temporal and spatial variations in foF2 before August 15, 1963 earthquake of magnitude M = 7.75 with topside (Alouette-1) as well as spatial observations from ground based ionosonde. They have demonstrated the role of electric field induced by earthquake preparatory processes in density distributions around the epicentre zone.

3. Discussion

This paper focuses on multiple factors on earthquake-time behaviour on ionosphere near Appleton anomaly crest region. Past studies on these aspects have shown that precursors to of low- latitude earthquakes manifest themselves as Appleton type EXB anomaly if the epicentre lies very near to the equator [6,7]. It is proposed that such anomaly is the result of generation of anomalous electric field above the epicenter. In this connection we examine here the variations in horizontal component of earth's magnetic field H around Appleton anomaly region prior to earthquakes by selecting eight magnetic observatory in the latitude zone from 8º28' to 30º 22' N within the longitude of 72º to 79º E (Table I). A few earthquake events are so selected to provide inputs associated with modifications of H. For this exercise, diurnal maximum in H of the relevant stations are analysed with respect to the quiet day average maximum of H. The results so obtained on $\Delta H = [H_{max}$ (Q-day) - H_{max} (any day)] for three such earthquake events are shown in Fig.3 [I, II, III] as case representatives. Considering the case I, i.e. for May 22, 1997 for an earthquake occurring near anomaly crest, we note large negative values of ΔH developed four days prior to the earthquake and then gradually returning to Q-day mean H, just prior to earthquake days. The pattern supports that low-latitude earthquake could induct changes in current system near to epicenter zone and could temporality enhances current system prior to an impending earthquake and return to normal situation just on the earthquake day. However for epicenters at off anomaly stations like case II and III, no consistent association of H with the earthquake could be seen.

4. Conclusion

Low-latitude earthquakes force changes on anomaly crest station TEC and prelude to earthquakes can be identified as a result of anomaly effect. Isolated equatorial earthquake has little influence in this aspect though its
role in presence of low- latitude one can not be neglected. Modification in low-latitude ionospheric current at the epicentre zone leads to changes in TEC features.

Table I : Shows earthquake epicenters magnitudes and station coordinates

H data taken from the stations	Earthquake Date	Magnitude	Epicentre	Position
Trivandrum 8°29′ N, 76°.57′ E Hyderabad 17°25′ N, 78 º33′ E	22.05.1997	6.0	23.1	80.8
Alibag 18°.38′ N, 72°.52′ E Jaipur 26°.55′ N , 77°.48′ E	09.01.1990	5.5	28.2	88.2
Ujjain 23°11′ N, 75° 47′ E Sabhawala 30˚.22′ N , 77˚.48′ E	09.08.1987	5.6	29.5	83.7

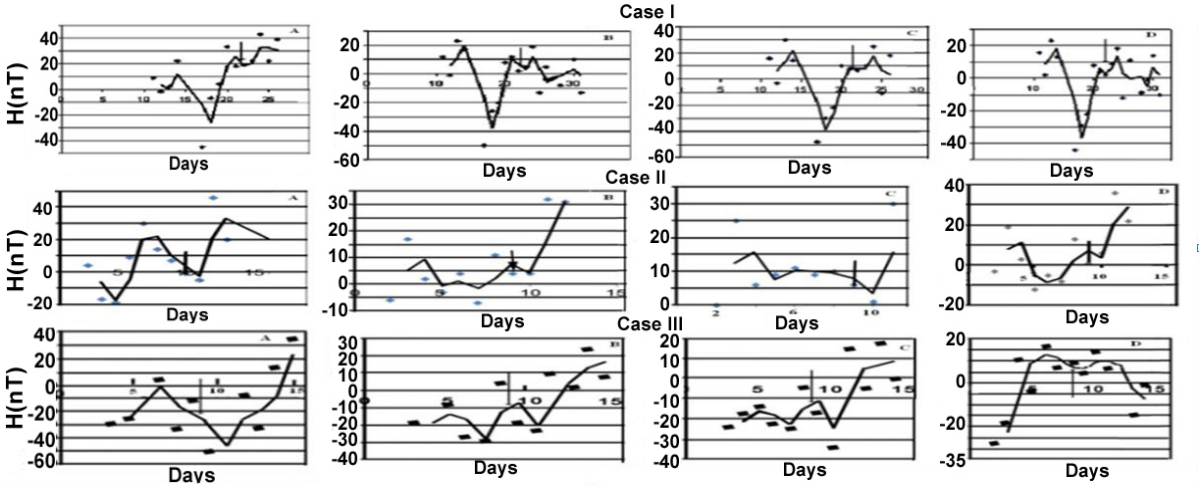

Fig.3. Earthquake-time variations on H for the three cases shown in the table.1.

References

[1.] G.O. Walker and H.F. Chen, "Computer simulation of the seasonal variations of ionospheric equatorial anomaly in East Asia under solar minimum conditions," *J. Atmos. Terr. Phys*. vol.51, pp. 953-974, 1989.

[2.] M. Devi, M.K. Barman, and A.K. Barbara, "Identification of quiet and disturbed days through TEC profile features over Anomaly Crest Station," *J. Atmos. Solar-Terr. Phys*. vol. 64, pp.1413-1423, 2002**.**

[3.] A.H. Depueva and Yu.Ya. Ruzhin, "Seismoionospheric fountain effect as analogue of active space experiment," *Adv. Space Re,* vol. 15, N.12, pp. 12-15, 1995.

[4.] Y.J. Liu, Y.J. Chino, S.A. Pulinets, H.F. Tsai, and Zeng Xiaoping, "A study on the TEC perturbation prior to the Rei-Li Chi-Chi and Chi-Yi earthquake. Seismo Electromagnetics: Lithosphere –Atmosphere – Ionosphere Coupling," *Eds. M. Hayakawa and O.A. Molchanov* , Terapub , Tokyo, pp.293-301, 2002.

[5.] M. Devi, A.K. Barbara, and A.H. Depueva, "Association of Total Electron content and foF2 variations with earthquake events at the anomaly crest region," *Annals of Geophysics,* vol**.** 47**,** pp.83-91, 2004.

[6.] A. Depueva**,** A. Mikhailov, M. Devi, and A.K. Barbara, "Spatial and time variations in critical frequencies of the ionospheric F region above the zone of equatorial earthquake preparation," *Geomagnetism and Aeronomy*, vol. 47, pp.129-133, 2007**.**

[7.] M. Devi, M.K. Barman, A.K. Barbara, and A.H. Depueva, "Total electron content near anomaly crest as precursor of earthquake," *Ind. J. Radio Space Phys,* vol**.** 30, pp.209-213, 2001.

Signal Processing of Ultra Low Frequency (ULF) magnetic field data related to seismic activity in Europe during 2008 and 2009.

G. Prattes [(1)], K. Schwingenschuh [(1)], H. Eichelberger [(1)], M. Stachel [(1)], W. Magnes [(1)], M Vellante [(2)], U. Villante [(3)], P. Nenovski [(4)], V. Westergom [(5)]

[(1)] Space Research Institute, Austrian Academy of Sciences, Schmiedlstraße 6, 8042 Graz, Austria, gustav.prattes@oeaw.ac.at

[(2)] Dipartimento di Fisica, University of L'Aquila, via Vetoio 10, 67010 Coppito, L'Aquila, Italy, massimo.vellante@aquila.infn.it

[(3)] Dipartimento di Fisica, University of L'Aquila, via Vetoio 6, 67100 L'Aquila, L'Aquila, Italy, umberto.villante@aquila.infn.it

[(4)] Geophysical Institute, Sofia, Bulgaria, nenovski@geophys.bas.bg

[(5)] Geodetic and Geophysical Research Institute of the Hungarian Academy of Science, Csatkai E. u. 6-8, H-9400 Sopron, Hungary, wv@ggki.hu

Keywords: Ultra Low Frequency, Earthquake, Power Spectral Density, Cross Correlation

Abstract: A strong earthquake (Ml=5.8, Mw=6.3) hit L'Aquila (Central Italy, Abruzzo region, LT=UT+1) on April 6, 2009, 01:32 UT, causing more than 300 deaths and damage. We present Ultra Low Frequency (ULF) magnetic field measurements in the range from 10 mHz to 50 mHz before and during time periods of strong seismic activity. In the frame of the South European GeoMagnetic Array (SEGMA) a European collaboration runs ULF facilities (fluxgate magnetometer) continuously monitoring the background in ULF variations related to geomagnetic phenomena. Among others, the immediate scientific objective is the investigation of signal variations due to seismic activity and the discrimination of other natural and human influences. Concerning the L'Aquila earthquake the closest recording SEGMA station in L'Aquila (AQU) provided data during the time period 2008 and 2009. The available data give the possibility to perform signal processing analysis for a 16 months lasting time period. The distance to the main stroke epicenter was ~ 6 km. For the analysis we consider the nighttime period from 22.00 - 02.00 UT and determine the power spectral density of the horizontal and vertical field components. To compare the results we use data from SEGMA stations in greater distance to L'Aquila which are Ranchio (RNC), Castello Tesino (CST), both Italy, and Nagycenk (NCK), Hungary. Two major noise generation effects related to earthquakes are analyzed. (i) A direct electromagnetic (EM) effect where signals are possibly emitted within the earthquake focal zone. (ii) Indirect precursor effects, like strong seismic activity, can lead to Atmospheric Gravity Waves (AGWs) causing turbulence in the lower ionosphere leading to a depression of ULF waves down going from the magnetosphere.

1. Introduction

The measurement equipment including the magnetometer instrument is described and a geographical SEGMA ULF station overview is given first. Second the seismic activity in the region L'Aquila during 2008 and 2009 is presented. Further the applied signal processing methodology based on the ratio of the horizontal over vertical magnetic field power spectral density is described based on Hayakawa et al. [1]. For the investigation the daily nighttime data period is extracted due to low man made noise level. A multi station comparison of results is performed for the epoch 2008 and the first quarter of 2009. To explain local, global and geomagnetic effects the Kp index is taken into consideration. A similar work has been performed by Prattes et al. [2]. Possible noise generation effects due to seismic activity are explained based on the work of Molachanov et al. [3] and the crust electrical resistivity profile introduced by Palangio et al. [4] in the area of L'Aquila is respected.

2. Instrument, data base and seismic examination

The CHIMAG (ChInese MAGnetometer) fluxgate magnetometer was originally developed to investigate magnetic pulsations in the ULF range. The vital parameters of the high temporal resolution 3-axes fluxgate magnetometer are the measurement range of ±512 nT, the compensation field of 60 000 nT in X and Z and ±30 000 nT in Y direction. The accuracy is 8 pT at a temporal resolution of 1 Hz, derived from the highest possible sampling frequency of 64 Hz. The 3-axes magnetometer measures in X (positive Northward), Y (positive Eastward) and Z (positive towards the centre of the Earth) direction. The CHIMAG magnetometer comes to application in the frame of the SEGMA project. Fig.1. shows by yellow markers the SEGMA observatories Castello Tesino (CST), L'Aquila (LAQ), both Italy and Nagycenk (NCK), Hungary, which are evaluated in the frame of this work contributing data for 2008 and 2009. The station Ranchio (RNC), Italy indicated by green contributes data during 2008 and Panagyurishte, Bulgaria shown by a white marker is not evaluated in the frame of this work. From April 6 - April 9 2009 USGS recorded 23 earthquakes in the region around L'Aquila with magnitude range M = 3.6 to 6.3, the strongest on April 6 01:32 UT in a depth of 10 km, indicated with EQ in Fig.1.

Fig.1. Overview about the SEGMA ULF stations contributing to the combined L'Aquila EQ study

Table 1 contains the SEGMA ULF stations with geographical coordinates and the distances to the L'Aquila earthquake epicenter region.

Table 1 SEGMA ULF chain and distances to L'Aquila

ULF Stations		Geographic Coordinates		Corr. Geomagnetic Coordinates		Dist
Name	Code	Lat.[° N]	Long.[° E]	Lat.[° N]	Long.[°E]	km
Castello Tesino	CST	46.0	11.7	40.7	87.0	420
Nagycenk	NCK	47.6	16.7	42.6	91.7	630
Ranchio	RNC	43.97	12.08	38.22	86.71	200
L'Aquila	**AQU**	**42.38**	**13.32**	**36.30**	**87.35**	**6**
Panagyurishte	PAG	42.51	24.18	36.98	97.21	890

3. Magnetic Field Data Processing Methodology

We extracted the local midnight period from 22:00-02:00 LT (UT+1) for further analysis and divided this 4 h time period into 8 half hour intervals equally distributed, 30 min each. Each of these segments was subjected to a Fast Fourier Transform (FFT) analysis taking into consideration data processing rules. The selected sampling frequency is f_S=1 Hz so the upper analyzable frequency is $f_{NY}=f_S/2$=500 mHz. The frequency response of the horizontal and vertical magnetic field component was separated focused on the frequency band from 10-15 mHz in the time span from 1.1.2008 to 15.4.2009. Further the Power Spectral Density (PSD) was determined. The improved polarization analysis introduced in Ida et al. [5] normalizes each geomagnetic field component as described in (1).

$$i_n = \frac{A_i - \mu_i}{\sigma_i} \qquad (1)$$

A_i is the daily average of the i component, μ_i is the monthly mean of the i magnetic field component and σ_i is the standard deviation of the monthly i component. In Villante et al. [6] is concluded that applying the standard polarization method no amplitude increases unambiguously related to the earthquake occur. The normalized polarization ratio is determined as described in (2).

$$P = \frac{Z_n}{H_n} \qquad (2)$$

4. Results and Discussion

In Fig.2. magnetic field variation measurements from the observatory LAQ for April 6 2009 are analyzed. The left panel shows δH, δD and δZ during 01:30 and 01:38. The red line indicates the EQ main shock. In the right lower panel a hodogram for this 8 minute time period is depicted. On the x-axis the δH variations and on the y-axis the δD variations are plotted in the frequency range from 22-100mHz (Pc3 range). The upper right panel shows the zoomed plot of the variations during the time interval from 01:31:39 to 01:33:39. A time delay between the EQ main shock at 01:32:40 indicated with the red line and the magnetic field variations at 01:32:49 of 9 seconds can be observed.

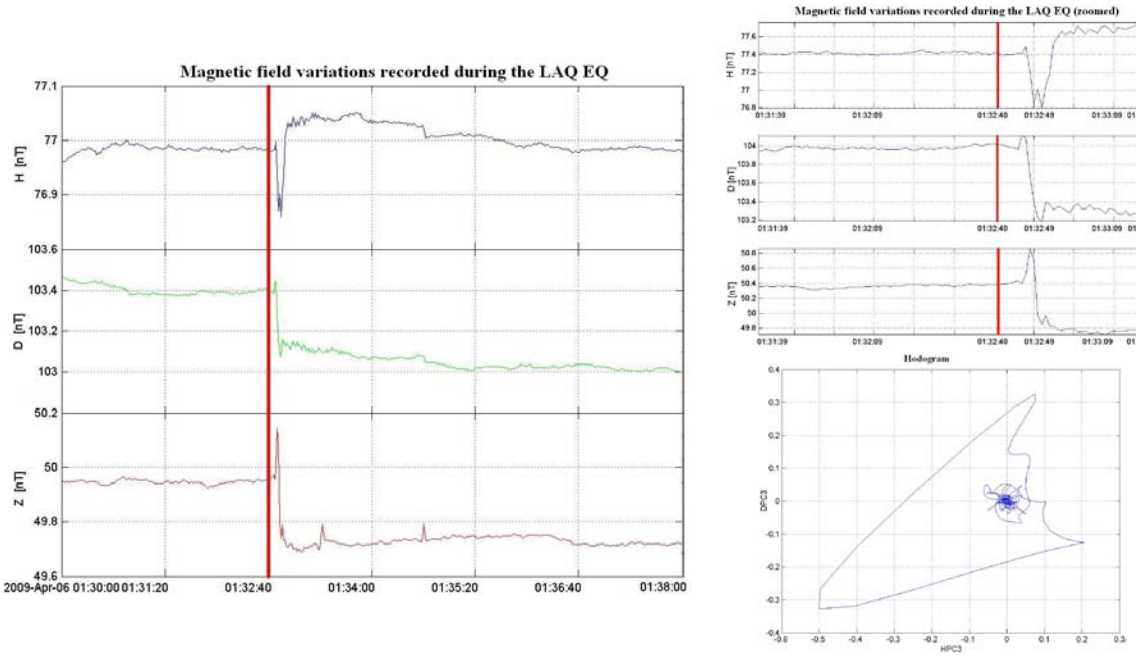

Fig.2. δH, δD and δZ magnetic field variations recorded at LAQ (left) and zoomed upper right panel and hodogram in the 22-100mHz range in the right lower panel

Fig.3. shows in the upper left and lower left panel the geomagnetic index Kp and the PSD for the (Z) and the (H) variations determined as described above for the SEGMA stations CST, NCK and LAQ in the time period 1.1.2008 to 15.4.2009. The right upper panel shows the Kp index and the standardized polarization ratio for the same time span. The red line indicates the LAQ EQ. In the period two weeks before the EQ, LAQ station shows strong polarization variations compared to NCK and CST. Fig.3. shows in the right lower panel a cross correlation comparison for the (Z) and (H) PSD and the stations LAQ and NCK during two time periods of 55 days. The orange lines in this panel show the correlation for the corresponding orange shaded time periods and the green lines show the correlation for corresponding green shaded time periods. CST is not analyzed in detail due to data gaps. To conclude, in the orange shaded time span of no geomagnetic or strong local effects positive correlation between LAQ and NCK can be observed. The green shaded time interval includes no geomagnetic influences but the LAQ EQ disturbances. This time period does not show positive correlation. Two major magnetic noise generation effects related to earthquakes are reported. (i) A direct EM effect, signals are possibly

emitted within the earthquake focal zone. Fast fluctuations of charge and an electromagnetic field are caused by microfractures. High frequency components are damped strong in the Earth's crust having a low skin depth but the ULF components penetrate without significant attenuation. (ii) Indirect precursor effects, strong seismic activity, can lead to AGWs causing turbulence in the lower ionosphere. A depression of ULF waves down going from the magnetosphere leads to a suppression of the horizontal variations measured on ground.

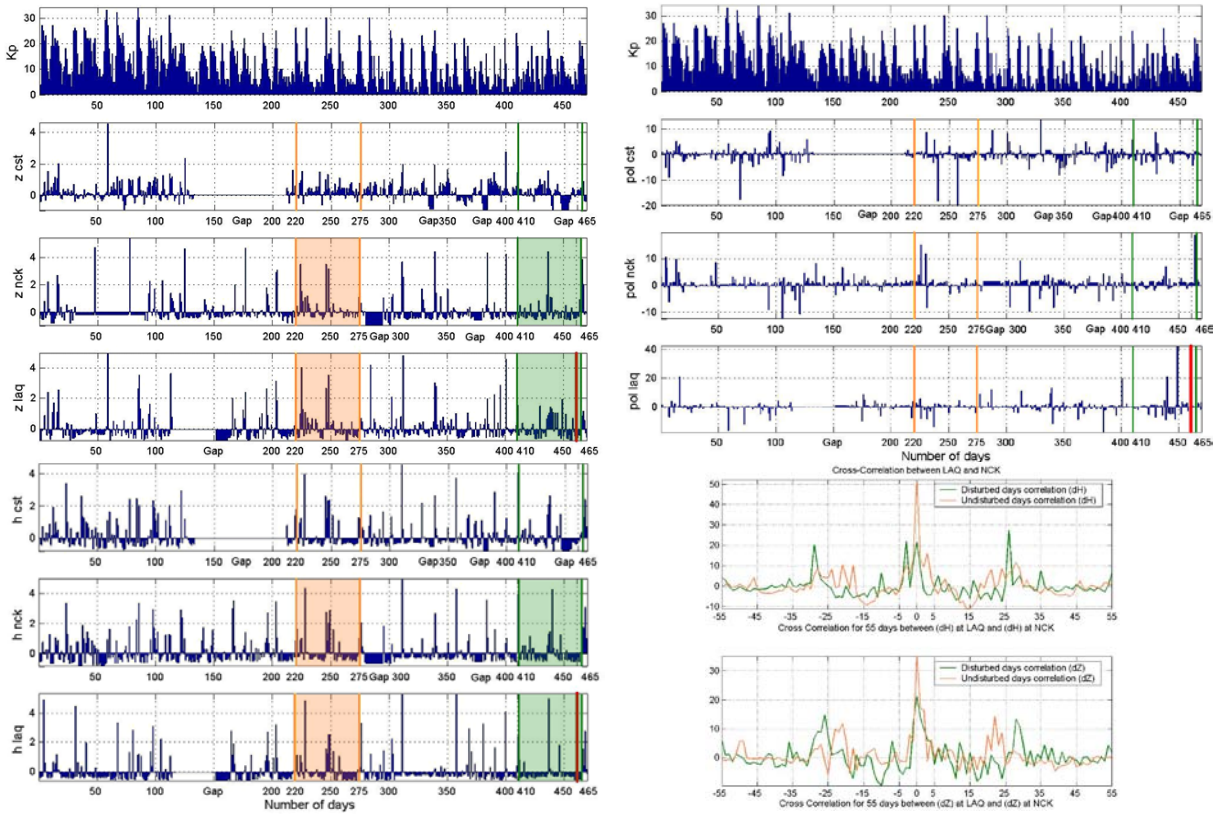

Fig.3. δH and δZ PSD (upper and lower left) and standardized ratios (upper right) for 3 stations during 1.1.2008 and 15.4.2009. The lower right panel shows the cross correlation comparison of δH and δZ for the stations LAQ and NCK in the undisturbed orange and disturbed green shaded periods.

References

[1.] M. Hayakawa, K. Hattori, K. Ohta, "Monitoring of ULF (ultra-low-frequency) Geomagnetic Variations Associated with Earthquakes", *Sensors,* Vol. 7, pp .1108-1122, 2007.

[2.] G. Prattes, K. Schwingenschuh, H. U. Eichelberger, W. Magnes, M. Boudjada, M. Stachel, M. Vellante,V. Wesztergom, and P. Nenovski, "Multi-point ground-based ULF magnetic field observations in Europe during seismic active periods in 2004 and 2005", *Nat. Hazards Earth Syst. Sci*., Vol. 8, pp. 501-507, 2008.

[3.] O. Molchanov, and M. Hayakawa, "On the generation mechanism of ulf seismogenic electromagnetic emissions", *Phys. of the Earth and Planet. Int.*, Vol. 105, pp. 201-210, 1998.

[4.] P. Palangio, C. Di Lorenzo, F. Masci, and M. Di Persio, "The study of the electromagnetic anomalies linked with the Earth's crustal activity in the frequency band [0.001 Hz-100 kHz]", *Nat. Hazards Earth Syst. Sci*., Vol. 7, pp. 507-511, 2007.

[5.] Y. Ida, D. Yang, Q. Li, H. Sun, and M. Hayakawa, "Detection of ULF electromagnetic emissions as a precursor to an earthquake in China with an improved polarization analysis", *Nat. Hazards Earth Syst. Sci*., Vol. 8, pp. 775-777, 2008.

[6.] U. Villante, M. De Lauretis, C. De Paulis, P. Francia, A. Piancatelli, E. Pietropaolo, M. Vellante, A. Meloni, P. Palangio, K. Schwingenschuh, G. Prattes, W. Magnes, and P. Nenovski, "The 6 April 2009 earthquake at L'Aquila: a preliminary analysis of magnetic field measurements", *Nat. Hazards Earth Syst. Sci.,* Vol. 10, pp. 203-214, 2010.

Sub-ionospheric and trans-ionospheric VLF wave propagations and its relation to seismo-electromagnetic phenomena.

K. Schwingenschuh [(1)], H. Eichelberger[(1)], G. Prattes[(1)], B.P. Besser[(1)], F. Simoes[(2)], A. Rozhnoi[(3)], M. Solovieva[(3)], O. Molchanov[(3)], M. Friedrich[(4)], G. Stangl[(1)], M.Y. Boudjada[(1)], H. Biernat[(1)], R. Döller[(5)], P.F. Biagi[(6)], P. Nenovski [(7)]

[(1)] Space Research Institute, Graz, Austria (konrad.schwingenschuh@oeaw.ac.at)
[(2)] NASA/GSFC, Space Weather Laboratory (Code 674), Greenbelt, USA
[(3)] IFZ, Moscow, Russian Federation
[(4)] University of Technology, Graz, Austria
[(5)] Institute of Physics, Department of Geophysics, Astrophysics and Meteorology, KF-University Graz, Austria
[(6)] University of Bari, Bari, Italy
[(7)] Geophysical Institute, Sofia, Bulgaria

Keywords: Seismicity, VLF, Transionospheric, Subionospheric, Atmospheric Electricity

Abstract: The Graz VLF facility is part of a European seismo-electromagnetic VLF/LF network. The radio paths between the European VLF/LF transmitters and ground- and satellite borne receivers are used in order to investigate the lithospheric-ionospheric coupling of European active seismic regions. Mainly the pre-, co-and after-seismo-electromagnetic phenomena of the 6-April-2009 earthquake in the Abruzzo region in Central Italy near L'Aquila have been used for this study. A major emphasis is on the analysis of the amplitude and phase variations of the seismo-electromagnetic VLF radio signals received by the European ground-based receiver network and aboard the DEMETER microsatellite.

1. Introduction

The radio paths formed by terrestrial VLF transmitters and receivers aboard satellites or on ground are an essential tool to study the influence of seismic phenomena on the ionosphere, Molchanov and Hayakawa [1]. Various models have been proposed in order to explain this lithospheric-ionospheric coupling: Acoustic waves can be generated by the seismic shock and will be amplified through the atmosphere by the decreasing atmospheric density, Trigunait et al. [2]. Gas releases before earthquakes can generate acoustic gravity waves which might generate ionospheric disturbances. The coupling between seismic regions and the ionosphere has recently been explained by the increase of the fair-weather conductivity before earthquakes, Harrison et al. [3].

2. The Graz VLF Facility

A VLF receiver of the ULTRAMSK type to register the phase and amplitude of signals in the frequency range 10-50 kHz is working in Graz since September 2009. The Graz VLF facility can receive the signals from up to 12 navigational transmitters simultaneously. From January 2008 until September 2009 an OmniPal VLF receiver was working in Graz and observed signal variations related to the EQ M=6.3 in L'Aquila on 6-April-2009 in high quality.
Phase and amplitude of the received signals are logged every 20 seconds and stored in the Graz database which can be accessed by the members of the European VLF/LF network via ftp. The network comprises stations in Italy, Greece, Romania, Turkey, Russia and Austria. Further stations are planned in Bulgaria, Germany and Portugal.

3. Seismo-Electromagnetic VLF Methods

It is a well-known radio-physical method, in which phase and amplitude of radio signals from navigational transmitters propagating inside the earth-ionosphere waveguide are monitored (sub-ionospheric method). If transmitter frequency and receiver distance are fixed, then the observed VLF signal parameters are mainly defined by the position of the reflection height which depends on the value and gradients of electron density near the atmosphere-ionosphere boundary. It is typically 80-85 km, in daytime it is about 70 km and in nighttime - about 90 km.
Therefore, the VLF signal method has become the standard for recording short-time electron density variations in the lower ionosphere and upper atmosphere connected with solar radiation (e.g. Roentgen flares), cosmic rays (Forbush effect), precipitation of energetic particles, lightning-induced ionization etc.
The main feature of VLF/LF signal is day variation.
Day variations of phase and amplitude of VLF signal depend on frequency, wave path length, illumination conditions along the trace and direction of the signal propagating relative to the magnetic field of the Earth. Each trace has its own diurnal variation. Besides day variation there are seasonal variations in the A and P of the signal.
The first suggestion to use this method for searching earthquake activity was made by Russian scientists about 20 years ago. The first paper has been published in 1989. They analyzed signal from Omega transmitters in Reunion and Liberia which received in Omsk (distance is about 7-8 thousand km) and found nighttime "baylike" anomalies in the P and A of the signal for several large earthquakes in the 3d Fresnel's zone.
This method is the nighttime "baylike" anomalies method or the residual method.
In this method we use for analysis a residual signal of phase dP or amplitude dA defined as the difference between the observed signal and the averaged monthly signal (calculated for quiet days). For each data we select the night and day intervals not including sunrise and sunset periods. For every month we select its own intervals. We analyze signal only in night period because it is more sensible to disturbances of different nature than signal in day time. Besides, in day time the signal is strongly influenced by SID from by X-rays. We consider a signal as an anomalous when dP or dA exceeds the level of two standard deviations.
Another method of signal analysis was developed by Molchanov and Hayakawa [1] in analysis of the famous Kobe earthquake (M = 7.1; January 17, 1995). It was named the Terminator Time method (TT). In this method the periods of sunset and sunrise are investigated. These are the periods when the boundary atmosphere-ionosphere is not stable. This method is based on determination of the characteristic minimums in the phase and amplitude daily variations of a signal during sunset and sunrise.
This method was first applied for processing the VLF signal received at Inubo observatory transmitted by Omega station in Tsushima (Japan). It was found that the evening TT deviated significantly from the monthly averaged value 3 days before the main shock. The distance between Tsushima and Inubo is only about 1000 km, which can be considered as short-distance propagation.

While the sub-ionospheric VLF radio path reveals the coupling of the lower ionosphere and the lithosphere before earthquakes, the coupling of the upper ionosphere and lower magnetosphere with the seismic active region can be explored with ELF/VLF radio receivers aboard satellites orbiting below 800 km, like the French DEMETER satellite. The amplitude of the VLF signals of ground transmitters or natural ionospheric sources can be used as indicator for the seismicity on the surface, Nemec et al. [4]. The variations of the ELF radio noise received aboard low orbiting satellites can also be used as earthquake precursors. This effect has recently been explained by the increase of the fair-weather conductivity before earthquakes, Harrison et al. [3].
Ground based ionosondes and GPS receivers can provide information on the variability of the ionospheric electron concentration, which is an essential parameter for seismo-electromagnetic studies of natural geophysical phenomena such as volcanic eruptions and earthquakes, Trigunait et al. [2].

4. The 6-April-2009 L'Aquila Earthquake

An earthquake (Ml=5.8, Mw=6.3) hit L'Aquila (Italy, LT=UT+1) on April 6, 2009, 01:32 UT, causing more than 300 deaths (including 47 students of the local university) and a tremendous devastation of the town and its territory.

Extensive sub-ionospheric studies of VLF anomalies of the transmitter signals received in Graz, Moscow and Bari have been performed (see Fig.1.). The analysis of the radio paths crossing the L'Aquila Fresnel zone revealed a precursor several days before the earthquake on 6-April-2009. Both sub-ionospheric seismo-electromagnetic VLF methods, the "residuum method" and the "Terminator Time method" have been used, Rozhnoi et al [5].

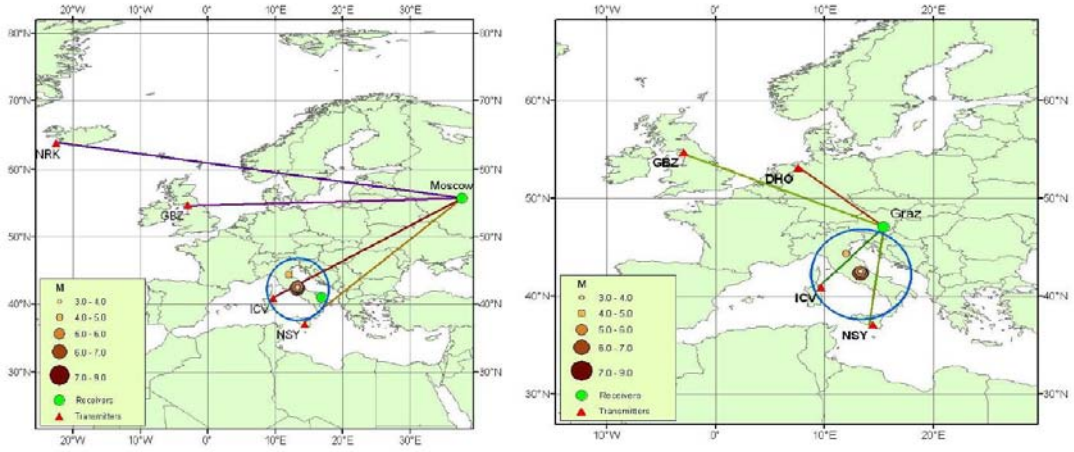

Fig.1. Map showing the epicenters of the earthquakes occurred in the Abruzzo area in the period 1–9 April 2009. The blue circle represents the projection on the ground surface of the perturbed zone in the atmosphere-ionosphere boundary, Rozhnoi et al. [5]. The seismic paths are related to the ICV (Sardinia, Italy) and NSY (Sicily, Italy) transmitters; the control paths are related to the GBZ (Great Britain) and DHO (Germany) transmitters. This method combines the use of receivers (green full circles) in Graz (left-panel) and in Moscow (right-panel).

Transionospheric studies have been performed used European VLF ground transmitters and the electric field experiment (ICE) aboard DEMETER, Boudjada et al. [6]. The ELF/VLF electromagnetic emissions recorded by ICE experiment onboard DEMETER micro-satellite above L'Aquila region showed typical variation of the averaged VLF intensity level (see Fig.2.). A drop of intensity was clearly seen 7 to 10 days before the earthquake occurrence Boudjada et al. [7].

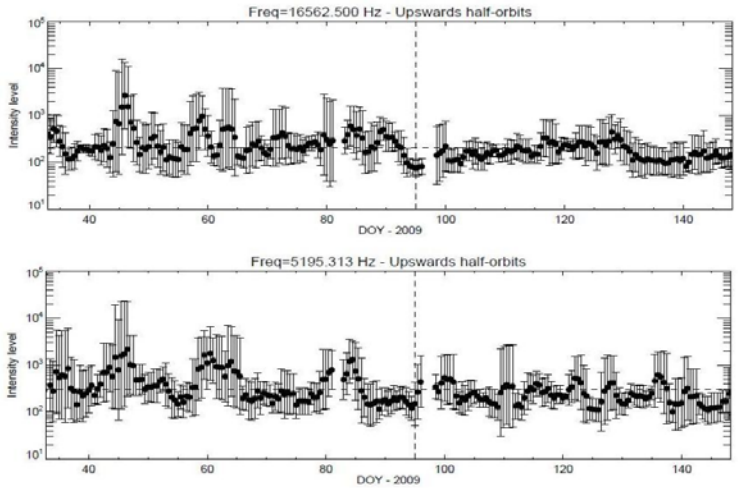

Fig.2. ELF/VLF electromagnetic emissions recorded by the ICE experiment onboard DEMETER micro-satellite above L'Aquila region. The figure shows the variation of the averaged VLF intensity level versus the day of the year 2009 (from 01st February to 28th May) at two frequencies. The vertical dashed lines indicate the day of the L'Aquila earthquake. The first frequency at about 16 kHz (first panel) is related to the DFY Germany transmitter (Long. = 13° *E*, Lat. = 52.5° *N*), and the second is associated to natural ionospheric emissions at about 5.2 kHz.

5. Summary and future outlook

Sub-ionospheric and trans-ionospheric radio paths in the VLF frequency range have been used in order to study the 6-April-2009 earthquake (EQ) in L'Aquila. Based on a careful analysis of the VLF signals seismic precursors have been found several days before the EQ.
It is planned to combine VLF radio paths observations and simulations in order to derive the electron density and conductivity fluctuations in the atmosphere and ionosphere prior to the EQ.

References

[1.] O. Molchanov, and M. Hayakawa, *Seismo-electromagnetics and related phenomena: History and latest results*, Terrapub, Tokyo, p. 190, 2008.

[2.] A. Trigunait, M. Parrot, S. Pulinets, and F. Li, "Variations of the ionospheric electron density during the Bhuj seismic event," *Ann. Geophys.*, vol. 22, pp. 4123-4131, 2004.

[3.] R. G. Harrison, K. L. Aplin, and M. J. Rycroft, "Atmospheric electricity coupling between earthquake regions and the ionosphere," *Journal Atmos. Solar-Terr. Phys.*, in press, corrected proof, doi:10.1016/j.jastp.2009.12.004, 2009.

[4.] F. Nemec, O. Santolik, M. Parrot, "Decrease of intensity of ELF/VLF waves observed in the upper ionosphere close to earthquakes: A statistical study," *J. Geophys. Res.*, vol. 114, pp. 1-10, 2009.

[5.] A. A. Rozhnoi, M. S. Solovieva, O. A. Molchanov, K. Schwingenschuh, M. Y. Boudjada, P. F. Biagi, T. Maggipinto, L. Castellana, A. Ermini, and M. Hayakawa, "Anomalies in VLF radio signals prior the Abruzzo earthquake (M=6.3) on 6 April 2009," *Nat. Hazards Earth Syst. Sci.*, vol. 9, pp. 1727-1732, 2009.

[6.] M. Y. Boudjada, K. Schwingenschuh, H.K. Biernat, J.J. Berthelier, J. Blecki, M. Parrot, M. Stachel, Ö. Aydogar, G. Stangl, and J. Weingrill, "Similar behaviors of natural ELF/VLF ionospheric emissions and transmitter signals over seismic Adriatic regions," *Nat. Hazards Earth Syst. Sci.*, vol. 8, pp. 1229-1236, 2008.

[7.] M. Y. Boudjada, K. Schwingenschuh, J. J. Berthelier, A. A. Rohznoi, M. Parrot, P. F. Biagi, P. H. M. Galopeau, M. S. Solovieva, O. A. Molchanov, H. K. Biernat, G. Stangl, I. Moldovan, W. Voller, R. Döller, and M. Ampferer, "Decrease of VLF transmitter signal and Chorus-whistler waves before L'Aquila earthquake occurrence," *Nat. Hazards Earth Syst. Science*, 2010.

Modelling the stochastic component of seismo-electromagnetic Time series recorded by Demeter

N. Zaourar [(1)], R. Mebarki [(1)], M. C. Berguig [(1)], M. Hamoudi [(1)] and M. Parrot [(2)]

[(1)] Laboratoire de Géophysique, FSTGAT, USTHB, BP 32, 16123 Bab- Ezzouar, Alger, Algérie
nzaourar@usthb.dz; hamoudi@ipgp.jussieu.fr
[(2)] LPC2E (Laboratoire de Physique et Chimie de l'Environnement et de l'Espace), 3A Avenue de la recherche scientifique, 45071 Orléans, Cedex 2, France
mparrot@cnrs-orleans.fr

Keywords: Demeter, ionosphere, continuous wavelet, scaling exponent, prediction.

Abstract: This work focuses on multiscale analysis of ionospheric disturbances recorded by the microsatellite Demeter. Firstly, we analyze the time series related to plasma experiments recorded above Italy. The spectral analysis of the seismo-ionospheric signals shows that Fourier power spectra follow power law behaviour, as f^{β} (f- frequency, β- spectral exponent), typical of fractal self affine process. Thus, the possibility that these time series show the scale invariance associated with correlation to long ranges led us to propose the use of Continuous Wavelets Transform as a natural tool for investigation of ionospheric perturbations. Secondly, we examine the seismo-electromagnetic signals using a Fourier spectral analysis. We observe that the spectral behavior varies from one signal to another which means that electric and magnetic measurements recorded by Demeter are complex. However, some parameters are characterized by self affinity, reflecting properties of persistence or anti-persistence. These observations open the way to a theoretical analysis based on local wavelet exponents, and poses several questions concerning the use of signals regularity and its link to prediction of the seismic activity.

1. Introduction

The ionosphere is a sensitive medium to the solid earth phenomena, so the main scientific objective of the DEMETER mission [1] is related to the study of the ionospheric perturbations associated with the seismic and volcanic activities. The data base DEMETER, includes several temporal series of measurements of ionospheric various parameters relating to certain regions, characterized by a variable seismicity. Data series generated by complex systems, such as ionosphere, exhibit fluctuations on a wide range of time scales and /or broad distributions of the values. In both equilibrium and non-equilibrium situations, the natural fluctuations are often found to follow a scaling relation over several orders of magnitude. The fractal characterisation can be used for modelling the time series, and deriving predictions regarding extreme events or future behaviour.

In this study, we address a wavelet analysis under the multiscale framework [2] to show a correlation between patterns of seimo-ionospheric and seimo-electromagnetic fluctuations recorded by Demeter. In particular, our attention is directed to whether distinct alterations in the associated scaling parameters emerge when an intense event approaches. The physical effects responsible for the fractal properties will not be discussed here, since the purpose of this work is simply to characterize the persistence of the time series and possible dependence with earthquake preparation.

2. Data

On April 06, 2009 at 01: 32: 39 UT, an Mw 6.3 L'Aquila earthquake with depth 8.8 km struck central Italy (epicentre at 42.334° N, 13.334 °E) or 85 km north-east of Rome. The ionospheric disturbances occurring a few hours and a few days before the main shock provide a good opportunity to study the existence of a correlation between the time dynamics of data recorded by Demeter and probably connected with the mechanism of earthquake preparation processes. For this purpose, we use the data collected by Demeter through the half orbit 25447 up above Italy on April 04 2009 at 20: 01 00 during 23mn. The image Quick Look (Fig.1) shows that the Burst mode [1] was active in the interval (20: 27: 7: 208, 20: 31: 36: 208). The red arrow at 20: 29: 15 indicate

the position of the earthquake which occurred two days after. First, we are interested in time series obtained from the plasma experiments onboard DEMETER: the ion spectrometer IAP [3] and the Langmuir probe experiment ISL [4]. Measurements made by IAP (sampled with $\Delta t = 4{,}506s$), let us access to a wide range of perturbations indicating the fluctuations of temperature, density (the majority of ions H^+, He^+, O^+), velocity of local plasma ions and its flow direction. While ISL data (sampled with $\Delta t = 1s$) measures total density of the plasma, electron temperature and potential of satellite. Second, we have used the electric and magnetic field data from the ICE [3] and IMSC [1] experiments, more specifically, the measurements made in the Ultra Low Frequency (ULF), Extreme Low Frequency (ELF) and Very Low Frequency (VLF) bands.

3. Multiscale wavelet analysis of time series

A second-order statistical method is generally used to investigate the temporal fluctuations of a signal in order to get information regarding its correlation properties. The spectral analysis represented the standard method to detect correlation features in time series fluctuations. The Fourier power spectrum describes how the power is concentrated at various frequency bands. The notion of scale-invariance is defined closely as the absence of characteristic scales of a time series. Its main consequence is that the whole and its parts cannot be statistically distinguished from each other. The concept of scaling behaviour is associated with different features such as long-range dependence , self-affinity or fractality. All these processes are governed by scale laws where the power spectra are approximately inversely proportional to the frequency $f > 0$, $S(f) \sim f^{-\beta}$. The spectral exponent β controls the degree of correlation between successive points. Two classes of signal have been widely used to model stochastic fractal time series fractional Gaussian noise (fGn) and fractional Brownian motion (fBm). For the case of the fGn model the scaling exponent β lies between -1 and 1, while the regime of fBm is indicated by β values from 1 to 3. The difficulty of the power spectrum is its dependence on the nonstationarities, often not well-known and whose presence can produce misleading scaling estimation in a time series. For this purpose, we perform a multi-scale wavelet analysis [2] on the Demeter data in order to derive the coefficients of its power spectrum. Wavelet-based estimators have been used very successfully for estimating scaling behaviour applied to time series. The central properties of self affine process enable one to establish a scaling relation between wavelet coefficients and scale. The local spectral exponent is then easily derived. Wavelet analyses have no inherent problems as those in Fourier analysis, such as windowing, detrending, etc. By considering analysing wavelets that make the wavelet transform blind to the low frequency trends, any bias in the raw data can be removed and the existence of power law correlation with scale invariance properties can be revealed accurately.

4. Results and discussion

The results of the wavelet analysis of the IAP (NH+, NHe+, NO+, Ti) and ISL (Ne, Te, Vp, Vf) time series are presented in top of Fig. 1. For all case, Fig. 1 shows that the power spectra take a power law form typical of scaling process, with the average exponent *b* corresponding to the slope of the best fitting line in the log-log plot. The suitability of the fit of a time series to the power-law is represented by the linear correlation coefficient r (r is always above 0.95). The spectral exponent restricted to $1<\beta<3$ is typical of fBms. The stochastic component of a time series has two main aspects, its statistical distribution of values and its persistence. The persistence measures the correlations between adjacent values within the time series and can be strong, weak, or nonexistent (case of a white noise). Values of a time series can affect other values in the time series that are not only nearby in time (short range), but also far away in time (long range). Since self-affine time series have a power-law dependence of the power-spectral density function on frequency, they exhibit long-range persistence. As example, we illustrate in Fig. 1 (bottom) the nature of the transition described by the temporal evolutions of $\beta\ (t)$ curves, related to four parameters of IAP data. The green horizontal line represents the threshold between antipersistent/persistent behaviour reflected by the scaling exponent $\beta(t)$. The power index seems to be correlated with the ionospheric activity of the sampled area. For the NH+, N0+ and Ti signals, the intense event or precursor, occurred at 20: 29: 15 is remarkable as a jump in the exponent (corresponding to 20: 28 in the Fig.1). The scaling exponents indicate persistent properties with $\beta(t) \sim 3$. In the case of the NHe+, we observe decreasing values $\beta(t)$ displaying an antipersistent behaviour near the onset of this precursor. All these observations are consistent with the fact that the fractality of the data signals IPA-ISL result of diffusion or

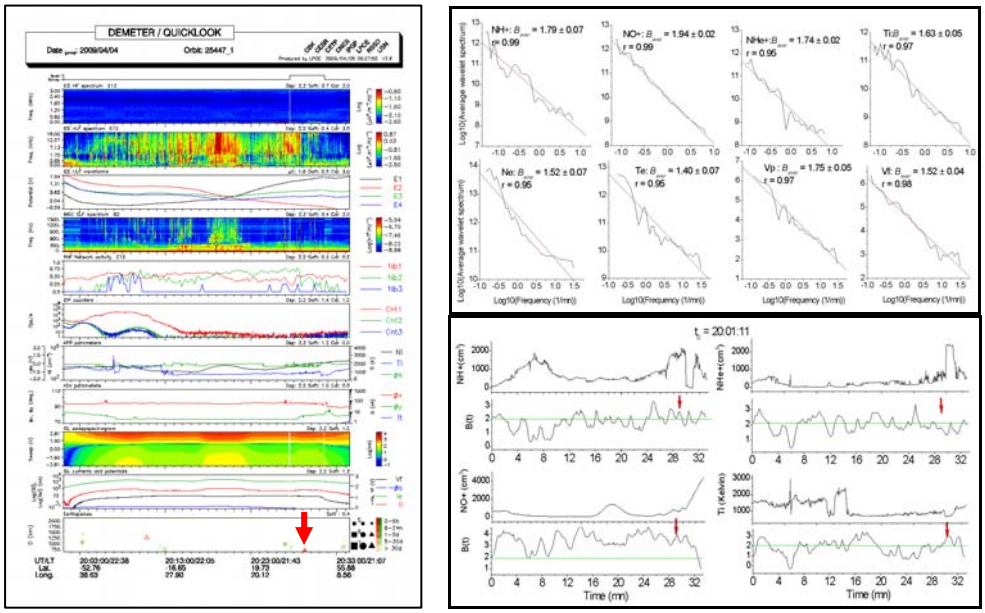

Fig. 1 Left: Demeter quicklook orbit_254471. Top: spectra of IAP and ISL data. The slope of the regression line, indicated on each plot, reveals the average scaling exponent β and the linear correlation coefficient r. Bottom: ions NH+, NHe+, NO+, Ti and associated dynamics of wavelet spectral exponents. Red vertical arrows above the scaling exponent indicate the phase transition near the precursor onset.

interaction elastic interaction occurring between the plasma particles excited by the propagation of the acoustic gravity- wave. We illustrate in Fig. 2 (a) examples of Fourier spectra for some electric and magnetic components. For ULF data, we note an approximately single scaling behaviour for the entire investigated frequency band. In ELF electric and magnetic component, the scaling behaviour is not uniform at all frequency band. The fluctuations curve related to VLF electric (E12) and magnetic (B2) spectra show a multi-scaling behaviour, which in some frequency region is also very rough and irregular. The scalograms (Fig. 2 (b)) show that larger energy wavelet coefficients are more frequent at low frequency. The decreasing energy towards high frequency confirms the scaling behaviour. For the tree components, the spectral exponents indicate transition from a less correlated to a more correlated pattern of multiscale fluctuations at 27mn, around the Demeter burst mode onset. During active interval contained the precursor event, the scaling exponents increase abruptly reaching a maximum value of $\beta(t) \sim 3$ for ULF Ey component. This behaviour indicates a gradual increase of the memory, and thus a gradual reduction in complexity in the underlying dynamics.

(a) (b)

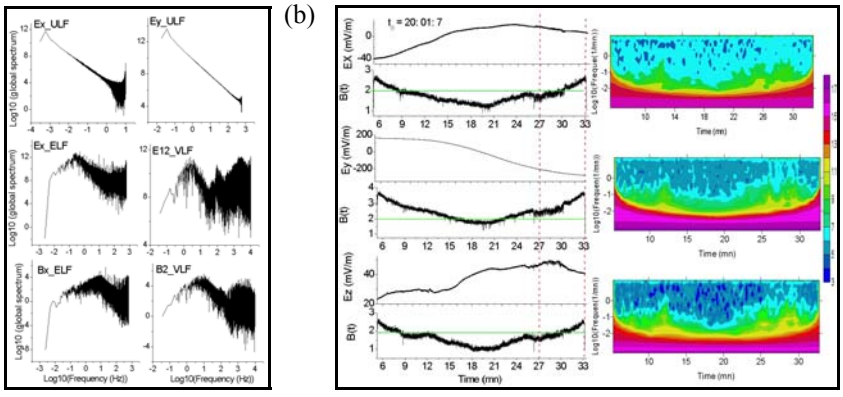

Fig. 2 (a) Fourier power spectra of ULF, ELF and VLF data. (b) Left: ULF time series and associated dynamics of wavelet exponents. Right: scalograms revealing the energy distribution of the wavelet coefficients

Fig. 3 show the electric and magnetic time series recorded in the ELF (sampled with $\Delta t = 0.0004$ s) and VLF frequency (sampled with $\Delta t = 2.5.10^{-5}$ s) band. For the VLF data, the signal exhibits a quasi uniform behaviour of the whole time series we use only 524288 points. We found that the spectral temporal fluctuations either implies fGn behavior (range with $-1 < \beta < 1$) for the ELF and VLF electric and magnetic data, or signifies an activity compatible with the fBm model possessing anti-persistent properties (range with $1 < \beta < 2$) for B2 component. The process fGn suggests that the temporal exponents are random (does not display correlations), where the B2 magnetic scaling index with mean value $\beta(t) \sim 1.84$ indicate antipersistency. Physically, this implies that fluctuations tend to induce stability within the system (negative feedback mechanism).

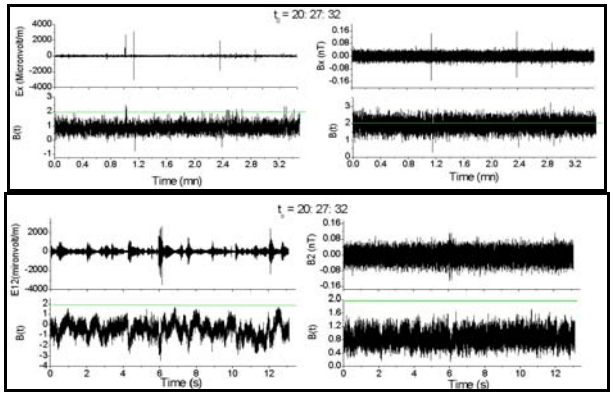

Fig. 3. Top Ex and Bx ELF components and associated temporal fluctuations exponents.
Bottom: E12 and B2 VLF components associated temporal fluctuations exponents

5. Conclusion

Our analysis suggests as a main result that a spectral signature related to the emergence of persistency of the seismo ionospheric time series precedes an intense event . Results from the analysis of data from another event related to Honshu earthquake support the findings reported in [5]. Similar results are observed in ULF electric data suggesting that the occurrence of an intense event may represent a gradual transition from a less orderly state to a more orderly state. As for future work, we will explore the ELF and VLF time series using Robust Statistics based on stochastic fractional differential equations

6. References

[1] M. Parrot, D. Benoist, J.J. Berthelier, J. Bleckid, Y. Chapuis, F. Colin, F. Elie, P. Fergeaua, D. Lagoutte, F. Lefeuvre, C..Legendre, M. Lévêque, J.L. Pincon, B. Poirier, H-C. Seran and P. Zamora, "The magnetic field experiment IMSC and its data processing onboard DEMETER: Scientific objectives, description and first results," *Planetary and Space Science*, vol. 54, pp. 441–455, April 2006

[2] N. Zaourar, R.Mebari, L. Briqueu, M. Mandea and M. Hamoudi, "Wavelet analysis applied to InterMagnet data: Singularity detections related to geomagnetic storms," *The Journal of National Research Institute of Astronomy and Geophysics,* Special Issue on the ACAG-1*,* pp. 295-309, October 2008.

[3] J.J. Berthelier, M. Godefroy, F. Leblanc, E. Seran, D. Peschard, P. Gilbert and J. Artru, *"*IAP, the thermal plasma analyzer on DEMETER", *Planet Space Science*, vol. 54, p. 487-501, April 2006

[4] J. P. Lebreton, S. Stverak, P.Travnicek, M. Maksimovic, D. Klinge, S. Merikallio, D.Lagoutte, B. Poirier, Z. Kozacek and M. Salaquarda, " The ISL Langmuir Probe experiment and its data processing onboard DEMETER: Scientific objectives, description and first results," *Planet Space Science*, vol.54, p. 472–486, .April 2006

[5] N. Zaourar, R. Mebarki, M. Hamoudi and M. Parrot, " La dynamique fractale des perturbations seismo-ionosphériques, " *Télédétection*, (submitted).

Commission “H”

Waves in Plasma

Whistler Waves as a Remote Sensing Tool for Plasma Fluctuations

Agapitov Oleksiy [1,2], ***Vladimir Krasnoselskikh*** [1]

[1] LPC2E / CNRS-Universite d'Orleans 3A Avenue de la Recherche Scientifique 45071 Orleans CEDEX 2 ; agapitov@lpce.cnrs.fr,
[2] National Taras Shevchenko University of Kyiv, Volodymyrska 64, Kyiv, Ukraine.

Keywords: Radiation Belts, Chorus waves, Propagation in randomly inhomogeneous plasma, Multipoint measurements in space.

Abstract: We present statistical model describing propagation of waves in randomly fluctuating plasma. These fluctuations result in variations of the refraction index, and the statistics of this last is supposed to be Gaussian with two characteristic correlation scales, along and perpendicular to the ray path. We show that multi-point measurements of these wave signals can allow one to determine these scales and the distance to the wave source. This technique is applied to real data of measurements of so called “chorus” waves that propagate as whistler mode waves onboard Cluster and THEMIS missions. The electron concentration perturbation scale was assumed and found to be much smaller than the estimated chorus generation region scale. The analysis performed allows to evaluate the parallel and transverse perturbation scales and to estimate the distance to the source along the magnetic field line. The discrete chorus elements were observed in the frequency range 0.15–0.25 of the local electron gyrofrequency typical for the outer magnetosphere. The field-aligned Poynting flux of whistler emissions shows that they propagate along the magnetic field lines in the direction away from the! magnetic field minimum that is consistent with the waves being generated there. The averaged amplitude correlation analysis allows us to estimate the characteristic spatial half-width of the source region transverse to the local magnetic field to be about 2800–3200 km. The phase cross-correlation time dependences give a correlation scale from 250 to 500 km transverse to the local magnetic field. The obtained distance to the source region varies from 400 to 2000 km. An interesting observation following from the analysis consists in an estimate of the source speed to be about 5–10 thousands km/sec along the magnetic field line.

1. Introduction

Discrete ELF/VLF chorus emissions, the most intense electromagnetic plasma waves observed in the Earth's radiation belts and outer magnetosphere, have received increased attention in the past several years. Characterized by rising and falling tones in the frequency range from a few hundreds to several thousands of hertz (e.g., reviews by [1], and [2],), these emissions play the significant role in local acceleration of energetic electrons in the outer radiation belts [3]. Chorus is a burst-like wave emission observed in the near-Earth magnetosphere outside the plasmapause. These emissions are most often observed on the Earth's dawn side between 2300 and 1300 MLT [4, 5]. Chorus emissions, which propagate in the whistler mode, usually consist of two narrow frequency range bands centered around one-half the electron gyrofrequency at the geomagnetic equator (Ω_e) of the magnetic field line on which the waves are observed [4]. If present, the upper band exists in the frequency range of $\omega/\Omega_e \approx 0.5-0.75$ and contains discrete chorus elements rising at a few kHz/s. The lower band exists in the frequency range of $\omega/\Omega_e \approx 0.2-0.45$ and contains both elements rising at a few kHz/s and diffuse elements.
In this paper we address the transverse dimensions of chorus sources using simultaneous observations of intense chorus In this paper we address the transverse dimensions of chorus sources using simultaneous observations of intense chorus by five THEMIS spacecraft (THA, THB, THC, THD, THE) before they were finally deployed into their designated orbits [6]. The analysis is done for regions close to the geomagnetic equator at a radial distance of 8—9 Earth radii (RE) which is not covered by previous work using CLUSTER data with new technique based on nonstationarity of the mutual statistic characteristics. We correlate and analyze waveform

data from the five spacecraft at different separations. Our study is based mainly on high-resolution, three-axis magnetic waveform data from the search coil magnetometer (SCM) [7] and two-axis electric waveform data from the electric field wave instrument (EFW) [8]. We also use supporting data from the electrostatic analyzer (ESA) and spin-averaged measurements from the flux-gate magnetometers (FGM) [9].

2. Submission Requirements

Chorus waves belong to the whistler wave mode. We shall consider the so-called electron whistler waves in the frequency range from the lower hybrid frequency to the electron gyrofrequency. Their refraction index can be found using the dispersion relation in the cold plasma approximation [10]:

$$n^2(\omega,\theta) = 1 + \omega_{pe}^2 \Big/ \omega\left(\Omega_e|\cos\theta| - \omega\right) \tag{1}$$

where ω_{pe}^2 is the electron plasma frequency, and θ is the angle between the wave $\vec{k}$-vector and the background magnetic field. This dependence upon the angle results in anisotropy of the phase and group velocities and dependence of the wave polarization upon the angle. We shall consider multipoint measurements of whistler waves that are supposed to have group velocities almost along the magnetic field. Our goal is to analyze multipoint correlations. Plasma density inhomogeneities are usually separated into two groups according to their characterristic scale with respect to the wavelength. Small-scale inhomogeneities can scatter whistler mode waves in all directions and profoundly change wave characteristics. Large-scale inhomogeneities with spatial scales comparable to and larger than the wavelength can produce slow variations in wave $\vec{k}$ -.vector amplitude and direction. This can be done using regular procedures based on small perturbations of the unperturbed solution. We describe such an approach making use of the simplified model developed for the wave propagation in random media.

The wave-related field perturbation can be written as

$$u = U_0 \exp(iS + \chi) \tag{2}$$

The amplitude level and wave phase fluctuation due to propagation effects are estimated from the Helmholtz equation with some assumptions. Taking advantage of the results of [11] and [12], let us consider the wave propagating from the source region in the plasma with large-scale random density fluctuations characterized by two scales parallel and perpendicular to the background magnetic field. The primary wave is thought to propagate along the magnetic field. Let us assume that wave propagation can be described in the geometrical optics approximation. With such an approach, one does not consider backward scattering and diffraction effects. Use of the geometric optic approximation is justified if the first Fresnel zone is much smaller than the characteristic inhomogeneity scale of the dielectric permeability (refractive index for wave propagation along the magnetic field). Let us suppose that the refractive index can be separated into mean value and fluctuations :

$$\varepsilon(\vec{r}) = \langle \varepsilon(\vec{r}) \rangle + \delta\varepsilon(\vec{r}) \tag{3}$$

Below we use the correlation function of the refractive index described by the anisotropic Gaussian correlation function:

$$\Psi_\varepsilon(\vec{r}) = \sigma_\varepsilon^2 \exp\left(-z^2 \Big/ 2l_{||}{}^2 - \left(x^2 + y^2\right) \Big/ 2l_{\perp}{}^2\right) \tag{4}$$

where the Z is the axis should be directed along the back ground magnetic field direction, X and Y are perpendicular to it, and the distribution in the perpendicular direction is isotropic. In the framework of assumptions made, the eikonal and amplitude level fluctuations are described by the Helmholtz equation

$$\Delta u + k^2 \varepsilon(\vec{r}) u = 0 \tag{5}$$

We are interested in the evaluation of the correlation function of eikonal (and related with the eikonal phase) and of the amplitude level correlation. Both characteristics can be found by using correlation function of the refractive index [12]. Assuming that the primary wave propagates approximately along the background magnetic field, one can find for Gaussian correlations of the refractive index with two characteristic scales, parallel and perpendicular, the phase correlation function in the following form:

$$\Psi_S(\vec{r}_1,\vec{r}_2)=\sqrt{\frac{\pi}{2}}\frac{z_{\min}l_{\|}k^2\sigma_\varepsilon^2}{2\langle\varepsilon(\vec{r})\rangle}\exp\left[-\frac{(\vec{\rho}_1-\vec{\rho}_2)^2}{2l_\perp^2}\right] \tag{6}$$

Here $z_{\min}=\min(z_1,z_2)$, $\Psi_S(\vec{r}_1,\vec{r}_2)$ is the correlation function of the refractive index. It follows then that

$$\sigma_S^2(z)=\sqrt{\frac{\pi}{2}}\frac{zl_{\|}k^2\sigma_\varepsilon^2}{2\langle\varepsilon(\vec{r})\rangle} \tag{7}$$

Comparing the amplitude and the eikonal variance, one finds which means that the amplitude variance should be substantially smaller than the eikonal variance and in the first Fresnel zone can be neglected. Making use of the relation $\left\langle e^{i\xi}\right\rangle=e^{-1/2\left\langle\xi^2\right\rangle}$ for normally distributed ξ with $\left\langle\xi\right\rangle=0$ and with use the phase structure function $D_S(\vec{r}_1,\vec{r}_2)=\left\langle\left(\tilde{S}(\vec{r}_1)-\tilde{S}(\vec{r}_2)\right)^2\right\rangle$ the following expression for the cross-correlation is obtained

$$\Gamma_u(\vec{r}_1,\vec{r}_2)_T\approx A(\vec{r}_1,\vec{r}_2)u_0^2\exp\left[-\frac{1}{2}D_S(\vec{r}_1,\vec{r}_2)\right] \tag{8}$$

Taking the exposure time long enough ($t>>\tau$). τ is the characteristic time for the plasma media changes) for two signals to be registered at separate points, i. e., having ray paths through the medium where the refractive index can be considered as partially independent ($D_S(\vec{r}_1,\vec{r}_2)\equiv D_{S12}$)

$$D_{S12}=\sigma_1^2+\sigma_2^2-2\sigma_1\sigma_2K_{S12} \tag{9}$$

For the $t<<\tau$ D_{S12} is a function of t and will grow with the exposure time approximately linearly

$$D_{S12}(t)\approx\sqrt{\left(\sigma_1^2+\sigma_2^2-2\sigma_1\sigma_2K_{S12}\right)\cdot t/\tau} \tag{10}$$

Then for the $t<<\tau$ for the coherence function dependence on expose time T one has

$$\Gamma_u(\vec{r}_1,\vec{r}_2)_T\approx A(\vec{r}_1,\vec{r}_2)u_0^2\frac{1-\exp(D_{12}T/\tau)}{D_{12}T/\tau} \tag{11}$$

where $A(\vec{r}_1,\vec{r}_2)$ is the coefficient less than 1. Let Z be the distance from the source to the closest spacecraft then the procedure employed is based on the solution of the system of equations

$$\frac{\sigma_{12}}{\tau}=\alpha\left[z\left(1-\exp\left(-\frac{\rho_{12}^2}{2l_\perp^2}\right)\right)+0.5z_{12}\right] \tag{12}$$

The application of the proposed technique to the THEMIS measurements of the same chorus element onboard three spacecraft THC, THD, and THE is shown in the Fig.1 (see [13] for details).

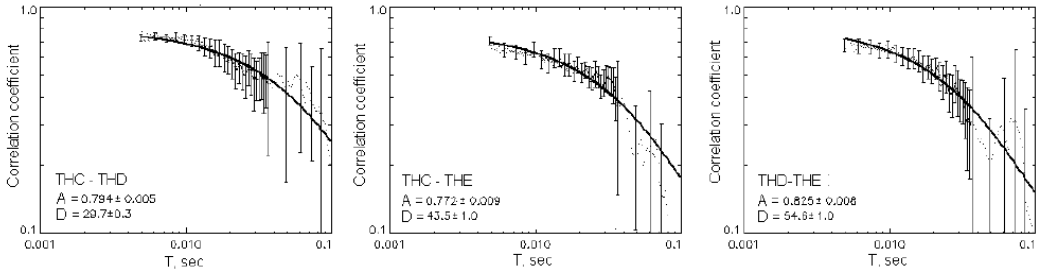

Fig.1. Cross-correlation analysis of the discrete chorus element observed at 13:12 UT on 17 July 2007 onboard THEMIS spacecraft. The correlation coefficient time dependence is shown for spacecraft THC-THD, THC-THE, and THD-THE, respectively. The approximation with function is shown with solid line. The approximation parameters are listed.

3. Conclusion

We propose the novel analysis technique aiming to estimate the characteristics of electron concentration fluctuations by solving the reverse problem of the wave propagation through the random media. This method

similar to interferometry technique is based on the multi spacecraft chorus waveform measurements near the source region. It allows one to evaluate the characteristic scales of fluctuations of dielectric constant of the medium along and transverse to the direction of the wave propagation and the characteristic distance to the chorus source. Since the electron concentration perturbation scale is much smaller than the estimated chorus generation region scale, the analyzed event allows us to obtain a good assumption for the chorus source region scale. Also propagation nearly parallel to the local magnetic field gives an opportunity to distinguish the parallel from the transverse perturbation scale and to estimate the distance to the source along the magnetic field line. The field-aligned Poynting flux of whistler emissions shows that they propagate along the magnetic field lines in the direction away from the magnetic field minimum that is consistent with the waves being generated there. The averaged amplitude correlation analysis allows us to estimate the characteristic spatial half-width of the source region transverse to the local magnetic field to be about 2800–3200 km. The correlation scale of refractive index and the electron concentration perturbation are estimated under the geometric optic assumption. The phase cross-correlation time dependence gives a correlation scale from 250 to 500~km transverse to the local magnetic field. The obtained distance to the source region varies from 400 to 2000~km with source speed about 5–10 thousands km/sec along the magnetic field line.

Acknowledgment

This work was supported by CNES through the grant "Modeles d'ondes", and by the ECO NET program of the EGIDE(France).

References

[1.] Omura, Y., Nunn, D., Matsumoto, H., and Rycroft, M. J., A review of observational, theoretical and numerical studies of VLF triggered emissions, *J. Atmos. Terr. Phys.*, *53*, 351—368, 1991.

[2.] Sazhin, S. S. and Hayakawa, M., Magnetospheric chorus emissions: A review, *Planet. Space Sci.*, *40*, 681—697, 1992

[3.] Horne, R. B., R. M. Thorne, Y. Y. Shprits, N. P. Meredith, S. A. Glauert, A. J. Smith, S. G. Kanekal, D. N. Baker, M. J. Engebretson, J. L. Posch,M. Spasojevic, U. S. Inan, J. S. Pickett, and P.M.E. Decreau, Wave acceleration of electrons in the Van Allen radiation belts, *Nature* ,*437* , 227—230, doi:10.1038/nature03939, 2005.

[4.] Tsurutani, B. T. and Smith, E. J., Postmidnight chorus: a substorm Phenomenon, *J. Geophys. Res.*, *79*, 118—127, 1974.

[5.] Meredith, N. P., R. B. Horne, and R. R. Anderson, Substorm dependence of chorus amplitudes: Implications for the acceleration of electrons to relativistic energies, *J. Geophys. Res.*, *106* , 13.165, 2001.

[6.] Sibeck, D.G. and Angelopoulos, V., THEMIS science objectives and mission phases, *Space Sci. Rev.*, doi: 10.1007/s11214-008- 9393-5, 2008.

[7.] Bonnell, J.W., Mozer, F. S., Delory, G. T., Hull, A. J., Ergun, R. E., Cully, C. M., Angelopoulos, V., Harvey, P. R., *Space Sci. Rev.*, *141*, 303, 2008.

[8.] Le Contel, O., Roux, A., Robert, P., Coillot, C., Bouabdellah, A., de la Porte, B., Alison, The Search Coil Magnetometer for THEMIS, *Space Science Reviews*, *141*, 0038—6308, 2008.

[9.] Auster, H., et al., The THEMIS fluxgate magnetometer, *Space Sci.Rev.*, doi:10. 1007/s11214-008-9365-9, 2008.

[10.] Helliwell R. A., Whistlers and related ionospheric phenomena,1967.

[11.] Rytov, S. M., Yu. A. Kravtsov, V. I. Tatarskiy, Introduction to the statistical radiphysics, *Moscow, Science, Volume 2*, 1978.

[12.] Agapitov, O. V., V. Krasnoselskikh, and G. Rolland Multi spacecraft Cluster observations of chorus emissions as a tool for the remote sensing of plasma density fluctuations, *J. Geophys. Res.*, 2009 (in press).

[13.] Agapitov O., V. Krasnoselskikh, Yu. Zaliznyak, V. Angelopoulos, O. Le Contel, and G. Rolland Chorus source region localization in the Earth's outer magnetosphere using THEMIS measurements, *Ann. Geophys.*(in press)

An investigation of Titan's resonant ionospheric cavity with the PWA instrument on the HUYGENS probe. The generation of ELF wave and the detection of a buried ocean at a depth of about 45 km.

M. Hamelin [(1)], C. Béghin[(2)], R. Grard[(3)], J.J. Lopez Moreno[(4)], O. Randrianboarison [(2)], K. Schwingenschuh(5), F. Simoes(1,6),C. Sotin(7)

[(1)] Université Versailles St Quentin CNRS/INSU LATMOS-IPSL, UPMC, 4, place Jussieu, Paris, France
michel.hamelin@latmos.ipsl.fr
[(2)] LPCE-CNRS-Université d'Orléans, 3A, Av. Recherche Scientifique, 45071 Orléans Cedex 2, France
cbeghin@cnrs-orleans.fr; randriam@cnrs-orleans.fr
[(3)] RSSD, ESA-ESTEC, European Space Agency, Keplerlaan 1, 2200 AG Noordwijk, The Netherlands
rgrard@rssd.esa.int
[(4)] Instituto de Astrofisica de Andalucia, CSIC, Granada, Spain.
lopez@iaa.es
[(5)] Space Research Institute, Austrian Academy of Sciences (IWF), Schmiedlstrasse 6, 8042 Graz, Austria
konrad.schwingenschuh@oeaw.ac.at
[(6)] NASA/GSFC, Greenbelt, MD, USA
fernando.a.simoes@nasa.gov
[(7)] Jet Propulsion Laboratory and California Institute of Technology, Pasadena, CA 91109, USA
christophe.sotin@jpl.nasa.gov

Keywords: Titan; Atmospheres; Ionospheres; Magnetospheres; Schumann resonances; Planet interiors.

Abstract: During the descent of the Huygens probe through the atmosphere of Titan, the PWA instrument did not only record the local profiles of the ion and electron conductivities, but also measured the global characteristics of the ionospheric cavity and boundaries from the observation of the electromagnetic wave environment. The instrument, originally designed for the detection of possible lightning events, that trigger Schumann resonances on Earth, did not record any electric discharge but observed a continuous strong, narrow band, emission at around 36 Hz. This paper reviews the detailed and careful analysis performed by the team during the last five years, including an assessment of the instrument performance and a critical evaluation of misleading artefacts. Conductivity profiles obtained via two complementary different techniques are found to fit theoretical models, except above ~90 km where electrons might be captured by aerosols. Following a close examination, it appears that the 36 Hz wave emission is likely a natural phenomenon. The energy that sustains the emission in the whole resonant cavity is generated by the interaction of Titan with the co-rotating Saturn magnetosphere. The fact that the electromagnetic wave amplitude does not vanish at the surface of Titan, a rather poor conductor, indicates that the reflecting boundary, possibly the top of Titan's H2O-NH3 buried ocean, must lie at a depth of ~45 km.

1. Introduction

Titan, one of the largest moons of the solar system holds a dense and extended atmosphere composed mainly of nitrogen. The similarities with the ancient Earth were a driver for the selection of experiments on board the

HUYGENS probe, and questions about the possible role of lightning on prebiotic chemistry (although no lightning activity was detected by the Voyager flybys) lead to include PWA (Permittivity, Waves and Altimetry), an atmospheric electricity instrument on board, as a part of HASI (HUYGENS Atmospheric Structure Instrument). The instrument was designed to measure the atmospheric conductivity *in situ* during the descent under parachute from ~140 km to the ground by two complementary techniques, the mutual impedance probe (MI) for electrons and the Relaxation probe (RP) for positive and negative charges. In the case of a soft landing PWA could also measure the ground permittivity. In a passive mode electromagnetic waves could be recorded in the ELF and VLF bands (see instrument description in [1]).
The conductivity measurements and the neutral atmosphere measurements of HASI aimed to provide conductivity and ionized density profiles for comparison with theoretical models [2-4], and the electromagnetic wave measurements were focused on the resonances in the ionospheric cavity for investigation of a possible lightning activity and characteristics of the boundaries, upper ionosphere and ground -or underground- reflector.
The real experiment showed difficulties and surprises. We present here a review of the analytical work, from the basic measurements compared with theoretical models of conductivity to the more general view of the physical processes in the ionospheric resonant cavity where no noticeable lightning activity was detected, and last but not the least the detection of a buried ocean at about 45 km depth.
There were technical difficulties that implied a very careful and long analysis. A first part will present the conductivity measurements with the two MI and RP concurrent techniques. The next part will report the investigations about electromagnetic waves and their interpretation as Schumann resonances in Titan's ionospheric cavity. The last part will present the overall picture of waves generated from the interaction of Titan with the rotating Saturn magnetosphere, with an amplitude profile indicating the presence of a reflector not on Titan's surface but at about 45 km depth, likely the top of Titan's buried putative ocean.

2. The conductivity and electromagnetic waves measurements

The PWA sensors setup is shown in Fig. 1 (left). The PWA booms hold the two MI emitting electrodes (small rings) and the two receiving ones (large rings), and the two RP disc electrodes. The MI instrument measures the mutual impedance between the two MI emitting and receiving couples of electrodes at a frequency of 45 Hz in the atmosphere of Titan, which allows to derive the conductivity hold by electrons. On the ground it operates at several frequencies in the range 45-5760 Hz to derive the ground complex permittivity. A passive mode using the receiving dipole allows to measure the related horizontal component of the electric field. The RP electrodes are discs charged at ±5 V. Then, they are returning to the floating potential by collecting positive or negative charges from the medium. Polar conductivities are deduced from the time constants of the relaxation. The MI and RP conductivity measurements have been analysed in [5-8] and the results are summarized in Fig. 1 (center). The MI measurements above 100 km have been discarded due to a probable incomplete deployment of the booms and velocity effects have been taken into account. The RP and MI values of the electron conductivity show some acceptable difference, but both show a conductivity peak around the altitude of 65 km, caused by the galactic cosmic radiation. The profile follows roughly the theoretical predictions [2,4] up to about 100 km, and above it collapses likely due to electron attachment to aerosols. Due to a failure of transmission only negative electron conductivity has been measured accurately; the positive ion conductivity was found close to the threshold of the instrument [6,8]. Ground measurements -if the electrode system geometry was kept at landing- lead to a dielectric constant of ~2.3 and a conductivity of ~1 nS/m. Possible deviations are under study.
ELF wave measurements are shown in Fig.1 (*right*). In the 0-100 Hz range dedicated for Schumann resonances investigations, a strong emission was detected around 36 Hz, that did not correspond to the fundamental Schumann mode for Titan. An extensive investigation of possible artefacts was undertaken till the last vibration tests of the PWA booms at cryogenic temperature in ESTEC (see [10] for details). A first study [9] showed that under particular conditions it could be the second mode of a Schumann resonance. However the ELF signal showed characteristics of a natural linearly or highly elliptically polarized wave [11], leading to the possibility of resonances different from the terrestrial case.

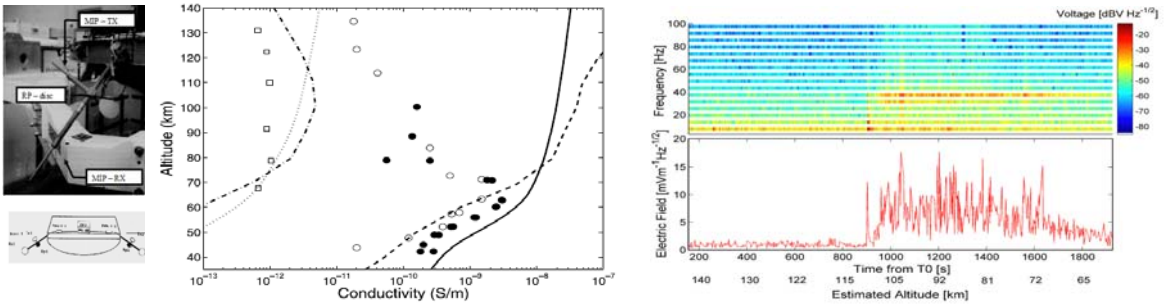

Figure 1. *Left*: the PWA sensors on the HUYGENS probe. *Center*: The two components of the conductivity of the atmosphere of Titan between 40 and 140 km altitude: positive charges (□) and negative charges (○) measured by RP2, and negative charges measured by MI (●). Lines show the conductivity predicted by Molina-Cuberos *et al*. [2], (…) and (–) and by Borucki and Whitten [4], (-.-.) and (--). *Right*: ELF spectogram 0-100 Hz in the range of altitudes 142-62 km, and amplitude of the 36 Hz line.

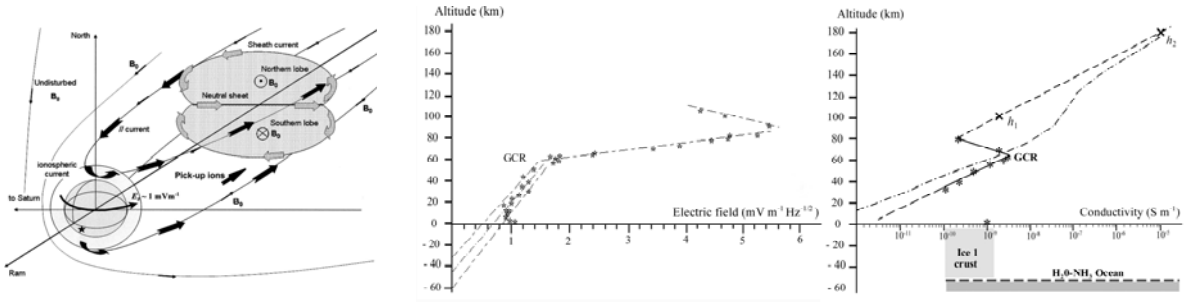

Figure 2. *Left*: Sketch of the wake interaction between Titan and Saturn's magnetosphere, and the induced driven current system (Huygens landing is site pointed out by a star). *Center*: Smoothed radial (vertical) altitude profile of the 36 Hz horizontal electric-field amplitude (*EH*); *stars*: average of 32 data packs containing 30 to 100 spectra each; *dash-dot lines*: least-square linear regression fits, extrapolated below the surface through a presumed lossless icy crust down to a highly conductive surface. *Right panel*: Measured and predicted electron conductivity profile; a*sterisks*: electron conductivity derived from PWA-MI instrument in the atmosphere and at the surface; *crosses* h_1, h_2 and *dash line*: conduction and reflection boundaries, respectively, and constrained model-profile (see text in [12]), *dash-dot line*: theoretical model-profile [4] assuming haze of aerosols with 7.2 eV photoemission threshold.

3. ELF Waves in Titan's resonant cavity and buried ocean boundary

Despite searching possible lighting activity on Titan no reliable clues were found from PWA as well as from the RPWS instrument on board CASSINI. It was shown in [10-12] that the source of energy could be found in the currents developed by the interaction of Titan with the rotating magnetosphere of Saturn (~thousands of MW available).The waves are excited through non linear processes , and after wards back scattered in the atmospheric cavity. The PWA conductivity measurements and deduced theoretical model that includes an insulating ice upper layer, together with the experimental fact that the electromagnetic wave amplitude profile

does not vanish at the surface of Titan leads to the presence of a reflector at 45±15 km depth, likely the top of a H20-NH3 buried ocean.

4. About some published erroneous data analysis and conclusion

The PWA data were released in the public ESA-NASA archive system in july 2007 and were immediately used with an erroneous signal processing technique by independent authors who claimed the detection of no more than 6 Schumann resonances from our 16 lines ELF spectral data. Such irrelevant processing and the claimed returns have been soon acutely disputed by PWA experimenters in a comment of the involved publication [13].
The overall interpretation of the rich PWA data is far to be achieved, and we are proceeding now with a careful analysis of the surface data to quantify the possible deviations introduced by possible system geometry changes at landing. The work is still supported by ESA, ASI, NASA, austrian, french and spanish agencies.

References

[1.] R. Grard, *et al.*, "An experimental investigation of atmospheric electricity and lightning activity to be performed during the descent of the Huygens Probe on Titan," *J.* from our 16 lines ELF spectral data *Atm. Terr. Phys*, vol. 57, pp. 575-585, 1995.

[2.] G.J. Molina-Cuberos *et al.*, "Chemistry of the galactic cosmic ray induced ionosphere of Titan", *J. Geophys. Res.*, vol. 104, pp. 21997-22024, 1999.

[3.] W.J. Borucki *et al.*, "Predictions of the electrical conductivity and charging of the aerosols in Titan's atmosphere." *Icarus*, vol. 72, pp. 604-622, 1987.

[4.] W.J. Borucki and R. C. Whitten, "Influence of high abundances of aerosols on the electrical conductivity of the Titan atmosphere", *Planet. Space Sci.*, vol.56, pp. 19– 26, 2008.

[5.] M. Fulchignoni *et al*., "The Characterisation of Titan's Atmospheric Physical Properties by the Huygens Atmospheric Structure Instrument (Hasi)," *Space Sci. Rev.*, vol. 104, pp. 395-431, 2002.

[6.] Grard, R. *et al*., «An experimental investigation of atmospheric electricity and lightning activity to be performed during the descent of the Huygens Probe on Titan". *J. Atmos. Terr. Physics*, 57, 575-585, 1995

[7.] M. Hamelin et al. " Electron conductivity and density profiles derived from the mutual impedance probe measurements performed during the descent of Huygens through the atmosphere of Titan." *Planet. Space Sci.*, vol. 55, pp. 1964-1977, 2007.

[8.] J.J. Lopez Moreno *et al.*, "Structure of Titan's low altitude ionized layer from the Relaxation Probe onboard HUYGENS." *Geophys. Res. Letters*, vol. 35, L22104, doi:10.1029/2008GL035338, 2008

[9.] F. Simoes *et al.*, "A new numerical model for the simulation of ELF wave propagation and the computation of eigenmodes in the atmosphere of Titan: did Huygens observe any Schumann resonance?" *Planet.SpaceSci*., vol. 55, pp. 1978–1989, 2007.

[10.] C. Beghin *et al.*, "A Schumann-like resonance on Titan driven by Saturn's magnetosphere possibly revealed by the Huygens Probe." *Icarus*, vol.191, pp. 251–266, 2007.

[11.] C. Béghin et al., "New insights on Titan's plasma-driven Schumann resonance inferred from Huygens and Cassini data." *Planet. Space Sci.*, vol. 57, pp. 1872-1888, 2009.

[12.] C. Beghin, C. Sotin and M. Hamelin, "Titan's native ocean revealed beneath some 45 km of ice by a Schumann-like resonance." *C.R. Geoscience*, vol. 342, pp. 425-433, 2010.

[13.] M. Hamelin *et al.*, "Comment on 'Evidence of electrical activity on Titan drawn from the Schumannresonances sent by Huygens probe' by J.A. Morente, J.A. Portí, A. Salinas, E.A. Navarro [2008, Icarus, 195, 802–811]", *Icarus*, vol. 204, pp. 349–351, 2009.

Global MHD Modeling of Coronal Mass Ejections and Related Shocks from Complex Active Regions

Ilia I. Roussev [(1)]***, Noé Lugaz*** [(1)]***, and Igor V. Sokolov*** [(2)]

[(1)] Institute for Astronomy, University of Hawaii, 2680 Woodlawn Drive, Honolulu, HI 96822, USA
iroussev@ifa.hawaii.edu; nlugaz@ifa.hawaii.edu
[(2)] Department of AOSS, University of Michigan, 2455 Hayward Street, Ann Arbor, MI 48109, USA
igorsok@umich.edu

Keywords: MHD–shock waves–Sun: corona–Sun: coronal mass ejections (CMEs)–Sun: magnetic fields–acceleration of particles

Abstract: The physical causes of coronal mass ejections (CMEs) have been debated by the solar community for over three decades now. The vast majority of proposed models agree that CMEs are the result of catastrophic loss of mechanical equilibrium or stability of the coronal magnetic field due to changes in the distribution of magnetic flux elements at the photosphere. These models usually involve idealized physical circumstances with either dipolar or quadrupolar underlying magnetic field geometries. The real Sun, however, demonstrates cases far more complex than those idealized configurations. Therefore, studying the actual magnetic field geometries involved during CMEs is crucial for understanding the dynamical time scales of the eruption, acceleration profiles, etc. By means of fully compressible 3-D magnetohydrodynamic simulations, we have investigated the CME events that took place on Apr 21 and Aug 24 of 2002. We have used high-resolution SoHO/MDI[1] data to set realistic boundary condition for the magnetic field at the Sun. The loss of equilibrium and subsequent eruption have been achieved by stretching and twisting the opposite polarity feet of a newly emerged magnetic dipole in the vicinity of the source region of the CME. As the result of reconnection at 3-D null points, magnetic flux and helicity are transferred from the compact flux system containing the emerged dipole to the larger-scale flux systems in the neighboring active regions. The CME dynamics have been found to proceed in a manner different than that predicted by earlier models, yielding fast ejections with properties similar to those observed. This paper summarizes the simulated dynamics of the CMEs and associated shock waves, and their comparison with observations.

1. Introduction

Coronal mass ejections (CMEs), also known as solar eruptions, are the most powerful consequences of solar activity in which vast amounts of magnetic flux (~ $10^{21\text{-}23}$ Mx) and solar plasma (~ $10^{15\text{-}16}$ g) are hurled into interplanetary space [1]. Because of their large scale and high energy, CMEs are thought to be important for reconfiguring the large-scale structure of the coronal magnetic field (CMF) over the solar cycle [2]. CMEs also play a leading role in the Sun-Earth connection because of their impact on Earth's protective magnetic environment, among other effects. That is why understanding the causes of CMEs are of fundamental importance not only for heliophysics, but also for all space sciences.

The solar corona is dominated by the magnetic field [3], i.e., the plasma-β << 1. Because of this, the electric currents producing the excess magnetic energy from the potential limit must be either force-free, i.e., field-aligned (except in prominences), or confined to thin current sheets (where plasma-β ~ 1). The latter are thought to be important in providing the energy release during small compact flares on the Sun, as argued in [3], and particle acceleration during impulsive SEP events (see [4]), but they cannot explain the ejections of mass and magnetic flux observed during CMEs. This implies that the energy for CMEs is most likely stored in the

[1] Michelson Doppler Imager (MDI) onboard the Solar and Heliospheric Observatory (SoHO).

non-potential magnetic fields generated by volumetric (i.e., non-sheet-like), field-aligned coronal currents.

The physical mechanisms of CME initiation are the subject of active research and debate [2,3,5]. The majority of existing CME models can be organized into two main groups depending on the state of the assumed CMF prior to the eruption. The first class of models [6,7,8,9,10,11,12] assumes that a magnetic flux rope exists prior to the eruption. Both theoretical and numerical studies of magnetic flux ropes suggest that they may suddenly lose mechanical equilibrium and erupt due to foot-point motions, or injection of magnetic helicity (or twist) at the photosphere. The second group of models [13,14,15,16,17,18,19] relies on the existence of sheared magnetic arcades, which become unstable and erupt once a critical state is reached in the corona. In this case, a flux rope does not exist prior to the eruption, but is created as the CMF reforms during the eruption process.

1.1. Flux-Rope Models

The basic magnetic topology in the flux-rope models is a twisted flux rope suspended in the corona by a balance between magnetic compression, hoop, and tension forces associated with the magnetic field of the rope and the background field. However, some models argue that the rope has emerged from below the convection zone as a coherent magnetic feature (see discussion in [3]). The majority of these models do not discuss the means by which the flux rope is formed in the corona prior to the eruption. Rather, they concentrate on exploring its stability properties in the context of CME production.

When the system comprising the flux rope is brought up to a critical point where a stable equilibrium no longer exists, the growth of MHD perturbations leads to an ideal (kink-like) instability, or a lack of equilibrium and a vertical current sheet forms [11]. The electric current in the vertical sheet is of the same sign as the flux rope current, so that the sheet attracts the current loop. Therefore, the erupting flux rope cannot escape unless a non-ideal process, such as magnetic reconnection, dissipates the current sheet fast enough; the reconnection process manifests itself through a solar flare. If the current does not dissipate fast enough (see [11]), then no CME occurs, only a flare. There are numerous examples of such failed eruptions on the Sun to support this scenario, for instance the event observed by TRACE on 2002 May 27 in association with a M2-class flare [20].

1.2. Sheared-Arcade Models

The basic topology in this class of models is a sheared magnetic arcade containing free energy in the form of volumetric electric currents. These models invoke magnetic reconnection to achieve an abrupt loss of equilibrium of the coronal magnetic field and a subsequent eruption. Unlike the previous group of models, here the magnetic reconnection is not a consequence of the eruption process, but the fundamental trigger of the eruption (i.e., responsible for its onset and growth in time). Another main difference is that in the sheared-arcade models a flux rope is formed *during the course* of the eruption, not before. Depending on the height at which the reconnection process occurs in these models, there are three sub-classes, namely, flux-cancellation, tether-cutting, and breakout models.

In the flux-cancellation models [14,15,16,17,18,19], magnetic reconnection takes place at the photosphere or near the base of the corona. Here a flux rope is formed by reconnecting the opposite polarity feet of a shared magnetic arcade. The dynamics of the eruption proceeds in much the same manner as in the flux-rope models discussed above.

In the tether-cutting models [21, 22], a CME is triggered by reconnection inside a coronal filament in the low corona–a process referred to as “runaway tether-cutting”. The filament here is comprised of a number of magnetic strands and the reconnection process occurs between the threads of opposite polarity that contact each other. The internal reconnection starts at the very beginning of the filament eruption and grows in time as the eruption advances. In this process, all connections (tethers) of the filament with the photosphere are broken (cut), except for those at the ends of the erupting flux rope.

In the breakout model of [13], the eruption is again triggered by magnetic reconnection, but here this process occurs in a curved, horizontal current sheet situated above the magnetic arcade being sheared. The basic concept in this two-dimensional model is as follows. As the central arcade of CMF above the solar equator is sheared, it begins to expand outward in the coronal volume. During the expansion, the sheared field lines push against the pre-existing X-line from below, thus forming a curved, horizontal current sheet. The sheet acts to confine the sheared arcade underneath, so that it cannot open in the volume above the sheet. The

only way for the sheared arcade to open up is by dissipating the current sheet. Once the reconnection process starts, the field lines above the sheet are moved out of the way of the expanding arcade and the newly formed field lines join the two magnetic flux systems on the side. However, rapid reconnection in the sheet does not occur at first. Rather, as the shear increases in the central arcade, the diffuse current transforms into a thin sheet, which then experiences fast reconnection. The rate of reconnection accelerates as the dissipating current sheet is pushed further away from the Sun. The nature of the transition from slow to fast reconnection in this model remains to be investigated.

1.3. Limitations of Present Models

To date, there are no sufficiently well developed CME models to explain the real events and related phenomena. Significant progress has been made, however, in understanding the basic physical processes involved in causing the CME phenomenon. There is a general agreement in the community that CMEs are the result of a catastrophic loss of mechanical equilibrium of solar plasma confined by the CMF. The existing theoretical models of CMEs differ in the details by which the eruption is achieved, and specifically in: (i) the physical driver of the eruption, and (ii) precise means of energy storage in the CMF prior to the CME.

In a recent study, [23] have found that: (i) 7 out of 26 CMEs can be interpreted with the "breakout model" of [13]; (ii) 12 events can be explained with other CME models (in dipolar geometries); and (iii) 7 events remain *unclassifiable*. This implies that ~27% of the observed CME events are more complex than those modeled in idealized magnetic configurations. This also proves necessary to study CMEs on a case-by-case basis, if we are to understand their energetics, dynamics, etc. This study focuses on modeling ejections from complex active regions (ARs), in particular those that took place on 2002 Apr 21 and Aug 24. We will discuss the magnetic field evolution in the CME source region, and the CME (and related shock wave) dynamics in the low corona.

1.4. CME Events Under Study

In this paper, we present simulation results for two events, namely the 2002 Apr 21 ejection (CME1 hereafter) and the 2002 Aug 24 ejection (CME2 hereafter). CME1 took place in active region (AR) 9906 on the west limb of the Sun. Magnetic field extrapolations in the corona have revealed the presence of large-scale field connections between AR 9906 and ARs 9902 and 9907 (see [19]). That is why CME1 has been classified as "CME originating from complex AR".

The CME drove a shock wave at a distance of ~ 1.6-1.7 R_S (as inferred from SoHO/UVCS observations), which traveled at a speed of ~ 1,500 km/s; the shock flank arrived at 1 AU in about 51 hrs. The event took place near an open field region, which was magnetically connected to the Earth. A gradual solar energetic particle (SEP) event also occurred during 2002 Apr 21-23 in association with the shock dynamics in interplanetary (IP) space. The observed SEP composition showed a decline in the Fe/C ratio for energies above 10 MeV/nuc, as reported by [4]. Quite the opposite behavior (increase in the Fe/C ratio for energies above 10 MeV/nuc) was observed for CME2, despite the fact that both CME1 and CME2 had very similar evolution in the corona. CME2 was similar to CME1 in that: (i) it also occurred on the west limb; (ii) the CME source region, AR 10069, was well connected to a number of nearby ARs (10067, 10068, and 10079), (iii) there was an X3.1-class flare associated with the eruption; (iv) a shock wave formed relatively close to the Sun[2] and traveled with comparable speed (shock flank arrived at 1 AU within 58 hrs.); and (v) a gradual SEP event occurred on 2002 Aug 24-25 in association with the eruption. Apparently, CME2 is another event belonging to the group of "CMEs originating from complex AR", which is found to be even more complex than CME1.

In [4], the observed behavior of SEP composition for the two events have been attributed to a difference in the shock geometry along the field lines connecting the Sun and the Earth–quasi-perpendicular for CME2 versus quasi-parallel for CME1–since heavy ions are preferentially accelerated at quasi-perpendicular shocks. This hypothesis remains to be investigated, however, which is what has motivated us to model these two events: they appear to be very similar in CME characteristics, but so different in SEP properties. In this paper, we compare CME1 and CME2 in terms of underlying magnetic geometry of the solar corona before and shortly after the

[2] This is inferred from the existence of metric and near-Sun interplanetary type II bursts (see event 49 discussed in [26]).

CME onset. The study comprises fully three-dimensional (3-D) compressible MHD simulations of the two events. Since they occurred on the west limb, it is difficult to infer from observations the dynamics of magnetic flux elements on the Sun, which could have led to the ejections. Here, we assume that magnetic flux emergence was the most likely mechanism that triggered the CMEs in both cases, and this is what we have modeled. Note that there is some indication from SoHO/MDI observations about ongoing flux emergence prior to the events.

2. Methodology

In our numerical models of CME1 and CME2, the steady-state solar corona and solar wind are constructed following the methodology of [19]. The time-dependent MHD equations for a single compressible fluid are solved using the BATS-R-US code [24]. The initial condition for the coronal magnetic field is calculated by means of potential field extrapolation, with a boundary condition for the radial magnetic field at the Sun provided by full-disk SoHO/MDI observations. The initial plasma properties of the corona are prescribed in an ad-hoc manner, through a variable polytropic index, in order to mimic the physical properties of helmet streamers and coronal holes in the solar atmosphere at steady-state conditions. (Note that the initial state is static, but not in equilibrium.) Following [25], the initially static corona with potential magnetic field everywhere is evolved to a new state with steady solar wind flow and non-potential magnetic field in the corona. The solar wind model is parameterized in a way that yields plasma and magnetic field structures in IP space that generally agree with in-situ observations by Ulysses and ACE. Further details about the simulation setup can be found in [19,25].

The CME initiation model adopted here utilizes one consequence of magnetic flux emergence, namely shearing motions, to evolve the coronal magnetic field to an out-of-equilibrium state followed by a CME. In some regard, this model is similar to the "breakout scenario" of [13]. In our model, a newly emerged AR is mimicked by the dipolar magnetic field of two point charges, $+q$ and $-q$ (see Fig. 1 in [19]), which are separated initially (at $t = 0$) by a distance $2L$ and are buried at a depth d below the solar surface, as in the model of [10]. The values of q, L, and d used in the simulations discussed here are 1.5×10^{11} G km^2, 5×10^3 km, and 3×10^4 km, respectively. These parameters yield a peak value of the radial magnetic field at the Sun of ~ 47 G.

The magnetic field produced by the two charges is superimposed into the extrapolated potential magnetic field constrained by SoHO/MDI data. The resulting coronal magnetic field comprises the new initial condition, which is still potential everywhere. This is then evolved with BATS-R-US to a new non-potential magnetic configuration with steady-state solar wind, as described above. Once the steady-state is reached at $t = 0$, the two magnetic charges are slowly moved apart in the way illustrated in Fig. 1 in [19] up to $t = 30$ min. Note here that the speed of charge separation is at most a few percent (~ 2%) of the local Alfvén speed. Further details about the CME model can be found in [19].

As a result of moving the two charges apart (i.e., flux emergence), the magnetic field lines connecting the two spots of the dipole are stretched and twisted. Thus, the magnetic energy and helicity of the dipole field gradually increase over time, which is what is required to power an eruption. Also, subject to change is the mutual helicity of the evolving dipole field with respect to the surrounding magnetic field of nearby flux systems. As the coronal field is evolved quasi-steadily, it approaches a state that is no longer stable. Then, as the result of loss of confinement with the overlying field, the "energized" magnetic field of the dipole erupts, yielding a CME. This procedure enables us to initiate CMEs in realistic CMF backgrounds in a physically plausible manner: that is, one that extracts magnetic energy stored in the corona by evolving the CMF to a point where stability breaks down. The magnetic configuration in the case of CME1 at $t = 0$ and $t = 30$ min is shown in Fig. 1.

3. Discussion of Results

At $t = 0$, the evolution of the small-scale dipole produced by the q charges commences and the CMF is gradually driven towards loss of equilibrium. In this process, electric currents start to build up at the NPs (and quasi-separator (QS) in the case of CME2) since the pressure balance there is perturbed. As the two charges move apart, an electric current is generated along the CMF, which flows along the loops connecting the moving magnetic spots of opposite polarity. As a result, the magnetic energy of the evolving dipole monotonically

increases in time, and the loops connecting the two moving spots gradually expand. The excess magnetic energy built in the stressed CMF prior to the onset of reconnection is 2.01×10^{32} ergs in the case of CME1 and 2.13×10^{32} ergs in the case of CME2. As the sheared field of the dipole expands, it begins to reconnect with the CMF from the neighboring flux systems (see right panel of Fig. 1) through the pre-existing NPs and QS (in the case of CME2). Due to reconnection, the overlying CMF is removed sideways, as in the "breakout model" of [13], and thus this field no longer has a restraining effect on the expanding field from below. Once the "magnetic breakout" sets in at $t \approx 18$ min ($t \approx 16$ min) in the case of CME1 (CME2), the free energy stored in the sheared coronal field starts to convert into kinetic energy of bulk plasma motions and heat. Our results show that as much as 17% (15%) of the excess magnetic energy built in the CMF prior to the onset of "breakout reconnection" is ultimately converted into kinetic energy in the case of CME1 (CME2), and roughly 12% (14%) of it goes into heat. We also found that 95% of the energy conversion occurs within 14 min (11 min) of the onset of "breakout reconnection" in the case of CME1 (CME2). In both cases, approximately 3×10^{15} g of solar plasma is ejected from the solar corona into IP space.

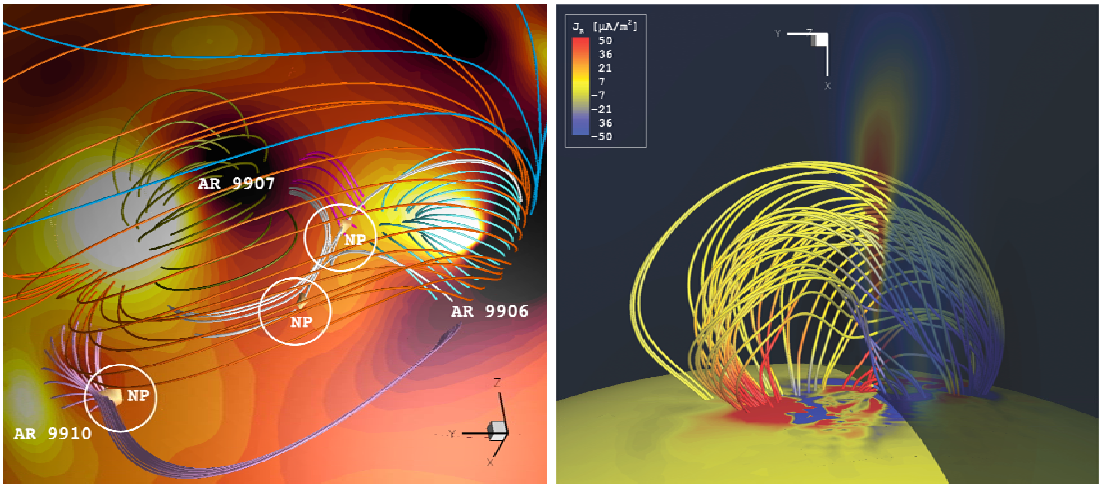

Fig. 1. (*Top*) Pre-event topology of the CMF of relevance to CME1. The ARs of interest are annotated as shown. The colored lines in the image are 3-D magnetic field lines, where each color represents a distinct flux system; the dark blue field lines are open in IP space. The magnetic null points (NPs) in the corona are encircled. The plasma-β has been used as a proxy to visualize the NPs, which are shown as iso-surfaces of $\beta = 0.2$ (from [19]). (*Bottom*) 3-D structure of the erupting magnetic field for the same event. The color code along the CMF lines visualizes the radial component of current density, J_R. The flow speed is shown on a translucent plane cutting through the middle of the magnetic flux rope; the red (yellow) color corresponds to a flow velocity of ~ 1,000 km/s (~ 700 km/s). The solar surface is shown as the yellow sphere (from [19]).

A very important result from these MHD simulations is that, because of the complexity of the underlying CMF geometry for both events, magnetic reconnection via NPs nearby, but sideways of the expanding field, serves to change the connectivity of the magnetic field. This results in jump-like changes in the CME footprint(s), which is not a feature of the classical "breakout" model (and other idealized CME models). Other important results are that: (i) the separation between CME's footprints increases over time, and (ii) the mutual helicity of the flux systems undergoing reconnection transforms into self-helicity. Also, in the case of CME2, the QS evolves into a current sheet above the expanding current loop, which undergoes rapid reconnection as the stressed field from below pushes against it. Fast reconnection in the sheet enables rapid outward acceleration of the current loop.

For both events studied here, the erupting field is found to be a mixture of magnetic patches from various flux systems. We argue that the majority of CMEs originating from complex ARs undergo similar evolution. The right panel of Fig. 1 shows the 3-D structure of the magnetic field for CME1.

Fig.2. (*Top*) SoHO/LASCO observation and simulated structure of the solar corona and CME2 in white light (at t = 48 min). (*Bottom*) Simulated 3-D structure of the CMF at t = 100 min. The color code at the Sun visualizes the

radial magnetic field. The colored lines are 3-D CMF lines, where the color code in the left (right) image illustrates the flow speed (mass density) along the lines. The 3-D structure of the CME can be assessed from the left image, whereas the right image shows the position of CME footprints on the Sun.

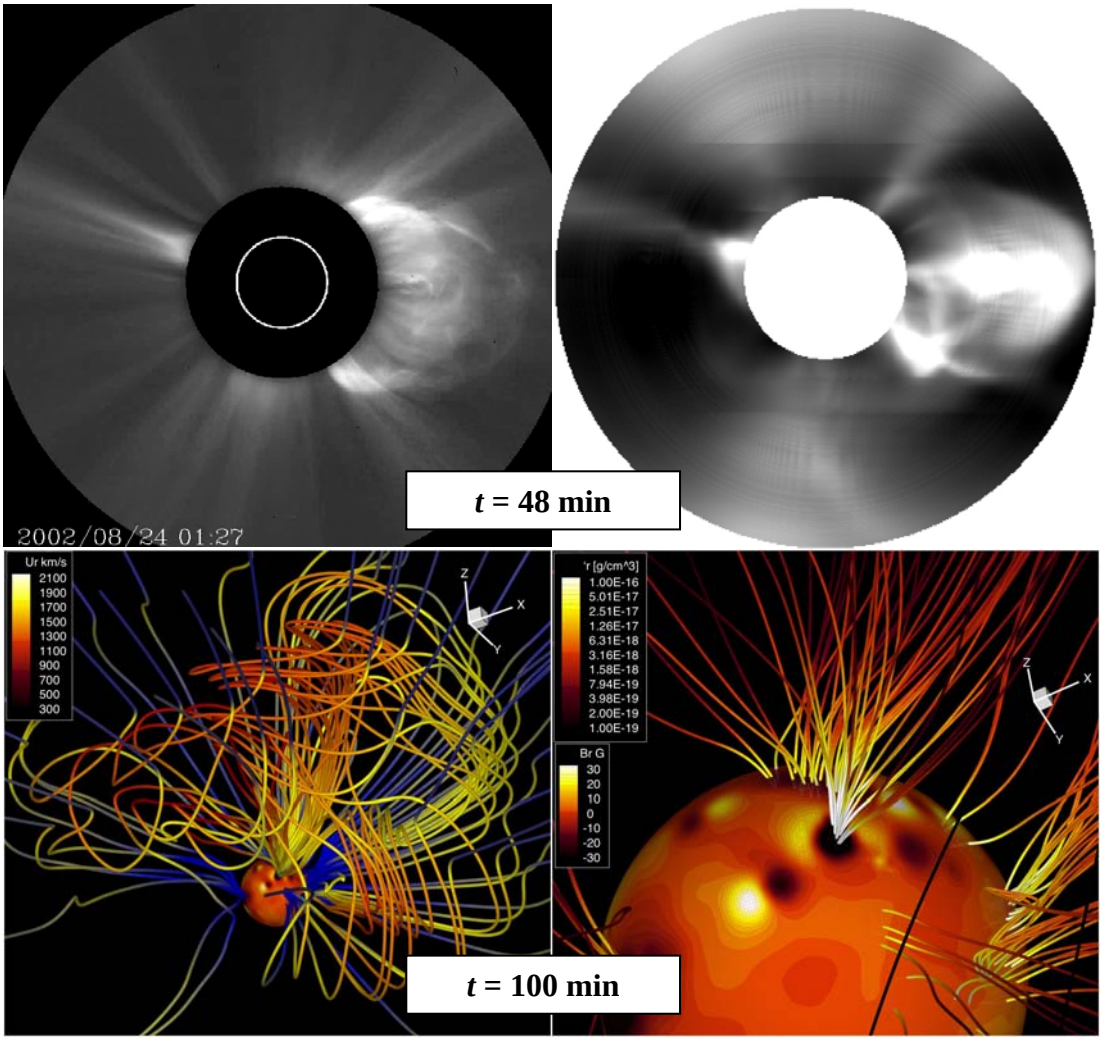

3.1 Shock Geometry and Evolution

The modeled CMEs in both cases drove shock waves near the Sun, which is in good agreement with SoHO/UVCS observations to within 0.2 R_S (0.1 R_S) in the case of CME1 (CME2). The height-time profiles of the CMEs also show good agreement with SoHO/LASCO observations. A comparison between the simulated CME2 structure in white light at t = 48 min and the corresponding LASCO observation is shown in the upper panel of Fig. 2. This comparison shows that our models of the background solar corona and CME reproduce rather well the structure seen in the white-light image. The 3-D structure of CME2 near the Sun and at large distances at t = 100 min is also shown.

In order to investigate the change in shock geometry along the IP magnetic field (IMF) connecting L1 with the Sun, IMFL1, in the case of CME2 the computational domain was extended to Earth's orbit. A time sequence showing the evolution of the CMF passing through the vicinity of L1, with over-plotted velocity flow vectors, is shown in Fig. 3. We found that the shock geometry along IMFL1 changes quite dramatically during the early stages of the CME-shock evolution, and the geometry changes from quasi-perpendicular to quasi-

parallel within ~ 7 R_S: the shock angle is 68°, 53°, and 39° at a radial distance of 4.4 R_S, 6.2 R_S, and 8.2 R_S, respectively.

Another important result is that the IMFL1 footprint at the Sun changes due to interchange reconnection over the course of the event: the field geometry changes from open to closed and back to open over the course of 45 min. We argue that this process of field connectivity change may enable suprathermal particles produced during the flare (reconnection process) to undergo diffusive shock acceleration once the closed flare loops become open again. It remains to be investigated whether the same process occurs during CME1 once the simulation domain is extended to 1 AU.

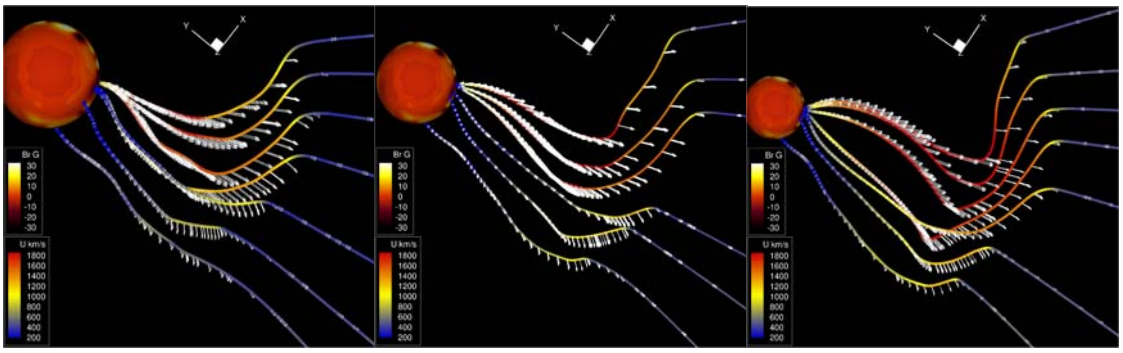

Fig.3. Time-sequence showing the evolution of the CMF passing through the vicinity of L1 with over-plotted velocity flow vectors. The images to the left, middle, and right correspond to t = 45 min, 60 min, and 75 min, respectively. The color code at the Sun visualizes the radial magnetic field (see upper color legend).

4. Conclusions

The models proposed to date agree in describing the general properties of CMEs, although the vast majority of models involve idealized magnetic settings. In the study by [23], it was found that ~ 27% of the observed events, like CME1 and CME2 discussed here, are more complex than those modeled in idealized configurations. This implies that such complex CMEs need to be studied on a case-by-case basis, as done here, in order to understand their dynamics, energetics, and IP consequences.

For the two events discussed in this paper we can draw the following conclusions. We found that a number of null points in the corona and a quasi-separator (in the case of CME2) played a role during the eruption process, and the modeled eruptions underwent major restructuring on the way out. As a result of magnetic reconnection, transfer of magnetic flux and helicity–from small to large scale–took place across a number of distinct flux systems. Also, the footprints of the erupting magnetic field did not remain stationary as the CME evolved: either one or both legs of the CME were found to migrate along the solar surface, with increasing separation between the two legs in the process.

The shock waves driven by the CMEs also underwent complex evolution. In the case of CME2, the shock geometry was found to change from quasi-perpendicular to quasi-parallel along the IMF line connecting the Sun with L1 (IMFL1). Also, the IMFL1 footprint at the Sun was found to change due to interchange reconnection over the course of the event, which may have some important implications for the production of solar energetic particles. Namely, suprathermal ions trapped along flare loops may undergo further acceleration at the CME-driven shock wave once these loops become open due to interchange reconnection. This effect remains to be investigated in our future studies, in which we will model in great detail the SEP events associated with CME1 and CME2.

Acknowledgment

This research work has been supported by the following grants: ATM-0639335 (NSF-CAREER), NNX07AC13G (NASA-LWS), and VU-NZ-01/06 (Bulgarian NSF).

References

1. J. T. Gosling, *AGU Monogr. Ser.* **58**, AGU, Washington, DC, 1990, pp. 343-364.
2. B. C. Low, *J. Geophys. Res.* **106**, 25,141-25,163 (2001).
3. T. G. Forbes, *J. Geophys. Res.* **105**, 23,153-23,166 (2000).
4. A. J. Tylka et al., *Astrophys. J.* **625**, 474-495 (2005).
5. I. I. Roussev and I. V. Sokolov, *Geophys. Monogr.* **165**, AGU, Washington, DC, 2006, pp. 89-99.
6. J. Chen, *J. Geophys. Res.* **101**, 27,499-27,520 (1996).
7. T. G. Forbes and P. A. Isenberg, *Astrophys. J.* **373**, 294-307 (1991).
8. T. G. Forbes and E. R. Priest, *Astrophys. J.* **446**, 377-389 (1995).
9. S. E. Gibson and B. C. Low, *Astrophys. J.* **493**, 460-473 (1998).
10. V. S. Titov and P. Démoulin, *Astron. & Astrophys.* **351**, 707-720 (1999).
11. I. I. Roussev et al., *Astrophys. J. Lett.* **588**, L45-L48 (2003a).
12. S. T. Wu, W. P. Guo, D. J. Michels, and L. F. Burlaga, *J. Geophys. Res.* **104**, 14,789-14,802 (1999).
13. S. K. Antiochos, C. R. Devore, and J. A. Klimchuk, *Astrophys. J.* **510**, 485-493 (1999).
14. T. Amari, J. F. Luciani, Z. Mikic, and J. Linker, *Astrophys. J. Lett.* **518**, L57-L60 (1999).
15. T. Amari, J. F. Luciani, Z. Mikic, and J. Linker, *Astrophys. J. Lett.* **529**, L49-L52 (2000).
16. J. A. Linker and Z. Mikic, *Astrophys. J. Lett.* **438**, L45-L48 (1995).
17. W. B. Manchester IV, *J. Geophys. Res.* **108**, 1,162 (2003).
18. I. I. Roussev et al., *Astrophys. J. Lett.* **605**, L73-L76 (2004).
19. I. I. Roussev, N. Lugaz, and I. V. Sokolov, *Astrophys. J. Lett.* **668**, L87-L90 (2007).
20. H. Ji et al., *Astrophys. J. Lett.* **595***,* L135-L138 (2003).
21. R. L. Moore, A. C. Sterling, H. S. Hudson, and J. R. Lemen, *Astrophys. J.* **552**, 833-848 (2001).
22. P. A. Sturrock, P. Kaufmann, R. L. Moore, and D. F. Smith, *Sol. Phys.* **94**, 341-357 (1984).
23. I. Ugarte-Urra, H. P. Warren, and A. R. Winebarger, *Astrophys. J.* **662**, 1,293-1,301 (2007).
24. K. G. Powell et al., *J. Comp. Phys.* **154**, 284-309 (1999).
25. I. I. Roussev et al., *Astrophys. J. Lett.* **595**, L57-L61 (2003b).
26. N. Gopalswamy et al., *J. Geophys. Res.* **110**, A12S07, doi:10.1029/2005JA011158 (2005).

Nonlinear effects in the diffusion of charged particles in 3-dimensional stochastic magnetic fields

Madalina Vlad, Florin Spineanu

National Institute of Laser, Plasma and Radiation Physics,
Street Atomistilor 409, Magurele, Bucharest, Romania
madi@ifin.nipne.ro; spineanu@nipne.ro

Keywords: space plasma, stochastic transport, magnetic turbulence.

Abstract: Charged particles transport in stochastic magnetic fields is studied for conditions relevant to astrophysical plasmas by developing a semi-analytical statistical method. This is a complex process due to the Lagrangian non-linearity determined by the space-dependence of the stochastic magnetic field. The transport coefficient for given particle energy is determined as function of the statistical characteristics of the stochastic magnetic field. We show that there are two nonlinear effects that produce trajectory trapping and a strong influence on the diffusion coefficient. These two trapping effects are the cause of the rich class of anomalous diffusion regimes identified in numerical simulations.

1. Introduction

Particle transport in stochastic media is an important topic in astrophysics [1]. A variety of problems, such as low-energy cosmic ray penetration into the heliosphere, the propagation of galactic cosmic rays in and out of the interstellar magnetic field, anomalous escape rates of runaways in the atmosphere, and so on, are directly related to charged particle motion in fluctuating fields. The interest of plasma physics, especially of nuclear fusion research, in stochastic transport has further increased in the last decay. An important progress was obtained in this period due to the development of statistical methods that permitted to go beyond the quasilinear regime and to understand the anomalous transport regimes generated by the nonlinearity. In particular, the problem of test particle diffusion in stochastic magnetic fields is an active topic studied by many authors (see for instance [2], [3] and the references therein). Important progress was obtained since the first papers of Jakipii and Parker [4] and Rechester and Rosenbluth [5]. However, the general solution has not yet been found.

The nonlinear processes in stochastic particle transport were studied in the context of laboratory magnetized turbulent plasmas (fusion experiments) using new semi-analytical statistical approaches: the decorrelation trajectory method [6] and the nested subensemble approach [7]. The most important nonlinear effect in turbulent fusion plasmas consists in trajectory trapping or eddying that appears when the stochastic field has a slow time variation and when the perturbation produced by collisions and average flows are weak. It strongly changes the diffusion coefficients and their dependence on the specific parameters. The transport in magnetic turbulence was studied in [3] where the diffusion of magnetic lines and the collisional particle transport were analyzed in the context of magnetically confined plasmas. It was shown that trapping of the magnetic lines generates stochastic magnetic islands, that appear as quasicoherent solenoidal structures. These stochastic magnetic islands strongly influence magnetic line and particle transport.

The aim of this paper is to present the nonlinear effects that appear in charged particle transport in magnetic turbulence for conditions relevant for space plasmas. The parameters of the stochastic magnetic field for the space and fusion plasmas are completely different. However, the fundamental difference between the two systems is not due to the parameters but to the configuration of the magnetic field. In fusion plasmas there is a very large average magnetic field while very small average magnetic field, of the same order as the fluctuating

component exists in space plasmas. Consequently, 2-dimensional stochastic models and guiding center approximation can be used in fusion plasmas. Lorentz force and 3-dimensional description of the transport is necessary for space plasmas, which makes the model much more complicated than that of fusion plasmas.

2. The model

We consider a stochastic magnetic field $\mathbf{B_t}=B_0\mathbf{e_z}+\mathbf{B}$ where B_0 is a constant average component directed along z-axis, and $\mathbf{B}$ is the stochastic component that depends on $\mathbf{x}=(x_1, x_2)$ and z, the Cartesian coordinates. The stochastic component has an arbitrary direction. Its structure is taken similar to the model in the numerical simulation presented in [2], which corresponds to the potential vector of the type $\boldsymbol{A}=[-\partial_2 A^{(2)}, \partial_1 A^{(2)}, A^{(1)}]$ where $A^{(1)}$, $A^{(2)}$ are scalar fields and ∂_i is the derivative with respect to x_i. The magnetic field is

$$\begin{aligned} B_1 &= \partial_2 A^{(1)} - \partial_1 \partial_z A^{(2)}, \\ B_2 &= -\partial_1 A^{(1)} - \partial_2 \partial_z A^{(2)}, \\ B_z &= \partial_1{}^2 A^{(2)} + \partial_2{}^2 A^{(2)}. \end{aligned} \tag{1}$$

Thus the magnetic field perpendicular on the average magnetic field $\mathbf{B}_\perp=(B_1, B_2)$ has a zero divergence component and a component along the direction of the gradient of $\partial_z A^{(2)}$ with non-zero divergence that is compensated by the parallel component B_z. The zero divergence component of $\mathbf{B}_\perp$ determines the tendency of magnetic line trapping on almost closed paths on the contour lines of $A^{(1)}$ and the formation of magnetic structures (stochastic islands). The other components of the fluctuating field contribute to release the trapped line. The same effect has the parallel motion for the trapped trajectories.

The two fields in Eq. (1) $A^{(1)}$, $A^{(2)}$ are considered to be a stationary and homogeneous Gaussian stochastic fields, with zero average and given two-point Eulerian correlation functions $E^{(1)}$, $E^{(2)}$ defined by the statistical average

$$E^{(i)} = \left\langle A^{(i)}(0,0) A^{(i)}(x,z) \right\rangle.$$

The statistical descriptions of the derivatives of the two fields are completely determined by those of $A^{(1)}$, $A^{(2)}$. They are stationary and homogeneous Gaussian stochastic fields and their two-point Eulerian correlations are obtained as derivatives of $E^{(1)}$, $E^{(2)}$. These correlation functions evidence four parameters: β_1, β_2 the amplitudes of the perpendicular magnetic field fluctuations produced by $A^{(1)}$ and respectively by $A^{(2)}$ normalized with B_0, $\lambda_\parallel$ the parallel correlation length and $\lambda_\perp$ the perpendicular correlation length. The correlation lengths are defined as the largest characteristic decay lengths of the two stochastic fields. The fields $A^{(1)}$, $A^{(2)}$ are considered statistically independent.

The motion of an ion with charge q and mass m is determined by the Lorentz force. Introducing the guiding center coordinate $\boldsymbol{\xi}$ and the Larmor radius $\boldsymbol{\rho}$ corresponding to the average magnetic field B_0

$$x_i = \xi_i + \rho_i, \quad \rho_i = -\varepsilon_{ij} u_j / \Omega_0, \tag{2}$$

where ε_{ij} is the antisymmetric tensor and $\Omega_0=qB_0/m$, the equations of motion can be written as:

$$\begin{aligned} \partial_t \rho_i &= \varepsilon_{ij} \overline{\Omega}_0 \rho_j \left[1 + b_z(\xi+\rho, z)\right] - u_z b_1(\xi+\rho, z) \\ \partial_t \xi_i &= -\varepsilon_{ij} \overline{\Omega}_0 \rho_j b_z(\xi+\rho, z) + u_z b_i(\xi+\rho, z) \\ \partial_t u_z &= \beta_1{}^2 \left[\rho_1 b_1(\xi+\rho, z) + \rho_2 b_2(\xi+\rho, z)\right] \\ \partial_t z &= \frac{u_z}{K_m}, \end{aligned} \tag{3}$$

where

$$b_z = K_m \alpha \left(\partial_1^2 A^{(2)} + \partial_2^2 A^{(2)} \right)$$
$$b_i = \varepsilon_{ij} \partial_j A^{(1)} - \alpha \partial_i \partial_z A^{(2)} \tag{4}$$

Dimensionless quantities were used in Eqs. (3)-(4) with the following units: $\lambda_\perp$ for the perpendicular lengths ξ, ρ; $\lambda_\parallel$ for z; the modulus of the initial velocity of the particles u_0 for u_z; the time of flight over $\lambda_\perp$ produced by $A^{(1)}$, $\tau = \lambda_\perp / b_1 u_0$ for time. The parameters of motion are the magnetic Kubo number

$$K_m = \frac{\beta_1 \lambda_{II}}{\lambda_\perp} = \frac{\tau_{II}}{\tau} \tag{5}$$

which is the ratio of the parallel decorrelation time $\tau_{II} = \lambda_{II} / u_0$ over the time of flight, β_1 the amplitude of the magnetic field fluctuations, $\alpha = \beta_2 / \beta_1$ and $\overline{\Omega}_0 = \Omega_0 \tau$. Two additional parameters: the initial kinetic energy of the particle and the initial Larmor radius appear in the initial conditions for Eqs. (3)-(4).

Starting from the statistical description of the stochastic magnetic field, we determine the correlation of the Lagrangian velocity of the guiding center, defined by the right side terms of the second equation in (3) and the time dependent diffusion coefficient, which is the time integral of the correlation of the Lagrangian velocity.

3. The decorrelation trajectory method

The decorrelation trajectory method [6] reduces the problem of determining the statistical behavior of the stochastic trajectories to the calculation of weighted averages of some smooth, deterministic trajectories determined from the Eulerian correlation of the stochastic field. This semi-analytical statistical approach is an approximation that satisfies the statistical consequences of the invariants of the motion.

The main idea in our approach is to study the stochastic equations (3)-(4) in subensembles of realizations of the stochastic field. The whole set of realizations R is separated in subensembles (S1), which contain all realizations with the fixed values of the stochastic fields in the starting point of the trajectories **x**=0, z=0:

$$(S1): \quad A^{(1)}(0,0,0) = a^1, \; \partial_i A^{(1)}(0,0,0) = a_i^1, \; A^{(2)}(0,0,0) = a^2 \tag{6}$$

The stochastic (Eulerian) fields $A^{(1)}$, $A^{(2)}$ and their derivatives are Gaussian fields in a subensemble but non-stationary and non-homogeneous, with space and time dependent averages and correlations. The correlations are zero in **x**=0, z=0 and increase with the distance. The average quantities in a subensemble depend on the parameters of that subensemble and are determined by the Eulerian correlations $E^{(1)}$, $E^{(2)}$ (see [6] for details). The stochastic equations (3)-(4) are studied in each subensemble (S1). The average Eulerian velocity determines an average motion in each (S1). Neglecting the fluctuations of the trajectories, the average trajectory in (S1) (*the decorrelation trajectory)* is obtained by averaging Eqs. (3)-(4) in (S1). This approximation is validated in [7]. One obtains average equations that have the same structure as the equations in each realization (3)-(4) but with the stochastic terms replaced by their subensemble averages. The latter are determined using the procedure presented in [6], which yields

$$B_z = \langle b_z \rangle_{S1} = K_m \alpha a^2 \left(\partial_1^2 + \partial_2^2 \right) E^{(2)}$$
$$B_i = \langle b_i \rangle_{S1} = \varepsilon_{ij} \partial_j \left(a^1 E^{(1)} - a_k^1 \partial_k E^{(1)} \right) - \alpha a^2 \partial_i \partial_z E^{(2)} \tag{7}$$

The average trajectories for particles with initial modulus of the velocity u_0 and initial Larmor radius ρ_0 are determined for the initial conditions

$$\langle \rho_1(0) \rangle_{S1} = \rho_0 \cos(\gamma), \quad \langle \rho_2(0) \rangle_{S1} = \rho_0 \sin(\gamma), \quad \langle \xi_i(0) \rangle_{S1} = -\langle \rho_i(0) \rangle_{S1}$$

where γ is the orientation of the initial Larmor radius, which is taken uniformly distributed.

The time dependent diffusion coefficient is obtained by summing the contribution of each subensemble (S1) weighted by the probability that a realization belongs to the subensemble. One obtains

$$D = \beta_1 u_0 \lambda_\perp F(t)$$

$$F(t) = \frac{1}{(2\pi)^2}\int_{-\infty}^{\infty} da^1 \exp\left(-\frac{(a^1)^2}{2}\right)\int_0^{\infty} da \exp\left(-\frac{a^2}{2}\right) a^2 \int_0^{2\pi} d\gamma \int_{-\infty}^{\infty} da^2 \exp\left(-\frac{(a^2)^2}{2}\right)\left\langle \xi_1(t)\right\rangle_{S1} \quad (8)$$

where $a^2=a_1^2+a_2^2$ and $\left\langle \xi_1(t)\right\rangle_{S1}$ is the average displacement of the guiding center in the subensemble (S1).

4. Results and conclusions

The topology of the decorrelation trajectories is directly correlated with the nonlinear effects in stochastic transport. They show in this case that there are two nonlinear effects that produce trajectory trapping. The first appears for the motion in the plane perpendicular to the average magnetic field and consists in helicoidal segments of the magnetic lines, which form localized magnetic structures (magnetic islands). This trapping process is specific to the 2-dimensional stochastic magnetic fields perpendicular to a large $\mathbf{B}_0$ but it could be observed also in the 3-dimensional case. The second trapping effect appears in particle motion along magnetic lines and is due to the formation of stochastic magnetic mirrors. Localized structures can appear due to this effect of trapping (trajectory clusters).

The interaction of the two types of trapping is rather complex and determines either the release of trajectories or a synergetic amplification or even chaotic behavior. Their effects on the diffusion coefficient depends on the statistical weight of each type of decorrelation trajectories. A rich class of anomalous diffusion regimes are identified, in agreement with the results of numerical simulations [2]. The magnetic Kubo number provides a measure of the nonlinear effects (as in the 2-dimensional case) but other parameters can change the diffusion regime. For instance, the dependence of D on K_m is step-like for Ω_0 above a limit value and irregular at smaller values. The mirror capture appears for large values of K_m and leads to the increase of the perpendicular trapping effect and thus of the perpendicular diffusion coefficient.

In conclusion, we have shown that the nonlinear effects are complex and strong in 3-dimensional magnetic fields. A physical image was obtained by analyzing the topology of the decorrelation trajectories.

Acknowledgment

We acknowledge financial support from the Romanian Ministry of Education and Research under Project LAPLAS2, contract No. PN 09 39.

References

[1.] P. Chuychai, D. Ruffolo, W. H. Matthaeus, and G. Rowlands, *Astrophys. J.*, vol. 633, L49 (2005).
[2.] P. Pommois, G. Zimbardo, P. Veltri, "Anomalous, non-Gaussian transport of charged particles in anisotropic magnetic turbulence", *Phys. Plasmas*, vol. 14, 012311-11, 2007.
[3.] M. Vlad, F. Spineanu, J.H. Misguich, R. Balescu, "*Magnetic line trapping and effective transport in stochastic magnetic fields*", Physical Review E, Vol. 67, 026406-12, 2003.
[4.] J.R. Jakipii and E. Parker, Astrophys J. Vol. 155, pp777, 1969.
[5.] A.B. Rechester and M.N. Rosenbluth, Phys. Rev. Lett., Vol. 40, pp. 38, 1978.
[6.] M. Vlad, F. Spineanu, J.H. Misguich, R. Balescu, *"Diffusion with intrinsic trapping in 2-d incompressible velocity fields"*, Phys. Rev. E, Vol. 58, pp. 7359-7368, 1998.
[7.] M. Vlad, F. Spineanu, *"Trajectory structures and transport",* Phys. Rev. E, Vol. 70, 056304-14, 2004.

Scintillation Measurements as a Means for Diagnosis of Ionospheric Plasma Turbulence

Andrzej W. Wernik [(1)], **Marcin Grzesiak** [(1)], **Massimo Materassi** [(2)]

[(1)]Space Research Center, Polish Academy of Sciences, Bartycka 18a, 00-716 Warsaw, Poland
aww@cbk.waw.pl, pajak@cbk.waw.pl
[(2)]Istituto dei Sistemi Complessi ISC-CNR, Florence, Italy,
massimo.materassi@fi.isc.cnr.it.

Keywords: Ionospheric scintillation, plasma turbulence

Abstract: Scintillation of radio waves traversing the ionosphere is caused by scattering and refraction on small scale electron density irregularities. Since their beginning, scintillation measurements have been used as a tool to study ionospheric irregular structure: its local and global morphology, statistical properties of the irregularities, dynamics, and generation mechanisms. We will briefly review the techniques in the scintillation analysis providing information about ionospheric plasma turbulence and present the most important results.

1. Introduction

Ionospheric plasma is highly non-homogeneous. In-situ plasma density and electric field measurements demonstrate that the high-latitude and equatorial regions ionosphere are characterized by a broad spectrum of irregularities, which are superimposed upon a slowly varying (in space and time) plasma background. Irregularities with scale-sizes of the order of several hundreds of meters cause scintillation (random fluctuations) of amplitude and phase of trans-ionospheric radio signals. Ionospheric scintillation has been observed over a wide band of frequencies, from HF to GHz.

The theory of wave propagation in random media relates the statistical properties of the medium to the statistics of measured wave parameters (c.f. [1]). Briefly, the scenario of ionospheric scintillation is as follows [2]. Let a plane wave be incident upon the ionosphere. The presence of electron density irregularities causes fluctuations of the refractive index which distort the original wavefront, giving rise to a randomly phase-modulated wave $k_0(\Delta\varphi)$, where for a radio wave of length λ $k_0=2\pi/\lambda$ is the free-space wavenumber, and $\Delta\varphi$ is the variation of the optical path length within the layer with irregularities. $\Delta\varphi$ is dependent on the fluctuations of the ionospheric total electron content ΔN_T caused by irregularities:

$$\Delta\varphi = -\lambda r_e \Delta N_T, \tag{1}$$

where r_e is the classical electron radius.

As the wave propagates toward the receiver, further phase mixing occurs, changing the modulation of the wave and eventually producing a complicated diffraction pattern on the ground. If the satellite and/or the ionosphere move relative to the receiver, temporal variations of intensity and phase are recorded. Simple considerations show that the amplitude fluctuations are mainly cased by irregularities with size of the order of the first Fresnel zone $d_F = \sqrt{\lambda(z - L/2)}$, where λ is the wavelength, z is the height of the upper boundary of the irregular layer, and L is the layer thickness

This scenario of scintillation generation is valid provided $\Delta\varphi$ is not too large. If the electron density fluctuations are significant, then the phase fluctuations can be so large that the wave is no longer coherent and interference of rays is not possible. Analysis show that when the phase fluctuations reach a certain limiting value, the intensity of amplitude scintillation cease to increase.

The general problem of propagation of waves in a random medium is difficult to treat numerically. However,

it can be greatly simplified if the wavelength is much smaller than the characteristic scale size of irregularities. In this case the wave is scattered predominantly in the forward direction and the wave propagation is described by the parabolic equation, which can be easily solved ([1], [3]). Further simplifications are possible if the irregular layer is so thin that $\sqrt{\lambda L}$ is much smaller than the size of largest irregularity contributing to scintillation. This assumption leads to so called phase screen theory of scintillation in which the irregular layer is replaced by a screen, which changes only the wave's phase. The screen is located in the ionosphere at the height of the peak electron density. Historically, the phase screen model was the first model of scintillation [4]. Later expansion ([5], [6], [7]) included the geometry of propagation, anisotropy of irregularities and strong scatter case.

It is interesting to find what kind of information about ionospheric plasma structure can be derived from the scintillation measurements. This information, which is hidden inside the scintillation pattern, can be retrieved using proper data analysis methods and propagation models. Two approaches are possible: statistical reconstruction and reconstruction employing the inverse propagation. In the first approach only statistical parameters of plasma fluctuations are derived. Those are, for instance: moments of the plasma density (or electric field) fluctuations, turbulence spectra and correlations etc. The second approach allows to reconstruct the irregular structure of the ionosphere from scintillation measurements assuming certain model of wave propagation. In this paper we will briefly describe these methods.

2. Plasma Turbulence Parameters Derivable from Scintillation Measurements

Table 1 summarizes the measured scintillation parameters and the corresponding derivable irregularity parameters [2],[8].

Table 1. Scintillation parameters and corresponding, derivable irregularity parameters

Scintillation parameters	Irregularity parameters
High-frequency part of the amplitude scintillation spectrum	Shape of the irregularity spectrum at scale sizes from just above the Fresnel size $\alpha\sqrt{\lambda z}$ down to V_0/fmax, where λ is the wavelength, z is a distance between the receiver and the irregularities slab, V_0 is the ray scan velocity, and f_{max} is the maximum observed frequency
Phase scintillation spectrum	Shape of the irregularity spectrum from V_0/f_{min} down to V_0/f_{max}, where f_{min} and f_{max} are the minimum and maximum observed frequencies, respectively
Peak at the Fresnel frequency on the amplitude spectrum	Scan velocity V_0, and if the scan velocity is known - the irregularities' transverse drift velocity or a distance to the irregularity slab, whichever is not otherwise known or assumed
Behavior of the low-frequency part of the amplitude spectrum	Irregularity axial ratio
Mutual coherence function	Variance of the electron density fluctuations integrated over the propagation path and the outer scale of turbulence (provided the scan velocity is known)
Spaced-receivers correlation analysis	Average transverse drift velocity, its variance, and irregularity axial ratio
Scintillation index and r.m.s. phase	Strength and morphology of irregularities

It is known from the in situ measurements that the spectrum of ionospheric plasma density fluctuations has a power law form κ^{-p}, where p is referred to as the spectral index. The scintillation theory demonstrates that, under weak scintillation conditions, the spectral index of the high-frequency end of amplitude and/or phase scintillation spectrum is the same as the spectral index of the irregularity spectrum (Fig. 1). This is a very important result since the irregularity spectrum is an essential parameter in studying the generation and evolution mechanisms of irregularities. The scintillation spectral index p_s is related to the spectral index p_i measured

in situ on a rocket or a satellite $p_i = p_s - 1$. If scintillation is moderately strong or strong the scintillation spectrum has a form close to Gaussian and it is not possible to determine the spectral index.

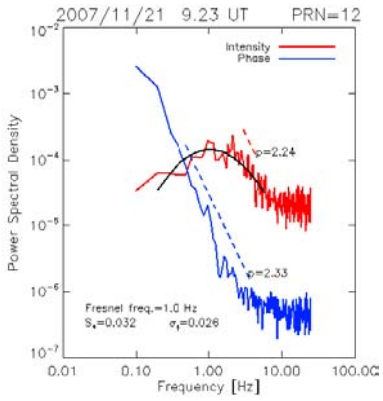

Fig. 1 Intensity (red line) and phase (blue line) power spectra computed from GPS scintillation data. Dashed, straight lines show the least squares fits over the frequency interval indicated by the end-points of lines. For the clarity of presentation lines are shifted vertically.

A maximum around 1 Hz on the amplitude spectrum is identified with the Fresnel maximum. The Fresnel frequency f_F can be computed by the least squares fit of a parabola (shown in the Fig. 1) and used to estimate the scintillation pattern velocity $V = f_F\sqrt{\lambda z}$, provided a slant distance z to the irregularity layer is assumed or known from other sources. Assuming the irregularity layer height 350 km, for the elevation angle 57 degrees, λ=0.19 m, and f_F =1 Hz, the pattern velocity estimated from the spectrum shown in Fig. 1 is close to 280 m/s.

It can be shown [1] that, independent of the scintillation strength, for a plane incident wave with constant amplitude A_0, the following relationship holds between the mean complex amplitude $< u >$ on the ground and the phase variance φ_0^2 introduced by electron density irregularities along the propagation path:

$$\langle u \rangle = A_0 \exp\left(-\varphi_0^2/2\right) \tag{2}$$

where $\phi_0^2 = (\lambda r_e)^2 \sigma_{\Delta N_T}^2$, and $\sigma_{\Delta N_T}^2$ is the variance of the deviation of the total electron content through the irregularity slab. When deriving (2) it was assumed that the phase fluctuations can be considered as a Gaussian random field with zero mean. This assumption is violated when fluctuations of electron density are not homogeneous and reveal jumps and sharp edges, as often observed in the equatorial ionosphere, but is acceptable at high latitudes.

The phase variance φ_0^2 calculated from (2) can be compared with the phase variance σ_s^2 directly derived from the phase measurements. It turns out that both quantities are close to each other, but φ_0^2 is systematically larger than σ_s^2 [9]. The estimated integrated irregularity amplitude is equal to $\sigma_{\Delta N_T} / N_T \cong 2 \cdot 10^{-4} (0.02\%)$

Figure 2 illustrates the idea of the reconstruction of the ionospheric irregular structure from scintillation using the inverse method [10]. The scintillation has been simulated by applying the multiple phase screen algorithm with the nonhomogeneous background electron density. The following reconstruction formula was used:

$$u(x,z) = \int u(k_x, z_0) \exp\left[-i\left(\frac{z k_x^2}{2k}\right) - i x k_x\right] dk_x \tag{3}$$

The above formula was applied starting from the ground and propagating the wave backwards towards the

transmitter on the satellite. At each step the scintillation index S_4 was calculated. Height z = 395 km, at which S_4

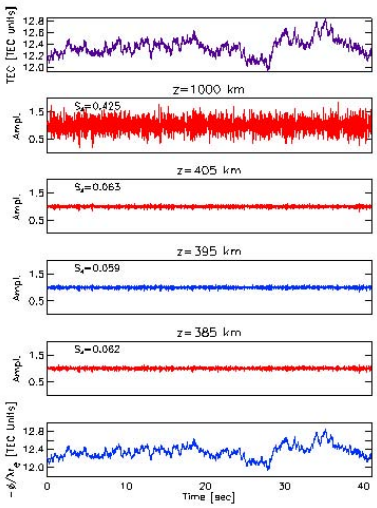

Fig. 3. Illustrates the reconstruction of the irregular structure from scintillations.

is minimum, is considered as the reconstructed height of the peak electron density. It agrees with the assumed peak height. Bottom panel shows the reconstructed TEC, which should be compared with the assumed TEC (top panel).

Acknowledgement

The work by AWW and MG has been supported by the Ministry of Science and Higher Education under the grant IPY/280/2006. The work by MM has been partially supported by the Italian National Space Agency (ASI) through the contract ISMB/ASIN.I./006/07/0.

References

[1.] K.C. Yeh, and C. H. Liu, "Radio wave scintillations in the ionosphere", *Proc. IEEE*, vol. 70, pp. 324 – 360, 1982.
[2.] A. W. Wernik, J. A. Secan, and E. J. Fremouw, "Ionospheric irregularities and scintillation", *Adv. Space Res*., vol. 31, pp. 971 – 981, 2003.
[3.] V. I., Tatarski, The effects of the turbulent atmosphere on wave propagation, *Natl. Tech. Inform. Serv.*, Springfield, VA, 1971.
[4.] H. G., Booker, J. A. Ratcliffe, and D. H. Shinn, "Diffraction from an irregular screen with application to ionospheric problems", *Phil. Trans. Roy. Soc. A.*, vol .242, pp. 579 – 607, 1950.
[5.] C. L., Rino, and E. J. Fremouw, "The angle dependence of singly scattered wavefields", J. Atmos. *Terr. Phys.,* vol. 39, pp. 859 – 868, 1977.
[6.] C. L., Rino, "A power law phase screen model for ionospheric scintillation, 1, Weak scatter", *Radio Sci.*, vol. 14, pp. 1135 – 1145, 1979.
[7.] C. L., Rino, "A power law phase screen model for ionospheric scintillation, 2, Strong scatter", *Radio Sci*., vol. 14, pp. 1147 – 1155, 1979.
[8.] A., Bhattacharyya, K. C. Yeh, and S. J. Franke, "Deducting turbulence parameters from transionosphericscintillation measurements", *Space Sci. Rev*., vol. 61, pp. 335-386, 1992.
[9.] A. W. Wernik, M. Pożoga, M. Grzesiak, A.Rokicki and M. Morawski, "MISTECS-Monitoring ionospheric scintillation and total electron content at the Polish Polar Station on Spitsbergen – instrumentation and preliminary results", *Acta Geophysica,* vol. 56, pp. 1129 – 1146, 2008.
[10.] K.C. Yeh and C. H. Liu, "Reconstruction of ionospheric irregularities using transionospheric radio waves", in *Proc. of the COSPAR/URSI Symposium "Scientific and Engineering Uses of Satellite Radio Beacons*", Polish Scientific Publishers, Warsaw, Poland, pp. 235 – 246, 1981.

Commission “SPS”

Solar Power Satellite Systems

STATUS OF SPACE SOLAR POWER SYSTEM AT USEF

Yoshiharu FUSE [(1)], ***Takashi SAITO*** [(2)], ***Shoichiro MIHARA*** [(3)], ***Koichi IJICHI*** [(4)]

[(1)] Institute for Unmanned Space Experiment Free Flyer, 2-12 Kanda-Ogawamachi, Chiyoda-Ku, Tokyo, JAPAN, fuse@usef.or.jp
[(2)] As (1) above, but Email : saito@usef.or.jp
[(3)] As (1) above, but Email : mihara@usef.or.jp
[(4)] As (1) above, but Email : ijichi@usef.or.jp

Keywords: Space solar power system (SSPS), Wireless Power Transmission(WPT), Japanese new space policy & new space plan, Ground microwave WPT

Abstract: Institute for Unmanned Space Experiment Free Flyer, USEF, has been studying Space Solar Power System, SSPS, from early 1990'. One of major activities is the development and demonstration of several important technologies for the realization of the microwave wireless power transmission system, WPT. They are beam steering, microwave transmission and microwave power utilization. As for the transmission and utilization, we have developed and tested light weight microwave transmission system and rectenna array. In 2008, new development plan for Ground microwave WPT has started in 2009. The system is intended to demonstrate microwave beam control and microwave wireless power transmission with about 100m distance and kilo watts level transmission power.

1. Introduction

USEF has been studying Space solar power system (SSPS) as an alternative future energy resource under a support of METI (Ministry of Economy, Trade and Industry) and the other related agency for the past several years.[1][2][3] The study has covered from basic laboratory testing level to the practical power plant level. In this couple of years, the new space policy and the new space plan were established. SSPS was selected one of nine important subjects to make research. The several kilo watts level microwave Wireless Power Transmission experiment is planned in next four years.

2. Summary of SSPS activities

The feasibility study of SSPS was carried out from FY2001 to FY2003. The Working Committee has investigated a simple, technically feasible, and practical configuration SSPS which consists of a large power generation /transmission panel or sandwich panel suspended by multi-tether wires from a bus system above the panel. [4][5] The study has been done for its dynamic stability, construction method on orbit, operation, economical aspect and development scenario.[2] In FY 2004, the feasibility study of wireless power transmission for the promotion of solar power energy has initiated. The application of WPT on the ground usage has been studied in FY 2004 and 2005. [6] Space system has been studied from FY 2006. Microwave reflection and emission from rectenna had been measured in 2005 and 2006.
In order to utilize wireless power transmission, we have to consider three main elements. First element is generation of RF energy from the electric power. The second element is to send the energy to the point of interest. The last element is the receiving RF energy and converting it to direct current electric power. We have covered these elements in our testing in some extent.
The beam control experiment was initiated from 2001. The active array panel with phase shifters, AIA#1[7], and the hardware retro-directive active integrated array panel, AIA#2[8], were developed and tested. The

combination transmission test was also carried out. The purpose of the development was to understand the issue derived by the microwave beam steering with integrated panels. And its evaluation was carried out in the anechoic chamber. In 2007, high accurate beam control experiment was carried out using the phased array antenna (5.8GHz, one-dimensional, 12 elements, about 40 cm wide).[9] Also, experiment of synchronized reference control system by closed loop technique for multiple phased array panels were carried out.[9]
The WPT to remote object is a preferable application of SSPS technology. The rectenna array for rover, light weight phased array panel for transmitter on 5.8GHz had been developed. We also confirmed the low power command communication, 10mw, in 100W level microwave power transmitting condition. [10][11]

3. SSPS on new space policy and plan

The Japanese new space policy was enacted in 2008 and the new space plan was established in 2009. They have selected 5 practical space systems to realize and 4 research development programs to promote. Space Solar Power system program was selected as one of the research development plans. Following issues were included relating to SSPS.
Though Space Solar Power System was selected as important project, budget for Large Space system was not yet declared to be supplied. The new development plan, which is limited to the Ground microwave WPT, is funded by METI, and it is planed from 2009 to 2013. (Fig 1) The plan will be conducted with JAXA team.

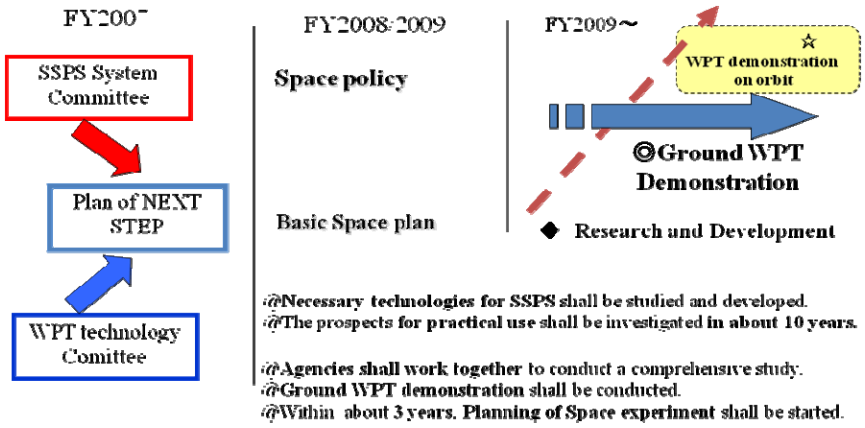

Fig.1. SSPS on New Space Policy and Plan

4. Property of Wireless Power Transmission

4.1. Frequency for SSPS

As for the microwave Wireless Power Transmission system, 5.8 GHz band is selected as candidate frequency to be applied for Space solar power satellite system. Fig 2 shows frequency selection and its properties. The attenuation in the atmosphere is large if the frequency is higher than 10GHz. Water (H_2O) Oxygen (O2) molecules attenuate microwave propagation from the outer space. The size of the system is proportional to the wave length. Therefore lower frequency system results large system size. But if we select millimeter wave length band, the components of the system need micro precision manufacturing technology. 5.8 GHz band has preferable characteristics by above reasons.

4.2. Active Phased Array Antenna and Rectenna array

For the microwave power transmission antenna, phased array antenna using the semiconductor to be able to do the small size, lightness, and highly effective by the expectation is preferable. Moreover, the antenna is composed several power transmission modules to achieve the high-power power transmission, and the phase synchronization of the micro wave is aimed at. And to convert the micro wave into the electrical energy highly effective, the receipt part is made with the Schottky barrier diode.

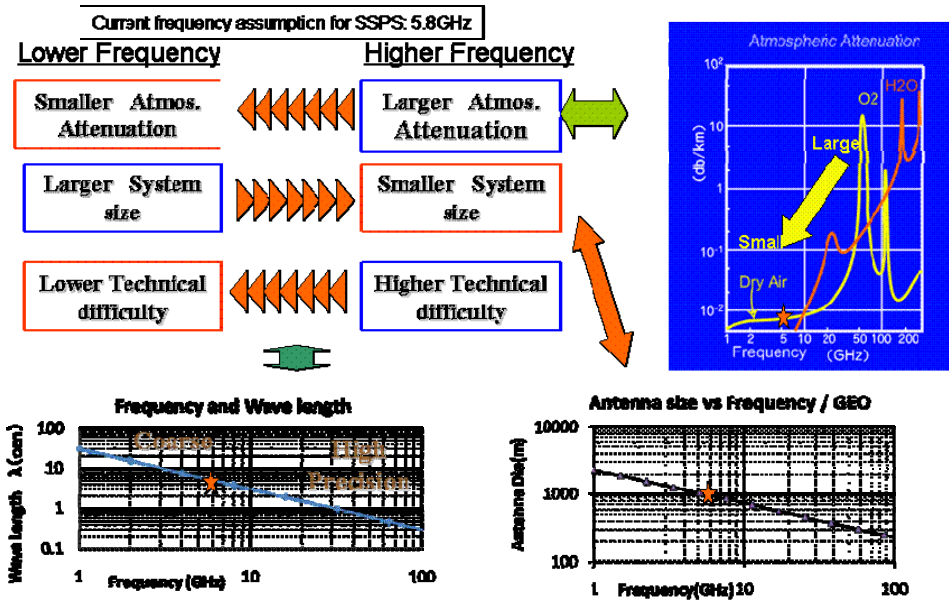

Fig.2. Frequency Selection for SSPS

5. New Ground WPT test project

Fig 3 and Fig 4 show new Ground WPT system plan. The system is intended to demonstrate microwave beam control and microwave wireless power transmission with about 100m distance and kilo watts level transmission power. It has following characteristics.

(1) The Frequency is in 5.8GHz ISM band.

(2) Four Phased Array Panels. One panel consists of 13x13 sub arrays. One sub array consists of 2x2 transmission elements.

(3) As the final configuration is space use, the thickness and weight of the panel shall be reduced. Target thickness is about 30mm. The final amplifiers in each element are all solid state.

(4) REV method, rotating-element electric-field vector method, will be applied for phase control of the elements.

(5) Software Retro-directive will be applied to control the direction of the transmission microwave power. Pilot signal detection and retro-directive direction pointing with phase shifter is JAXA's role.

(6) Rectenna array panels for effective RF-DC power conversion will be developed.

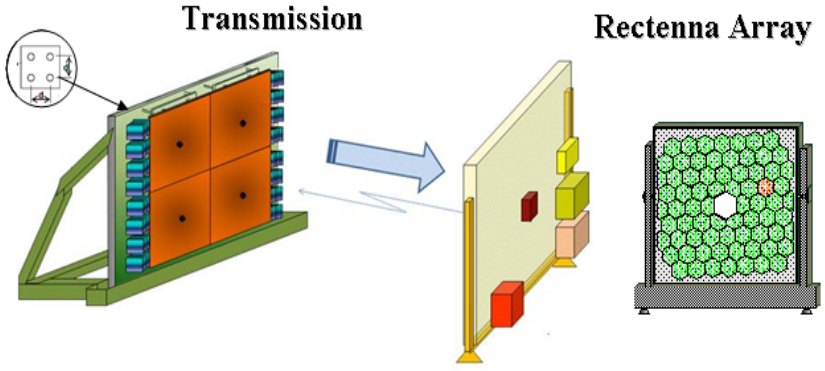

Fig.3. New Ground WPT Configuration

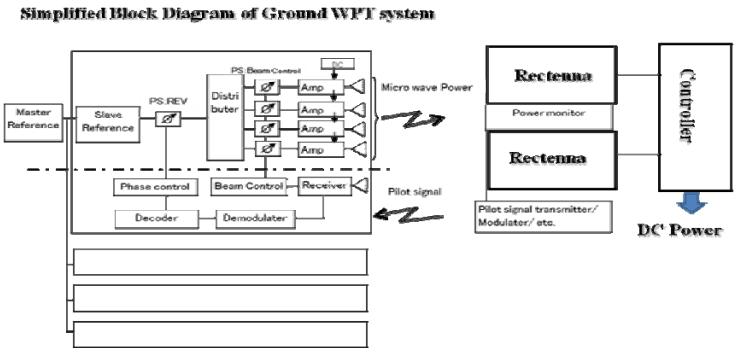

Fig.4. Simplified Block Diagram

6. Conclusions

We proceed work with the aggressive target in Ground WPT test project, started in 2009, using the study results executed in the past. That should be carried out to realize the practical space solar power system for humankind in the future.

Acknowledgment

At New Ground WPT system, Transmitting section partner is Mitsubishi Electric Co. (MELCO), and Rectenna section partner is IHI Aerospace. The chairman of Microwave Wireless Power Transmitting Committee is Prof. Naoki Shinohara, Kyoto University. USEF is grateful to all members of the committee and authors of all references.

References

[1.] Kobayashi Y, Saito T, Ijichi K, Kanai H, Space Solar Power System for Terrestrial Power Utilities, SPS'04/WPT5, June 2004.
[2.] Mihara S, Saito T, Kobayashi Y, Kanai H, Overview of activities for Solar Power Systems in USEF, IAC-05-C3.1.02, Oct 2005.
[3.] Mihara S, Saito T, Kobayashi Y, Ijichi K, Consideration of Next Logical Step for Wireless Power Transmission of SSPS Based on Activities at USEF, IAC-09-C3.1.5, Sep 2009.
[4.] Sasaki S., Tanaka K., Higuchi K. Okuizumi N, Kawasaki S, Shinohara N, Senda K, Ishimura K, Tethered Solar Power Satellite, ISSN 1349-1113, JAXA RR-03-005E, 2004
[5.] Senda K., Ishimura K., Takai N., Analysis of System Dynamics of USEF SSPS Models, prepared for USEF, prepared by Kanazawa University and Hokkaido University, May 2004
[6.] Mihara S, Saito T, Kobayashi Y, Kanai H, "Activities Results of Experiments for Space Solar Power Systems at USEF", IAC-06-C3.3.2, Oct 2006
[7.] Kimura T, Yamamoto K, Nakada T, Kito K, Development of Highly Efficient Active Integrated Antenna, Proc. Of SPS'04, 2004
[8.] Mizuno T., et al., "Development of a PLL-Heterodyne Hardware Retrodirective Antenna",1B06, Proc of the 48th SSTC,2004
[9.] Kobayashi Y, Mihara S, Saito T, Ijichi K, Summary of concept study for Space Solar Power Systems at USEF, IAC-08-C3.1.5, Oct 2008
[10.] Shinohara N, Nagano K, Ishii T, Kawasaki S, Fujiwara T, Nakayama S, Takahashi Y, Sasaki S, Tanaka K, Hisada Y, Fujino Y, Mihara S, Anzai T, Kobayashi Y, Experiment of Microwave Power Transmission to the Moving Rover, Proc. of ISAP2007, in print, 2007
[11.] Furukawa M, et al, "5.8-GHz Planar Hybrid Rectenna for Wireless Powered Applications", FR-2E1, APMC 2006

Opportunities and Challenges for Wireless Power Transmission

Frank E. Little,

Space Engineering Research Center, Texas A&M University, College Station, TX 77843-3118, USA
f-little@tamu.edu

Keywords: Wireless Power Transmission, Microwave, Space-based Solar Power, Solar Power Satellite,

Abstract: Recent announcements in the United States and Japan have brought renewed interest in space based solar power and wireless power transmission. In the United States, the first commercial contract to deliver electric power from space to the electric utility grid was announced between Pacific Gas and Electric Company and Solaren Corporation. In Japan, the government announced a phased program leading to a full-scale demonstration solar power satellite in 2030. Opportunities for using wireless power transmission have been identified on earth and beyond.

While judged technically feasible since the 1981 National Research Council report on the NASA Definition Study, the deployment of an operational space based solar power system still presents many challenges. These challenges are both technical and programmatic. Similar challenges will be encountered in other applications of wireless power transmission.

1. Introduction

The first practical application of wireless power transmission was the demonstration of the sustained flight of a microwave powered tethered helicopter by William Brown in 1964 [1]. The application of wireless power transmission for aerial platforms was further demonstrated by: the Canadian Stationary High Altitude Relay Platform (SHARP) program, including a 20 minute low altitude microwave powered flight [2]; the Japanese MIcrowave Lifted Airplane eXperiment (MILAX), including a phased array transmitter [3]; and the Japanese Energy Transmission toward High altitude long endurance airship ExpeRiment (ETHER) airship [4]. Terrestrial fixed point-to-point wireless power transmission demonstrations include: the Raytheon laboratory experiment that achieved 54 % dc power out from dc power in [5]; the Raytheon/Jet Propulsion Laboratory test at the National Aeronautics and Space Administration's (NASA) Goldstone Facility where more than 30 kiloWatts was received at the rectenna [6]; a Japanese test at Kansai Power Company [7]; and a low power Japanese-US demonstration of over 100 kilometers in Hawaii, from the summit of Haleakala on the island of Maui to Mauna Loa on the island of Hawaii [8].

The closest that has been achieved to wireless power transmission from space or in space are the Japanese led sounding rocket experiments: the Microwave Ionosphere Nonlinear Interaction experiment (MINIX), flown in 1983 [9]; the International Space Year-Microwave Energy Transmission in Space (ISY-METS), an international follow-on experiment to confirm and extend MINIX, that included contributions from Texas A&M University and the International Space University, flown in 1993 [3]; and a retrodirective transmission experiment flown as part of an antenna deployment project in 2006 [10].

2. Opportunities for Application of Wireless Power Transmission

Wireless power transmission is defined to be the transmission of electric energy through conversion to microwaves, the transmission of the microwaves, their reception and conversion to electricity, thereby effecting a wireless link in the real-time transmission of electric energy.

2.1 Solar Power Satellite

The first major opportunity for implementation of wireless power transmission for the transport of electrical energy was the solar power satellite proposed by Dr. Glaser [11]. The solar power satellite concept to provide base load electric supply to the grid was developed into a reference design in the NASA – US Department of Energy (DoE) study [12] that was spurred by the energy crisis of the mid 1970s. Wireless power transmission research continued at a low level in several countries [13] until new interest resulting from the 2007 US Department of Defense study of space-based solar power [14], spurred by global concern over the role of burning fossil fuel in climate change. Several countries, including China, India and South Korea have begun research and development projects for space-based solar power, however, the most advanced projects are the plan announced by Japan for a roadmap leading from ground based experiments through low earth orbit technology demonstration to an operating geostationary orbit solar power satellite pilot plant in the 2030s [15] and the commercial power purchase agreement announced in California in the US [16]. The rate agreed between Solaren and Pacific Gas and Electric Company is the same premium rate paid by the utility for terrestrial solar electric power. Although Solaren is the first private company to negotiate a purchase agreement with a utility, they are not the only company attempting to establish a space-based solar power supply market (others include Space Energy, and PowerSat).

A study published by the International Space University [17] examined the economic feasibility of wireless power transmission at millimeter wave frequency (35 GHz) for a solar power satellite, the trade being the economic effect of smaller aperture sizes (compared to 2 – 10 GHz microwave) with reduced atmospheric transmission efficiency and rain fade. Potential alternate uses for a geostationary satellite generating station operating at high frequency could be power for electric propulsion [18] and emergency power for disaster relief using small diameter portable rectennas.

2.2 Terrestrial Point-to-Point

Wireless power transmission has been proposed for point-to-point electric distribution on the ground for short distance by line-of-sight [19, 20] and for longer distances by relay satellite [21]. Applications include: electric grid transmission to a remote site or where cables are impractical, such as bridging the Strait of Belle Isle in Canada [22]; powering long duration aircraft for observation and communications [2]; Remote charging/powering of electric vehicles [23].

2.3 Space Operations

Space applications of wireless power transmission include: the analogue to the solar power satellite for powering surface operations from orbit [24]; short range surface rovers; powering satellites (or habitats) from a central power facility; orbit raising via electric propulsion [25].

3. Challenges for Wireless Power Transmission

The challenges facing the use of wireless power transmission include the primarily political issues of public perception and spectrum allocation. Both are essentially political fights and beyond the scope of this paper, but also barriers that must be overcome. Maximum microwave beam energy density at the ground for the NASA – DoE Reference design was 250 W/m^2, which caused health and safety concerns. Potential health and safety issues must be addressed for higher frequency, more focused beams with higher beam energy density.

3.1 Increasing Component Efficiency

The best demonstrated laboratory end-to-end efficiency for a wireless power transmission is 54% at 2.45 GHz [5]. The electric to microwave conversion had the lowest efficiency of all components in that 1975 test. That is still the case, regardless of the frequency of transmission. Designs for depressed collector klystron and

gyrotron tubes have been developed to increase efficiency, but not implemented [26]. Solid state amplifiers have progressed as new materials, particularly gallium nitride, have become available and are now available in the few GHz range, where designs for 80% efficient e-class amplifiers have been reported [27].

Most of the research on microwave to electric conversion has been in the 2 — 10 GHz range, with greater than 80 efficient elements reported at 2.45 and 5.8 GHz [13]. Millimeter wave rectenna designs have been reported for 35 GHz [28] and 96 GHz [29], with maximum measured efficiency of greater than 70% for the 35 GHz rectenna. Higher frequency elements should be pursued for space and point-to-point application.

3.2 System Demonstration

Among the system issues for wireless power transmission that must be developed and demonstrated are: rectenna designs for efficient conversion from microwave to electric power over a broad range of power density; reduction of broadcast frequency harmonics from both the transmitter and rectenna to avoid interference with other spectrum users; a fully operational retrodirective beam control system (Rodenbeck and Chang [30] showed that a small scale retrodirective system can suffer from angular displacement of the microwave beam when non-isotropic transmitting elements are used).

The ability to transmit multiple power beams from a single aperture without invoking the "curse of the sparse array" where a significant fraction of the beam energy is lost in grating lobes still has not been demonstrated even in the laboratory.

Conclusions

Opportunities for wireless power transmission are expanding, both on earth and in space. Of particular note are the announced national and commercial plans to develop space-based solar power. Wireless power transmission technology exists, but can be improved. Efficient high power, microwave and millimeter-wave sources and rectennas (or other conversion devices) are needed to fully exploit these opportunities.

Experiments and demonstrations (particularly in space) are necessary to reduce the technical risk of implementation and inform the public.

References

[1.] W. C. Brown, "The History of Power Transmission by Radio Waves", *IEEE Transactions on Microwave Theory and Techniques*, 32 (9) 1230-1242 (1984)

[2.] J. J. Schlesak, A. Alden and T. Ohno, "A Microwave Powered High Altitude Platform", *IEEE MTT-S Digest,* pp. 283-286 (1988)

[3.] N. Kaya, H. Matsumoto, H. Kojima, Y. Fujino, and M. Fujita, "Test Projects for Microwave Energy Transmission (MILAX, ISY-METS and Future IPSAT)" in *WPT-93: First Annual Wireless Power Transmission Conference*, Center for Space Power, Texas A&M University, College Station, Texas, pp. 245-253 (1993)

[4.] M. Onda, *et al,* "Preliminary Tests of Ground-to-Airship Microwave Transmission for the Future Stationary High-Altitude Platform" presented at WPT-95 Second Wireless Power Transmission Conference, Kobe, Japan, October 16-19, 1995

[5.] R. M. Dickinson and W. C. Brown, "Radiated Microwave Power Transmission System Efficiency Measurements" Tech Memo 33-727, Jet Propulsion Lab. Cal. Inst. Technol., Mar. 15, 1975

[6.] R. M. Dickinson, "Evaluation of a Microwave High-Power Reception-Conversion Array for Wireless Power Transmission" Tech Memo 33-741, Jet Propulsion Lab. Cal. Inst. Technol., Sept. 1 1975

[7.] H. Matsumoto, "Microwave Power Transmission from Space and Related Nonlinear Plasma Effects" *Space and Radio Science Symposium: 75th Anniversary of URSI,* 26-27 April 1995, Brussels, Belgium, pp. 155-190

[8.] Discovery channel series "Ways to Save the Planet: Orbital Power Plant", broadcast September 2008, http://www.discoverychannel.co.uk/web/ways-to-save-the-planet

[9.] N. Kaya, H. Matsumoto, S. Miyatake, I. Kimura, M. Nagatomo, and T. Obayashi, (1986) "Nonlinear

Interaction of Strong Microwave Beam with the Ionosphere", *Space Power*, 6 pp. 181-186, 1986
[10.] N. Kaya, M. Iwashita, K. Tanaka , S. Nakasuka , and L. Summerer, "Rocket experiment on microwave power transmission with Furoshiki deployment", *Acta Astronautica* 65, 202-205
[11.] P. E. Glaser, US Patent 3,781,647 "Method and Apparatus for Converting Solar Radiation to Electrical Power" December 25, 1973.
[12.] DOE 1978 "Satellite power system (SPS) concept development and evaluation program (CDEP) Reference System Report", DOE/ER-0023, October 1978
[13.] J. C. Mankins and J. O. McSpadden, "Space Solar Power Programs and Microwave Wireless Power Transmission Technology", *IEEE Microwave Magazine,* December 2002, pp. 46-57
[14.] Department of Defense, "Space-Based Solar Power as an Opportunity for Strategic Security" Report to the director, National Security Space Office, 10 October 2007
[15.] "Mitsubishi, IHI to Join $21 Bln Space Solar Project (Update1)", Bloomberg.com news story September 1, 2009, (http://www.bloomberg.com/apps/news?pid=20601101&sid=aJ529lsdk9HI)
[16.] "PG&E makes deal for space solar power", MSNBC news story, April 13, 2009, (http://www.msnbc.msn.com/id/30198977/)
[17.] S. Xin, E. Panier, C. Zünd, and R. Gutiérrez Gómez, "Financial and Organizational Analysis for a Space Solar Power System (A business plan to make Space Solar Power a reality)", A Multicultural Team Project submitted in partial fulfillment for the degree of Master of Business Administration in Aerospace Management at Toulouse Business School, Toulouse, France
[18.] T. Cummings, *et al,* "Microwave Power-Beaming Demonstration with 6-kV Rectenna and Ion-Breeze Thruster", Paper AIAA-2003-4431, 39th AIAA/ASME/SAE/ASEE Joint Propulsion Conference and Exhibit, Huntsville, Alabama, July 20-23, 2003
[19.] P. L. Haldane and B. W. Schupp, "Alaska '21: A Terrestrial, Point-to-Point Wireless Power Transmission System", in *WPT-93: First Annual Wireless Power Transmission Conference*, Center for Space Power, Texas A&M University, College Station, Texas, pp. 191-198 (1993)
[20.] A. Celeste, J.D. Lan Sun Luk, J.P. Chabriat and G. Pignolet, "The Grand-Bassin Case Study: Technical Aspects" *Proceedings, SPS '97 Conference,* Montréal, Canada, August 24-28, 1997, pp. 255-258
[21.] P. E. Glaser, "The Power Relay Satellite" in *WPT-93: First Annual Wireless Power Transmission Conference*, Center for Space Power, Texas A&M University, College Station, Texas, pp. 199-209 (1993)
[22.] R. M. Dickinson and O. Maynard, "Ground Based Wireless and Wired Power Transmission Cost Comparison" 34th IECEC, Vancouver, BC, 1999 (file 99-1291 JPL TRS 1992+ in JPL Technical Report Server)
[23.] R. J. Parise, "All Electric for the Millennium - Mobile Vehicle Recharge", Paper 2000-01-1058, SAE 2000 World Congress, Detroit, Michigan, March 6-9, 2000
[24.] H. W. Brandhorst, Jr. and F. Little, "POWOW Revisited – Beamed Power for Mars Exploration", Paper 2004-5642, *Proceedings of 2nd International Energy Conversion Engineering Conference,* Providence, Rhode Island, August 16-19, 2004
[25.] W. C. Brown and B. W. Schupp, "A Transportronics Solution to the Problem of Interorbital Transportation", in *WPT-93: First Annual Wireless Power Transmission Conference*, Center for Space Power, Texas A&M University, College Station, Texas, pp. 85-101 (1993)
[26.] F. E. Little, "A Wireless Power Based Space Transportation System", Paper No. 2006-g-10, *Proceedings of the 25th International Space Technology and Science Conference,* Kanazawa, Japan, June 4-11, 2006
[27.] D. Schmelzer and S. I. Long, "A GaN HEMT Class F Amplifier at 2 GHz With <80% PAE", *IEEE Journal of Solid-state Circuits,* Vol. 42, No. 10, pp. 2130-2136, October 2007
[28.] P. Koert and J.T. Cha, "35 GHz Rectenna Development", in *WPT-93: First Annual Wireless Power Transmission Conference*, Center for Space Power, Texas A&M University, College Station, Texas PP. 457-466, 1993
[29.] G. Chattopadhyay, *et al*, "Millimeter-Wave Wireless Power Transfer Technology for Space Applications", Asia Pacific Microwave Conference 2008, Hong Kong, China, December 16-20, 2008
[30.] C. T Rodenbeck and K. Chang, "A Limitation on the Small Scale Demonstration of Retrodirective Microwave Power Transmission from the Solar Power Satellite", *IEEE Antennas and Propagation Magazine,* Vol. 47, No. 5, pp. 67-72, August 2005

Demonstration Experiments of Microwave Power and Information Transmission from an Airship

Tomohiko Mitani [(1)]***, Hiroshi Yamakawa*** [(1)]***, Naoki Shinohara*** [(1)]***, Kozo Hashimoto*** [(1)]***, Shigeo Kawasaki*** [(1,2)]***, Fumito Takahashi*** [(1)]***, Hideaki Yonekura*** [(1)]***, Takahiro Hirano*** [(1)]***, Teruo Fujiwara*** [(3)]***, Kenji Nagano*** [(4)]***, Hideki Ueda*** [(5)]***, and Makoto Ando*** [(5)]

[(1)] Research Institute for Sustainable Humanosphere, Kyoto University, Gokasho, Uji, 611-0011 Japan
mitani@rish.kyoto-u.ac.jp; yamakawa@rish.kyoto-u.ac.jp; shino@rish.kyoto-u.ac.jp
[(2)]Institute of Space and Astronautical Science, Japan Aerospace Exploration Agency, Japan
[(3)] Sho Engineering Corp., Japan, [(4)] Space Technology, Japan, [(5)] Tokyo Institute of Technology, Japan

Keywords: Phase-Controlled Magnetron, Radial Line Slot Antenna, Direction-of-Arrival Estimation, Rectenna.

Abstract: The world's first experiments: "Demonstration Experiments of Microwave Power and Information Transmission from an Airship" (abbreviated as "Airship Experiments") were conducted on the Uji campus ground, Kyoto University on March 5th and 10th, 2009. The objectives of the Airship Experiments are to demonstrate wireless transmission of electrical power and information simultaneously, to reduce the size and weight of microwave transmitting system, and to remote-control the microwave transmitting system. The Airship Experiments consist of a transmitting system, a direction-of-arrival estimation system, a remote control and telemetry system, and a receiving system. The transmitting system consisted of lithium-ion battery, power supply, two magnetrons, waveguide couplers, two-element radial line slotted antennas. The 17m-long airship was launched at an altitude of around 30m. Total microwave power of 220 W was radiated from the transmitting system mounted on the bottom of the airship. The Airship Experiments were successful with regard to demonstration of wireless power transmission, direction-of-arrival detection received by a pilot signal, remote control by 429MHz specified low-power radio communication.

1. Introduction

Microwave power transmission has been studied in Kyoto University [1], especially for solar power station/satellite (SPS) projects [2] and ground-based applications such as wireless power distribution in a building [3]. As a new ground-based application of microwave power transmission, we conducted the world's first experiments: "Demonstration Experiments of Microwave Power and Information Transmission from an Airship" (abbreviated as "Airship Experiments"). Microwave power transmission from an airship can be applied as an emergency power source to a disaster area. The objectives of the Airship Experiments are to demonstrate wireless transmission of electrical power and information simultaneously, to reduce the size and weight of microwave transmitting system, and to remote-control the microwave transmitting system. These objectives are also linked to SPS projects.

2. Configurations of the Airship Experiments

Fig.1 shows A conceptual diagram of the Airship Experiments. The Airship Experiments consists of a transmitting system, a direction-of-arrival estimation system, a remote control and telemetry system, and a receiving system. The diameter and length of the airship is 4m at maximum and 17m, respectively. Microwave power density on the ground is designed below 1mW/cm^2.

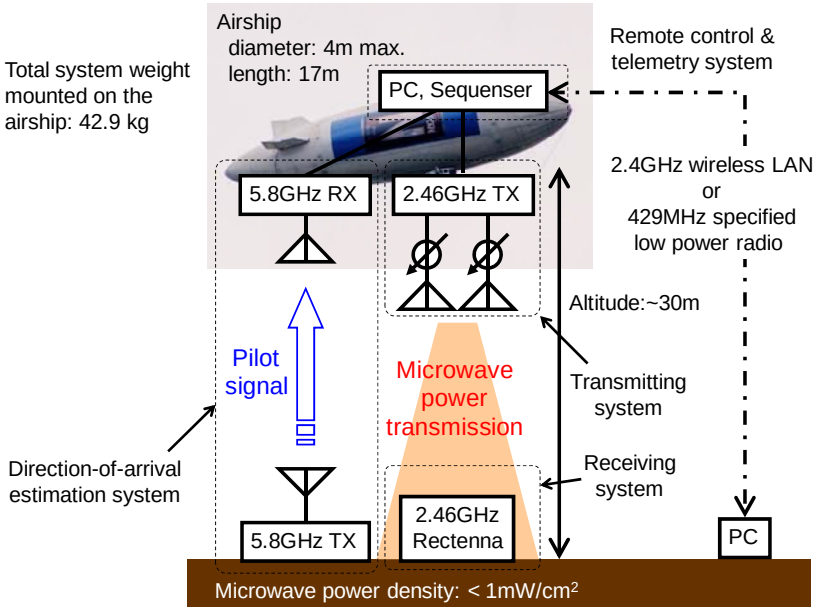

Fig.1 A conceptual diagram of the Airship Experiments.

2.1. Transmitting System

Fig. 2 shows a photograph of the transmitting system. The transmitting system consists of two phase-controlled magnetrons [1, 4], which are driven by lithium-ion battery. The magnetron frequency is fixed at 2.46GHz by phased locked loop. Each magnetron output is attached to a radial line slot antenna (RLSA) with honeycomb structure [5] through a waveguide coupler. The diameter of the RLSA is 72cm and the distance between two RLSA is 116cm. The RSLA gain was measured to be 22.7 dBi. A microwave power of 110W is radiated from each RLSA; hence the total microwave power of 220W is radiated from the transmitting system. The transmitting system is mounted on the bottom of the airship.

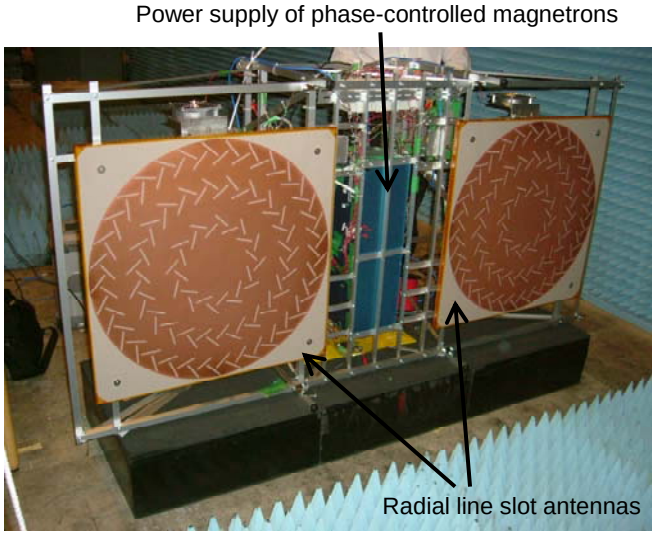

Fig.2 A photograph of the transmitting system. Two phase-controlled magnetrons are set up behind the antennas.

2.2. Direction-of-Arrival Estimation, Remote Control and Telemetry Systems

The direction-of-arrival estimation system consists of a pilot signal transmitter on the ground and two receivers on the airship. The pilot signal frequency is 5.8GHz. A lightweight computer mounted on the airship conducts the direction-of-arrival estimation by calculating the phase difference between the receivers.

The transmitting system is remote-controlled via 2.4GHz-band wireless LAN or 429MHz specified low-power radio communication. The telemetry system monitors battery voltage, magnetron current and microwave output power, and these data are stored in the lightweight computer. Also, a USB camera is attached on the airship to a downward direction, and it records demonstration experiments from the airship.

2.4. Receiving System

Three types of 2.46GHz rectennas were prepared as the receiving system: 4-elements rectenna with dc-dc converter for a LED lighting test, 4-elements rectenna with dc-dc converter for an electronic buzzer test, and 12-elements rectenna for a cell phone charging test. Fig. 3 shows photographs of a 4-elements rectenna with dc-dc converter for the LED lighting test. All the rectennas were successfully driven over a microwave power density of 0.4mW/cm^2 with a conversion efficiency of around 45% to 50%.

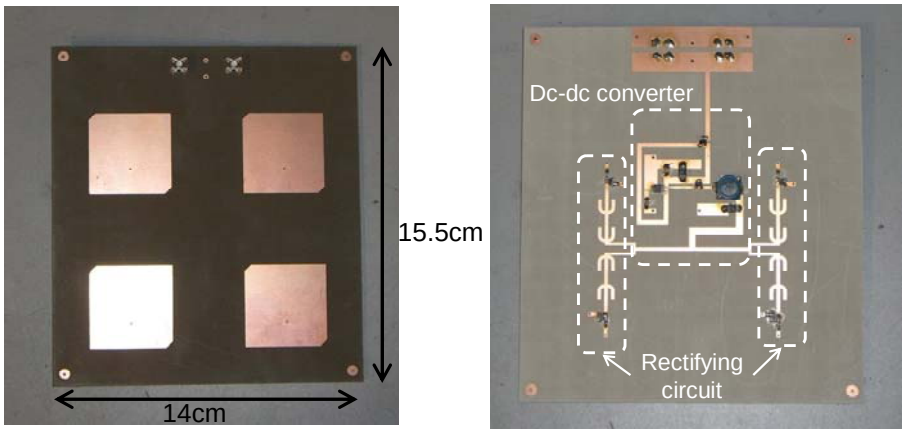

Fig. 3 Photographs of a 4-elements rectenna with dc-dc converter for a LED lighting test. The left photograph shows the antenna side, and the right photograph shows the rectifying circuit side.

3. Demonstration Experiments

The Airship Experiments were conducted on the Uji campus ground, Kyoto University, on March 5th and 10th, 2009. Fig, 4 shows a photograph of the Airship Experiments. The total system weight mounted on the airship was 42.9kg. The airship was launched at an altitude of around 30m. Although 2.4GHz wireless LAN did not work due to a compatibility problem with microwave power transmission, the transmitting system was successfully driven and remote-controlled via 429MHz specified low-power radio communication. After microwave had been radiated from the transmitting system, we confirmed that all the rectennas were successfully driven by the microwave power. The direction-of-arrival estimation also worked successfully. With respect to phase control of the transmitting system, it was impossible to confirm whether or not microwave beam was controlled because the airship uncontrollably swayed in the wind.

4. Conclusions

The Airship Experiments were succeeded for the first time in the world, with regard to demonstration of wireless power transmission, direction-of-arrival detection received by a pilot signal, remote control by 429MHz specified low-power radio communication. This demonstration is an important step for realization of ground-base applications of microwave power transmission as well as SPS projects.

Acknowledgment

The Airship Experiments were supported by Grant-in-Aid for Scientific Research (B, No.18360171), Japan Science and Technology Agency, the KDDI foundation, the Okawa foundation, and Kyoto University.

References

[1.] H. Matsumoto, "Research on solar power station and microwave power transmission in Japan," IEEE Microwave Magazine, vol. 3, no. 4, pp. 36-45, Dec. 2002.
[2.] P. E. Glaser, F. P. Davidson, and K. Csigi, *Solar Power Satellites*, Chichester, U.K.: Wiley, 1998.
[3.] N. Shinohara, Y. Miyata, T. Mitani, N. Niwa, K. Takagi, K. Hamamoto, S. Ujigawa, J. P. Ao, and Y. Ohno, "New Application of Microwave Power Transmission for Wireless Power Distribution System in Buildings," *2008 Asia-Pacific Microwave Conference (APMC)*, H2-08, Dec. 2008.
[4.] N. Shinohara, H. Matsumoto, and K. Hashimoto, "Solar Power Station/Satellite (SPS) with Phase Controlled Magnetrons," *International Union of Radio Science (URSI) General Assembly 2002*, Proceedings p.1475, Aug. 2002.
[5.] H. Ueda, J. Hirokawa, M. Ando, O. Amano, and Y. Kamata, "A Lightweight Radial Line Slot Antenna with Honeycomb Structure for Space Use, " *IEICE Transactions on Communications*, vol. E91-B, no.3, pp. 871-877, Mar. 2008.

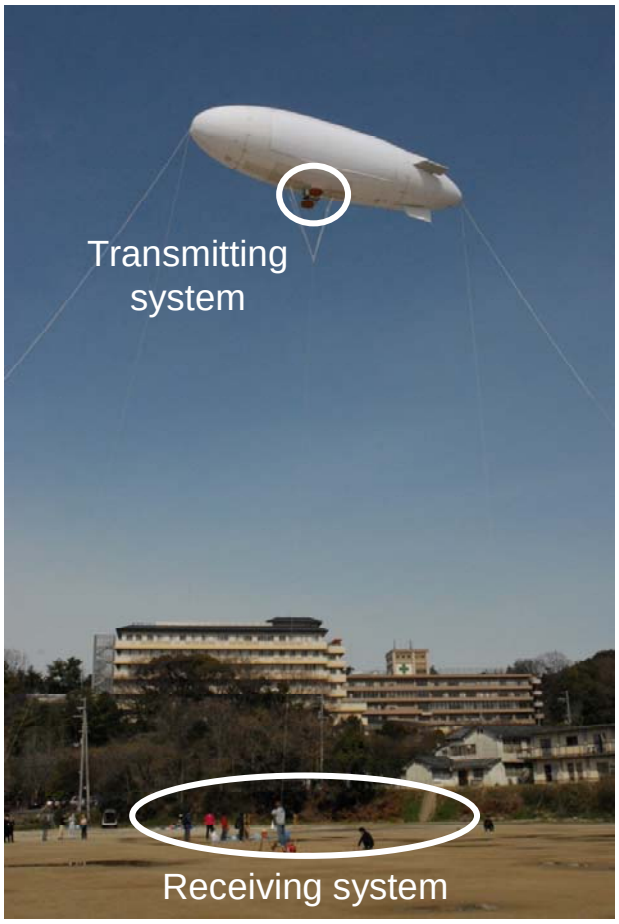

Fig. 4 A photograph of the Airship Experiments.

Development of High Efficient Phased Array for Microwave Power Transmission of Space Solar Power Satellite/Station in Kyoto University

Naoki Shinohara [(1)]

[(1)] Research Institute for Sustainable Humanosphere, Kyoto University
shino@rish.kyoto-u.ac.jp

Keywords: SPS, Microwave Power Transmission, Phased Array

Abstract: The SPS (Space Solar Power Satellite/Station) is most huge and important application of the wireless power transmission via microwaves. For the SPS, we need 'higher efficient' 'higher accurate' 'lighter weight' 'lower cost' phased array with 'huge number of antenna elements'. However, there was no suitable phased array and no project of developing the phased array for the MPT. In Kyoto University, we have a governmental budget to develop the high efficient phased array as an experimental equipment for all SPS engineers. We are developing the phased array with GaN semiconductors. In the phased array, there are software phase adjustments with REV (Rotating Electromagnetic Vector) method and software retrodirective target detecting with mono pulse pilot signal for beam controlling

1. Introduction

The SPS (Space Solar Power Satellite/Station) is most huge and important application of the wireless power transmission via microwaves. For the SPS, we need 'higher efficient (>75% @ JAXA2006[1], >85% @ NASA/ DOE1980[2])' 'higher accurate (<5-10^{o} which include DOA error, structure error, etc. @JAXA2004[3])' 'lighter weight (<2g/W @ JAXA2005[4])' 'lower cost (<300 yen/W @ JAXA2006[1])' phased array with 'huge number of antenna elements (>20x10^{9} elements @ JAXA2005[4])'. However, there was no suitable phased array and no project of developing the phased array for the MPT. For military use, <10,000 elements phased array is used for the radar[5].We have to develop the advanced phased array for the SPS.

2. Phased Array Equipment in Kyoto University

In Kyoto University, we have a governmental budget to develop the high efficient phased array as experimental equipment for all SPS engineers (Fig.1). We are developing the phased array as following parameters ;:

1) 5.8GHzCWN0N
2) Separated module antenna/active circuits system
3) rigid antenna plane
4) 256 elements
5) active phased array with 1 active circuit for 1 antenna
6) 1.5kW output microwave power
7) F class power amplifiers with GaN FETs
8) > 7W output in microwave high power amplifier as final stage
9) > 70% power added efficiency in microwave high power amplifier as final stage
10) > 40% as total DC-microwave conversion efficiency
11) 5-bit MMIC phase shifters

12) <30cm thickness as universal experimental equipment

In the phased array, there are software phase adjustments with REV (Rotating Electromagnetic Vector) method and software retrodirective target detecting with mono pulse pilot signal for beam controlling. The phased array is developed with Mitsubishi Electric Corporation and it will be developed before the end of the FY2010. It is a multi-purpose equipment for the microwave power transmission research. You can use it through the inter-universities collaboration in RISH of Kyoto University. The Mitsubishi is developing the other phased array for the SPS with METI's budget in Japan. The METI's phased array is conducted by all Japan SPS committee in USEF and it will be developed in FY2013[6]. This is a first trial of very thin-type (<30mm) phased array development.

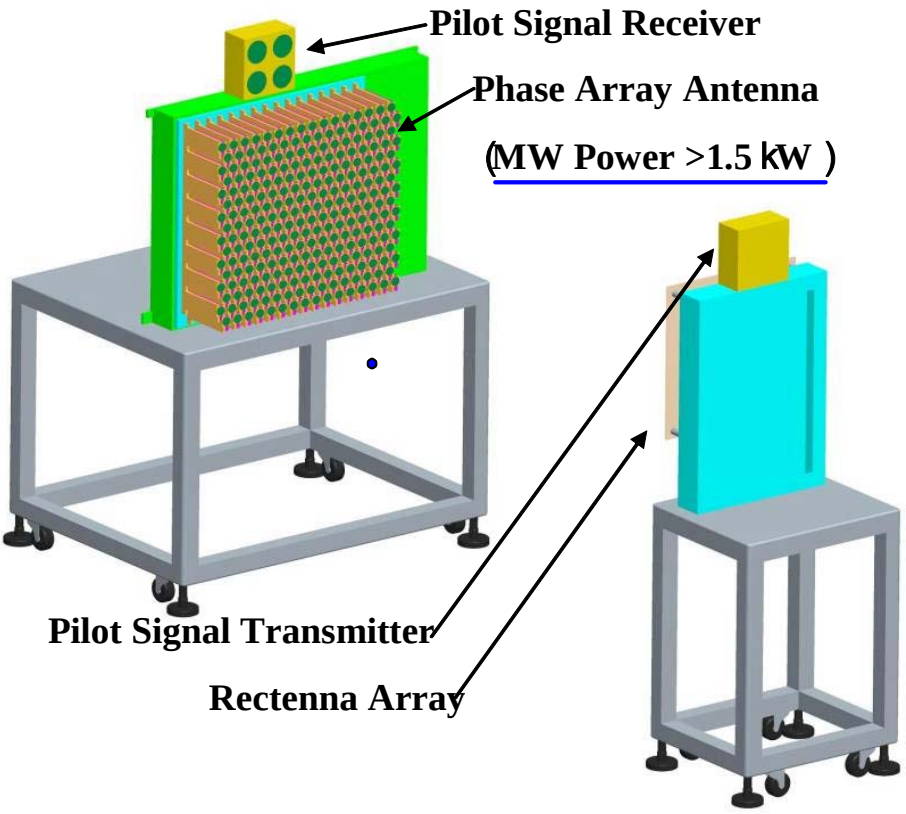

Fig. 1 Phased Array Equipment in Kyoto University

3. Rectenna Equipment in Kyoto University

We are also developing a rectenna array for the phased array equipment as shown in Fig.1. The high efficient weak power rectennas are adopted in the equipment. The parameters for the rectenna array are as follows ;

1) 5.8GHzCWN0N
2) 256 elements
3) >50% @ 1mW microwave input without LPF
4) Frequency Selective Surface (FSS) for suppression of re-radiation
5) Load control system for keeping load matching

Mitsubishi Electric Corporation and Kyoto University developed the high efficient weak power rectennas as shown in Fig.2[7]. It included LPF for suppression of re-radiation. However, we choose FSS[8] for suppression of re-radiation in the rectenna array. It is easy to put on/away in front of the rectenna array. It means that it is easy to use the rectenna array for multi-purposes.

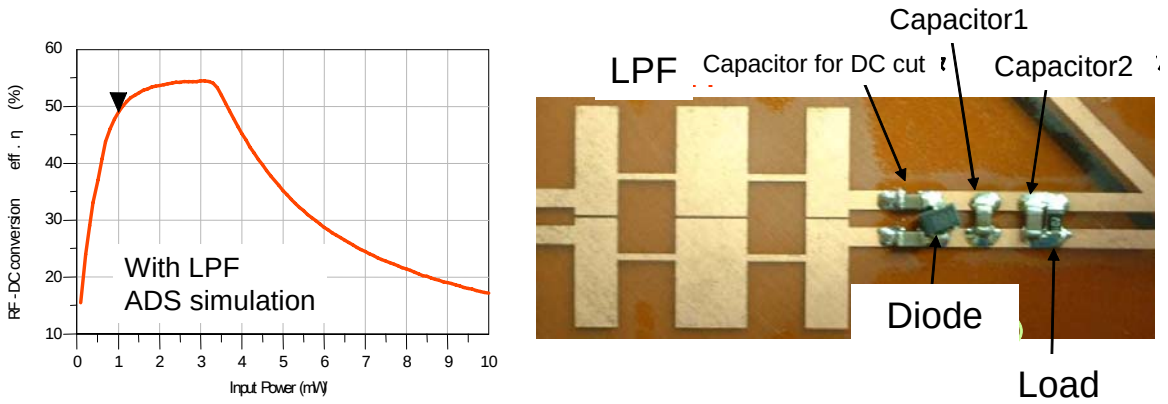

Fig. 2 High efficient weak power rectenna

4. Additional Equipment for the Phase Array in Kyoto University

Additionally we develop some experimental equipment for the phased array. We adopt the other DOA algorism and experimental equipment except REV method. 'PAC (Position and Angle Correction) method', 'Closed loop method', and 'Parallel method' will be installed. The 'PAC method' detects the position error of each antenna panel by using the pilot beam from the rectenna, and corrects this error for the high efficient beam forming. The 'Parallel method' uses phase modulation signals to achieve same purpose as 'PAC method'. The 'Closed loop method' monitors the beam direction error at rectenna and corrects this error for the high accuracy beam direction controlling. These algorisms are proposed by Mitsubishi Heavy Industry LTD. (MHI). We can carry out the DOA and beam forming experiments with these three algorisms in the phased array equipment. MHI will develop two additional experimental equipments for the rectenna array. One is an experimental equipment to suppress re-ration from the rectenna array. The other is an equipment to control optimum load for the rectenna array.

IHI Aerospace will develop the other phase control system with PLL. The phase control system will consist of phase command equipment, phase shifters, PLL control units, power amplifiers and heat rejection antennas. The system conforms the output of final power amplifier to the phase shift command by giving the output phase information of the final power amplifier to the PLL control units. This system will make it possible to correct phase variation of the power amplifier output automatically. IHI Aerospace will also develop 'taper' rectenna array composed of two types of rectennas optimized to different microwave input power. We can carry out experiments of rectenna connection by using the rectenna array.

5. Conclusions

In Japan, 'Basic plan for space policy' was established by Strategic Headquarters for Space Policy in June 2009. This Basic Plan for Space Policy forged this time is based on the Basic Space Law established in May 2008 and is a Japan's first basic policy relating to space activities. In the plan, the SPS was selected on measure nine systems and programs for the use and R&D of space as follows;

"As a program that corresponds to the following major social needs and goals for the next 10 years, a Space Solar Power Program will be targeted for the promotion of the 5-year development and utilization plan." and "Government will conduct ample studies, then start technology demonstration project in orbit utilizing "Kibo" or small sized satellites within the next 3 years to confirm the influence in the atmosphere and system check."[9][10]. The new equipments of the WPT in Kyoto University will be used for advancing the SPS based on the 'Basic plan for space policy'. We also use the results of development of METI's phased array project for the SPS. We will use both special phased array to advance the SPS in Japan and in the world.

References

[1.] Research and Study of SSPS (Space Solar Power System) (in Japanese), JAXA/MRI, Science and Technology Agency, 2005
[2.] US Department of Energy and NASA; Satellite Power System; Concept Development and Evaluation Program, Reference System Report, Oct. 1978 (Published Jan. 1979).
[3.] Research and Study of SSPS (Space Solar Power System) (in Japanese), JAXA/MRI, Science and Technology Agency, 2007
[4.] Research and Study of SSPS (Space Solar Power System) (in Japanese), JAXA/MRI, Science and Technology Agency, 2006
[5.] E. Brookner, "Phased Arrays and Radars —Past, Present and Future", *Microwave Journal*, Cover Feature, Jan. 2006.
[6.] N. Shinohara, "Development of High Efficient Phased Array for Microwave Power Transmission of Space Solar Power Satellite/Station", *Proc. of APS/URSI2010*, in print, July 2010.
[7.] N. Shinohara, H. Matsumoto, A. Yamamoto, H. Okegawa, T. Mizuno, H. Uematsu, H. Ikematsu, and I. Mikami, "Development of High Efficiency Rectenna at mW input (in Japanese)", *Tech. Report of IEICE* SPS2004-08 (2005-01), pp.15-20, Jan. 2005
[8.] Z. L. Wang, K. Hashimoto, N. Shinohara, and H. Matsumoto, "Frequency Selective Surface for Microwave Power Transmission", *IEEE-Trans. MTT*, Vol. 47, No.10, pp.2039-2042, 1999
[9.] http://www.kantei.go.jp/jp/singi/utyuu/basic_plan.pdf
[10.] http://www.kantei.go.jp/jp/singi/utyuu/keikaku/pamph_en.pdf

On the Optimization of Side-Lobes in Large Antenna Arrays for Microwave Power Transmission

B. Shishkov[(1)], N. Shinohara[(2)], H. Matsumoto[(3)], K. Hashimoto[(2)], T. Mitani[(2)]

[(1)] Institute of Mathematics and Informatics, Bulgarian Academy of Sciences, Sofia, Bulgaria, bshishkov@math.bas.bg

[(2)] Research Institute for Sustainable Humanosphere, Kyoto University, Kyoto, Japan, shino@rish.kyoto-u.ac.jp; kozo@rish.kyoto-u.ac.jp; mitani@rish.kyoto-u.ac.jp

[(3)] Kyoto University, Kyoto, Japan, matsumoto@hq.kyoto-u.ac.jp

Keywords: microwave power transmission, large antenna array, uniform spacing, random spacing, spatial and amplitude tapering, side lobe level, grating lobes, workspace, transmitting efficiency.

Abstract: The concept of placing enormous Solar Power Satellite (SPS) systems in space represents one of a handful of new technological options that might provide large scale, environmentally clean base load power to terrestrial markets. Recent advances in space exploration have shown a great need for antennas with high resolution, high gain and low side lobe level (SLL). The last characteristic is of paramount importance especially for the Microwave Power Transmission (MPT) in order to achieve higher transmitting efficiency (TE) and higher beam collection efficiency (BCE). In order to achieve low side lobe levels, statistical methods play an important role. Various interesting properties of a large antenna arrays with randomly, uniformly and combined spacing of elements have been studied, especially the relationship between the required number of elements and their appropriate spacing from one viewpoint and the desired SLL, the aperture dimension, the beamwidth and TE from the other. We propose a new unified approach in searching for reducing SLL by exploiting the interaction of deterministic and stochastic workspaces of proposed algorithms. Our models indicate the side lobe levels in a large area around the main beam and strongly reduce SLL in the entire visible range. A new concept of designing a large antenna array system is proposed. Our theoretic study and simulation results clarify how to deal with the problems of side lobes in designing a large antenna array, which seems to be an important step toward the realization of future SPS/MPT systems.

1. Introduction

For the conventionally designed arrays where all elements are spaced uniformly, there exists an upper limit to the spacing if the grating lobes are not permitted to appear in the visible region.

The deterministic non-uniformly spaced algorithms are numerically difficult to implement for large antenna arrays.

The randomly spaced algorithms (the concept of “thin” arrays) are easier to implement, but need of further study in order to determine their merits and drawbacks.

In this paper we develop further the existing algorithms [1-4] and our previous research [5-8], proposing a new techniques to deal with side lobes and grating lobes.

2. Randomly and Uniformly Spaced Arrays

Consider a linear array along the X axis in Cartesian coordinate system and suppose we are given N+1 equally excited antenna elements by isotropic radiation to be placed at random within an aperture defined by $|X| \le a/2$ in wavelength, in accordance with a common probability density function (pdf) $f(x)$.

Assume that the random positions $\{X_n\}$ are independent. Then for each sample vector $\{X_n\}$, $X_n \in R^{N+1}$, there is a sample radiation pattern function given by the magnitude of [2]

$$P(u) = \frac{1}{N+1} \sum_{n=-N/2}^{N/2} \exp(jux_n) \tag{1a}$$

$$P(\theta) = \frac{1}{N+1} \sum_{n=-N/2}^{N/2} \exp\{j2\pi(\sin\theta - \sin\alpha)\} X_n \tag{1b}$$

θ - the observation angle measured from the normal to the array axis
α - the scan angle measured from the normal to the array axis
$u = a\pi(\sin\theta - \sin\alpha)$ - the observation angle parameter
$\{x_n = 2X_n / a\}$ - normalized workspace
$a = Nd_x$ - the aperture, measured in wavelength.

We can determine the array factor (AF) $= |P(u)|^2$ or $|P(\theta)|^2$ as a random function. In (1) if $\{X_n\}$ is considered as positions of conventional uniform spacing $\{X_n = nd_x\}$ the model is automatically transformed in the deterministic one – see (2).

$$P(\theta) = \frac{1}{N+1} \sum_{n=-N/2}^{N/2} \exp\{j2\pi(\sin\theta - \sin\alpha)\}\, nd_x = \frac{1}{N+1} \sum_{n=-N/2}^{N/2} \exp(j\psi_n) \tag{2}$$

where $\psi_n = \frac{2\pi}{\lambda}(\sin\theta - \sin\alpha) nd_x$ and normalized work space equals to $x_n = 2nd_x / N$. We can determine the array factor AF $= |P(\theta)|^2$ as a periodic function [3].

A linear array with its peak at α can also have other peak values subject to the choice of spacing d_x. This ambiguity is apparent, since the summation also has a peak whenever the exponent is some multiple of 2π or

$$\frac{2\pi}{\lambda}(\sin\theta - \sin\alpha) d_x = 2\pi p, \quad p = \pm(1,2,...) \tag{3}$$

Such peaks are called grating lobes and are shown from the above to occur at angles θ_p such that

$$\sin\theta_p = \sin\alpha + \frac{p\lambda}{d_x}, \quad p = \pm(1,2,...) \tag{4}$$

for values of p that define an angle with a real sine $\left(\left|\sin\theta_p\right| \le 1\right)$. This implies that the maximum element spacing for an array scanned to a given angle α at frequency f is $\lambda/2$.

The model (1) is pure stochastic model and was first investigated by Y.T. Lo [2] and will be coded as RA (random array). The model (2) is well known deterministic model of uniform spacing and will be coded as UA (uniform array). In [2, 3] was found the distribution of maximum of SLL outside of the main beam region and that at any "*u*" the probability of antenna response being less than any level *r* is given by

$$\Pr\left\{ \left|P(u)\right| < r, all\ u : \delta < |u| < 2\pi a \right\} \approx \left[1 - \exp^{-Nr^2}\right]^{[4a]} \tag{5}$$

$$\varphi(u) = E\{\exp(jux)\} = \int_{-\infty}^{\infty} f(x)\exp(jux)dx \tag{6}$$

where δ is the first positive zero of characteristic function and the bracket $[4a]$ is the integer part of $4a$. This is a chi-squared distribution with two degrees of freedom.

This expression gives the number of elements required to achieve the desired SLL (maximum, not average) with predetermined confident probability of success such as 0.9, 0.95, etc.

The equation (6) is important. It is seen that the mean pattern is identical to the pattern which would be obtained by taking $f(x)$ as a continuous aperture excitation.

3. Combined Stochastic Algorithm

Let's consider the sample radiation pattern function given by the magnitude

$$P(\theta) = \frac{1}{N+1}\sum_{n=-N/2}^{N/2} \exp\{j2\pi(\sin\theta - \sin\alpha)(nd_x + X_n)\} \tag{7}$$

where the positions are a linear combination of deterministic one and random one. The AF $\left|P(\theta)\right|^2$ consists of two parts: The first part is a periodic function and if $d_x > \lambda/2$ grating lobes can not be avoided.

Unlike, periodicity of the second part is strongly destroyed from random positions of x_n. It is equivalent of non-uniform spacing and there is no grating lobes, but on the price of relatively high SLL.

The basic role of the algorithm for optimization both side lobes and grating lobes play positions $\{X_n\}$ of antenna elements. This vector $\{X_n\}$, $X_n \in R^{N+1}$, or its normalized version $\{x_n\}$ creates the work space which plays a fundamental role. Generally $\{x_n\} = \{x_{n\det}\} + \{x_{nrand}\}$. In section 2, we have considered the models $\{x_{nrand}\}$ and $\{x_{n\det}\}$ separately that were called RA and UA respectively.

Let's consider the model (7) over

$$\{x_n\} = \{x_{n\det}\} + \{x_{nrand}\}, \tag{8}$$

which operates over two times larger workspace. It is non-uniform spacing stochastic algorithm, which suppresses grating lobes, but with respect to SLL it is almost the same as RA algorithm, even with two time larger aperture.

Let's put forward the model (7) over

$$\{x_n\} = \{x_{n\,\mathrm{det}}\} + \{\varepsilon_{nrand}\} \tag{9}$$

where $\{\varepsilon_{nrand}\} = \{x_{nrand}\}/N$ is a small random perturbation of the deterministic workspace and N is the number of elements. This model will be called Combined Stochastic Algorithm (CSA) and will compete with existing UA and RA algorithms. Our algorithm is a non-uniform spacing stochastic algorithm, where random workspace is strongly reduced, and positions $\{x_{nrand}\}/N$ play the role of very small random perturbations around the deterministic positions $\{x_{n\,\mathrm{det}}\}$. The aperture of antenna array remains unchanged. This algorithm as we will see has any advantages with respect to both UA and RA algorithms. To compare all these models with respect to near and far SLL is more convenient to represent array factor

$$AF = |P(\theta)|^2 \tag{10}$$

or its averaged version as a function of observation angle θ. So we can directly observe, that when N increases the beamwidth becomes narrower and the effect of broadening the beamwidth, when we apply non-uniform amplitude tapering.

4. Further Development of the Problem of Minimization of SLL

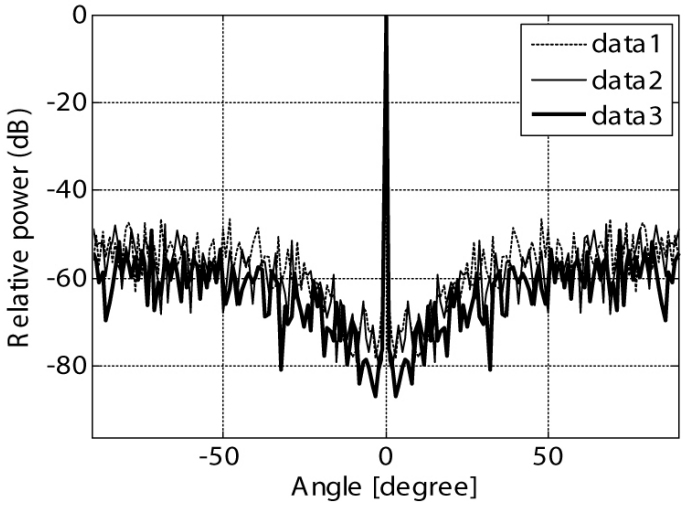

Fig.1 Radiation characteristics of the ICSA, *N*=16000 (data1), *N*=32000, (data2) and *N*=64000 (data3), $d_{av} = 2\lambda$

Let's rewrite Eqn. (8) as follows:

$$\{x_n\} = c_1\,\{x_{n\,\mathrm{det}}\} + c_2\{x_{nrand}/N\} \tag{11}$$

The influence of these two constants c_1 and c_2 over the behavior of the workspaces $\{x_{n\,\mathrm{det}}\}$ and $\{x_{nrand}\}$ reveals an interesting properties of our algorithm, which was studied in previous section with $c_1 = 1$ and $c_2 = 1$. We have found experimentally the following set of constants $\{c_1 = 0.93,\ c_2 = 0.1\}$ to

improve minimization of SLL and no gratings lobes appear – see Fig. 1. Let's call this model improved combined stochastic algorithm (ICSA). From now on into entire visible range will be used suitable amplitude excitation function which concerns the beamwidth and influence to transmitting efficiency. On Fig.2 is represented a Block Chart of Considerable SPS transmitting array.

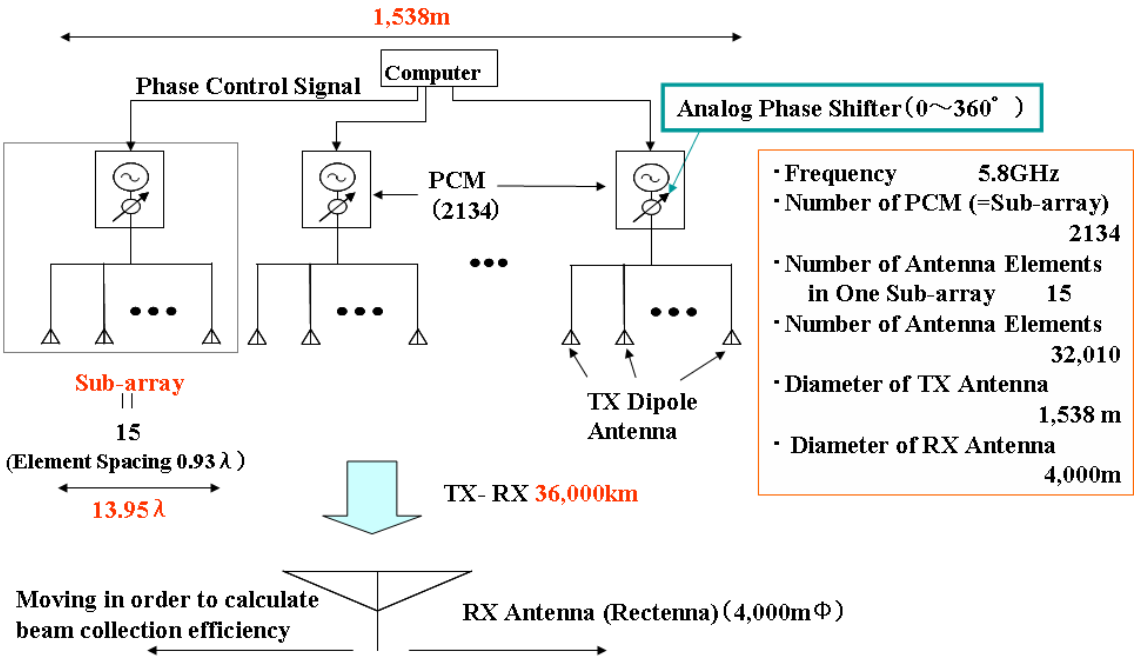

Fig. 2 Block Chart of Considerable SPS transmitting array.

5. Transmitting Efficiency

To be determined the transmitting efficiency (TE) will be used the area under the peak SLL and the area under the main beam. Then transmitting efficiency can be presented as follows

$$TE = \frac{MB_{area}}{MB_{area} + SLL_{area}} \tag{12}$$

where MB_{area} is main beam area and SLL_{area} is side lobe area. The main beam area is defined as 4 kmϕ at the center of beam in this paper.

When N increases, the area of main beam decreases, but average SLL decreases too. It is not accurate to use average SLL, but rather the envelope of peak values of SLL obtained with large amount of observation points $N_{data} = 1801$ in our simulations.

In the Table 1 are presented the features of the transmitting part of the system for MPT. η_{1D} is one dimensional transmitting efficiency of linear array, calculated on the base of the equation (12) and η_{2D} is two dimensional transmitting efficiency calculated as product of η_{1D} by itself and finally used; The diameter of transmitting antenna in [m] is indicated for different number of antenna elements.

The basic conclusion is that with ICSA we can achieve a low SLL and no grating lobes appear with reduced number of antenna elements in comparison with conventional Uniform array.

Table 1 Characteristics of the transmitting part of the system for MPT

Number of PCM	Number of Antenna Elements	Number of elements in Sub-array	Power [GW]	Diameter[m]	TE $d_{av}=c_1\lambda$ η_{1D} η_{2D}
1600	16000	10	1.02	769	0.9067 0.8221
2134	32010	15	1.82	1538	0.8831 0.7799
2560	64000	25	2.62	3076	0.8580 0.7362

6. Conclusion

1. The pure stochastic algorithms with average spacing more than λ (thinned arrays) really suppress grating lobes but on the price of sufficiently high SLL. So a large amount of elements need to decrease a little SLL.

2. Deterministic non-uniformly spaced algorithms are numerically difficult to implement for large antenna arrays.

3. We propose a new combined stochastic algorithm. It is a new unified approach in searching for reducing SLL by exploiting the interaction of deterministic and stochastic workspaces. It is a non-uniform spacing stochastic algorithm. Really, stochastic part of our algorithm plays the role of very small perturbations of deterministic workspace. So we have succeeded to reduce SLL considerably with out grating lobes appear and achieve high TE and BCE.

4. We propose a new concept of designing the transmitting part of the whole system for MPT.

5**.** Our study and simulation results clarify how to deal with the problems of side lobes and grating lobes in designing a large antenna array, which seems to be an important step toward the realization of future SPS/MPT systems.

References

[1.] R. F. Harrington, “Sidelobe Reduction by Nonuniform Element Spacing”, *IRE Trans. AP,* Vol. 9, March 1961, pp. 187-192.

[2.] Y. T. Lo, “A Mathematical Theory of Antenna Arrays with Randomly Spaced Elements”, *IEEE Trans. AP*, Vol. 12, May 1964, pp. 257-268.

[3.] R. J. Mailloux, “Phased Array Antenna Handbook”, *Artech House, Inc*., 2005.

[4.] H. Matsumoto, “Research on Solar Power Satellites and Microwave Power Transmission in Japan”, *IEEE microwave magazine*, December 2002, pp. 36-45.

[5.] H. Matsumoto, N. Shinohara and B. Shishkov, “Design Method of Array Antenna Instrument and its Relevant Instrument”, *Patent No. 2003-368387*, Oct. 29, 2003, (pending, Japan).

[6.] B. Shishkov, H. Matsumoto and N. Shinohara. “Probabilistic Approach to Design of Large Antenna Arrays”, *Pliska Studia Mathemarica Bulgarica,* Vol. 17, pp.249-269, 2005.

[7.] Shinohara, N., B. Shishkov, H. Matsumoto, K. Hashimoto, A.K.M. Baki “New Stochastic Algorithm for Optimization of Both Side-lobes and Grating lobes in Large Antenna Arrays for MPT”, *IEICE Transactions on Communications*, Vol.E91-B, No.1, pp.286-296, Jan.2008.

[8.] Shishkov, B., K. Hashimoto, H. Matsumoto, N. Shinohara, T. Mitani “ Direction Finding Estimators of Cyclostationary Signals in Array Processing for Microwave Power Transmission”, *Pliska Stud. Math. Bulgar*., volume 19, 2009, pp. 245–268.

AUTHOR INDEX

Family, Name	From	e-mail	page
Lugaz, Noé	USA	nlugaz@ifa.hawaii.edu	131
Magnes, W.	Austria		109
Materassi, Massimo	Italy	massimo.materassi@fi.isc.cnr.it	143
Matsumoto, Hiroshi	Japan	matsumoto@hq.kyoto-u.ac.jp	165
Mebarki, R.	Algérie		117
Mihara, Shoichiro	Japan	mihara@usef.or.jp	149
Mitani, Tomohiko	Japan	mitani@rish.kyoto-u.ac.jp	157, 165
Miura, Amane	Japan	amane@nict.go.jp	5, 57
Molchanov, O.	Russia		113
Moreno, J.J. Lopez	Spain	lopez@iaa.es	127
Moy, Christophe	France	christophe.moy@supelec	33
Nagano, Kenji	Japan		157
Narahashi, Shoichi	Japan	narahashi@nttdocomo.co.jp	21,29
Nenovski, P.	Bulgaria	nenovski@geophys.bas.bg	109, 113
Nickolov, Eugene	Bulgaria	eugene.nickolov@nlcv.bas.bg	25
Ohkawara, Junya	Japan	ookawaraj@nttdocomo.co.jp	21
Okada, Minoru	Japan	mokada@is.naist.jp	83
Okazaki, Hiroshi	Japan	okazakih@nttdocomo.co.jp	29
Orikasa, Mitsuteru	Japan	t.orikasa@nict.go.jp	5
Ozawa, Jun	Japan	joza19@gmail.com	75
Palicot, Jacques	France	jacques.palicot@supelec	33
Panayırcı, Erdal	Turkey	eepanay@khas.edu.tr	37
Parrot, Michel	France	mparrot@cnrs-orleans.fr	117
Potapov, Viacheslav	Russia	aletam@mail.ru	79
Prattes, Gustav.	Austria	gustav.prattes@oeaw.ac.at	109, 113
Radev, Dimitar	Bulgaria	dradev@abv.bg	41, 71
Radeva, Svetla	Bulgaria	svetla_ktp@abv.bg	41
Randrianboarison, O.	France	randriam@cnrs-orleans.fr	127
Rohling, Hermann	Germany	rohling@tu-harburg.de	9
Roussev, Ilia I.	USA	iroussev@ifa.hawaii.edu	131
Rozhnoi, A.	Russia		113
Ruzhin, Ya Yu	Russia		105
Saito, Takashi	Japan	saito@usef.or.jp	149
Sato, Masaski	Japan	sato@nict.go.jp	5
Schwingenschuh, Konrad.	Austria	konrad.schwingenschuh@oeaw.ac.at	109, 113, 127
Shinohara, Naoki	Japan	shino@rish.kyoto-u.ac.jp	157, 161, 165
Shishkov, Blagovest	Bulgaria	bshishkov@math.bas.bg	165
Shmelev, Alexander	Russia	abshmelev@yahoo.com	45
Simoes, F.	USA	fernando.a.simoes@nasa.gov	113, 127
Slavova, Angela	Bulgaria	slavova@math.bas.bg	49
Sokolov, Igor V.	USA	igorsok@umich.edu	131
Solovieva, M.	Russia		113
Sotin, C.	USA	christophe.sotin@jpl.nasa.gov	127
Spineanu, Florin	Romania	spineanu@nipne.ro	139
Stachel, M.	Austria		109
Stangl, G.	Austria		113
Stankovski, Dragan	Bulgaria	draganstankovski@gmail.com	41
Suzuki, Ryutaro	Japan	ryutaro@nict.go.jp	5, 57
Suzuki, Yasunori	Japan	suzukiyasu@nttdocomo.co.jp	21

ISRSSP 2010

Organized by

JICREST

In cooperation with:

INSTICC

1869 BULGARIAN ACADEMY OF SCIENCES

TECHNICAL UNIVERSITY of Sofia

Technical Co-sponsorship:

Ruse UNIVERSITY "Angel Kanchev"

Sofia Municipality

ARMSTECHNO Ltd.

Proceedings of ISRSSP 2010
International Symposium on Radio Systems and Space Plasma

http://www.isrssp.org